

**Alma Mater Studiorum - Università di Bologna**

**DOTTORATO DI RICERCA IN  
INGEGNERIA BIOMEDICA, ELETTRICA E DEI SISTEMI**

Ciclo XXXV

**Settore Concorsuale:** 09/E1 - ELETTROTECNICA

**Settore Scientifico Disciplinare:** ING-IND/31 - ELETTROTECNICA

**ANALYSIS AND DESIGN CONSIDERATIONS OF  
RESONATOR ARRAYS FOR INDUCTIVE POWER  
TRANSFER SYSTEMS**

**Presentata da:** Mattia Simonazzi

**Coordinatore Dottorato**

Michele Monaci

**Supervisore**

Leonardo Sandrolini

**Co-supervisore**

Gabriele Grandi

**Esame finale anno 2023**



*To all those who have supported me  
in this journey of intellectual  
and personal growth.*



# Acknowledgements

With immense pleasure and deep sense of gratitude, I wish to express my sincere thanks to my supervisor Prof. Leonardo Sandrolini. Without his motivation and continuous encouragement, this research would not have been successfully completed. I offer him my sincere appreciation for the learning opportunities he offered me, having been the mentor and a point of reference in these years. This work is the result of a continuous exchange of knowledge. For his continuous support, I am truly grateful.

I express my sincere thanks to Prof. Emeritus Ugo Reggiani, for his kind help and support whenever needed, allowing me to widen my research from various perspectives. I like to acknowledge the support rendered by Prof. Andrea Mariscotti in several ways throughout my research work. His guidance and brilliant ideas allowed me to progress in times of trouble.

I express my sincere thanks to the colleagues of the University of Pisa and, in particular, Prof. Sami Barmada, Nunzia Fontana, Agostino Monorchio and Dr. Danilo Brizi for their support and encouragement, alongside guided me in the exotic world of metamaterials.

I like to acknowledge the support rendered by my colleagues in several ways throughout my research work, with whom I shared difficult but also happy and funny times. Really thanks to Antonio, Alessandro and Riccardo. The continuous exchange of ideas and experiences has allowed me to greatly enrich my research.

I wish to extend my profound sense of gratitude to my family for all the sacrifices they made during my research and also providing me with moral support and encouragement whenever required.

Finally, I would like to thank Carlotta for her constant encouragement and moral support along with patience and understanding.



# Abstract

In the frame of inductive power transfer (IPT) systems, arrays of magnetically coupled resonators have received increasing attention as they are cheap and versatile due to their simple structure. They consist of magnetically coupled coils, which resonate with their self-capacitance or lumped capacitive networks.

Of great industrial interest are planar resonator arrays used to power a receiver that can be placed at any position above the array. A thorough circuit analysis has been carried out, first starting from traditional two-coil IPT devices. Then, resonator arrays have been introduced, with particular attention to the case of arrays with a receiver. To evaluate the system performance, a circuit model based on original analytical formulas has been developed and experimentally validated. The results of the analysis also led to the definition of a new doubly-fed array configuration with a receiver that can be placed above it at any position. A suitable control strategy aimed at maximising the transmitted power and the efficiency has been also proposed. The study of the array currents has been carried out resorting to the theory of magneto-inductive waves, allowing useful insight to be highlighted. The analysis has been completed with a numerical and experimental study on the magnetic field distribution originating from the array.

Furthermore, an application of the resonator array as a position sensor has been investigated. The position of the receiver is estimated through the measurement of the array input impedance, for which an original analytical expression has been also obtained. The application of this sensing technique in an automotive dynamic IPT system has been discussed.

The thesis concludes with an evaluation of the possible applications of two-dimensional resonator arrays in IPT systems. These devices can be used to improve system efficiency and transmitted power, as well as for magnetic field shielding.



# Contents

<b>1</b>	<b>Introduction</b>	<b>21</b>
1.1	Automotive IPT Systems . . . . .	24
1.1.1	Automotive IPT Standards . . . . .	26
1.2	Multi Coil IPT Systems . . . . .	26
1.2.1	Magneto-Inductive Waves . . . . .	28
1.3	Outline of the Thesis . . . . .	28
<b>2</b>	<b>Basics of Inductive Power Transfer (IPT)</b>	<b>31</b>
2.1	Physical Principle: the Magnetic Induction . . . . .	31
2.2	Coils Circuit Modelling . . . . .	32
2.2.1	Coil Power Losses . . . . .	37
2.2.2	Core Losses . . . . .	39
2.2.3	Power and Efficiency . . . . .	40
2.2.4	Voltage Gain and Transadmittance . . . . .	43
2.3	Compensation Networks . . . . .	44
2.3.1	Series-Series compensation . . . . .	46
2.3.2	Series-Parallel Compensation . . . . .	48
2.3.3	Series-Series/Parallel Compensation . . . . .	49
2.3.4	Series/Parallel Primary Compensation . . . . .	50
2.4	Power Source . . . . .	52
2.4.1	Zero Voltage Switching . . . . .	53
2.5	Receiver Circuit . . . . .	54
2.6	Conclusions . . . . .	56
<b>3</b>	<b>Circuit-Based Design of IPT Systems</b>	<b>57</b>
3.1	Design Procedure . . . . .	57
3.2	Load Modelling: Battery Pack for Automotive Applications . . . . .	59
3.3	Design of a Series-Parallel Compensated IPT System . . . . .	60
3.3.1	Load Matching . . . . .	62
3.3.2	Design for Constant Voltage Output . . . . .	63
3.3.3	Design for Coupling Independent ZPA . . . . .	64
3.3.4	Case Study . . . . .	65
3.3.5	Efficiency Characterisation . . . . .	69
3.4	Design of a Series-Series Compensated IPT System . . . . .	70

3.4.1	Case Study . . . . .	72
3.5	Conclusions . . . . .	75
<b>4</b>	<b>Resonator Arrays for IPT</b>	<b>77</b>
4.1	1D Resonator Arrays . . . . .	79
4.1.1	Resonator Array Equivalent Circuit . . . . .	80
4.1.2	Two-port Representation . . . . .	82
4.1.3	Model Validation . . . . .	83
4.1.4	Results . . . . .	84
4.1.5	Power and Efficiency . . . . .	84
4.2	Resonator Arrays with a Receiver . . . . .	88
4.2.1	Circuit Model . . . . .	89
4.2.2	Two-port Representation . . . . .	91
4.2.3	Model Validation . . . . .	93
4.2.4	Results . . . . .	94
4.2.5	Transformer Equivalent Circuit . . . . .	98
4.3	Experimental Validation . . . . .	103
4.3.1	Power and Efficiency . . . . .	107
4.4	Doubly-Fed Resonator Array for Maximum Efficiency and Power Transfer . . . . .	112
4.4.1	Design Considerations . . . . .	113
4.5	Conclusions . . . . .	115
<b>5</b>	<b>Distribution of Currents in Resonator Arrays: Magneto-inductive waves and Standing Wave Pattern</b>	<b>117</b>
5.1	Magneto-Inductive (MI) Waves . . . . .	118
5.2	Standing Waves and Current Peaks . . . . .	121
5.2.1	Numerical Simulations . . . . .	123
5.2.2	Lossless and low-loss array . . . . .	125
5.3	Resonator array with a receiver . . . . .	126
5.3.1	Equivalent transmission line . . . . .	127
5.3.2	Perfectly aligned receiver . . . . .	128
5.3.3	Receiver coupled to two array resonators . . . . .	129
5.3.4	Numerical Simulations . . . . .	131
5.4	Experimental verification . . . . .	138
5.5	Magnetic Near-Field of the Resonator Array with a Receiver . . . . .	139
5.5.1	Shielding the IPT System . . . . .	143
5.6	Conclusions . . . . .	144
<b>6</b>	<b>Receiver Coil Position Sensing in Resonator Arrays</b>	<b>147</b>
6.1	Input Impedance of a Resonator Array with a Receiver . . . . .	148
6.1.1	Simulations and Discussion . . . . .	151
6.2	Resonator Array as a Linear Position Sensor: Design and Choice of the Array Parameters . . . . .	155

---

6.2.1	Termination conditions . . . . .	155
6.2.2	Sensitivity . . . . .	156
6.2.3	Algorithm for the External-Coil Position Detection . . . . .	156
6.3	Receiver-Coil Location Detection in a Dynamic Inductive Power Transfer System for Electric Vehicle Charging . . . . .	163
6.3.1	System Architecture and Receiver Location Detection . . . . .	164
6.3.2	Simplified Receiver Location Algorithm . . . . .	173
6.4	Conclusions . . . . .	175
<b>7</b>	<b>2D Resonator Arrays in IPT Systems: Considerations for Future Works</b>	<b>177</b>
7.1	2D Resonator Arrays for IPT . . . . .	177
7.2	Currents in 2D Resonator Arrays . . . . .	178
7.2.1	Effect of the resonator quality factor on current distribution . . . . .	180
7.2.2	Effect of couplings on current distribution . . . . .	181
7.2.3	Controlling the Resonator Currents: Terminated 2D Array . . . . .	184
7.2.4	Optimisation Procedure . . . . .	186
7.3	2D Resonator Arrays as Metamaterials . . . . .	187
7.3.1	Metamaterial for Magnetic Field Focusing . . . . .	189
7.3.2	Optimisation Procedure . . . . .	191
7.3.3	2D Resonator Array for Magnetic Field Shielding . . . . .	194
7.3.4	Optimisation Procedure . . . . .	195
7.4	Conclusions . . . . .	196
<b>8</b>	<b>Conclusions</b>	<b>199</b>
<b>A</b>	<b>Inductance Calculation</b>	<b>203</b>



# List of Figures

1.1	Tesla's resonant coils for wireless power transmission [1]. . . . .	22
1.2	Classification of wireless power transfer technologies. . . . .	23
1.3	(a) DD pads architecture as originally proposed in [2] and (b) layout of DD pad described in the SAEj2954 [3] for WPT3/Z1 (see categories in [3]) system. . . . .	25
1.4	Schematic illustration of a 1D resonator array [4]. The power injected in the array reaches the receiver through the intermediate relay resonators. . . . .	27
1.5	Schematic illustration of a metasurface devoted to the magnetic field focusing in two-coil IPT system [5]. . . . .	28
2.1	Representation of coupled inductors: a) Schematic representation b) equivalent circuit representation. . . . .	34
2.2	T model equivalent circuit of an IPT system. . . . .	36
2.3	Transformer equivalent circuit of an IPT system. . . . .	37
2.4	Cross-section of (a) a generic Litz wire and (b) two turns of the winding considered in the analysis. . . . .	38
2.5	Coupled inductors equivalent circuit of an IPT system with winding resistances. . . . .	40
2.6	(a) generic two-port model fed by a real voltage source and powering a resistive load and (b) the Thévenin equivalent network comprising the cascade of the real voltage source and the two-port network and that powers a resistive load. . . . .	41
2.7	Series-series (SS) compensation of magnetically coupled coils. . . . .	46
2.8	Series-parallel (SP) compensation of magnetically coupled coils. . . . .	48
2.9	Series-series/parallel (SSP) compensation of magnetically coupled coils. . . . .	50
2.10	Schematic of (a) series/parallel - series (SPS) and (b) series/parallel - parallel (SPP) compensation topology. . . . .	51
2.11	(a) Schematic of an H-bridge inverter and (b) inverter leg voltage waveforms showing phase shift between inverter legs and the resulting output voltage waveform $v_{in}(t) = v_{ab}$ , with $v_{ab} = v_{ag} - v_{bg}$ . . . . .	53
2.12	Passive full bridge rectifier. . . . .	55

3.1	Flow chart illustrating the design steps for the IPT link with the compensation networks based on the load requirements. The green boxes indicate the specifications, the grey boxes the degrees of freedom and the blue boxes the calculation steps. . . . .	58
3.2	Characteristics of the battery pack: a) voltage and current profiles b) absorbed power and equivalent resistance. . . . .	60
3.3	Flow chart illustrating the design algorithm for the inductive coupling and the compensation networks based on the selected output characteristic. The load resistance $R_l$ and the coupling coefficient $k$ refer to actual parameters during variable operating conditions. . . .	61
3.4	Equivalent circuits of the resonant inductive link with primary and secondary decoupled inductors and series controlled voltage sources. .	64
3.5	( <b>a</b> ) Voltage gain magnitude and ( <b>b</b> ) input impedance angle as a function of the frequency for the inductive link designed for CV operations at $f_0 = 85$ kHz. . . . .	67
3.6	( <b>a</b> ) Voltage gain magnitude and ( <b>b</b> ) input impedance angle as a function of the frequency for the inductive link designed for coupling independent ZPA operations at $f_0 = 85$ kHz. . . . .	68
3.7	Input impedance angle as a function of the frequency for different coupling coefficients in case of inductive link designed for ( <b>a</b> ) CV output and ( <b>b</b> ) coupling independent ZPA operations at $f_0 = 85$ kHz.	69
3.8	Overall link efficiency of a WPT system designed for CV or coupling independent ZPA, operating at $f_0$ , as a function of the receiver equivalent load $R_l$ , for different coupling coefficients $k$ . . . . .	70
3.9	( <b>a</b> ) Transadmittance magnitude and ( <b>b</b> ) voltage gain magnitude as a function of the frequency for the SS compensated IPT link designed for CC operations at $f_0 = 85$ kHz. . . . .	73
3.10	Input impedance angle as a function of the frequency for different ( <b>a</b> ) receiver loads and ( <b>b</b> ) coupling coefficients of the SS compensated IPT link designed for CV operations at $f_0 = 85$ kHz. . . . .	74
3.11	Overall link efficiency as a function of the receiver equivalent load $R_l$ and for different coupling coefficients $k$ of the SS compensated IPT link designed for CV operations at $f_0 = 85$ kHz, operating at $f_0$ , . .	75
4.1	Schematic representation of (a) strongly misaligned IPT system (SPS) and (b) the same system with two intermediate relay coils. . . . .	78
4.2	Schematic representation of 1D resonator arrays in a (a) coaxial arrangement (b) planar structure along a line and (c) generic planar arrangement. The direction $x$ denoted by the dashed line indicates the path of the power travelling along the array. . . . .	79
4.3	Equivalent frequency-domain circuits of a resonator array. . . . .	81

4.4	Impedance matrix parameters for arrays with different numbers of resonators at the resonant frequency $f_0$ . The square markers refer to the formulas (4.10)-(4.12) and the circle markers to the numerical solution of (4.6). . . . .	85
4.5	Considering a different number of array resonators, (a) shows the optimal resistance values for maximum efficiency, (b) the maximum efficiency achievable with the considered resonator parameters and (c) the efficiency for different loads. . . . .	86
4.6	Equivalent Thévenin (a) voltage source and (b) impedance for arrays as a function of the number of cells. . . . .	87
4.7	Available power at the receiver port of the resonator array as a function of the number of cells. . . . .	88
4.8	Schematic representation of an IPT system with a resonator array and a receiver over it. . . . .	89
4.9	Equivalent circuit of an IPT system with a resonator array and a receiver over it. . . . .	90
4.10	Schematic representation of (a) an array of $n$ resonators with a receiver R over the $i$ th cell, terminated with $\hat{Z}_T$ and (b) the correspondent compacted array terminated with the equivalent impedance (4.21). . . . .	92
4.11	Impedance matrix parameters as a function of the receiver position for an array of 25 cells terminated in short-circuit. The square markers refer to the formulas (4.10)-(4.12) and the cross markers to the numerical solution of (4.6). . . . .	95
4.12	Impedance matrix parameters as a function of the receiver position for an array of 25 cells terminated in open-circuit. The square markers refer to the formulas (4.10)-(4.12) and the cross markers to the numerical solution of (4.6). . . . .	96
4.13	Impedance matrix parameters as a function of the receiver position for an array of 25 cells terminated in the optimal load. The square markers refer to the formulas (4.10)-(4.12) and the cross markers to the numerical solution of (4.6). . . . .	97
4.14	Equivalent frequency-domain circuits of a resonator array. . . . .	99
4.15	Real transformer parameters as a function of the receiver for an SC terminated array. . . . .	100
4.16	Real transformer parameters as a function of the receiver for a OC terminated array. . . . .	101
4.17	Real transformer parameters as a function of the receiver for an optimally terminated array. . . . .	102
4.18	Experimental Setup. . . . .	103
4.19	Voltage (in yellow) and current (in orange) waveforms at the receiver port when the receiver is coupled to (a) the 3rd and (b) the 4th array cell. . . . .	104

4.20	Two-port impedance parameters as a function of the receiver position for an array of 6 resonators at the resonant frequency of 45.1kHz in case of SC termination. The circle and cross markers refer to the formulas (4.24)-(4.26) and experimental results, respectively. . . . .	105
4.21	Two-port impedance parameters as a function of the receiver position for an array of 6 resonators at the resonant frequency of 45.1kHz with the array terminated in $\hat{Z}_{T_{opt}}$ . The circle and cross markers refer to the formulas (4.24)-(4.26) and experimental results, respectively. . . . .	106
4.22	(a) Resistive load values that allow maximum efficiency and (b) maximum achievable efficiency as a function of the receiver position, for an array of 25 cells in different termination conditions. . . . .	107
4.23	System efficiency as a function of the receiver position and for different loads when the array is terminated in (a) SC, (b) OC and (c) $\hat{Z}_{T_{opt}}$ . . . . .	109
4.24	(a) Thévenin equivalent impedance and (b) maximum available power at the receiver port. . . . .	110
4.25	Power transferred to a load (a) $R_l < \hat{Z}_{th_{AVR}}$ (b) $R_l = \hat{Z}_{th_{AVR}}$ and (c) $R_l > \hat{Z}_{th_{AVR}}$ , as a function of the receiver position and for different terminations. . . . .	111
4.26	Doubly-fed array with fixed termination. . . . .	114
4.27	Power transferred to a load (a) $R_l < \hat{Z}_{th_{AVR}}$ (b) $R_l = \hat{Z}_{th_{AVR}}$ and (c) $R_l > \hat{Z}_{th_{AVR}}$ , as a function of the receiver position and for different terminations for a doubly-fed array controlled to maximise efficiency and power transfer. . . . .	115
5.1	Equivalent frequency domain circuits of a resonator array. . . . .	119
5.2	Equivalent representation of a resonator array by a cascade connection of two-port networks. . . . .	120
5.3	MI wave standing wave patterns for different termination loads. . . . .	125
5.4	Standing wave ratio for arrays of different lengths and different termination conditions. . . . .	126
5.5	IPT system with a resonator array and a receiver over it. . . . .	127
5.6	Mutual inductance between the receiver and three consecutive resonators of the array, as a function of the receiver position at a receiver height of 10mm. . . . .	128
5.7	Section of the equivalent TL of a resonator array with a receiver coupled with the $i$ th resonator. . . . .	128
5.8	Section of the equivalent TL of a resonator array with a receiver coupled to the $i$ th and $(i + 1)$ th resonators. . . . .	130
5.9	Current magnitude of each resonator as a function of the receiver position, for a matched array and different load resistances. . . . .	133
5.10	Standing wave patterns for different positions of the perfectly aligned receiver, a matched array and different load resistances. . . . .	133

5.11	Magnitude of the currents of the array resonators as a function of the receiver position, for different terminations and a receiver load $\hat{Z}_{load} = 0.7\Omega$ . . . . .	135
5.12	Standing wave patterns for different positions of the receiver, different terminations and a receiver load $\hat{Z}_{load} = 0.7\Omega$ . . . . .	135
5.13	Magnitude of the currents of the array resonators as a function of the receiver position, for different terminations and a receiver load $\hat{Z}_{load} = 5\Omega$ . . . . .	136
5.14	Standing wave patterns for different positions of the receiver, different terminations and a receiver load $\hat{Z}_{load} = 5\Omega$ . . . . .	136
5.15	Magnitude of the currents of the array resonators as a function of the receiver position, for different terminations and a receiver load $\hat{Z}_{load} = 15\Omega$ . . . . .	137
5.16	Standing wave patterns for different positions of the receiver, different terminations and a receiver load $\hat{Z}_{load} = 15\Omega$ . . . . .	138
5.17	Comparison between the numerical and experimental values of the resonator current magnitude for different receiver positions in the case of $\hat{Z}_T = 1.5\Omega$ and $\hat{Z}_{load} = 5\Omega$ . . . . .	139
5.18	Experimental setup for the magnetic field measurements. . . . .	140
5.19	FEM calculated magnetic flux density on a plane 9.6cm above the array in (a) vector representation (b) magnitude. . . . .	141
5.20	Comparison between magnetic flux density values obtained from measurements, FEM simulations and analytical calculation at the centre of the array resonators on a plane placed (a) 9.6 cm above and (b) 12.5 cm below the array. . . . .	143
5.21	Shielding effectiveness of a single-layer aluminium planar shield and two-layer aluminum-Mumetal <sup>®</sup> registered planar shield . . . . .	144
6.1	(a) Schematic representation of a resonator array with an external coil and (b) its equivalent circuit. . . . .	148
6.2	Array input impedance as a function of the receiver position with short-circuit termination for different values of load resistance $\hat{Z}_{rc}$ , in magnitude (a) and phase (b). . . . .	152
6.3	Array input impedance as a function of the receiver position with matched termination for different values of load resistance $\hat{Z}_{rc}$ , in magnitude (a) and phase (b). . . . .	153
6.4	Array input impedance as a function of the receiver position with open-circuit termination for different values of load resistance $\hat{Z}_{rc}$ , in magnitude (a) and phase (b). . . . .	154
6.5	Input impedance trajectory as a function of the receiver position for the resonator array described in Sec. 6.1.1 with short-circuit termination and $\hat{Z}_{rc} = 1\Omega$ . The function evolves for increasing $x$ in the direction of the red arrows. . . . .	157

6.6	Feature of the input impedance magnitude of the resonator array described in Sec. 6.1.1, where the blue curve represents the calculated continuous function $ \hat{Z}_{eq} (x)$ and the dark-red dashed line its discrete version $ \hat{Z}_{eq} (x_k)$ . The black line indicates the value of the measured input impedance magnitude $\hat{Z}^*$ (also indicated with $\hat{\tilde{Z}}$ ) and the red dotted line the value of the function at the coordinate $x_k$ . The green box represents the tolerance interval for $x_2$ , bounded by the associated tolerance margins $\delta_Z^B(x_2)$ and $\delta_Z^F(x_2)$ . . . . .	159
6.7	Flow chart illustrating the algorithm for the detection of the moving coil position. . . . .	161
6.8	Schematic of the proposed dynamic IPT system. The EV detector block is devoted to the high-frequency measurement of the array input impedance. . . . .	164
6.9	Equivalent circuit of the coil driver. It consists of the cascade of an H-bridge inverter and an LCC compensation network. The coil is modelled with a lumped impedance, resistance and the series-controlled voltage source to represent the coupling with the receiver and adjacent coils. . . . .	165
6.10	<b>(a)</b> Magnitude and <b>(b)</b> phase of the driver coil impedance $\hat{Z}$ as a function of the frequency. . . . .	167
6.11	High-frequency equivalent circuit of the resonator array at $\omega_1 = 2\pi f_1$ with an additional termination coil (with $\hat{Z}_{acT}$ ) and the receiver coil terminated on the impedance $\hat{Z}_{rc}$ . The “Z measurement” block estimates the array input impedance. . . . .	168
6.12	Mutual inductance between the receiver and three consecutive resonators (( $i - 1$ )th, $i$ th and ( $i + 1$ )th) of the array, as a continuous function of the position $x$ . . . . .	168
6.13	Array input impedance as a function of the receiver position with SC termination for different values of load resistance $\hat{Z}_r$ , in magnitude (a) and phase (b). . . . .	169
6.14	Array input impedance as a function of the receiver position with matched termination for different values of load resistance $\hat{Z}_r$ , in magnitude (a) and phase (b). . . . .	170
6.15	Array input impedance as a function of the receiver position with OC termination for different values of load resistance $\hat{Z}_r$ , in magnitude (a) and phase (b). . . . .	171
6.16	Input impedance trajectory as a function of the receiver position for the resonator array with a series-compensated receiver and SC termination. . . . .	172
6.17	Input impedance trajectory as a function of the receiver position for the resonator array with 6 cells and series-compensated receiver, terminated with $\hat{Z}_T = 0.8\Omega$ . . . . .	172

6.18	Input impedance trajectory as a function of the receiver position for the resonator array with 12 cells and series-compensated receiver, terminated with $\hat{Z}_T = 0.8\Omega$ . . . . .	173
7.1	Schematic representation of a 2D array of resonators. . . . .	178
7.2	Current distribution of a $51 \times 51$ 2D array excited in the central resonator considering the interaction of each coil in case of (a) $Q = 40$ and (b) $Q = 260$ at the frequency $f_0$ . . . . .	180
7.3	Current distribution of a $51 \times 51$ 2D array with (a) $Q=25$ and (b) $Q=170$ , excited in the central resonator considering all couplings between coils. The values have been normalised to the current of the central resonator. . . . .	181
7.4	Current distribution of a $51 \times 51$ 2D array with (a) $Q=25$ and (b) $Q=170$ , excited in the central resonator considering the couplings between adjacent coils in the $x$ , $y$ and diagonal directions of the lattice. The values have been normalised to the current of the central resonator. . . . .	182
7.5	Current distribution of a $51 \times 51$ 2D array with (a) $Q=25$ and (b) $Q=170$ , excited in the central resonator considering the nearest-neighbour approximation. The values have been normalised to the current of the central resonator. . . . .	183
7.6	Current distribution of a $5 \times 5$ 2D array with $Q=170$ excited in the central resonator considering: (a) all couplings between coils, (b) the couplings between adjacent coils in the $x$ , $y$ and diagonal directions and (c) the nearest-neighbour approximation. The values have been normalised to the current of the central resonator. . . . .	184
7.7	Schematic representation of the 2D array of resonators. . . . .	185
7.8	Current distribution of a $5 \times 5$ metasurface excited in the central resonator considering all couplings between coils. The values have been normalised to the current of the central resonator. . . . .	188
7.9	Isometric view of the system composed of a transmitter and a receiver square wound coils with the interposed $5 \times 5$ array made of round wound coils. . . . .	189
7.10	Schematic representation of the 2D array of $5 \times 5$ resonators. The cells with the same tuning are indicated with the same parameter $K$ . Six different tunings are possible. . . . .	192
7.11	Resonant frequency of the metamaterial cells normalised with respect to the operating frequency $\omega_0$ of the IPT system when the slab lies on the planes (a) $z_1$ , (b) $z_2$ and (c) $z_3$ . . . . .	193
7.12	Isometric view of the system composed of the transmitting and a receiving square wound coils with the $5 \times 5$ array made of round wound coils. The green circles indicate the field probe coils. . . . .	194

---

7.13 (a) Average SE in the plane $z_{SE} = 40\text{mm}$ above the metamaterial and (b) resonant frequency of the cells normalised with respect to the operating frequency $\omega_0$ of the IPT system when the slab is positioned at $z = 131\text{mm}$ . . . . .	196
A.1 $n$ turn wound coil of size $W \times H$ and its equivalent thick current loop.	203
A.2 Equivalent DD coils. . . . .	206

# Chapter 1

## Introduction

WIRELESS power transfer (WPT) technologies are penetrating more and more into everyday life, since they offer many advantages with respect to wired ones, such as increased electrical safety (electrical contacts are avoided) and the ability to transfer energy in dry and wet environments. The dawn of WPT can be attributed to Maxwell’s “Treatise on Electricity and Magnetism”, published in 1873 [6], where the idea of transmitting power between two points in free space has been first proposed. In 1886, Heinrich Rudolf Hertz succeeded for the first time in producing and detecting electromagnetic waves, confirming Maxwell’s predictions. At the early beginning of the previous century, other experiments to transmit electrical power without wires between two points in space have been carried out by Nikola Tesla, leading to several industrial patents regarding the wireless transmission of power, including the classical two coils WPT system [1, 7], illustrated in Fig. 1.1, introducing the concept of electromagnetic resonance for the first time in history. Tesla’s original idea was to transfer power for lighting distant cities or districts from places where cheap power is obtainable, but it never materialised on an industrial scale. There are several stories and legends regarding this theory, but the most reasonable cause for its lack of diffusion concerns the dubious feasibility and electrical safety issues. However, Maxwell’s and Tesla’s ideas inspired engineers who have developed over the years WPT strategies and devices exploiting different physical phenomena [8], finally allowing diffusion on an industrial scale of this technique.

Techniques for wireless electric energy transmission can be divided into two main families: far-field techniques, in which energy is transmitted via electromagnetic waves and near-field techniques, in which energy is transferred by means of an electric or magnetic field which varies in time. A schematic summary of the different WPT technologies is reported in Fig. 1.2. The far-field WPT allows the power to be transported for long distances, up to several kilometres, since it travels with electromagnetic radiation. To enhance the electromagnetic propagation phenomenon, the far-field WPT systems usually operate in the radio frequency spectrum [9], even if applications working in the visible spectrum have also been developed [10, 8]. However, these systems allow very little power to be transferred with a generally modest

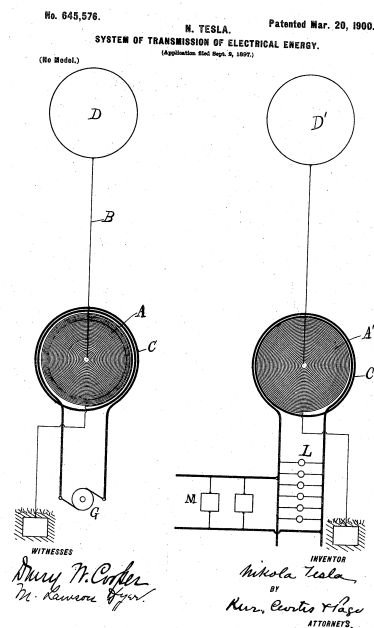


Figure 1.1: Tesla's resonant coils for wireless power transmission [1].

efficiency and are then mainly devoted to power wireless sensor networks, “Internet of Things” devices, radio-frequency identification (RFID) systems, and wireless-powered unmanned air vehicles. An interesting generalised analysis applicable to both far- and near-field WPT systems is presented in [11], with a particular focus on electromagnetic energy harvesters. Near-field wireless power transfer can instead reach very high power rates, preserving good efficiency (generally higher than 90%). They can be developed to exploit the electric or magnetic induction principles, and are then classified as capacitive or inductive power transfer systems, respectively. In capacitive power transfer (CPT) devices the energy is delivered from the transmitting to the receiving circuit through capacitively coupled metallic plates, that have to be fed with a time varying voltage [12, 13]. Inductive power transfer (IPT) devices instead consist in systems of magnetically coupled coils, and the energy is transferred through the magnetic field generated by time-varying currents. According to Maxwell's equations of electromagnetism [6], both the electric and magnetic induction phenomena are emphasised as the frequency increases, which is however limited according to the electrical dimensions of the system, therefore in such a way as to prevent the energy from being radiated. The applications of near-field WPT systems range from powering consumer electronics devices and biomedical implants [14, 15] with a few tens of watts up to heavy industrial equipment and electric vehicles (EVs), that require tens of kW [16, 17, 18, 19]. Different research proved that IPT systems can achieve very high power transfer levels [20, 21], but the coupling

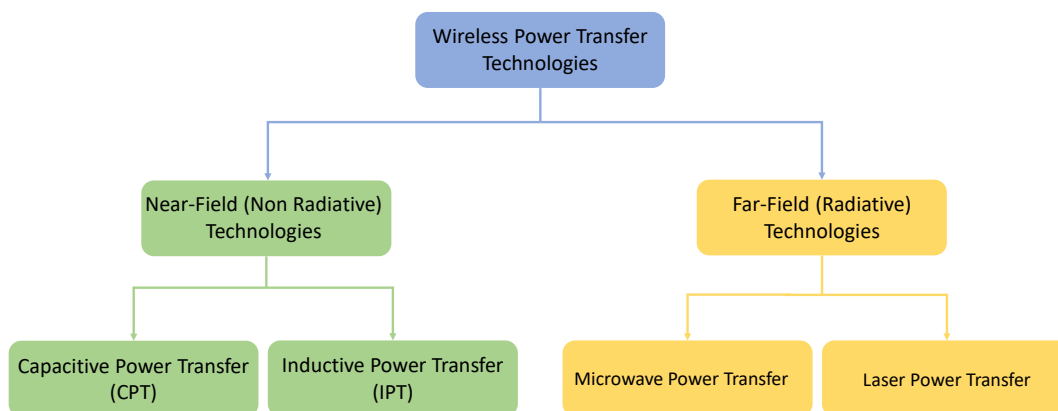


Figure 1.2: Classification of wireless power transfer technologies.

device (i.e. the magnetically coupled coils) is heavy and bulky. Moreover, to confine the magnetic flux density and thus improve the efficiency, planar ferrite cores are usually introduced in high-power applications, leading to a further increase in weight, costs and power losses. Despite ferrite cores involve losses, in terms of efficiency, it is still convenient to introduce them. Ferromagnetic cores also limit the operating frequency of the IPT system, being somehow proportional to the frequency [22, 20]. However, bounding the magnetic flux density, they play a crucial role in increasing the safety of the system. Human exposure to magnetic fields is one of the main concerns that limit the large scale diffusion of IPT systems [23, 24]. The coupling link of CPT apparatuses is much lighter than that of IPT systems and can operate at higher frequencies, being made of conductive plates only [12, 13, 22]. CPT systems have been proved to achieve kW-level power transfer at more than 90% of efficiency [25], the power transfer remains lower than that achieved by IPT systems [22]. Along with the frequency, the voltage applied to the conductive plates should also be raised as high as possible to increase the performance of the system, resulting in a negligible electrical hazard. Furthermore, humid and dirty environments can alter their functioning [13, 26].

To improve the system performance in terms of efficiency and transmitted power, compensation networks are typically introduced in both CPT and IPT systems. The basic idea was suggested by tesla as early as the beginning of the last century in [1] (see also Fig. 1.1), in which the magnetically coupled coils are both connected to lumped capacitors (with appropriate capacitance values) to trigger the so-called magnetic resonance phenomenon. In this way, the magnetic energy required by the coils for the power transfer is supplied by the capacitors and not by the power source, improving the efficiency of the system. Analogously, in CPT systems, the

electrical energy required by the capacitive coupling can be supplied by special lumped inductors introduced in the circuitry connected to the metallic plates. In modern WPT systems, compensation networks with various topologies are now always used [27, 28]. In addition to improving performance, they also allow particular operating conditions to be reached, that are necessary to power the load with the appropriate voltage or current [28]. The CPT and IPT systems generally require an auxiliary circuitry which involves, in addition to the coupling system, the compensation networks and the energy conversion systems, connected at both system input and output. Although the basic idea of these two WPT techniques is similar (and dual), in most practical applications the WPT systems in the near field exploit the principle of magnetic induction.

In this frame, a further focus on IPT system is addressed, which aims at providing a broader overview of the most recent developments in this technique. The increasingly widespread use of these systems has led to the development of particular solutions designed to overcome some limits that the physical nature of the system imposes.

## 1.1 Automotive IPT Systems

The fundamental parameters of an IPT system can be summarised in transferred power, transfer efficiency and transfer distance. Based on this, it is also possible to identify the limits of the systems and, consequently, to introduce solutions to overcome them. Among the high-power IPT apparatuses, the most widespread and of common interest applications concern charging systems for electric vehicles. Indeed, in recent years, IPT systems have been considered as the main solution for the wireless charging of electric vehicles (EV). In view of reducing carbon emissions, authorities of many countries are now encouraging the transition from internal combustion engine vehicles (ICEV) to battery electric vehicles (BEV) or plug-in hybrid electric vehicles (PHEV). The European Commission has set the year 2035 (with some exceptions to 2036) as a reference deadline from which only BEVs or PHEVs will be commercialised, while several other organisations have reported EV adoption projections ranging from 10% to 60% by the year 2040 [29]. The main problem of EVs is nothing else but the electric storage system, i.e. the battery pack, which is the bottleneck today due to its unsatisfactory energy density, limited lifetime and high cost [18, 16]. In addition to the already included advantages of practicality and safety, IPT systems for EV charging can be considered a (probably partial) solution to the problem of low energy availability of EVs. Indeed, by installing wireless charging systems in multiple areas along the way, you can recharge more frequently by taking advantage of the moments when the vehicle is stationary. For long distance travel, electric roads have also been introduced and tested, which allows the EV to continuously take power from the road through an integrated dynamic WPT system, thereby dramatically reducing the required battery storage capacity [19]. A wide and exhaustive overview of both static and dynamic IPT systems is provided

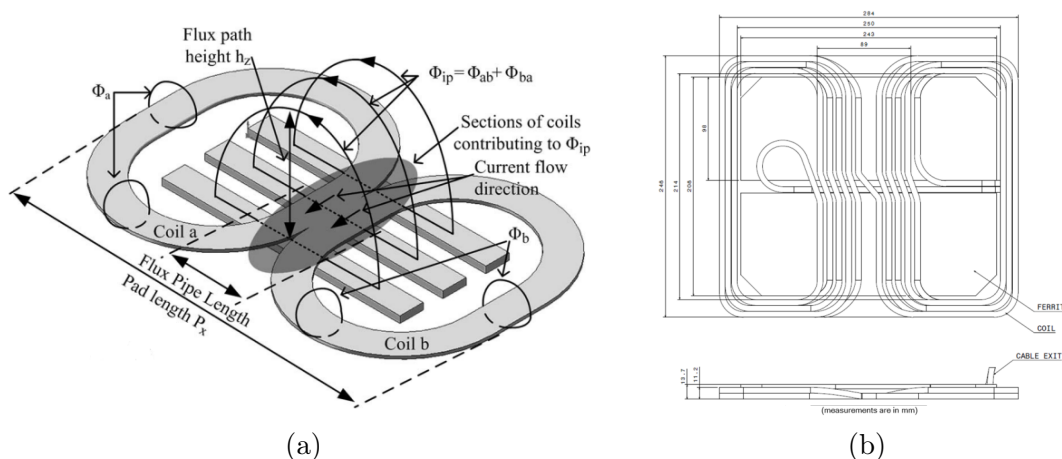


Figure 1.3: (a) DD pads architecture as originally proposed in [2] and (b) layout of DD pad described in the SAEj2954 [3] for WPT3/Z1 (see categories in [3]) system.

in [16, 17, 19, 18].

Static IPT systems are in fact composed of a transmitter and a receiver, magnetically coupled through two or more coils. In general, since the power involved is very high, each coil is controlled by an appropriate circuit, composed of switching power converters and compensation networks. In the most common applications, rectangular or circular coils are used (the latter have a stronger coupling with the same surface area of the coil [30]) or the so-called “DD” coils, introduced by G. Covic *at al.* and exhaustively described in [2]. Figs. 1.3a shows a representation of the original DD coil architecture proposed in [2], in which the path of the magnetic flux is also illustrated, while in Fig. 1.3b the DD coils suggested for WPT3/Z1 IPT systems (see categories in [3]) is depicted. The resulting winding is the union of two identical windings lying side by side, fed with anti-phase currents. In this way, instant by instant, they generate magnetic fields with parallel axes but opposite directions and therefore at each instant of time one coil acts as a north pole and the other as a south pole. In this way, a polarised single-sided flux pad is obtained, which in fact corresponds to a pad that enhances the field in the centre and cancels it at the edges. The resulting magnetic flux configuration allows the mutual coupling of the coils to be improved. However, it must be noticed that if DD coils are employed, both the transmitting and receiving coils must present this configuration. To improve performances in misalignment conditions, “DDQ” coils have also been proposed [2], which however require a further winding to be introduced. An interesting research carried out by R. Bosshard *at al.* [20] highlighted that, a 50-kW square-rectangular coils IPT system is more efficient than an equivalent one with DD coils, due to the increased core losses in correspondence of the centre of the DD coils. DD coils however proved to be safer than the rectangular ones in terms of magnetic field emissions, since a lower magnetic flux density is measured in the vicinity of the apparatus [20]. This kind of coil can also be employed for dynamic IPT, which

is today the last frontier of research regarding IPT systems [2, 31]. In both static and dynamic IPT compensation networks are strongly required. A comprehensive description of their aim, operations and design considerations are provided in [27], but further developments have been proposed with both passive [32, 33, 34] and active circuitry [28].

### 1.1.1 Automotive IPT Standards

In recent years, given the growing diffusion and commercialisation of static IPT systems, dedicated standards have been developed since 2015 [35]. In particular, the main ones are noted: IEC 61980–1, SAE J2954 RP and GSO ISO/PAS 19363:2021, EN ISO 19363:2021, which have many common points. The main aspects that these standards aim at defining concern the system power rate, operating frequency, the distance between transmitter and receiver and the interoperability conditions for different systems. They also indicate the limits for electromagnetic emissions, both conducted and radiated.

## 1.2 Multi Coil IPT Systems

Starting from two-coil static IPT systems, different solutions that provide for multiple windings have been proposed, with the aim of extending the transmission range. In high-power multi coil systems, that are mainly devoted to EVs charging and to moving parts in industrial automatic machines, each coil is independently fed by its own power supply [31, 36]. However, alternative configurations with passive intermediate resonant coils have also been developed [37, 38, 39, 40]. In these systems, one-dimensional (1D) arrays of magnetically coupled resonators are arranged in between the transmitter and receiver resonators, thereby allowing a more efficient power transfer [41]. These resonant structures have been first proposed by a research group of the Massachusetts Institute of Technology in 2007 [42], in a paper considered a milestone in modern IPT. The basic structure is composed of a transmitter and a receiver coil, with two intermediate self-resonant coils. This arrangement is also named as “four-coils” IPT system [43] but generalised analyses for arrangements with a higher number of resonators have also proposed [44, 45, 40]. Overall, these systems have proven to be able to improve the efficiency and the transmitted power even when the transmitting and receiving coils are far apart and their coupling would be almost zero. A representation of a 1D array of resonators is shown in Fig. 1.4. In fact, if it is possible to interpose all the resonators forming an array, it is reasonable to think that it may be also possible to feed directly the one closest to the source. Moreover, although it is possible to design them adequately, the controllable variables of the system are only the currents and voltages of the input and output ports. Therefore, the currents and voltages of the intermediate resonators can also assume very high values and it is not possible to modify them directly in real time. Among these systems, one of the most promising applications

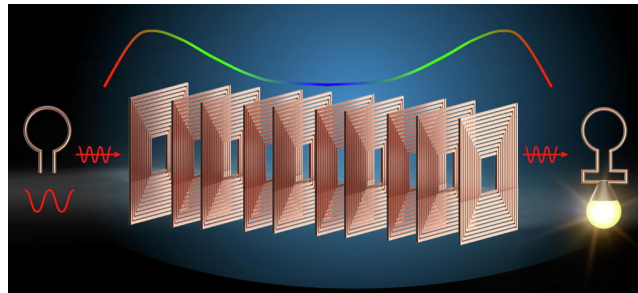


Figure 1.4: Schematic illustration of a 1D resonator array [4]. The power injected in the array reaches the receiver through the intermediate relay resonators.

consists in a resonator array that powers a receiver which can be placed at any position above it. In this case, the array acts as a transmitter, even if only the first coil is powered. This system exhibits peculiar behaviour in terms of efficiency and transmitted power and has been thoroughly analysed in [46, 47, 47]. In order for the power transfer to be efficient, it is necessary to adopt appropriate control strategies, also by inserting some additional components, as proposed in [48, 49].

Further extensions to bi-dimensional (2D) arrays of passive resonators have also been proposed. In this case, a plane composed of magnetically coupled resonant circuits is interposed between the transmitter and the receiver. Depending on the resonator tuning (i.e. their resonant frequency), the 2D array can either amplify or attenuate the incident field. To compare their effect with that of natural lattice materials, it is possible to derive a homogeneous model of the array [50]. The resulting magnetic permeability can therefore be greater or less than that of vacuum, and in some cases (with appropriate resonator tuning) even negative [51, 52]. Due to the possible unnatural properties, these 2D array configurations are also referred to as metamaterials or metasurfaces. It is crucial to mention that metamaterials have been first introduced to control electromagnetic waves [53, 52], with revolutionary applications in the field of optics [51, 54].

More recently, metamaterials have been also introduced in near-field IPT systems [55, 56, 57], as a way to increase the system efficiency [55, 58, 59] or shielding applications [57, 60], resulting in a structure similar to those of Fig 1.5. Similarly to the case of 1D arrays, a 2D resonator array can be used as a transmitter to feed a receiver that can be placed at any position over it. This possibility has been explored in [61, 62, 63]. In all works, the goal is to transfer power efficiently to multiple positions on the table, reducing the complexity of the system and the necessary circuitry. However, as in the case of 1D arrays, controlling the input voltage and current alone is not sufficient to achieve the desired performance. In [61], the resonators are made to work out of resonance to modify the structure of the piano from the electromagnetic point of view, in [62] more superimposed planes are used and in [63] particular resonator structures have been introduced.

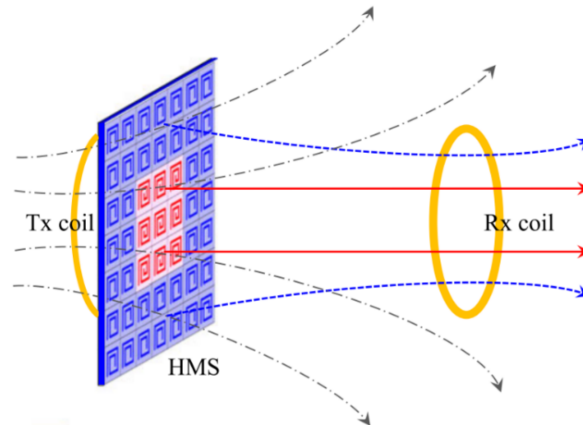


Figure 1.5: Schematic illustration of a metasurface devoted to the magnetic field focusing in two-coil IPT system [5].

### 1.2.1 Magneto-Inductive Waves

The studies on structures of magnetically coupled resonators lead Solymar *et al* to introduce a new type of slow wave, that is the magneto-inductive wave [64]. By resorting to the analogy between transmission lines and coupled resonant circuits, it is possible to consider the arrays of magnetically coupled resonators as the cascade of transmission line segments. Indeed, the time and space behaviour of the resonator currents and voltages is analogous to the one of a wave that propagates in the line [65, 66]. In this frame, magneto-inductive waves, which are current waves, have been defined for 1D, 2D and 3D resonator arrays [67]. The study of resonator arrays through the theory of magneto-inductive waves allows us to better understand the behaviour of the physical system than its description through Kirchhoff's laws, as the latter allows only the analysis and not the synthesis of circuit problems of this complexity. Through the theory of magneto-inductive waves, interesting results about the transmitted power [47], current distribution [68, 64] and impedance of maximum power transfer have been obtained [47, 69].

## 1.3 Outline of the Thesis

Several wireless energy transmission systems based on the IPT technique have been developed. Based on the application, power and dimensions may vary and, consequently, also the architecture of the system. In this context, this thesis aims to evaluate the feasibility of resonator arrays when used in power applications, also considering the installation context. In fact, the research on the state of the art of these multi-coil systems (summarised in the sections above) has highlighted the lack of systems that can be used in concrete practical applications. Although functioning, the resonator arrays presented in the literature have always been characterised by modest power and efficiencies. In this thesis, after a first illustration of the basic concepts of the IPT technique in Chapter 2, Chapter 3 discusses a circuit-based design

---

methodology for two-coils IPT systems with two types of compensation networks, chosen because they are simple but effective. Chapter 4 goes inside the analysis of resonator arrays, coming to define a control technique that allows the maximisation of both the transmitted power and efficiency. In Chapter 5, an analysis of the current distribution and the magnetic field generated by the structure has been carried out, resorting to the theory of magneto-inductive waves. Taking advantage of the peculiar characteristic of the input impedance of 1D resonator arrays with a receiver, a technique for the detection of its position has been proposed in Chapter 6, with relative application to IPT dynamic systems. Chapter 7 concludes the work by discussing the potential and limits of 2D arrays of resonators. In particular, these systems have been studied as transmitters for WPT apparatuses and as metamaterials, that can be designed to shield or amplify the magnetic field in the region where they are inserted.



# Chapter 2

## Basics of Inductive Power Transfer (IPT)

With the attempt to harmonize the background, the basic operating principle of IPT systems is illustrated in this chapter. Then, a general circuit model is derived, from which the system parameters of practical interest can be defined. The presented model can be extended to more complex systems involving multiple coils and compensation networks.

### 2.1 Physical Principle: the Magnetic Induction

IPT systems exploit the magnetic induction principle, firstly discovered by Michael Faraday in 1831. In 1834, Emil Lenz specified the direction of the induced field, while the mathematical formulation has been established by Franz Ernst Neumann in 1845. The principle states that:

*The electromotive force along a closed path is equal to the negative of the time rate of change of the magnetic flux enclosed by the path [70, 71].*

Mathematically, it can be expressed as:

$$emf = -\frac{d\Phi_c}{dt} \quad (2.1)$$

where the acronym *emf* denotes the electromotive force acting on the closed path  $\gamma$ ,  $\Phi_c$  is the flux of the magnetic field  $\vec{B}$  through the oriented surface  $\Sigma$  bounded by  $\gamma$  and  $t$  refers to the time. In general, the time variation of the magnetic flux through a surface can be written as:

$$\frac{d\Phi_c}{dt} = \frac{d}{dt} \iint_{\Sigma} \vec{B} \cdot d\vec{\Sigma} \quad (2.2)$$

where both the magnetic field and the oriented surface can vary in time, each of them contributing to the resulting *emf*. To highlight the two different contributions,

it is possible to rearrange the right-hand-side term of (2.1). According to [70] and assuming a generic rigid path  $\gamma$ , it yields:

$$emf = -\frac{d\Phi_c}{dt} = -\iint_{\Sigma} \frac{\partial \vec{B}}{\partial t} \cdot d\vec{\Sigma} - \oint_{\gamma} \vec{B} \wedge \vec{v} \cdot d\vec{l}. \quad (2.3)$$

It is then possible to define

$$emf_T = -\iint_{\Sigma} \frac{\partial \vec{B}}{\partial t} \cdot d\vec{\Sigma} \quad (2.4)$$

as transformer  $emf$ , which originates from the variation of the magnetic field when  $\Sigma$  is not changing in time, and

$$emf_M = -\oint_{\gamma} \vec{B} \wedge \vec{v} \cdot d\vec{l} \quad (2.5)$$

as motional  $emf$ , which originates from the movement of the closed path  $\gamma$  at the speed  $\vec{v}$  in presence of a constant  $\vec{B}$ . It is worth mentioning that the motional  $emf$  is non-null only if the magnetic field  $\vec{B}$  is non-uniform (even though it is stationary). Indeed, a uniform  $\vec{B}$ , can be considered a constant in the integral and, consequently, also the term  $\vec{B} \wedge \vec{v}$ . The line integral would result therefore zero.

The magnetic induction principle is very widely exploited in the field of electrical engineering. Indeed, the majority of the electric machines works based on this phenomenon. While in electric motors and actuators both the transformer and motional  $emf$  contribute to the operations, static machines only exploit the transformer one. Similarly, the most widespread IPT systems are designed to emphasise the  $emf_T$ , regardless the  $emf_M$  is present or not. In dynamic IPT apparatuses both the  $emf_T$  and the  $emf_M$  are generated, but the system is specifically designed to make the  $emf_M$  negligible with respect to the  $emf_T$ , as it will be discussed in the following.

## 2.2 Coils Circuit Modelling

The operation of an IPT system can be described considering the magnetic induction principle applied to the electric circuits forming that system, that are realised with conductors wound in air or on a ferromagnetic core. For safety reasons, a conductive shield can also be introduced. The following analysis is however valid for any kind of magnetically coupled circuits and, for simplicity, it will start considering air-core coils.

For a generic system of  $n$  circuits and in the hypothesis of current loops, it is possible to define the self-inductance coefficient  $L_i$  of the generic  $i$ th loop as:

$$L_i = \left. \frac{\Phi_{ii}}{I_i} \right|_{I_j=0} \quad \begin{array}{l} j = 1, \dots, n \\ j \neq i \end{array} \quad (2.6)$$

where  $\Phi_{ii}$  is the magnetic flux linked to the  $i$ th loop and produced by the current  $I_i$  of the same loop, while the other currents are null. Similarly, it is possible to define the mutual inductance coefficient  $M_{ij}$  between the  $i$ th and  $j$ th loop as:

$$M_{ij} = \left. \frac{\Phi_{ij}}{I_j} \right|_{I_i=0} \quad \begin{array}{l} i = 1, \dots, n \\ i \neq j \end{array} \quad (2.7)$$

where  $\Phi_{ij}$  denotes the magnetic flux produced by  $I_j$  and linked to the  $i$ th loop. It can be proved that the self-inductance coefficients are non-negative, while the mutual ones can have any value (over  $\mathbb{R}$ ). Moreover, the mutual inductance coefficient between two loops is unique, namely  $M_{ij} = M_{ji}$ . Based on these definitions, two circuits are considered magnetically coupled if they are characterised by a non-null mutual inductance. To quantify the coupling between the two coils, the coupling coefficient  $k$  is introduced and defined as:

$$k_{ij} = \frac{M}{\sqrt{L_i L_j}}. \quad (2.8)$$

It is a dimensionless parameter ranging from 0 to 1. The value of this parameter makes it possible to identify the strength of the coupling which is in this work considered weak if  $k < 0.4$  and strong if  $k > 0.8$ , as it is usually assumed. Due to their distance, the coupled coils of IPT systems present coupling coefficients in the order of  $0.1 \div 0.35$ , even in presence of magnetic materials bearing the windings. Instead, the coils of traditional transformers are characterised by  $k \approx 1$ , being them wound on the same ferromagnetic core.

**Coupled Inductors Model** The simplest configuration of IPT system involves two magnetically coupled coils, one connected to the power source and named “primary coil” or “transmitter coil” and the other connected to the load, named as “secondary coil” or “receiver coil”. The (ideal) coupled coils are represented in Fig. 2.1 with the corresponding inductors, characterised by their self-inductance and mutual inductance coefficients. The black dots denote the direction of the induced *emf* acting on the coil, which depends on the orientation of the loop (already indicated as the curve  $\gamma$ ). Practically speaking, it depends on the winding arrangement. The transmitter and receiver voltages are denoted as  $v_1(t)$  and  $v_2(t)$ , respectively, while the transmitter and receiver currents as  $i_1(t)$  and  $i_2(t)$ , respectively. In this configuration, the magnetic induction principle can be used to express the inductors voltages and, considering the Kirchhoff voltage law (KVL) applied to the circuit of Fig. 2.1, the governing equations can be written as:

$$\begin{aligned} v_1(t) &= \frac{d\Phi_{11}(t)}{dt} + \frac{d\Phi_{12}(t)}{dt} \\ v_2(t) &= \frac{d\Phi_{22}(t)}{dt} + \frac{d\Phi_{21}(t)}{dt} \end{aligned} \quad (2.9)$$

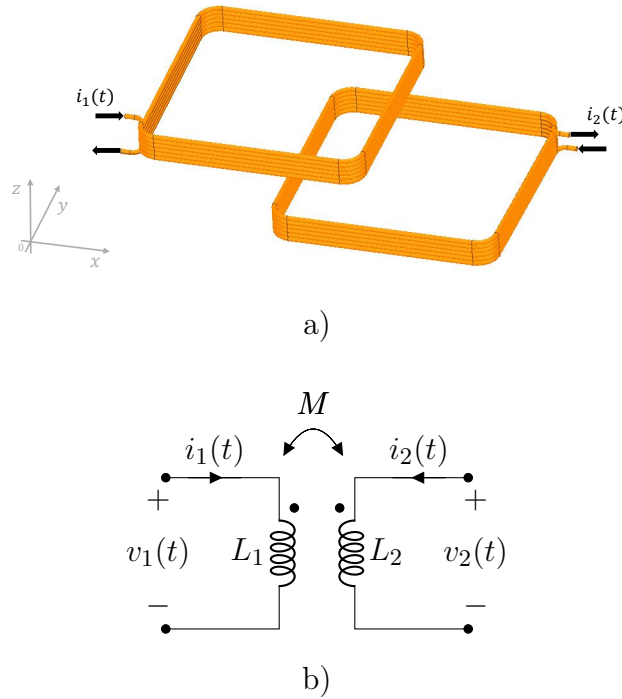


Figure 2.1: Representation of coupled inductors: a) Schematic representation b) equivalent circuit representation.

where the linked fluxes  $\Phi_{11}(t)$ ,  $\Phi_{12}(t)$ ,  $\Phi_{21}(t)$  and  $\Phi_{22}(t)$  can be expressed as functions of the loop currents from which originates through the inductance coefficients as:

$$\begin{aligned}\Phi_{11}(t) &= L_1 i_1(t) & \Phi_{12} &= M i_2(t) \\ \Phi_{22}(t) &= L_2 i_2(t) & \Phi_{21} &= M i_1(t).\end{aligned}\tag{2.10}$$

As introduced in Sec. 2.1, the flux through a loop can vary due to both the time variation of the magnetic field and the time variation of the loop geometry, resulting in the  $emf_T$  and  $emf_M$ , respectively. Focusing on IPT systems, two possible configurations can be identified:

- static IPT systems
- dynamic IPT systems

**Static IPT** In static IPT systems the coils are standstill, only the  $emf_T$  is present and the governing equations (2.2) can be simplified considering that the self- and mutual inductance coefficients are fixed, leading to:

$$\begin{aligned}v_1(t) &= L_1 \frac{di_1(t)}{dt} + M \frac{di_2(t)}{dt} \\ v_2(t) &= L_2 \frac{di_2(t)}{dt} + M \frac{di_1(t)}{dt}\end{aligned}\tag{2.11}$$

The system can then be controlled acting on the voltages and currents.

**Dynamic IPT** In dynamic IPT systems, the transmitting and receiving circuits are in relative motion, making the self- and mutual inductance functions of the relative position between the loops. In general, the parameter variation can be due to a translation or rotational motion, with one, two or three degrees of freedom. In most common applications, the receiver circuit moves with respect to the transmitting one, which is usually installed under the ground. Thus, with reference to Fig. 2.1, a linear movement in the  $x$  direction of the space is assumed. Moreover, in IPT systems of practical interest,  $L_1$  and  $L_2$  can be considered constant, since their variation (due to the presence of magnetic cores) is negligible with respect to the variation of the mutual inductance. Anyway, in some researches, the  $L_1$  and  $L_2$  position dependence is taken into account to improve the performances of the control system. The mutual inductance between the transmitter and receiver coils is then considered as a function of the position  $x$  and thus the governing equations (2.2) become:

$$\begin{aligned} v_1(t) &= L_1 \frac{di_1(t)}{dt} + M(x(t)) \frac{di_2(t)}{dt} + i_2(t) \frac{dM(x(t))}{dt} \\ v_2(t) &= L_2 \frac{di_2(t)}{dt} + M(x(t)) \frac{di_1(t)}{dt} + i_1(t) \frac{dM(x(t))}{dt} \end{aligned} \quad (2.12)$$

and, applying the chain rule to the time derivative of the mutual inductance, it yields:

$$\begin{aligned} v_1(t) &= L_1 \frac{di_1(t)}{dt} + M(x(t)) \frac{di_2(t)}{dt} + i_2(t) v(t) \frac{dM(x(t))}{dx} \\ v_2(t) &= L_2 \frac{di_2(t)}{dt} + M(x(t)) \frac{di_1(t)}{dt} + i_1(t) v(t) \frac{dM(x(t))}{dx} \end{aligned} \quad (2.13)$$

where  $v(t)$  is the relative speed of the coils in the direction of the coordinate  $x$ . The  $emf_M$  contribution is then expressed as the product of the relative speed with the space variation of  $M$ : both the instantaneous speed and the coil geometry play a crucial role in the behaviour of the system. It must be noticed that, in general, the time behaviour of the transformer and motional  $emf$  can be different. In fact, the coil currents are usually sinusoidal, leading to a sinusoidal  $emf_T$ . The time behaviour of the  $emf_M$  is more difficult to be predicted, being dependent on the geometry of the coils and the relative speed. The  $emf_M$  is usually not desired, since it complicates the time behaviour of the voltages and, consequently, the control of the system. However, the operating frequency of IPT systems ranges from tens of kHz up to tens of MHz and thus, in these conditions, the  $emf_T$  can be considered dominating over the  $emf_M$  [72]. Unless otherwise stated, this work mainly considers position-independent parameters. Awareness of this phenomenon is however necessary to predict the correct system behaviour.

Rearranging (2.11) it is possible to obtain different equivalent circuit representations of coupled inductors, that can highlight different parameters of practical interest.

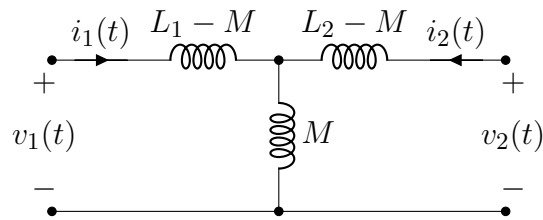


Figure 2.2: T model equivalent circuit of an IPT system.

**T Model** The most common is the so called “T-model” circuit, depicted in Fig. 2.2, for which the primary and secondary voltages can be expressed as:

$$\begin{aligned} v_1(t) &= (L_1 - M) \frac{di_1(t)}{dt} + M \frac{d}{dt} (i_1(t) + i_2(t)) \\ v_2(t) &= (L_2 - M) \frac{di_2(t)}{dt} + M \frac{d}{dt} (i_1(t) + i_2(t)). \end{aligned} \quad (2.14)$$

With this representation all the inductors are decoupled, thereby simplifying the circuit analysis. When adopting this model, the parameters  $(L_1 - M)$  and  $(L_2 - M)$  are usually named as “primary and secondary leakage inductances”, respectively, and  $M$  as “magnetising inductance”. The former parameters highlight the amount of flux produced by a coil which does not link to the other coil and, typically, it is minimised by design. Conversely, the magnetising inductance (which corresponds to the mutual inductance) is desired to be maximised, making the coupling stronger.

**Transformer Model** Historically, magnetically coupled coils are represented with the so called “transformer model”, which can be directly deduced from the T model considering an additional parameter: the transformer ratio (here denoted as  $n$ ). In the modelling of traditional wound transformers, the transformer ratio is widely used since it represents the relation between the primary and secondary voltages and currents during full load operations. Moreover, if the windings are solenoids (as the ones of traditional transformers), the transformer ratio corresponds to the turn ratio.

In general, these conditions are not matched. Indeed, the transformer ratio relates the input and output circuit variables only if the leakage inductance is negligible with respect to the magnetising inductance, or, equivalently, only if  $k$  is closed to the unity. In case of weakly coupled inductors, as it is for typical IPT systems,  $k \ll 1$  and the low value of  $M$  (with respect to  $L_1$  and  $L_2$ ) leads to a not negligible magnetising current. Moreover, transformer windings can have shapes for which it is not possible to identify the turns, and thus  $n$  does not corresponds to the turn ratio [73, 74].

Being a mathematical artifice, the transformation ratio can still be defined in terms of inductance, even though it is not sufficient to relate the primary and sec-

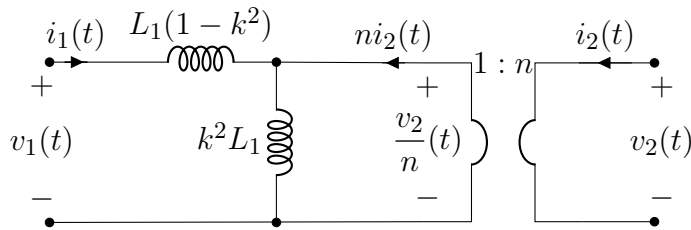


Figure 2.3: Transformer equivalent circuit of an IPT system.

ondary voltages and currents during operations. By choosing:

$$n = \frac{1}{k} \sqrt{\frac{L_2}{L_1}} \quad (2.15)$$

and introducing (2.15) in (2.14), it yields:

$$\begin{aligned} v_1(t) &= L_1(1-k^2) \frac{di_1(t)}{dt} + k^2 L_1 \frac{d}{dt} \left( i_1(t) + n i_2(t) \right) \\ \frac{v_2(t)}{n} &= k^2 L_1 \frac{d}{dt} \left( i_1(t) + n i_2(t) \right). \end{aligned} \quad (2.16)$$

This system of KVL equations allows the definition of the so called “transformer model” of coupled inductors, which is the one typically adopted in power transformers and it is depicted in Fig. 2.3. The choice of  $n$  made in (2.15) allows the secondary series inductance to be eliminated from the equivalent circuit, where the unique leakage inductance is referred to the primary side. Other choices can lead to different equivalent circuits and must be done based on the specific needs of the study.

It can be concluded that, despite the physical nature of the operating principle (and consequently its mathematical description) is the same for IPT systems and traditional transformers, the optimal system operations and performances require different gimmicks.

### 2.2.1 Coil Power Losses

Modern IPT systems operate at frequencies ranging from 79kHz up to 90kHz, as suggested by the standard SAE J2954. Increasing the operating frequency clearly emphasises the magnetic induction principle and allows the size of inductors to be kept limited, saving in costs and weight. The frequency is limited only for safety reasons, since the damage to health and the electromagnetic interference caused by the magnetic field generated by the coils increases with increasing frequency [3, 24]. However, the behaviour of the conductors is strongly affected by the frequency of the circulating currents and undesired phenomena lead to a considerable increase of the wire resistance with respect to its DC value. These phenomena are referred as skin effect and proximity effect, and the effect of both is proportional to the

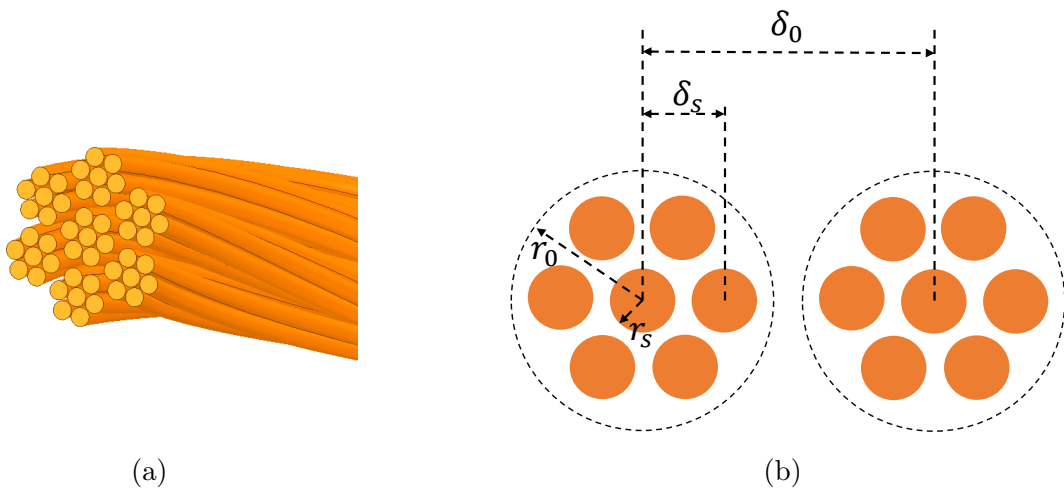


Figure 2.4: Cross-section of (a) a generic Litz wire and (b) two turns of the winding considered in the analysis.

operating frequency. The skin effect forces the current to concentrate in the outer region of the conductor, while the proximity effect to concentrate in a limited region where the influence of an external magnetic field (i.e. the one of near conductors) is more intense. The resulting current crowding makes the AC resistance much larger than the DC one. To reduce the impact of skin and proximity effects, stranded, twisted, and, in particular, Litz wires are employed. A cross-section of a possible arrangement of Litz wire is shown in Fig.2.4a. The main drawbacks of this solution are: the reduced filling area of the wire section with respect to a solid wire and the increased DC resistance, which is due to the longer conductor path of the strands with respect to a cross-sectional equivalent straight conductor. The resulting coil AC resistance  $R_{ac}$  must be evaluated considering the parasitic effects, besides the geometry and material. Different models have been proposed in literature, based on both numerical or (approximated) analytical formulas [75, 76, 77]. In any case, the calculation of the resistance of a winding made of Litz wire requires the knowledge of the strands arrangement, which is expressed through geometrical coefficients. A winding with  $N$  turns of radius  $r_0$  at a centre-to-centre distance  $\delta_0$  is considered. The copper Litz wire is composed of  $n_s$  strands of radius  $r_s$  at a centre-to-centre distance  $\delta_s$ . A cross-section of two turns of the winding is depicted in Fig. 2.4b. The DC resistance  $R_{dc}$  is calculated as:

$$R_{dc} = \frac{\rho}{n_s \pi r_s^2} N l_T \quad (2.17)$$

where  $l_T$  is the average length of a winding turn and  $\rho$  is the wire resistivity. To introduce the skin and proximity effects, the strands arrangement must be considered through the packaging factor  $p$ , which is defined as

$$p = \frac{N \pi r_s^2}{\pi r_0^2} \quad (2.18)$$

and the internal and external porosity factors, which are defined, as:

$$\eta_{in} = \frac{2r_s}{\delta_s} \sqrt{\frac{\pi}{4}} \quad (2.19)$$

and

$$\eta_{out} = \frac{2r_s}{\delta_o} \sqrt{\frac{\pi}{4}} \quad (2.20)$$

respectively. Then, defining  $\gamma_s$  at the operating angular frequency  $\omega$  as:

$$\gamma_s = \frac{d_s}{\sqrt{\omega\mu\sigma}} \quad (2.21)$$

the final formulation of  $R_{ac}$  can be expressed as [76, 77]:

$$R_{ac} = R_{dc} \frac{\gamma_s}{2} \left[ \frac{1}{n_s} K_{skin}(\gamma_s) - 2\pi \left( \frac{4(N_l^2 - 1)}{3} + 1 \right) n_s \left( \eta_{ext}^2 + \eta_{int}^2 \frac{p}{2\pi n_s} \right) K_{prox}(\gamma_s) \right] \quad (2.22)$$

where

$$K_{skin}(\gamma_s) = \frac{ber\gamma_s bei'\gamma_s - bei\gamma_s ber'\gamma_s}{ber'^2\gamma_s + bei'^2\gamma_s} \quad (2.23)$$

and

$$K_{prox}(\gamma_s) = \frac{ber_2\gamma_s ber'\gamma_s - bei_2\gamma_s bei'\gamma_s}{ber^2\gamma_s + bei^2\gamma_s}. \quad (2.24)$$

An accurate calculation of the  $R_{ac}$  is crucial for both the determination of the system losses and control strategy since it dramatically affects the behaviour of the apparatus. Different empirical approaches for the choice of the number of strands and layers of Litz wire are proposed, which however are not here discussed. Due to the exigency of matching the market availability, the employed Litz wires have been chosen among the standard ones proposed by the manufacturer based on the resulting  $R_{ac}$  calculated as in (2.22). Introducing the winding resistances  $R_1$  and  $R_2$  in the coupled inductors model, it modifies as depicted in Fig. 2.5 and the governing equations (2.11) become:

$$\begin{aligned} v_1(t) &= R_1 i_1(t) + L_1 \frac{di_1(t)}{dt} + M \frac{di_2(t)}{dt} \\ v_2(t) &= R_2 i_2(t) + L_2 \frac{di_2(t)}{dt} + M \frac{di_1(t)}{dt}. \end{aligned} \quad (2.25)$$

## 2.2.2 Core Losses

In practical applications, a ferromagnetic ferrite core is often employed to bound the magnetic field and increase both the coils self- and mutual inductances. Due to the non ideal behaviour of this component, the ferrite presents a non-null electrical conductivity. The alternated magnetic field generated by the coils induces currents

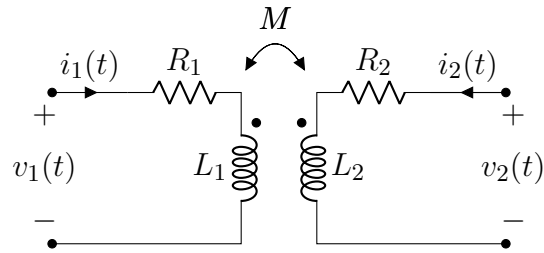


Figure 2.5: Coupled inductors equivalent circuit of an IPT system with winding resistances.

in the core leading to further power losses. Since the magnetic field is generated by almost sinusoidal currents, it will be almost sinusoidal and the Steinmetz formula can be adopted. According to [30], the core loss per unit of volume can be calculated as:

$$p_{core} = cf^\alpha |\hat{B}|^\beta \quad (2.26)$$

where  $c$ ,  $\alpha$  and  $\beta$  are the Steinmetz coefficients that depend on the specific core material. The resulting core losses can be estimated by integrating the core loss density  $p_{core}$  over the entire volume of the ferromagnetic material (both the transmitter and receiver cores).

### 2.2.3 Power and Efficiency

Assuming a linear behaviour of the magnetic system, it is possible to represent the circuit in frequency domain and exploit the phasor representation of currents and voltages. For the generic two-port network represented in Fig. 2.6a, the governing equations are:

$$\begin{aligned} \hat{V}_1 &= \hat{Z}_{11}\hat{I}_1 + \hat{Z}_{12}\hat{I}_2 \\ \hat{V}_2 &= \hat{Z}_{22}\hat{I}_2 + \hat{Z}_{21}\hat{I}_1 \end{aligned} \quad (2.27)$$

where  $\hat{Z}_{11}$ ,  $\hat{Z}_{12}$ ,  $\hat{Z}_{21}$  and  $\hat{Z}_{22}$  are the impedance matrix parameters. For reciprocal networks  $\hat{Z}_{12} = \hat{Z}_{21}$  and a unique mutual impedance  $\hat{Z}_m = \hat{Z}_{12} = \hat{Z}_{21}$  is introduced, leading to:

$$\begin{aligned} \hat{V}_1 &= \hat{Z}_{11}\hat{I}_1 + \hat{Z}_m\hat{I}_2 \\ \hat{V}_2 &= \hat{Z}_{22}\hat{I}_2 + \hat{Z}_m\hat{I}_1. \end{aligned} \quad (2.28)$$

The efficiency of the power transfer can be defined as the ratio between the active power dissipated on the load and the active power provided by the power source:

$$\eta = \frac{|\hat{V}_2|^2}{Re[\hat{V}_1\hat{I}_1^*]}. \quad (2.29)$$

It can be then expressed in terms of the impedance parameters as [78]:

$$\eta = \frac{R_{load}}{Re[\hat{Z}_{in}]} \left| \frac{\hat{Z}_m}{\hat{Z}_{22} + R_{load}} \right|^2 \quad (2.30)$$

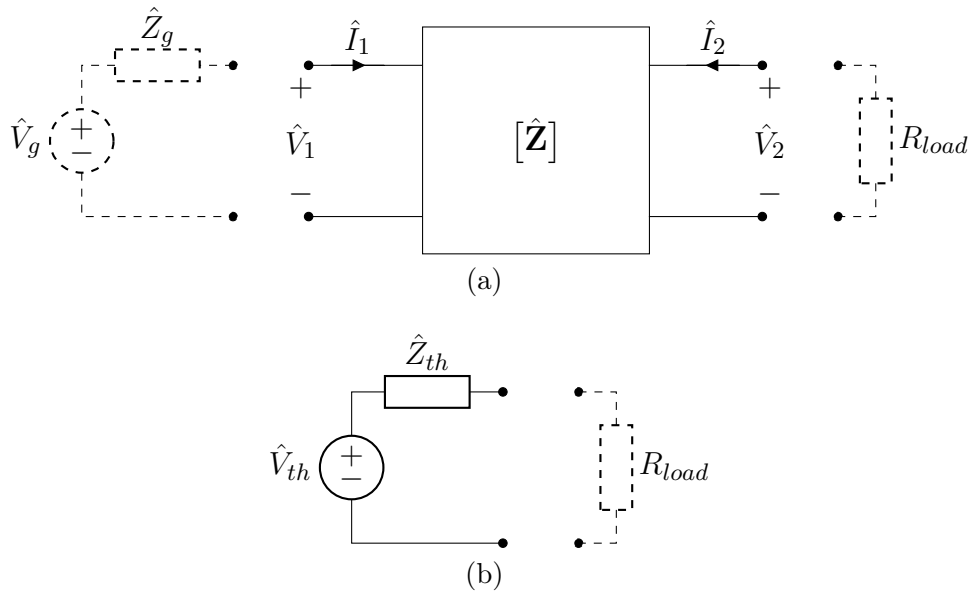


Figure 2.6: (a) generic two-port model fed by a real voltage source and powering a resistive load and (b) the Thévenin equivalent network comprising the cascade of the real voltage source and the two-port network and that powers a resistive load.

where  $\hat{Z}_{in}$  is the two-port input impedance defined as the ratio between  $\hat{V}_1$  and  $\hat{I}_1$  that can be calculated from (2.28) as:

$$\hat{Z}_{in} = \frac{\hat{V}_1}{\hat{I}_1} = \hat{Z}_{11} - \frac{\hat{Z}_m^2}{\hat{Z}_{22} + R_{load}}. \quad (2.31)$$

The condition for the maximum efficiency is obtained enforcing:

$$\frac{\partial \eta}{\partial R_{load}} = 0 \quad (2.32)$$

which lead to the expression of the required load  $R_{load}^{\eta_{max}}$  [78]:

$$R_{load}^{\eta_{max}} = R_2 \sqrt{1 + \chi^2} \sqrt{1 - \zeta^2} \quad (2.33)$$

where:

$$\chi^2 = \frac{Im[\hat{Z}_m]^2}{Re[\hat{Z}_{11}]Re[\hat{Z}_{22}]} \quad \zeta^2 = \frac{Re[\hat{Z}_m]^2}{Re[\hat{Z}_{11}]Re[\hat{Z}_{22}]}. \quad (2.34)$$

The general expression of the maximum efficiency as a function of the impedance matrix parameters is presented in [78]:

$$\eta = \frac{\chi^2 + \zeta^2}{(\sqrt{1 + \chi^2} \sqrt{1 - \zeta^2} + 1)^2 + \chi^2 \zeta^2}. \quad (2.35)$$

For what concerns the power transferred to the load, it can be maximised resorting to the classic theorem of the maximum AC power transfer. It states that the

generator impedance must be equal to the complex conjugate of the load impedance. In this case, the coupling system can be considered a part of the generator and, according to the Thévenin theorem, the cascade of the generator and coupled inductors can be represented with an equivalent bipole composed of the series of a voltage source  $\hat{V}_{th}$  and an impedance  $\hat{Z}_{th}$ , depicted in Fig. 2.6b. Their expressions as a function of the network parameters can be easily found from (2.28) considering  $\hat{V}_1 = \hat{V}_g - \hat{Z}_g \hat{I}_1$  and result in:

$$\begin{aligned}\hat{Z}_{th} &= \hat{Z}_{22} - \frac{\hat{Z}_m^2}{\hat{Z}_{11} + \hat{Z}_g} \\ \hat{V}_{th} &= \frac{\hat{Z}_m}{\hat{Z}_{11} + \hat{Z}_g} \hat{V}_g.\end{aligned}\tag{2.36}$$

It is then possible to define an expression for the active power  $P_l$  transmitted to the load. In particular, it can be also normalised with respect to the maximum available power  $P_{th}$  of the equivalent source (cascade of the real voltage generator and the inductive link) to characterise the network independently on the operating conditions, defined by the value of the voltage source  $\hat{V}_g$ . For the reduced network of Fig. 2.6b, the maximum available active power for the load is:

$$P_{th} = \frac{|\hat{V}_{th}|^2}{8\text{Re}[\hat{Z}_{th}]}\tag{2.37}$$

and the expression of the load power  $P_l$  is found using (2.36), resulting in:

$$P_l = \frac{1}{R_{load}} \left| \hat{V}_{th} \frac{R_{load}}{\hat{Z}_{th} + R_{load}} \right|^2.\tag{2.38}$$

The normalised load power  $P'_l = P_l/P_{th}$  is expressed as:

$$P'_l = \frac{8R_{load}\text{Re}[\hat{Z}_{th}]}{|\hat{Z}_{th} + R_{load}|^2}\tag{2.39}$$

which is valid for any operating conditions of a two-port network fed by a real voltage source that powers the resistive load  $R_{load}$ .

The maximum power transfer is realised if  $\hat{Z}_{th} = R_{load}^{P_{max}}$  and, being  $R_{load}^{P_{max}}$  real, it leads to  $R_{load}^{P_{max}} = \text{Re}[\hat{Z}_{th}]$ . This requirement is often very hard to achieve but, in any case, the cancellation of the imaginary part of  $\hat{Z}_{th}$  is required. It must be also noticed that, in general,  $R_{load}^{P_{max}} \neq R_{load}^{\eta_{max}}$ .

Considering the coupled inductors model to represent the coils and a real sinusoidal voltage source represented by  $\hat{V}_g$  and  $\hat{Z}_g = R_g + jX_g$ , at the angular frequency  $\omega$  the equations (2.28) become:

$$\begin{aligned}\hat{V}_1 &= (R_1 + j\omega L_1)\hat{I}_1 + j\omega M\hat{I}_2 \\ \hat{V}_2 &= (R_2 + j\omega L_2)\hat{I}_2 + j\omega M\hat{I}_1.\end{aligned}\tag{2.40}$$

For this circuit it holds:

$$\chi^2 = \frac{(\omega M)^2}{R_1 R_2} \quad \zeta^2 = 0 \quad (2.41)$$

and thus the maximum efficiency is achieved when:

$$R_{load}^{\eta_{max}} = R_2 \sqrt{1 + \frac{(\omega M)^2}{R_1 R_2}}. \quad (2.42)$$

which leads to:

$$\eta_{max} = \frac{\chi^2}{(1 + \sqrt{1 + \chi^2})^2}. \quad (2.43)$$

The maximum efficiency monotonically increases as  $\chi$  increases, that corresponds to a decrease in the winding resistance. In particular, it can be seen that  $\eta_{max} \rightarrow 1$  for  $\chi \rightarrow \infty$ , which corresponds to the case of ideal coupled inductors.

The maximum power transfer further requires  $Im[\hat{Z}_{th}] = 0$ , which can be fulfilled only introducing suitable reactive elements to provide the magnetic energy required by the coupling system. If the system is properly compensated, the maximum power transfer is achieved with [78]:

$$R_{load}^{P_{max}} = R_2 + \frac{(R_1 + R_g)(\omega M)^2}{(\omega L_1 + X_g)^2 + (R_1 + R_g)^2} \quad (2.44)$$

and the maximum transferable power is:

$$P_{max} = P_g \frac{\chi^2}{1 + \chi^2}. \quad (2.45)$$

where

$$P_g = \frac{|\hat{V}_g|^2}{8R_g} \quad (2.46)$$

is the available generator active power. Also in this case, a very high  $\chi$  is desired, being  $P_{max} \rightarrow P_g$  for  $\chi \rightarrow \infty$ .

## 2.2.4 Voltage Gain and Transadmittance

The main aim of IPT systems is the maximisation of the transferred power to the load, preserving a great efficiency. However, adjustment of the load voltage and current is often necessary, even in presence of additional power conversion stages upward the receiver. The whole IPT apparatus is basically controlled by acting on the primary voltage, which is usually imposed by a voltage source inverter. Thus, an accurate and efficient control requires to know the relation between the input voltage and the load voltage and current. With reference to the generic two-port network model of Fig. 2.6a, it is then defined the voltage gain  $\hat{G}_v$  of the coupling system as:

$$\hat{G}_v = \frac{\hat{V}_2}{\hat{V}_1} = \frac{\hat{Z}_m R_{load}}{\hat{Z}_{11}(\hat{Z}_{22} + R_{load}) - \hat{Z}_m^2} \quad (2.47)$$

and the transadmittance  $\hat{G}_m$  as:

$$\hat{G}_m = \frac{\hat{I}_2}{\hat{V}_1} = -\frac{\hat{Z}_m}{\hat{Z}_{11}(\hat{Z}_{22} + R_{load}) - \hat{Z}_m^2} \quad (2.48)$$

which are simply related as:  $\hat{G}_v = -R_{load}\hat{G}_m$ . Based on these parameters, the control system varies  $\hat{V}_1$  to achieve the required  $\hat{V}_2$  or  $\hat{I}_2$ , depending on the load profile. These expressions clearly show that, to increase  $\hat{G}_v$  and  $\hat{G}_m$ , the coil impedances  $\hat{Z}_{22}$  and  $\hat{Z}_m$  should be minimised, again suggesting the need of compensation networks. Moreover, from (2.47) it can be seen that a constant voltage gain (for any load) can be obtained at a certain  $\omega$ . Rearranged, (2.47) can be written as:

$$\hat{G}_v = \frac{\hat{Z}_m}{\frac{\hat{Z}_{11}\hat{Z}_{22} - \hat{Z}_m^2}{R_{load}} + \hat{Z}_{11}} \quad (2.49)$$

and thus  $\hat{G}_v$  is independent on  $R_{load}$  if:

$$\hat{Z}_{11}\hat{Z}_{22} - \hat{Z}_m^2 = 0. \quad (2.50)$$

Indeed, the term  $R_{load}$  would not be present in (2.49) and this operating condition is referred to as constant voltage (CV) mode. Similarly, it is also possible to obtain load-independent current operations at a certain  $\omega$  by simply enforcing:

$$\hat{Z}_{11} = 0 \quad (2.51)$$

which is usually referred to as constant current (CC) mode. These conditions can be obtained with the proper tuning of compensation networks, that cancel the undesired impedance contributions.

## 2.3 Compensation Networks

As introduced in Sec. 2.2.3, optimal IPT operations need a dedicated circuit to compensate the reactive power the source exchanges with the coils. The low magnetising flux results in a lower magnetising (or mutual) inductance, requiring high reactive power rates (with respect to traditional transformers) to transfer a certain amount of active power. The compensation networks aim at providing the reactive power required by the coupling system, maximising the efficiency and the power transfer. Moreover, with the proper tuning, the voltage gain and transadmittance can be made constant for any load resistance value at the desired operating frequency [27]. Besides the increased cost and complexity, the main drawback of compensation networks is the so called ‘‘bifurcation phenomenon’’ [79], which refers to the multiple zero-crossing the angle of the input impedance can present. This means that there can be more frequencies at which  $Im[\hat{Z}_{in}] = 0$ . Indeed, a perfect IPT link compensation requires a zero phase angle (ZPA) for the input impedance, which is desirable

at the system operating frequency. This condition strongly depends on the load value and operating frequency [27]. If not properly considered in the control strategy, the system can deviate the working frequency from the design one or move unstably between several undesirable operating conditions. As a consequence, the power transfer capability dramatically drops and the bifurcation phenomena can lead to the system instability [79]. The objective of the compensation networks can be summarised as:

- maximise the efficiency
- maximise the power transfer capability
- minimise the reactive power
- realise constant voltage or current output

and must be achieved avoiding the bifurcation phenomenon.

Compensation network topologies have been vastly explored in literature, both active and passive. Active compensations require additional components and control drivers, increasing costs and system complexity [80, 81, 82, 28]. However, if properly designed, passive networks fulfil the aforementioned requirements still preserving simplicity and reliability. Passive compensations basically mix reactive elements whose combination defines the specific characteristics the network can achieve. The basic resonant topologies are the series-series (SS), series-parallel (SP), parallel-series (PS) and parallel-parallel (PP) configurations [79, 30]. However, the primary parallel compensation is not of interest for applications, since it requires an additional inductor (whose value may not be negligible) connected in series between the inverter output port and the resonant tank [30]. Then, SS and SP configurations have been comprehensively compared and discussed in [27, 83, 84], showing the main benefits and drawbacks. Some improvements to these basic topologies have been presented, still using only capacitive elements. It is the case of the series-series/parallel compensations [34], series/parallel - series [85] and parallel/series - series network [86], which have been specifically developed for inductive wireless chargers. In the frame of high-power IPT systems, more complex topologies have been introduced, involving also lumped inductors. They are based on LCC networks, such as LCC-LCC compensation [32, 87], or the other variants LCC-S [88] and LCC-P [89]. The main advantage with respect to the above mentioned classic networks consists in the increased tolerance to the receiver misalignment, being the tuning (usually) independent on the coupling conditions. The most widespread passive compensation networks are the Series-Series (SS), Series-Parallel (SP) and LCC-LCC topologies [90, 91, 87, 32, 83]. Among them, SS and LCC-LCC are the most adopted, since they can fulfil both the CC-CV reference profiles, still preserving ZPA condition. However, they are always exploited in system with similar primary and secondary self-inductance [30, 32]. It must be noticed that, due to their physical constitutions, lumped inductors are much less efficient than lumped capacitors. For these reasons, passive capacitive compensation networks are considered hereinafter.

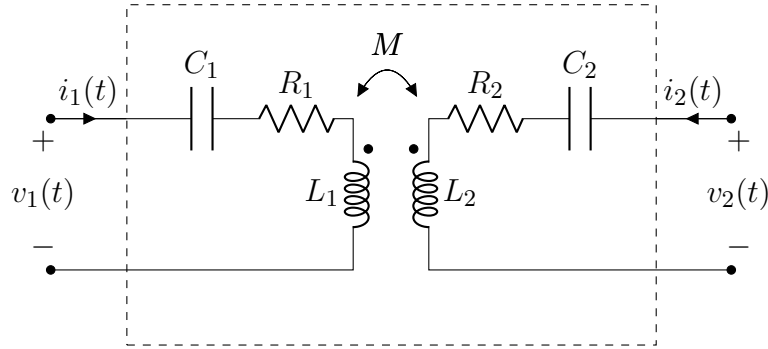


Figure 2.7: Series-series (SS) compensation of magnetically coupled coils.

### 2.3.1 Series-Series compensation

The so called series-series (SS) compensation network involves two capacitors connected in series with the primary and secondary coil inductances, as depicted in Fig. 2.7. With reference to the generic two-port model of Fig. 2.6a, the coils impedances of the IPT link modify as:

$$\begin{aligned}\hat{Z}_{11} &= R_1 + j(\omega L_1 - \frac{1}{\omega C_1}) \\ \hat{Z}_{22} &= R_2 + j(\omega L_2 - \frac{1}{\omega C_2}) \\ \hat{Z}_m &= j\omega M.\end{aligned}\tag{2.52}$$

With the proper capacitor tuning, the SS compensation ideally allows both constant voltage and constant current operations, but at different frequencies. However, while the CC mode guarantees a null input phase angle, in CV mode it cannot be reached. These features are explained in the following considering ideal networks. The presence of the winding resistance is not negligible in real applications, but only slightly modifies the frequency response of the system if the coil design is optimised.

**CC mode** According to (2.51), CC operations can be easily achieved by compensating the inductance of the primary coils with its series capacitor, and it is obtained if:

$$\omega_{cc}^{SS} = \frac{1}{\sqrt{L_1 C_1}}.\tag{2.53}$$

Then, the secondary capacitor  $C_2$  can be chosen to guarantee ZPA, namely to cancel the imaginary part of the input impedance at the desired angular frequency  $\omega$ , leading to

$$C_2 = \frac{1}{(\omega_{cc}^{SS})^2 L_2}.\tag{2.54}$$

In this condition, the input impedance results:

$$\hat{Z}_{in}^{SS}(\omega_{cc}^{SS}) = \frac{(\omega_{cc}^{SS} M)^2}{R_{load}}.\tag{2.55}$$

It is important to notice that, in real systems, the winding resistance cannot be cancelled. Thus,  $\hat{Z}_{11}(\omega_{cc}^{SS}) = R_1$  and  $\hat{G}_m$  slightly changes for varying loads.

**CV mode** Constant voltage (CV) operations are still allowed for more than one operating angular frequency and can be deduced from (2.50) applied to this SS configuration. Considering the system of ideal coupled coils, the condition becomes:

$$\omega^4(L_1L_2 + M^2) - \omega^2\left(\frac{L_1}{C_2} + \frac{L_2}{C_1}\right) + \frac{1}{C_1C_2} = 0. \quad (2.56)$$

Mathematically, four different values of  $\omega$  can verify (2.56), but only positive real values are clearly allowed. The angular frequencies  $\omega_{cv1,2}^{SS}$  that allow CV operations are:

$$\omega_{cv1,2}^{SS} = \sqrt{\frac{\left(\frac{L_1}{C_2} + \frac{L_2}{C_1}\right) \pm \Delta_\omega}{2(L_1L_2 + M^2)}} \quad (2.57)$$

where:

$$\Delta_\omega = \sqrt{\left(\frac{L_1}{C_2} + \frac{L_2}{C_1}\right)^2 - 4\frac{(L_1L_2 + M^2)}{C_1C_2}} \quad (2.58)$$

and  $\Delta_\omega \in \mathbb{R}$ . It must be noticed that, at these frequencies, ZPA is no more guaranteed and the SS compensation is usually exploited for CC operations only. The choice of the CV mode angular frequency can be done by looking at the input phase angle. Indeed, classic H-bridge converters require an inductive input impedance to realise soft switching and maximise the efficiency. In [92] it is shown that:

$$\begin{aligned} \text{Im}[\hat{Z}_{in}^{SS}(\omega_{cv1}^{SS})] &> 0 \\ \text{Im}[\hat{Z}_{in}^{SS}(\omega_{cv2}^{SS})] &< 0 \end{aligned} \quad (2.59)$$

and thus operations as  $\omega_{cv1}^{SS}$  are preferred. It must be also noticed that an inductive behaviour of the inverter allows the soft-switching, but if the impedance magnitude is too large, the efficiency drops. Thus, to reduce (and control) the input impedance still preserving CV operations, other compensation methods have to be adopted.

To avoid bifurcation phenomena in SS topologies, [79] proved that the following condition must be verified when operating at  $\omega_{cc}^{SS}$ :

$$Q_1 > \frac{4Q_2^3}{4Q_2^2 - 1} \quad (2.60)$$

where

$$Q_1 = \frac{\omega_0 L_1}{R_1} \quad Q_2 = \frac{\omega_0 L_2}{R_2} \quad (2.61)$$

are the primary and secondary coils quality factor, respectively.

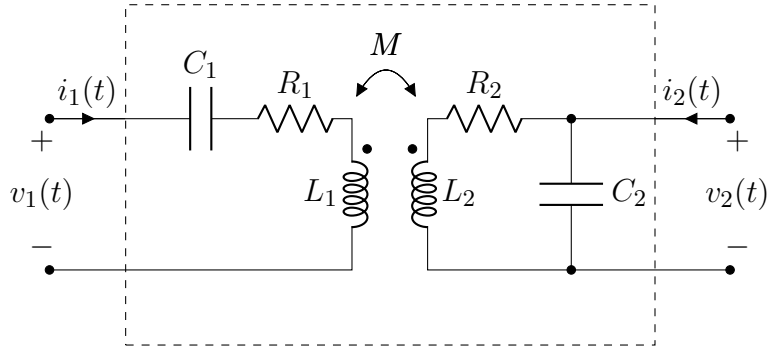


Figure 2.8: Series-parallel (SP) compensation of magnetically coupled coils.

### 2.3.2 Series-Parallel Compensation

The series-parallel (SP) compensation still involves two capacitors, one connected in series with the primary inductance and the other connected in parallel to the secondary inductance, as depicted in Fig. 2.8. To describe the network, the generic two-port can be resorted, whose impedance parameters are:

$$\begin{aligned}\hat{Z}_{11} &= R_1 + j\left(\omega L_1 - \frac{1}{\omega C_1}\right) + \frac{(\omega M)^2}{R_2 + j\left(\omega L_2 - \frac{1}{\omega C_2}\right)} \\ \hat{Z}_{22} &= \frac{(R_2 + j\omega L_2)}{1 + j\omega R_2 C_2 - \omega^2 L_2 C_2} \\ \hat{Z}_m &= \frac{j\omega M}{1 + j\omega R_2 C_2 - \omega^2 L_2 C_2}.\end{aligned}\tag{2.62}$$

It can be easily proved that the network is still reciprocal, but the mutual impedance  $\hat{Z}_m$  is no more purely imaginary and this can be addressed to the secondary winding resistance. To better understand the role of the compensation capacitors, it is possible to simplify the expressions assuming ideal windings, namely  $R_1 = R_2 = 0$ . The impedance terms then result:

$$\begin{aligned}\hat{Z}_{11} &= j\left(\omega L_1 - \frac{1}{\omega C_1}\right) + (\omega M)^2 \frac{j\omega C_2}{1 - \omega^2 L_2 C_2} \\ \hat{Z}_{22} &= \frac{j\omega L_2}{1 - \omega^2 L_2 C_2} \\ \hat{Z}_m &= \frac{j\omega M}{1 - \omega^2 L_2 C_2}.\end{aligned}\tag{2.63}$$

**CC mode** Operating at angular frequencies for which  $\hat{Z}_{11} = 0$  guarantees that the output current is independent of the load. It easy to prove that the roots of (2.56) also makes  $\hat{Z}_{11} = 0$  and thus

$$\omega_{cc1,2}^{SP} = \omega_{cv1,2}^{SS}.\tag{2.64}$$

The criterion to ensure a unique ZPA at the desired angular frequency is in this case [79]:

$$Q_1 > \frac{Q_2^2 + 1}{Q_2} \quad (2.65)$$

**CV mode** Constant voltage operations can be found from (2.50) applied to this system configuration, yielding:

$$\frac{L_2 + (\omega M)^2}{C_1(1 - \omega^2 L_2 C_2)} - \frac{\omega^2 L_1 L_2}{(1 - \omega^2 L_2 C_2)} = 0 \quad (2.66)$$

whose positive root is:

$$\omega_{cv}^{SP} = \sqrt{\frac{1}{C_1(L_1 - \frac{M^2}{L_2})}}. \quad (2.67)$$

It can be noticed that a CV output can be achieved regardless the tuning of the secondary compensation, which can be usually done with the aim of compensating the reactive part of the receiver load or realizing ZPA input impedance at the desired  $\omega$  [93]. This can be ensured by simply enforcing:

$$\omega_{cv}^{SP} = \frac{1}{\sqrt{L_2 C_2}} \quad (2.68)$$

resulting in the input impedance at  $\omega_{cv}^{SP}$

$$\hat{Z}_{in}^{SP}(\omega_{cv}^{SP}) = \frac{M^2}{L_2} R_{load}. \quad (2.69)$$

The main drawback of this tuning is the dependence of  $\omega_{cv}^{SP}$  on the coupling condition, expressed by  $M$ . In IPT applications, the alignment of the coils is not always guaranteed, endangering CV operation of the SP compensated systems.

The SP and SS compensations are the basic networks from which the more complicated topologies can be derived. Indeed, SS and SP are very simple and effective, even if they can be improved, at the cost of increasing losses, complexity and costs. Based on the above analysis, the SS resulted to be a great solution for achieving coupling independent CC operations, still ensuring ZPA. Instead, the SP compensation strategy can be used to easily achieve CV output in ZPA condition, but this is possible at operating frequencies that depend on the coupling conditions (see eq. (2.67)). This dependence requires control strategies able to track and vary the operating frequency, with the risk of working out of resonance. A careful design is then necessary.

### 2.3.3 Series-Series/Parallel Compensation

The series-series/parallel (SSP) configuration can be seen as an improvement of the SP topology to guarantee an higher tolerance to the receiver misalignment. It

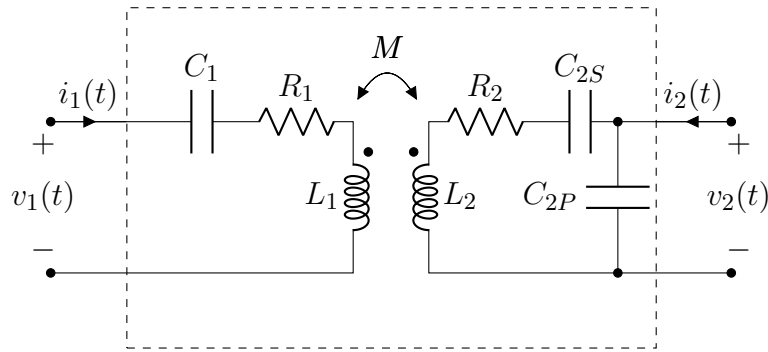


Figure 2.9: Series-series/parallel (SSP) compensation of magnetically coupled coils.

is represented in Fig. 2.9. According to [94], the series capacitors compensate the coils leakage inductances, while the parallel one compensates the mutual inductance. Intuitively, this latter capacitor aims at providing the reactive power required by the magnetizing inductance. The capacitors are tuned so that:

$$\omega_{cv}^{SSP} = \frac{1}{\sqrt{(L_1 - M)C_1}} = \frac{1}{\sqrt{(L_2 - M)C_{2S}}} = \frac{1}{\sqrt{MC_{2P}}}. \quad (2.70)$$

This expression clearly indicates that the tuning is still dependent on the coupling condition, but the resulting voltage gain is much more stable with respect to coupling variations.

### 2.3.4 Series/Parallel Primary Compensation

The series/parallel - series (SPS) and series/parallel - parallel (SPS) topologies have been introduced to combine the benefits of the series and parallel primary compensation. They are represented in Figs. 2.10a and 2.10b, respectively, and are realised starting from parallel-series or parallel-parallel networks introducing a series primary capacitor. Then, the desired operating mode can be realised and the exceeded input impedance can be compensated with the primary series capacitor. In particular, these networks can be exploited for merging:

- CV operations and ZPA with a secondary series compensation
- CC operations and ZPA with a secondary parallel compensation.

As discussed in Sec. 2.5, a passive receiver rectifier requires a sinusoidal input current to ensure diode soft-switching. This condition cannot be achieved with a capacitor in parallel with the rectifier input port, since it enforces the voltage to be sinusoidal, resulting in a distorted current. Thus, a secondary series compensation is preferred.

A general idea about the benefits and drawbacks of these compensation networks is discussed in [85, 33]. It states that these configurations allow the input impedance

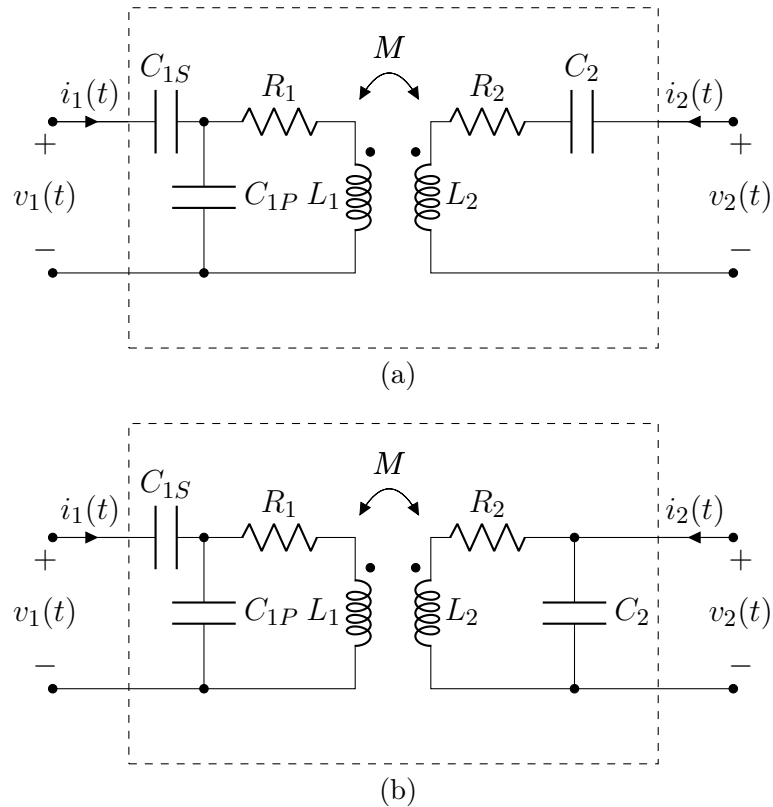


Figure 2.10: Schematic of (a) series/parallel - series (SPS) and (b) series/parallel - parallel (SPP) compensation topology.

to be adjusted as desired while preserving the secondary coil and capacitors required for optimal operations. However, undesired sub-resonances may complicate the practical implementation.

In [95] safety concerns are also discussed. In general, it can be seen that IPT links operating in CV mode behave as voltage sources. This implies that, at the angular frequency that allows CV operations, the link equivalent impedance seen from the load towards the source tends to infinite values. In case of faults and short-circuit events, the coils, compensation networks and power source are intrinsically protected. Conversely, the CC operations lead to an ideal null impedance of the system seen from the load, and possible faults can damage the system components. In general, secondary compensated systems are more suitable for CV operations, even if the optimal operating angular frequency is affected by the coupling conditions [85, 95, 33]. For CC operations, SS compensated IPT systems are chosen, being the inductive link perfectly compensated and thus very efficient when operating at  $\omega_{cc}^{SS}$ . However, safety countermeasures must be adopted.

## 2.4 Power Source

With the aim of enhancing the magnetic induction phenomenon, modern IPT systems are fed by a high-frequency alternating voltage, provided by a DC/AC switching power converter. Due to recent developments in semiconductor technologies, the inverter power MOSFETs can reach switching frequencies in the order of tens of kHz. This is the case of silicon carbide (SiC) and gallium nitride (GaN), which have been tested up to 400 kHz for high-power applications and up to 1 MHz for consumer electronic devices [96].

In practical applications, the DC bus is usually fed by a power factor correction (PFC) stage, which rectifies the grid voltage and whose main role consists in fixing the DC bus voltage [3]. However, in this work, it is not discussed and a DC ideal voltage source  $V_{dc}$  is considered as upward power source.

In this work, the H-bridge (single-phase) inverter depicted in Fig 2.11a has been considered. Depending on the adopted modulation strategy, the output inverter voltage  $v_{in}(t)$  can be a two or three-level square wave, with a peak value equal to the DC bus voltage  $V_{dv}$  and peak-to-peak value of  $2V_{dc}$ . The signal frequency corresponds to the MOSFETs switching frequency  $f_{sw}$ . The main control parameters of an H-bridge converter are: the MOSFETs switching frequency  $f_{sw}$ , the MOSFETs duty cycle  $D$  and the time delay between the opening and closing of MOSFETs of different legs. This latter parameter leads to a displacement angle  $\delta$  between the output voltage of the two inverter legs, whose minimum value is the so called “dead time”, necessary to avoid the switch short circuit. While  $f_{sw}$  basically acts on the period of  $v_{in}(t)$ , the duty cycle and the phase-shift  $\delta$  change the width of the positive and negative pulses of the waveform, depicted in Fig. 2.11b. The phase shift control is generally referred to as duty cycle control since  $D$  and  $\delta$  are related as:

$$D = \sin\left(\frac{\delta}{2}\right). \quad (2.71)$$

The effect of these parameters can be better appreciated in the frequency domain. The square voltage  $v_{in}(t)$  can be expressed as as:

$$v_{in}(t) = V_{dc} \sum_{n=1}^{\infty} \frac{4}{n\pi} \sin\left(\frac{n\delta}{2}\right) \cos(n\omega_{sw}t). \quad (2.72)$$

where  $\omega_{sw} = 2\pi f_{sw}$  is the switching angular frequency and  $n$  the harmonic order. The expression shows that the phase shift directly acts on the amplitude of the spectral components, while  $f_{sw}$  on its frequency.

The large coil inductance makes the coupling system behaves as a filter for the input voltage  $v_{in}(t)$  and, in particular, a third order low-pass filter. Thus, the harmonic components of the receiver voltage  $v_r(t)$  are strongly smoothed and the fundamental component dominates over them. It follows that a sufficiently accurate description of the IPT system behaviour can be obtained considering operations at a single frequency, namely at the frequency of the fundamental component of the

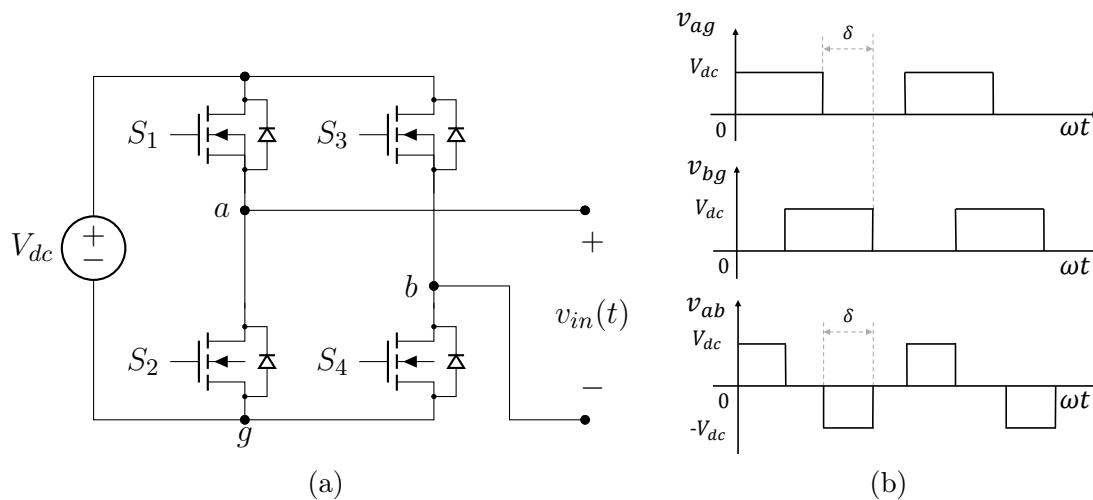


Figure 2.11: (a) Schematic of an H-bridge inverter and (b) inverter leg voltage waveforms showing phase shift between inverter legs and the resulting output voltage waveform  $v_{in}(t) = v_{ab}$ , with  $v_{ab} = v_{ag} - v_{bg}$ .

primary coil input voltage. This assumption is usually referred to as “first harmonic approximation” and allows the phasor representation of the circuit variables. The phasor associated to the fundamental component of  $v_1(t)$  at the switching angular frequency  $\omega_{sw}$  is:

$$\hat{V}_1 = \frac{4}{\pi} V_{dc} \sin\left(\frac{\delta}{2}\right) e^{j0}. \quad (2.73)$$

whose phase angle is assumed null in this work. According to [97], the internal impedance of voltage source inverters is usually negligible with respect to the equivalent impedance of the IPT system seen from the inverter output port. Thus, the inverter can be considered an ideal voltage source with value  $\hat{V}_1$ .

### 2.4.1 Zero Voltage Switching

Power electronic converters are characterised by a high versatility still preserving great efficiency. However, in high-power and high-frequency applications saving in losses becomes crucial. The main contribution to the converter losses are the conduction and the switching losses, both due to the non ideal behaviour of the switches [98]. The conduction losses are due to the presence of a parasitic resistance, which dissipates power when crossed by a current. The switching ones are instead related to the commutation of the switches, which is not instantaneous (not ideal). Thus, both the turn on and turn off operations take some time in which neither the switch current nor the voltage are null. Their product corresponds to the dissipated power. This occurs at each commutation and thus the switching losses are proportional to the switching frequency [98].

While the conduction losses can be limited only by acting on the switch technology, the switching losses can be reduced ensuring the switch turn off occurs when the

voltage is null. This condition is referred as “zero voltage switching (ZVS)” and is especially applied when employing MOSFETs. It is important to notice that it can be achieved for the turn off only. ZVS is basically achieved charging the parasitic capacitance  $C_{oss}$  of the switch, so that it behaves as it is ideal (the MOSFET  $V_{GS}$  is null). During the commutation, the load current (that deviates from flowing through the closed switch to the open one) charges the parasitic output capacitance of the opening switch and discharges the one of the closing switch. If the closing switch capacitance is fully charged before the current crosses its zero value, then a nearly ideal turn off commutation occurs [99, 98]. This requires that the load current is sufficiently high and lags the square voltage. These conditions can be achieved ensuring the load presents an inductive behaviour and thus, considering a sinusoidal load current, the condition can be written as:

$$\arg[\hat{Z}_{load}(\omega_{sw})] > 0. \quad (2.74)$$

In IPT systems, the inverter load basically corresponds to the cascade of compensation networks, coupling system and receiver circuit. Equation (2.74) is a fundamental condition that must be taken into account in the system design. Alternatively, (2.74) can be fulfilled adjusting the operating frequency, thereby requiring a more sophisticated control. Overall, ZVS guarantees:

- Zero turn-off power losses
- Reduced EMI / RFI at transitions
- No power loss due to discharging  $C_{oss}$
- High efficiency with high voltage inputs at any frequency
- Reduced gate drive requirements (no Miller effects being  $V_{GS} = 0$  during turn-off)

while the main disadvantage consists in a more complex design, with the further requirement expressed by (2.74). The ZVS technique can be applied to any switching converter, whose topology only affects the required current and load constraint.

## 2.5 Receiver Circuit

The receiver circuit is basically devoted to the conditioning of the transmitted power and, depending on the specific application, it can involve a passive or active rectification [100, 101, 102]. The latter can also allow bidirectional power flow [103, 104], which has encountered growing interest over the past few years due to the increasing diffusion of electric vehicles. The output power is commonly used to feed generic loads or charge batteries, along with to power more complex powertrain architectures. In this frame, the most widespread solution consists in a first passive rectification stage followed by a DC/DC converter that adjusts the voltage to fulfil the

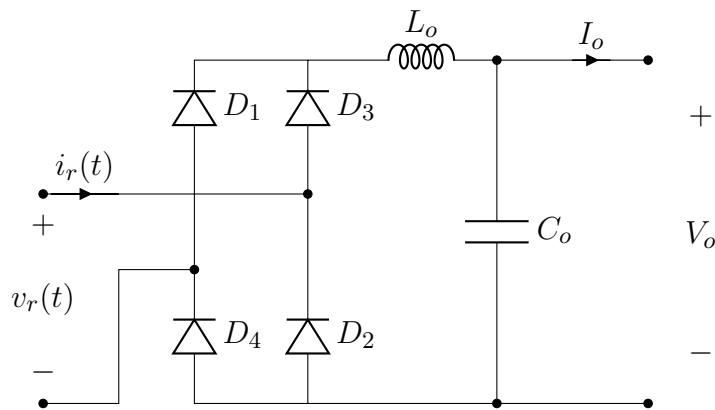


Figure 2.12: Passive full bridge rectifier.

load requirements [3, 103, 101]. Depending on the nature of the converter, different receiver voltage and current may be required. Indeed, in presence of a DC/DC conversion stage upward the battery management system (BMS), the IPT link can be controlled to simply set the desired chopper DC bus voltage. Conversely, in case of passive rectification, the IPT system is required to provide the required battery voltage and current. This can be achieved by acting on the primary voltage through the inverter. In this work, a passive full-bridge rectifier with a second order output filter is chosen. The circuit is depicted in Fig. 2.12. A nearly sinusoidal receiver current allows the rectifier diodes to commute at zero current, thereby dramatically reducing the rectifier switching losses. The output filter sizing is strictly correlated to the specific application and it is assumed it makes the ripple in the DC output current  $I_o$  and voltage  $V_o$  negligible. In first harmonic approximation, the rectifier circuit can be modelled as a resistance, whose value is defined as the ratio between the phasors of the receiver voltage  $\hat{V}_r$  and the current  $\hat{I}_r$  as:

$$R_{ac} = \frac{\hat{V}_r}{\hat{I}_r}. \quad (2.75)$$

The nature of the secondary compensation basically defines the calculation of the  $R_{ac}$ . Indeed, the current and voltage of a non linear load can be discontinuous and, in general, at least one of the two variables is. As discussed in [105], if the rectifier input voltage is enforced to be sinusoidal and the rectifier output filter presents an inductive behaviour, then the current will be distorted and (2.22) becomes:

$$R_{ac} = \frac{\pi^2}{8} R_o \quad (2.76)$$

where  $R_o$  is the equivalent DC load. This is the typical case of a parallel compensated receiver, where the parallel capacitor forces the output receiver voltage to be continuous and makes the system behaves as an equivalent voltage source. Conversely, if the rectifier input current is sinusoidal and the rectifier filter is capacitive,  $R_{ac}$  modifies as:

$$R_{ac} = \frac{8}{\pi^2} R_o \quad (2.77)$$

which is the case of a series compensated receiver. Indeed, the secondary coil inductance forces the output current to be continuous and the system matches the characteristics of a current source.

## 2.6 Conclusions

The operation of IPT systems is based on the principle of magnetic induction and the power is then transferred between two magnetically coupled coils. In addition to the optimisation of the coil coupling coefficient and self-inductance, modern wireless power transfer systems provide for the use of compensation networks. These circuits allow the efficiency and the transmitted power to be maximised and, with the proper tuning, also allow particular operating modes to improve the control of the load voltage and current. Among the possible operating strategies, constant voltage and constant current operations have been analysed, which are obtained by making the voltage gain or transadmittance independent of the load. Due to the intense filtering action of the IPT link (which comprises the cascade of the compensation networks and the inductive coupling), the harmonics of voltages and currents in the circuits are dramatically smoothed, and the first harmonic approximation can hold. Overall, although the device architecture appears simple and similar to those of traditional transformers, appropriate measures are required to achieve good performance in terms of efficiency and power transfer.

## Chapter 3

# Circuit-Based Design of IPT Systems

Modern inductive power transfer systems have proved to be capable of transmitting a very large amount of power alongside ensuring high efficiency. However, depending on the specific application, these systems have to fulfil also other load requirements, i.e. adequate output voltage and current. To achieve these goals, a proper circuitry is used to feed the primary coil and to convert the power received by the secondary coil, resulting in complex system architectures whose components require an adequate design procedure. The first and major issue concerns the dependence of the system behaviour on the adopted network topology, which makes a general design algorithm very difficult to be defined. In this section, the passive parts forming the IPT system are described and their behaviour analysed. Different solutions are discussed and compared with the aim of providing useful design guidelines.

### 3.1 Design Procedure

The definition of a suitable design procedure requires the main system specifications and degrees of freedom to be harmonised with the system physical constraints. In IPT apparatuses, both the size and the connections of the circuit components can be freely chosen. It is therefore important to provide guidelines so that the device meets the requirements and is optimised for the specific application. While the main goal of any IPT device can be considered the efficient transmission of the desired power, different voltage and current profiles may be required to be fulfilled, which are defined by the particular nature of the load. In high-power applications, the load usually consists of a battery, fed by its own passive or active rectifying circuitry as discussed in Sec. 2.5. All these features clearly affect the design, which should be carried out once the circuit topology is chosen, and thus the work frame of the system must be first identified. The presented design procedure has been defined enforcing:

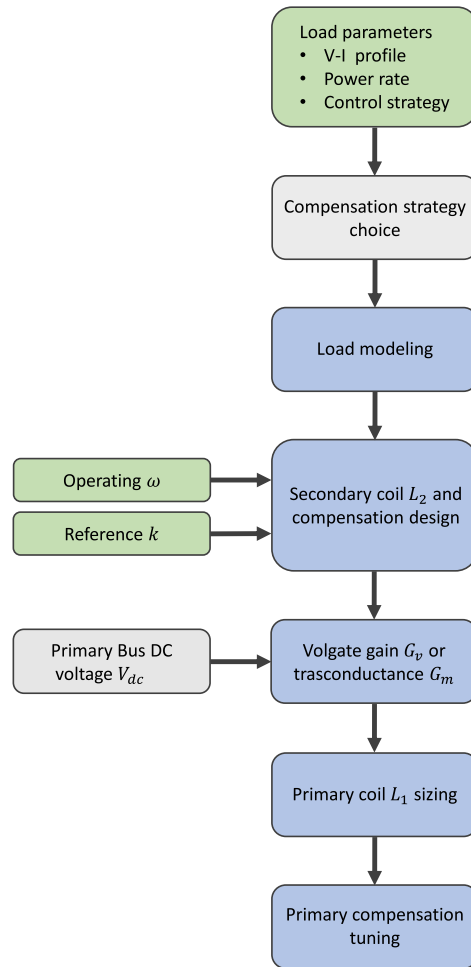


Figure 3.1: Flow chart illustrating the design steps for the IPT link with the compensation networks based on the load requirements. The green boxes indicate the specifications, the grey boxes the degrees of freedom and the blue boxes the calculation steps.

- Maximum system efficiency
- Lightweight vehicle assembly
- Fulfilment of the required voltage gain
- Zero voltage switching (ZVS)
- Minimum circulation of reactive power (ZPA)

and the main steps are summarised in the flow chart of Fig. 3.1. The first design step consists in the choice of the compensation network, that must be addressed based on the desired operating mode. In automotive applications and, in general, in the majority of high-power chargers, the battery is fed by a DC/DC converter and

the IPT system is driven to regulate its DC bus voltage [3]. Thus, CV operation is usually the best control strategy, which can be easily achieved with an SP compensation network. However, this network has the disadvantage of coupling-dependent capacitor tuning and thus the SS topology may be preferred.

Once the compensation strategy has been defined, the design passes through the modelling of the load, as discussed in Sec. 2.5. In particular, a DC load  $R_{l0}$  is derived based on the type of battery pack. The next step consists in the matching of the receiver. Indeed, the presented procedure exploits the condition of maximum efficiency for defining the optimal secondary capacitance value, but requires to choose a reference coupling coefficient  $k_0$  and primary and secondary coils quality factors ( $Q_1$  and  $Q_2$  respectively). They can be chosen so that the bifurcation is avoided, as suggested in [79]. From the secondary capacitance value, the size of the secondary coil inductance  $L_2$  is defined to make the receiver resonate at the desired frequency. As a rule of thumb, deviating this inductance value of about 15%–20% ensures pole splitting phenomena to be avoided [79].

The primary coil inductance  $L_1$  can be designed to achieve the desired voltage gain or transadmittance of the converter (the choice depends on the adopted control strategy and operating mode). These parameters are usually referred to the IPT link input voltage  $\hat{V}_1$ , which however is strictly correlated to the inverter control strategy and DC bus voltage  $V_{dc}$ . In general, it holds  $|\hat{V}_1| = 4V_{dc}/\pi$ . The last step consists in the tuning of the primary compensation at the design operating frequency for achieving the prefixed IPT link behaviour.

## 3.2 Load Modelling: Battery Pack for Automotive Applications

High-performance lithium-ion batteries are the most used energy storage systems, especially for electric vehicle (EV) applications [106, 107]. In particular, modern automotive powertrain systems are now mainly equipped with 400V battery packs composed of either high-power or high-density cylindrical cells [106, 107, 108]. In this chapter, as a case study, a battery pack composed of 21700 cylindrical cells with a nominal voltage equal to 3.6V is considered, which are driven with a voltage that ranges from a minimum of 3.2V up to a maximum of 4.2V. Then, considering 100 series connected cells, the battery pack voltage ranges from 320V to 420V and the resulting maximum power is 3.6kW (corresponding to the first level described in [3]). The typical charging profile consists of a first constant current (CC) mode followed by a constant voltage (CV) mode, represented in Fig. 3.2a as a function of the battery state of charge (SOC) for the considered pack. The charger must then provide the proper DC voltage and current to the battery, which depends on the SOC conditions and is estimated through current or voltage measurements. The power  $P_0$  absorbed by the battery can be easily derived from this profile and it is reported in Fig. 3.2b. It strongly varies during the charging and reaches the maximum value

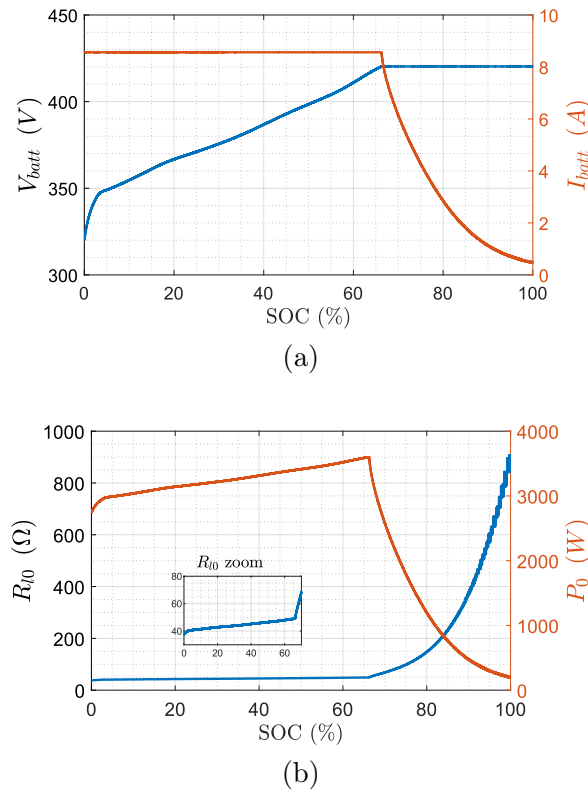


Figure 3.2: Characteristics of the battery pack: a) voltage and current profiles b) absorbed power and equivalent resistance.

in the transition region (from CC to CV mode). The DC conversion stage and the battery can be globally modelled as a variable resistance  $R_{l0}$  as:

$$R_{l0} = \frac{V_{batt}^2}{P_0}. \quad (3.1)$$

It strongly depends on the charging profile and behaves nearly linearly only in the range 44 $\Omega$  - 60 $\Omega$ . Considering the battery lifetime and recycle time, a battery charger must provide sufficiently accurate charging current and voltage for safe operation. From the charging profile shown in Fig. 3.2, the battery equivalent resistance increases significantly as the charging operation goes from CC to CV modes.

### 3.3 Design of a Series-Parallel Compensated IPT System

As discussed in Sec. 3.1, passive capacitive compensations are preferred in practical applications. In this section, the SP topology is analysed, with the aim of evaluating its feasibility for static charging systems. The SP compensation has the main advantage of allowing high-efficiency operations when working in CV mode [30, 109]. The presence of the DC/DC converter does not require the IPT link

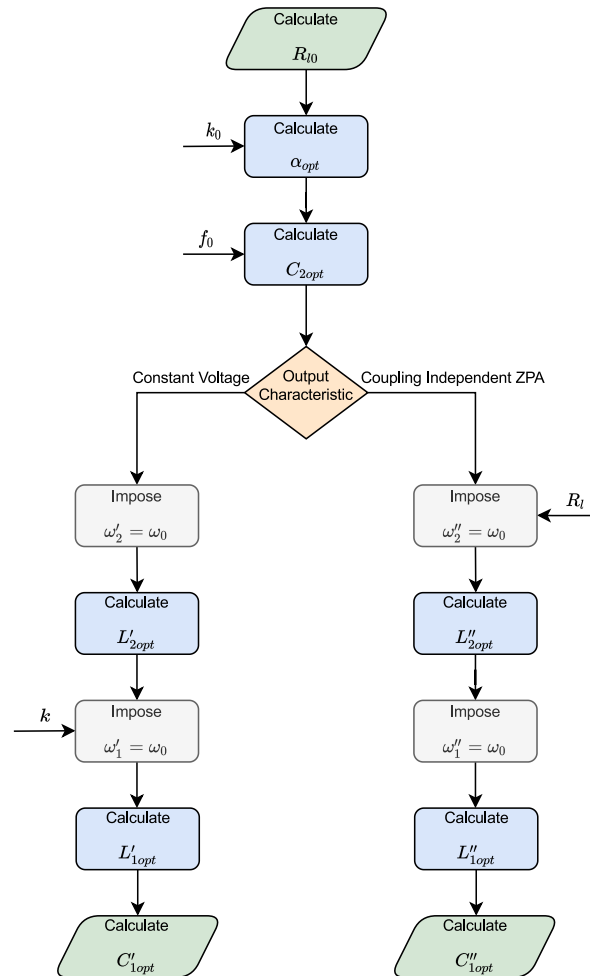


Figure 3.3: Flow chart illustrating the design algorithm for the inductive coupling and the compensation networks based on the selected output characteristic. The load resistance  $R_l$  and the coupling coefficient  $k$  refer to actual parameters during variable operating conditions.

to follow the complete voltage and current profile. Moreover, an optimised design allows the secondary inductance to be kept 3 ÷ 4 times smaller than the transmitter one, allowing saving in space and weight. This condition does not occur in SS compensated systems, for which the optimal design leads to a less pronounced difference between the primary and secondary inductances. Lightness is one of the fundamental requirements for mechanical components, especially in the automotive sector. The main drawback of SP compensation is the dependence of the primary compensation tuning on coupling conditions. However, automotive IPT systems usually include several sensors to drive the vehicle positioning and thus only slight variations of the inductance parameters occur. A good alignment is indeed crucial to limit the magnetic field emissions, for which stringent requirements are reported in the standards [3, 23]. Two different design procedures are proposed for achieving either a CV or ZPA at the desired resonant frequency and are summarised in the

flow chart depicted in Fig. 3.3. All the calculations are reported and discussed in the following and the different parameter choices motivated.

### 3.3.1 Load Matching

The SP compensation makes the IPT link behave as a current source while the rectifier involves a second order filter at its output [105]. As discussed in Sec. 2.5, in the hypothesis of ideal components and first harmonic approximation, the overall load seen from the receiver port can be modelled as an equivalent resistance defined as:

$$R_l = \frac{\pi^2}{8} R_{l0} = \frac{\pi^2}{8} \frac{V_{batt}^2}{P_0}. \quad (3.2)$$

With the aim of maximising the power delivered to the reference load, the optimal receiver tuning can be done enforcing the efficiency is maximised. This condition can be found analytically, as discussed in [93, 110]. The total link efficiency can be defined as the ratio between the load power and the one at the input of the primary coil (the primary compensation is not considered):

$$\eta_{Tlink} = \frac{P_{load}}{P_{inlink}} = \frac{\frac{|\hat{V}_2|^2}{R_l}}{\operatorname{Re} \left[ \hat{V}_{L_1} \hat{I}_{L_1}^* \right]} \quad (3.3)$$

where  $\hat{V}_{L_1}$  is the phasor voltage across the primary coil and  $\hat{I}_{L_1}$  its phasor current. This expression can be rearranged as [93]:

$$\eta_{Tlink} = \frac{k^2 Q_1 Q_2^2}{(\alpha + Q_2) \left( 1 + k^2 Q_1 Q_2 + \frac{Q_2}{\alpha} \right)} \quad (3.4)$$

with  $\alpha = \omega C_2 R_l$  and  $\omega = 2\pi f$ , that is the angular frequency associated to the operating frequency  $f$ . It is important to notice that this expression is valid for any primary compensation strategy and receiver tuning. Indeed, different choices can be done for the secondary capacitance value. By differentiating the link efficiency and enforcing:

$$\frac{\partial \eta_{Tlink}}{\partial \alpha} = 0 \quad (3.5)$$

it is possible to find the value of  $\alpha$  that maximises the efficiency, referred as  $\alpha_{opt}$ , which results in:

$$\alpha_{opt} = \frac{Q_2}{\sqrt{1 + k_0^2 Q_1 Q_2}}. \quad (3.6)$$

In the hypothesis of high-quality factors  $Q_1$  and  $Q_2$  and assuming a reference coupling factor  $k_0$ ,  $\alpha_{opt}$  is uniquely determined. The optimal value of the secondary capacitance  $C_{2opt}$  is thus found for the design load  $R_{l0}$  and resonant frequency  $f_0$  as:

$$C_{2opt} = \frac{\alpha_{opt}}{\omega_0 R_{l0}}. \quad (3.7)$$

### 3.3.2 Design for Constant Voltage Output

From the definition of the receiver angular frequency it is possible to find the secondary inductance  $L_{2_{opt}}$  that allows the receiver to resonate at the design resonant frequency. Nevertheless, different definitions of receiver angular frequency are possible. With the aim of achieving a constant voltage output at  $\omega_0$ , a parallel compensated receiver has to be tuned as:

$$\omega_0 = \frac{1}{\sqrt{L_2 C_2}} \quad (3.8)$$

and thus the optimal value of  $L_2$  can be obtained straightforwardly as:

$$L_{2_{opt}}^{CV} = \frac{1}{\omega_0^2 C_{2_{opt}}^{CV}} \quad (3.9)$$

or, equivalently,

$$L_{2_{opt}}^{CV} = \frac{1}{\alpha_{opt}} \frac{R_{l0}}{\omega_0}. \quad (3.10)$$

The optimal value  $L_{1_{opt}}$  of primary inductance is defined based on the desired voltage gain magnitude, which can be expressed as a function of the generic  $\alpha$  parameter as:

$$|\hat{G}_v^{CV}| = \sqrt{\frac{L_2}{L_1}} \left[ \frac{\alpha Q_1 k_0}{1 + \alpha Q_1 k_0^2} \right]. \quad (3.11)$$

Introducing the expression of  $\alpha_{opt}$  in (3.11), after some mathematical manipulations the primary inductance value is found to be:

$$\begin{aligned} L_{1_{opt}}^{CV} &= L_{2_{opt}}^{CV} \left( \frac{1}{|\hat{G}_v|} \frac{\alpha_{opt} Q_1 k_0}{1 + \alpha_{opt} Q_1 k_0^2} \right)^2 \\ &= L_{2_{opt}}^{CV} \left( \frac{1}{|\hat{G}_v|} \frac{k_0 Q_1 Q_2}{k_0^2 Q_1 Q_2 + \sqrt{1 + k_0^2 Q_1 Q_2}} \right)^2. \end{aligned} \quad (3.12)$$

As last, the primary capacitor value is tailored to compensate the overall link impedance (already referred as  $\hat{Z}_{in}$ ) for realising ZPA as:

$$C_{1_{opt}}^{CV} = \frac{1}{\omega_0^2 L_{1_{opt}}^{CV} (1 - k_0^2)}. \quad (3.13)$$

Due to the dependence of the primary compensation tuning on  $k_0$  (coupling condition), a possible misalignment between the transmitter and receiver can strongly deviate the system behaviour from the design one.

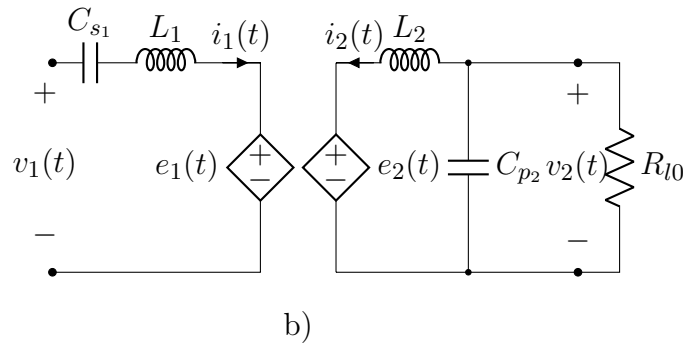


Figure 3.4: Equivalent circuits of the resonant inductive link with primary and secondary decoupled inductors and series controlled voltage sources.

### 3.3.3 Design for Coupling Independent ZPA

The main objective of compensation networks is to provide the coupling device with the reactive power necessary for the transfer of active power. In this view, it is possible to calibrate the secondary compensation in order to perfectly compensate the receiver. This corresponds to cancelling the reactive part of the receiver impedance seen by the ideal controlled voltage source  $e_2(t)$  which represents the induced voltage in the secondary, as it can be seen in Fig. 3.4. For a parallel compensated receiver, the impedance can be expressed as:

$$\hat{Z}_2 = R_2 + j\omega L_2 + \frac{R_{l0}}{1 + j\omega C_2 R_{l0}} \quad (3.14)$$

$$= R_2 + \frac{1}{1 + (\omega C_2 R_{l0})^2} + j\omega \left( L_2 - \frac{C_2 R_{l0}^2}{1 + (\omega C_2 R_{l0})^2} \right) \quad (3.15)$$

and thus it is possible to have  $\text{Im}[\hat{Z}_2] = 0$  at  $\omega_0$  if:

$$\sqrt{\frac{C_2 R_{l0}^2 - L_2}{L_2 C_2^2 R_{l0}^2}} = \omega_0. \quad (3.16)$$

It can be noticed that the tuning of this compensation network described in (3.8) allows CV operations, but it does not allow the imaginary part of the receiver impedance to be completely compensated. Indeed,  $\hat{Z}_2$  presents a “residual” real term due to the parallel connection of the load and secondary capacitor.

Mathematically, a real receiver impedance that would maximise the power transferred for a fixed  $e_2(t)$  is obtained with an imaginary resonant frequency only, which is, of course, meaningless. From (3.16), it is possible to find the optimal secondary inductance value at  $\omega_0$  as:

$$L_{2_{opt}}^{ZPA} = \frac{C_{2_{opt}} R_{l0}^2}{1 + (\omega_0 C_{2_{opt}} R_{l0})^2} \quad (3.17)$$

or, equivalently,

$$L_{2_{opt}}^{ZPA} = \frac{\alpha_{opt}}{1 + \alpha_{opt}^2} \frac{R_{l0}}{\omega_0}. \quad (3.18)$$

The primary compensation can be exploited to ensure ZPA, namely cancelling the imaginary part of the link input impedance. With the receiver tuned according to (3.16), this can easily be achieved if:

$$\omega_0 = \frac{1}{\sqrt{L_1 C_1}}. \quad (3.19)$$

In this condition, the voltage gain magnitude results:

$$|\hat{G}_v^{ZPA}| = \sqrt{\frac{L_2}{L_1}} \frac{k Q_1 Q_2 \sqrt{\alpha^2 + 1}}{\alpha k^2 Q_1 Q_2 + \alpha + Q_2}. \quad (3.20)$$

The optimal primary inductance value can then be found considering the matched receiver ( $\alpha = \alpha_{opt}$ ) as:

$$\begin{aligned} L_{1_{opt}}^{ZPA} &= L_{2_{opt}}^{ZPA} \left( \frac{k_0 Q_1 Q_2 \sqrt{\alpha_{opt}^2 + 1}}{|\hat{G}_v| (\alpha_{opt} k_0^2 Q_1 Q_2 + \alpha_{opt} + Q_2)} \right)^2 \\ &= L_{2_{opt}}^{ZPA} \left( \frac{k_0 Q_1 \sqrt{\frac{1+k_0^2 Q_1 Q_2 + Q_2^2}{1+k_0^2 Q_1 Q_2}}}{|\hat{G}_v| (1 + \sqrt{1 + k_0^2 Q_1 Q_2})} \right)^2 \end{aligned} \quad (3.21)$$

and thus the primary capacitor results:

$$C_{opt}^{ZPA} = \frac{1}{\omega_0^2 L_{1_{opt}}^{ZPA}}. \quad (3.22)$$

With this choice, the resonant frequencies of the primary and secondary circuits are independent of the alignment conditions of the transmitting and receiving coils, since the coupling coefficient parameter  $k$  does not appear in the expressions defining the capacitance values. It is however important to note that for the calculation of the condition of maximum efficiency a reference value  $k_0$  has been assumed for the coupling coefficient. The misalignment affects the optimal value of  $\alpha$ , which would slightly deviate the optimal values of primary and secondary inductances and capacitances. However, the system always works in resonance, guaranteeing maximum efficiency with the resulting parameters.

### 3.3.4 Case Study

The design procedures presented in Sec. 3.1 were applied in a test case involving an automotive IPT battery charging system with a battery pack of the type described in Sec. 3.2. The specifications for the IPT system design are given in the first part of Table 3.1, the resulting parameter values are reported in the second part, while the third part lists the inductive link components. The design assumptions are:

Table 3.1: Case study system parameters for the SP design.

<i>Quantity</i>	<i>Symbol</i>	<i>Value</i>	<i>Unit of Measure</i>
<b>Specifications</b>			
On board DC bus rated voltage	$V_{dc}$	420	V
Inverter DC bus rated voltage	$V_{DC}$	230	V
Power rate	$P_{dc}$	3	kW
Operating frequency	$f_0$	85	kHz
Primary inductor quality factor	$Q_1$	$\gg 100$	-
Secondary inductor quality factor	$Q_2$	$\gg 100$	-
Reference coupling coefficient	$k_0$	0.3	-
<b>CV Output</b>			
Primary inductor	$L_{1opt}^{CV}$	89.8	$\mu\text{H}$
Secondary inductor	$L_{2opt}^{CV}$	26.77	$\mu\text{H}$
Primary capacitor	$C_{1opt}^{CV}$	43	nF
Secondary capacitor	$C_{2opt}^{CV}$	131	nF
<b>Coupling Independent ZPA</b>			
Primary inductor	$L_{1opt}^{ZPA}$	89.8	$\mu\text{H}$
Secondary inductor	$L_{2opt}^{ZPA}$	24.5	$\mu\text{H}$
Primary capacitor	$C_{1opt}^{ZPA}$	42.9	$\mu\text{F}$
Secondary capacitor	$C_{2opt}^{ZPA}$	131	$\mu\text{F}$

- inductor quality factors  $Q_1$  and  $Q_2$ ;
- reference coupling coefficient  $k_0$ .

The results reported in the Tab. 3.1 show that the value of the secondary inductance is about 4 times lower than that of the primary for both design approaches, in accordance with expectations. Similarly, but in opposite relationship, are the capacities. The overall energy of the system is therefore completely comparable, even if the nature of the prevailing one changes. It can then be noted that the optimum values of the primary inductance are approximately the same for the two different tuning approaches, while the receiving coil inductances slightly differ. In addition, studying the trends of  $L_{2opt}^{CV}$  and  $L_{2opt}^{ZPA}$  as a function of  $\alpha$  it can be found that the two inductances present approximately the same value for  $\alpha_{opt} > 6$ , regardless of the particular system specifications. Indeed, the ratio between  $L_{2opt}^{CV}$  and  $L_{2opt}^{ZPA}$  is expressed as:

$$\frac{L_{2opt}^{CV}}{L_{2opt}^{ZPA}} = \frac{1 + \alpha_{opt}^2}{\alpha_{opt}^2} \quad (3.23)$$

that tends to 1 for  $\alpha_{opt} \rightarrow \infty$ . This corresponds to the case of ideal coils with null resistance, again testifying the impact of the coils quality factors on the optimal

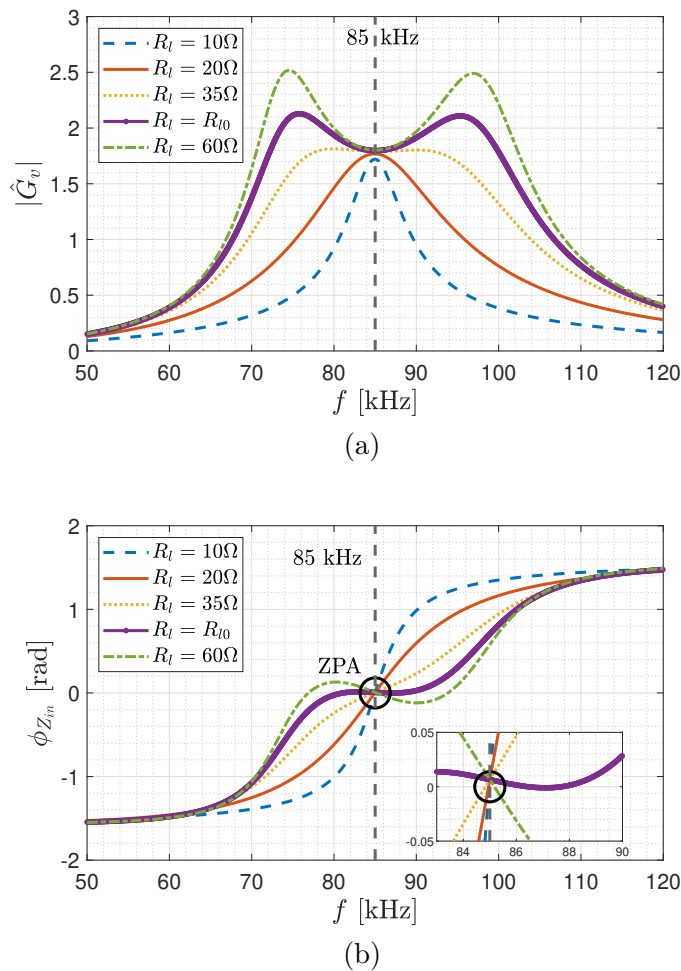


Figure 3.5: **(a)** Voltage gain magnitude and **(b)** input impedance angle as a function of the frequency for the inductive link designed for CV operations at  $f_0 = 85$  kHz.

performance and, in turn, on the design.

The voltage gain and the input phase angle of the IPT system tuned for CV operations are reported in Fig. 3.5 as a function of the frequency and for different load values. From Fig. 3.5a, it can be seen CV operations can be achieved if the system exactly works at the resonant frequency, being  $|\hat{G}_v^{CV}|$  strongly affected by the frequency shift. The input phase angle can become negative if  $R_l > R_{l0}$ , with the consequent risk of increasing the switching losses. From Fig. 3.6 is instead possible to see the voltage gain and input phase angle as functions of the frequency in case of tuning for coupling independent ZPA. Different curves at different loads show the strong variation that both  $|\hat{G}_v^{CV}|$  and  $\Phi_{in}$  can experience during the charging cycle. The most critical condition is represented by the trend of the input phase angle, which can present negative values for small loads. However, for small loads, the primary current is also low and the switching losses are limited. The main advantage of the tuning proposed in Sec. 3.3.3 can be appreciated from Fig. 3.7, which reports the input phase angle of the IPT system as a function of the frequency for different

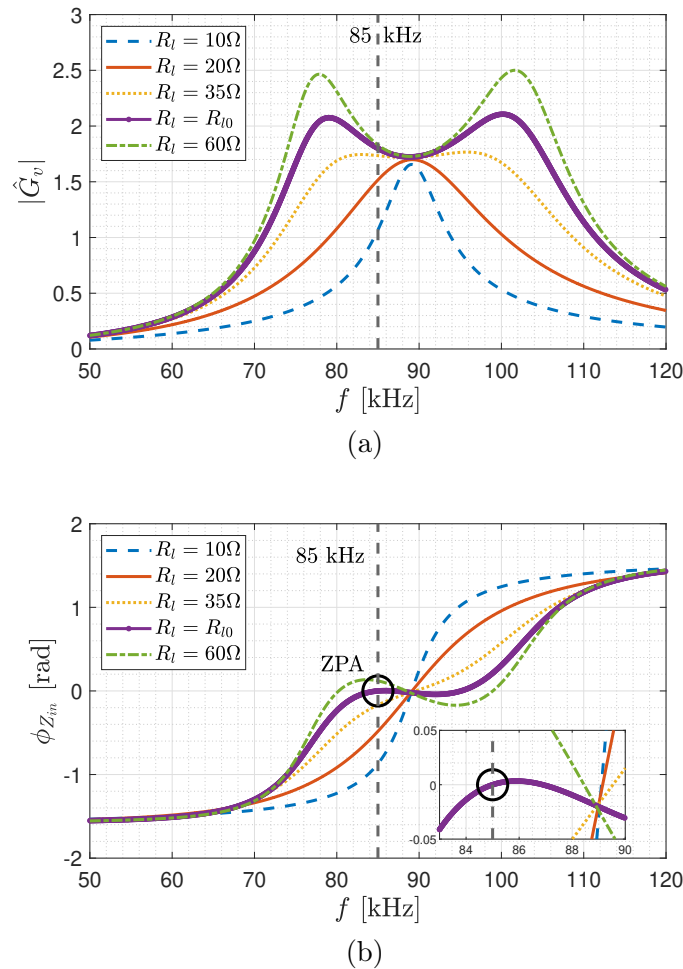


Figure 3.6: **(a)** Voltage gain magnitude and **(b)** input impedance angle as a function of the frequency for the inductive link designed for coupling independent ZPA operations at  $f_0 = 85$  kHz.

values of the coupling coefficient. In particular, Fig. 3.7a refers to the tuning for CV operations and clearly highlights that the input phase angle is strongly affected by the coupling conditions, with the risk of deviating from the optimal operating value (slightly larger than zero). From Fig. 3.7b it can be seen that the system designed for coupling independent ZPA is capable of preserving a perfect compensation for each value of  $k$ , namely the resonance frequency is independent of the coupling coefficient. It must be noticed that ZVS operations are necessary to limit the inverter losses. They require the input phase angle to be slightly larger than zero, which can be easily achieved by deviating the value of the primary resonant capacitor from the optimum one (derived from the analytical formulas). However, an increase in  $k$  can lead the system to work in capacitive region, decreasing the efficiency. It is therefore essential to dimension the system considering the strongest coupling condition that the system is assumed to experience.

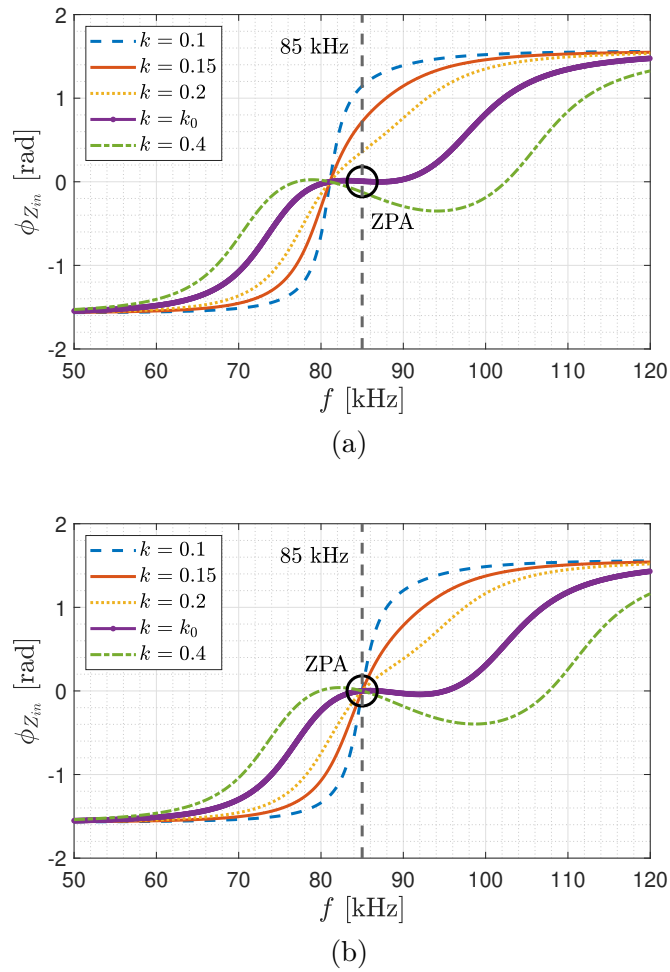


Figure 3.7: Input impedance angle as a function of the frequency for different coupling coefficients in case of inductive link designed for (a) CV output and (b) coupling independent ZPA operations at  $f_0 = 85$  kHz.

### 3.3.5 Efficiency Characterisation

The efficiency of the SP compensated IPT system designed for CV or coupling independent ZPA has been calculated for different operating conditions and is reported in logarithmic scale in Fig. 3.8. The efficiency is calculated unless iron and diodes losses as a function of the equivalent load resistance  $R_l$  for different coupling coefficients  $k$  at the operating frequency is  $f_0 = 85$  kHz. The system tuned for coupling independent ZPA appears slightly more efficient with respect to the one tuning for CV operations. This result can be addressed to the receiver tuning, which is perfectly compensated when the condition (3.16) is fulfilled. However, for a certain value of  $R_l$ , an higher coupling coefficient leads to higher efficiency, as it can be expected. The maximum value of the efficiency is found for loads closed to the reference one  $R_{l0}$  and is 97.8%. The efficiency is higher as the coupling coefficient increases, while the maximum of the efficiency curves occur in correspondence of

higher equivalent loads as the coupling coefficient decreases. The difference between the two trends is more significant approaching high loads and the curves referred to the system tuned for CV operations overlap. When used as a battery charger, the system load can vary drastically, going from very low to very high values. It is therefore important to verify that the efficiency is acceptable throughout the load range foreseen for the specific application.

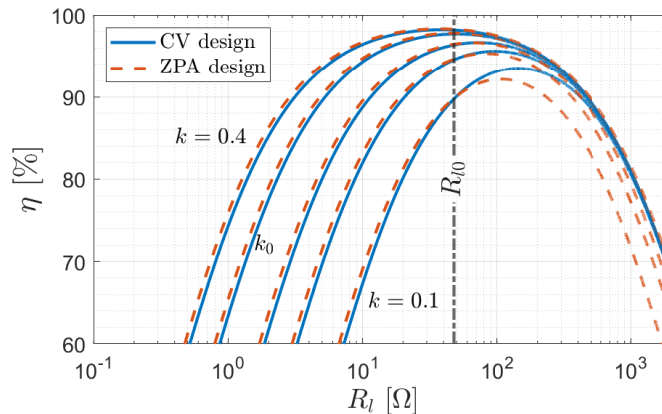


Figure 3.8: Overall link efficiency of a WPT system designed for CV or coupling independent ZPA, operating at  $f_0$ , as a function of the receiver equivalent load  $R_l$ , for different coupling coefficients  $k$ .

### 3.4 Design of a Series-Series Compensated IPT System

In this section, a design procedure for SS compensated IPT systems is presented, in analogy to the algorithm proposed in Sec. 3.3. The same load and specifications are then considered. Avoiding making hypotheses on the choice of the compensation tuning, we proceed as previously illustrated, maximising the power transferred to the load and therefore the efficiency of the transmission. The first step consists in the load modelling and the definition of the specifications, which are considered the same as in the SP case. For series compensated receivers, the equivalent resistance representing the whole receiver load is defined as:

$$R_l = \frac{8}{\pi^2} R_{l0} = \frac{8}{\pi^2} \frac{V_{batt}^2}{P_0}. \quad (3.24)$$

Then, the efficiency of the IPT link that considers the coupled coils and the receiver compensation is written in terms of  $\alpha = \omega R_l C_2$  as [93]:

$$\eta_{link} = \frac{\alpha k^2 Q_1 Q_2}{(1 + \alpha Q_2 + k^2 Q_1 Q_2)(1 + \alpha Q_2)} \quad (3.25)$$

and, enforcing

$$\frac{\partial \eta_{link}}{\partial \alpha} = 0 \quad (3.26)$$

the optimum  $\alpha$  value  $\alpha_{opt}$  that maximises the efficiency is found:

$$\alpha_{opt} = \frac{Q_2}{\sqrt{1 + k_0^2 Q_1 Q_2}}. \quad (3.27)$$

This expression is analogous to the same obtained for the SP compensation and still requires hypotheses on the quality factors  $Q_1$  and  $Q_2$  and coupling coefficient, together with the operating frequency  $f_0$  and load  $R_{l0}$ . Assuming high values of  $Q_1$  and  $Q_2$  and a reference coupling coefficient  $k_0$ , the optimal value of the secondary capacitance  $C_{2opt}$  is thus found for the design load  $R_{l0}$  and resonant frequency  $f_0$  as:

$$C_{2opt} = \frac{\alpha_{opt}}{\omega_0 R_{l0}}. \quad (3.28)$$

Differently from the SP topology, there is no ambiguity in the choice of the secondary compensation tuning, being the imaginary part of the receiver impedance completely cancelled when tuned as in (3.28). Despite different operating modes are possible (see Sec. 2.3.1), constant current operation mode is the preferred one, requiring a simple tuning which is also independent on the coupling conditions. Thus, the primary and secondary capacitors are dimensioned to compensate the primary and secondary coil inductance, respectively. The secondary inductance  $L_2$  is the found as:

$$L_{2opt}^{CC} = \frac{1}{\alpha_{opt}} \frac{R_{l0}}{\omega_0}. \quad (3.29)$$

Following the work flow reported in Sec. 3.1, it is now possible to design the primary inductance according to the desired voltage gain or transadmittance. Being the SS topology well suited to CC operations, the transadmittance is chosen. However, it must be noticed that these two parameters are related as:

$$\hat{G}_v = -R_l \hat{G}_m \quad (3.30)$$

and thus, once the load is fully characterised in terms of current and voltage, they can be used equivalently. In terms of the  $\alpha$  parameter, the transadmittance magnitude of a SS compensated IPT system can be written as:

$$|\hat{G}_m| = -\frac{1}{R_l} \sqrt{\frac{L_2}{L_1}} \left[ \frac{\alpha k Q_1 Q_2}{1 + \alpha Q_2 + k^2 Q_1 Q_2} \right] \quad (3.31)$$

from which the optimal primary inductance  $L_{1opt}$  is found considering the reference coupling coefficient  $k_0$  and  $\alpha_{opt}$ :

$$\begin{aligned} L_{1opt} &= L_{2opt} \left[ \frac{1}{|\hat{G}_m| R_l} \frac{\alpha_{opt} k_0 Q_1 Q_2}{1 + \alpha_{opt} Q_2 + k_0^2 Q_1 Q_2} \right]^2 \\ &= L_{2opt} \left[ \frac{1}{|\hat{G}_m| R_l} \frac{k_0 Q_1 Q_2 \sqrt{1 + k_0^2 Q_1 Q_2}}{\sqrt{1 + k_0^2 Q_1 Q_2} + Q_2 + k_0^2 Q_1 Q_2} \right]^2. \end{aligned} \quad (3.32)$$

Table 3.2: Case study system parameters for the SS design.

<i>Quantity</i>	<i>Symbol</i>	<i>Value</i>	<i>Unit of Measure</i>
<b><i>Specifications</i></b>			
On board DC bus rated voltage	$V_{dc}$	420	V
Inverter DC bus rated voltage	$V_{DC}$	230	V
Power rate	$P_{dc}$	3	kW
Operating frequency	$f_0$	85	kHz
Primary inductor quality factor	$Q_1$	$\gg 100$	-
Secondary inductor quality factor	$Q_2$	$\gg 100$	-
Reference coupling coefficient	$k_0$	0.3	-
<b><i>CC Output</i></b>			
Primary inductor	$L_{1_{opt}}^{CV}$	141	$\mu\text{H}$
Secondary inductor	$L_{2_{opt}}^{CV}$	297	$\mu\text{H}$
Primary capacitor	$C_{1_{opt}}^{CV}$	25	nF
Secondary capacitor	$C_{2_{opt}}^{CV}$	12	nF

The design is concluded with the choice of the primary capacitor  $C_1$  that aims at compensating the primary inductance in the condition of maximum link efficiency. The optimal value  $C_{1_{opt}}$  is simply defined as:

$$C_{1_{opt}}^{CV} = \frac{1}{\omega_0^2 L_{1_{opt}}}. \quad (3.33)$$

Both the primary and secondary compensations are independent on the coupling coefficient, meaning that the system can efficiently operate also in misalignment conditions (even if an efficiency reduction inevitably occurs).

### 3.4.1 Case Study

The validation of this design procedure can be done considering the system specifications presented in Sec. 3.2. The resulting IPT link parameter values are reported in Tab. 3.2. The self-inductance values of the primary and secondary coils result in a ratio of approximately 2, which is equivalent to the voltage gain of the system. This characteristic is also common to traditional transformers that employ solenoid windings, in which the transformer ratio coincides with the ratio between the number of turns of the primary and secondary windings. In an IPT system, the coils typically have a planar geometry, and thus the number of turns does not have the same meaning as in solenoid windings. However, it is possible to find an analogy if we consider the square root of the inductance ratio.

The capacitors are sized with the aim of fully compensating the inductances of the two windings. It can be seen that the values of  $C_{1_{opt}}$  and  $C_{2_{opt}}$  are also in ratio 2,

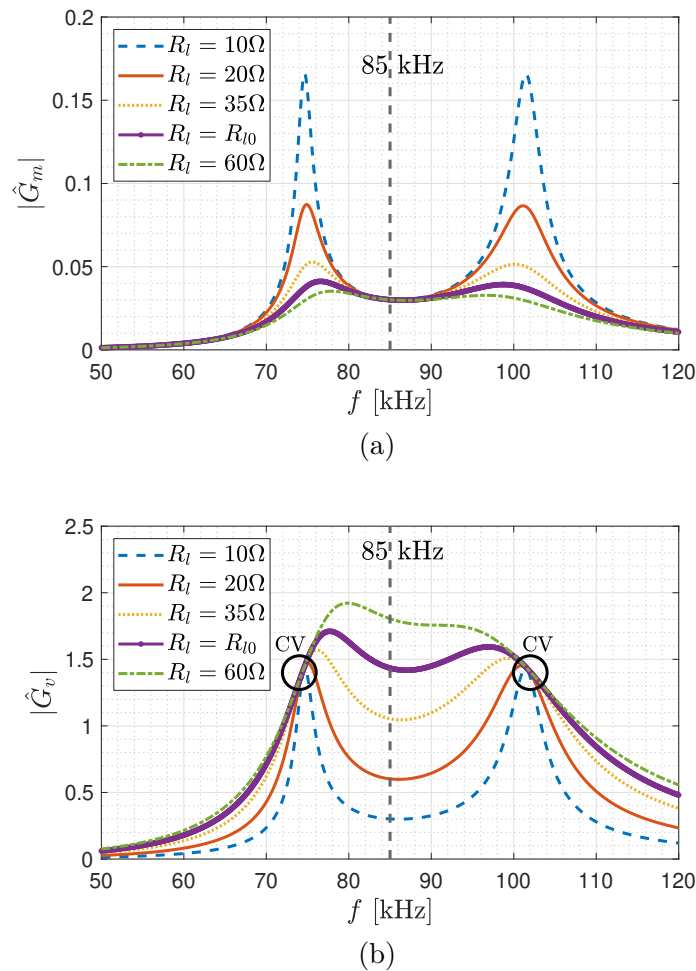


Figure 3.9: (a) Transadmittance magnitude and (b) voltage gain magnitude as a function of the frequency for the SS compensated IPT link designed for CC operations at  $f_0 = 85\text{ kHz}$ .

like the inductances. This simply demonstrates how the system (reactive) energy is conserved and that the compensation networks provide all the reactive power required by the coupling system.

One of the main features of SS compensated IPT systems is the load independent behaviour of the transadmittance. In Fig. 3.9a is represented the transadmittance of the system as a function of the frequency for different loads and it is noted how the curves intersect at the resonant frequency. The voltage gain is instead shown in Fig. 3.9b as a function of the frequency and for different loads. It results load dependent at the resonant frequency, as expected. However, there are two points at two different frequencies where the gain curves intersect for any load value, as announced in Sec. 2.3.1. They are highlighted with black circles. For those frequencies, the voltage gain is independent of the load. They can be calculated as in (2.57) and for this system result in  $f_{cv_1}^{SS} = 74\text{ kHz}$  and  $f_{cv_2}^{SS} = 102\text{ kHz}$ . As discussed in Sec. 3.1, IPT systems for automotive applications usually feature in-vehicle DC/DC converters

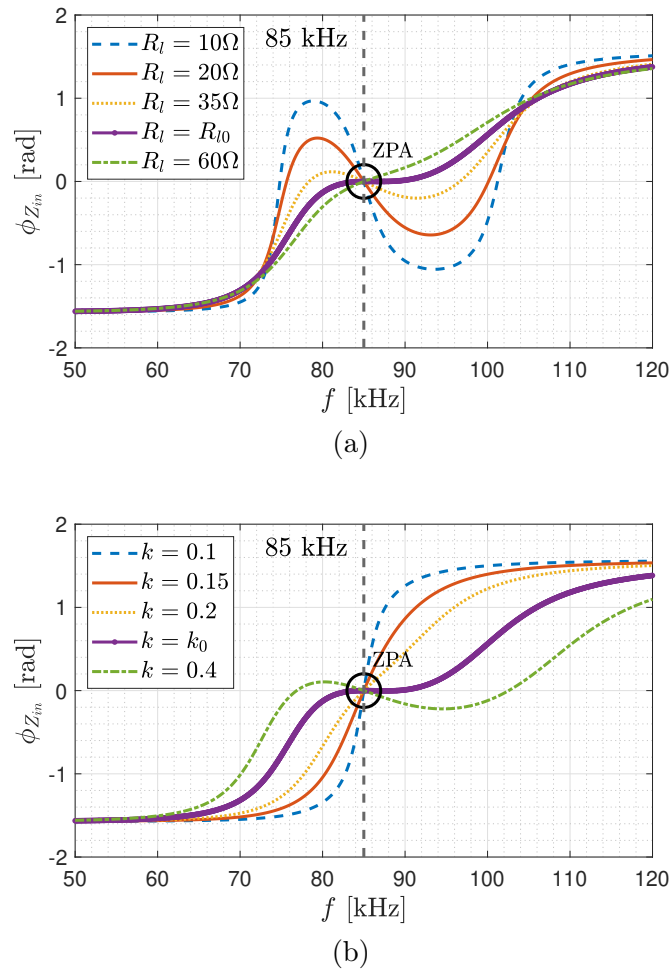


Figure 3.10: Input impedance angle as a function of the frequency for different (a) receiver loads and (b) coupling coefficients of the SS compensated IPT link designed for CV operations at  $f_0 = 85$  kHz.

to regulate the battery voltage and current. In these conditions the system must therefore operate in CV mode. However, it is disadvantageous to work in CV mode (therefore far from the resonant frequency) in SS compensated systems as the tuning of the compensation networks no longer guarantees a null input phase angle at the working frequency and, above all, not independent on the coupling conditions. In Figs. 3.10a and 3.10b the system input angle is shown as a function of the frequency for different loads and different alignment conditions between the transmitter and receiver coils. It can be noticed that, still working at the resonant frequency, it is possible to obtain both load independent and coupling independent ZPA behaviour. Moving away from that frequency it is likely to incur in negative values of the input phase angle, which does not allow the source converter to work in ZVS. In practical implementations, the capacitance of the primary capacitor is chosen slightly lower than that necessary to guarantee ZPA operations, so that the IPT link is globally slightly inductive and allows the ZVS of the inverter MOSFETs. In this frame, it

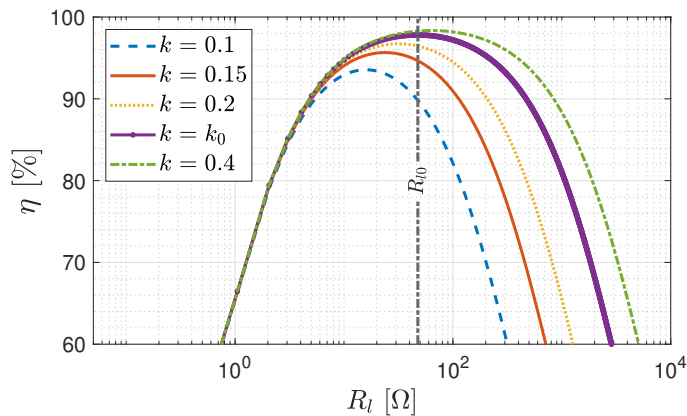


Figure 3.11: Overall link efficiency as a function of the receiver equivalent load  $R_l$  and for different coupling coefficients  $k$  of the SS compensated IPT link designed for CV operations at  $f_0 = 85$  kHz, operating at  $f_0$ ,

is essential to consider that, for loads lower than the reference one, the input phase angle becomes negative. It is therefore necessary to properly evaluate  $R_{l0}$ , choosing it among the lowest values that the system will have to deal with. The efficiency of the system (without considering the core and capacitor losses) is shown in Fig. 3.11. As expected, it has maximum values in correspondence with the reference load and decreases dramatically as the coupling coefficient decreases. In particular, the efficiency of the system is very sensitive to the coupling condition at high loads, while at light loads it always presents approximately the same trend. This suggests once again that it is essential to consider an appropriate reference load, which should be as close as possible to that of steady state, but with a tolerance such as to consider the light load conditions.

## 3.5 Conclusions

A design workflow for passive compensated IPT systems has been discussed and defined for inductive links with SP and SS compensation networks. The methodologies were applied to the design of a wireless charging system for automotive applications. These devices are mostly equipped with an on-board DC/DC converter that regulates the voltage and current of the battery. It is therefore important to ensure efficient and robust power transfer against load and coupling coefficient variations. In general, it can be assumed that it is sufficient to control the voltage of the receiver (which corresponds to that of the DC bus of the on-board converter) by keeping it at a predetermined value.

As it results from the analysis of the two compensated systems SS and SP, the ideal solution requires a voltage operation independent of the load and the coupling coefficient. With an SP compensated system it is easy to reach the first condition, but the resulting voltage gain is strongly affected by the coupling coefficient. Con-

versely, a  $k$ -independent tuning can be achieved with a SS compensation, at the cost of having a voltage gain that is not constant as the load varies. In this configuration, however, constant current operation is obtained, which can be exploited to control the current of the circuit downstream the receiver. This mode of operation is typical of single-stage battery chargers. Starting from the same project specifications, it is evident that the SP compensation allows the same power to be transmitted with similar efficiency using a receiving coil approximately three times lower than that of the transmitting one in terms of inductance. As already discussed, a lower inductance leads to a smaller weight and volume, which are very important characteristics in the automotive environment. However, it is important to note that this system is very sensitive to coupling conditions, which, in the field, may not correspond to the ideal ones. For this reason, SS compensated systems are preferred in an industrial environment, where there are fewer constraints of size and weight.

As last consideration, it can be noticed that the parallel compensated receiver experiences a very large current, being it limited by the winding resistance only. Besides overload issues, that can be avoided with a suitable coil design, high receiver currents can lead to high magnetic fields, with the risk of exceeding the standard limits. Special attention should be paid to shielding strategies in SP compensated systems.

## Chapter 4

# Resonator Arrays for IPT

Arrays of resonators have been introduced as coupling devices in IPT systems to overcome one of the major limitations of near-field WPT apparatuses, that is the weakness of the transmitter-receiver coupling. Indeed, the transmitter and receiver are often strongly misaligned, as schematically illustrated in Fig. 4.1a, resulting in a coupling coefficient  $k \ll 0.1$  which dramatically limits the performance of the system. In fact, larger misalignments lead to important decrease in efficiency and transferred power, together with an increase of the magnetic field in the surrounding, that mirrors the increased coil leakage inductances. Whenever possible, the coupling is dramatically improved employing magnetic cores that drive the transmitter flux towards the receiver, but these solutions are not always possible. Indeed, besides the cost, magnetic cores are basically made of ferrite or surrogates, whose mechanical characteristics make their manufacturing (especially the shaping) very difficult. They are also very fragile, with a consequent risk of fractures when subjected to vibrations, events that can easily occur in automotive and industrial environments. It must also be noticed that, even if ferrite cores present a reduced electrical conductivity with respect to traditional magnetic materials (and consequently lower losses), they operate efficiently up to a frequency close to 500 kHz. However, there are several applications that exploit higher frequencies for IPT, such as biomedical and consumer electronics IPT devices, that work around tens of MHz. For these solutions, ferrite cores generate too many losses. A widely exploited alternative is the use of intermediate relay coils, that can be placed in between the transmitter and receiver coils, resulting in a structure of magnetically coupled circuits as depicted in Fig 4.1b. The relay coils are basically wound coils or PCB-printed inductors connected to a lumped capacitor tuned so that the circuit resonates at the IPT system operating frequency. They basically relay the magnetic field received by the previous coil, enhancing the magnetic coupling between the transmitter and receiver coils. Consequently, also the transmitted power and efficiency increase and are limited by the internal resistance of the coils only. Thus, the crucial parameter that affects the performance of the system is the quality factor of the relay resonators, which should be maximised by design. The resulting device can be considered a

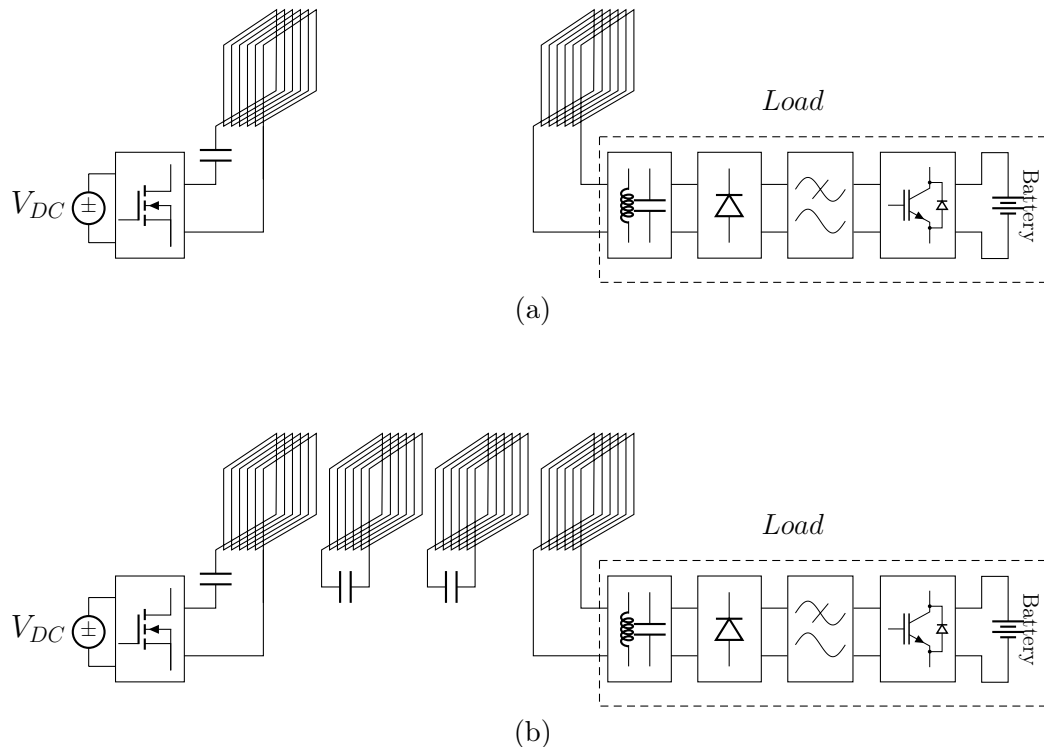


Figure 4.1: Schematic representation of (a) strongly misaligned IPT system (SPS) and (b) the same system with two intermediate relay coils.

simple extension of the original two-coils system, but some issues concerning power reflection phenomena may lead to system glitches or, in the worst case, even to the complete breakdown. An accurate and general model is then crucial for the design and analysis of resonator arrays.

The structure of these devices can widely vary depending on the applications, with the resonators arranged in different ways [41, 43, 111, 112] and there not exist conventional coils and array structures. These kinds of systems behave differently depending on the coils arrangement, shape and parameters. The majority of the applications employ resonator arrays to transmit small power in the range of a few watts and operate at very high frequency for near-field operations, namely around tens of MHz. This chapter aims to evaluate the feasibility of resonator arrays to operate in the industrial and automotive environment, where high power rates are required and the operating frequency must not exceed tens of kHz. As already mentioned in Chapter 3, the frequency is limited by the technology of the power electronic components and, more stringently, for safety reasons (magnetic field limits). As a power supply, a switching converter is still considered, while the load is the passive rectifier with a filter and battery pack described in Sec. 2.5. This analysis starts considering a generic resonator array where the transmitter feeds a receiver through the intermediate relay coils to then deal with the case of resonator array used as a transmitter, which feeds a receiver placed over it at any position.

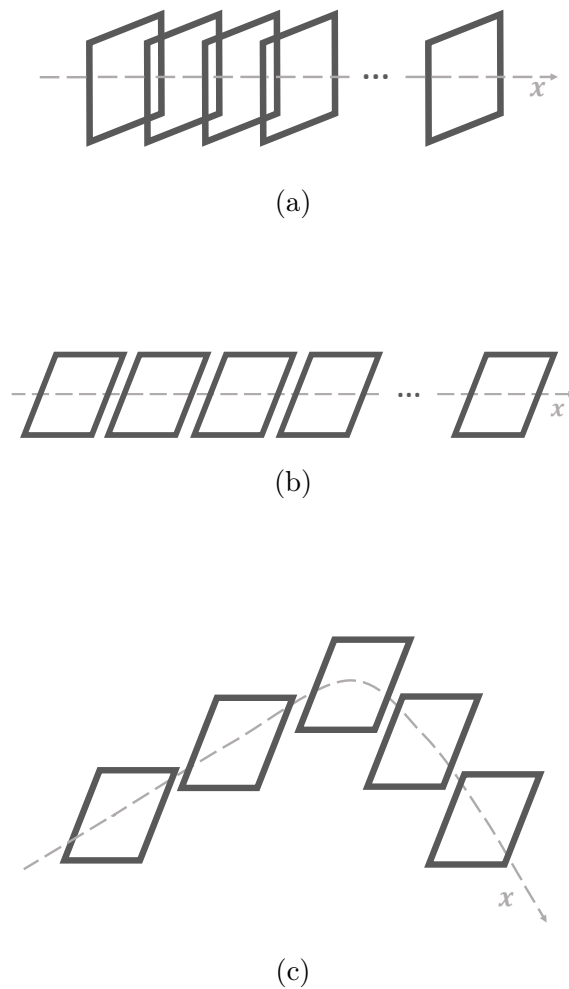


Figure 4.2: Schematic representation of 1D resonator arrays in a (a) coaxial arrangement (b) planar structure along a line and (c) generic planar arrangement. The direction  $x$  denoted by the dashed line indicates the path of the power travelling along the array.

## 4.1 1D Resonator Arrays

This section considers 1D resonator arrays composed of  $n$  magnetically coupled resonant circuits, called resonators or cells. In general, any system of coupled resonators can be considered a 1D array if the mutual inductance between adjacent coils prevails over that defined between non-adjacent coils and the pairs of adjacent cells consecutively lie in a direction of the space. Some examples are schematically illustrated in Fig. 4.2, where the coils can be coaxial or arranged in a plane along a line. The former structure is schematically depicted in Fig. 4.2a while the latter in Figs. 4.2b and 4.2c. The array in Fig. 4.2c can still be considered planar, even if the resonators lie along a bent line. The main difference between coaxial and planar structures consists in the mutual inductance, whose sign is positive for coupled (and

close enough) coaxial coils and negative for the planar coupled ones. The magnitude is in general expected to be larger for coaxial coils, but clearly depends on the inter-cell distance. For the purposes of power transfer, the sign of the mutual inductance is irrelevant, proving that it is the same for any pair of coupled resonators.

### 4.1.1 Resonator Array Equivalent Circuit

The equivalent circuit of a one-dimensional resonator array feeding a load and powered by a half-bridge inverter is reported in Fig. 4.3. For simplicity, all the resonators are assumed to be equal in terms of self-inductance and lumped capacitance, arranged symmetrically so that mutual inductance is the same for any couple of adjacent resonators. Moreover, the mutual coupling between nonadjacent cells is much lower than that between adjacent resonators, and thus it is neglected. In literature, this assumption is commonly adopted when dealing with periodic resonant structures [64] and it is also known as “nearest-neighbour interaction”. The resonators are then characterised by a self-inductance  $L$  and resistance  $R$ , while the mutual inductance between adjacent coils is denoted by  $M$ . Each coil is series connected to a lumped capacitance  $C$  so that they resonate at the frequency:

$$f_0 = \frac{1}{\sqrt{LC}}. \quad (4.1)$$

The resonators are labelled in increasing order from 1 to  $n$ , where the first is connected to the power source and the  $n$ th to the load, as depicted in Fig. 4.3. Operations at the cell resonant frequency guarantee that the resonator currents are sinusoidal, and that the first harmonic approximation can hold. An associated equivalent circuit of the resonator can be easily derived, while the power source and the load can be modelled as discussed in Sec. 2.4. As a power source, any other voltage source inverter can be used, provided that the correspondent Thévenin equivalent voltage  $\hat{V}_s$  and impedance  $\hat{Z}_s$  are appropriately modified. According to Sec. 2.4, at the frequency  $f_0$  and assuming  $\delta = \pi$ , the equivalent voltage source defined in (2.73) can be expressed as:

$$\hat{V}_s = \frac{2V_{dc}}{\pi} e^{j0} \quad (4.2)$$

and

$$\hat{Z}_s = \frac{8R_{on}}{\pi^2} e^{j\frac{t_d\omega_0}{2}} \quad (4.3)$$

where  $R_{on}$  is the resistance of the MOSFETs. The dead time  $t_d$  can be considered negligible with respect to the period  $T_0 = 1/f_0$  of the fundamental voltage component, and for operations at  $f_0$  the inverter is assumed an ideal voltage source  $\hat{V}_s$ . Being the resonator series compensated, the equivalent load is represented by the resistance

$$R_{load} = \frac{8}{\pi^2} R_{battery} \quad (4.4)$$

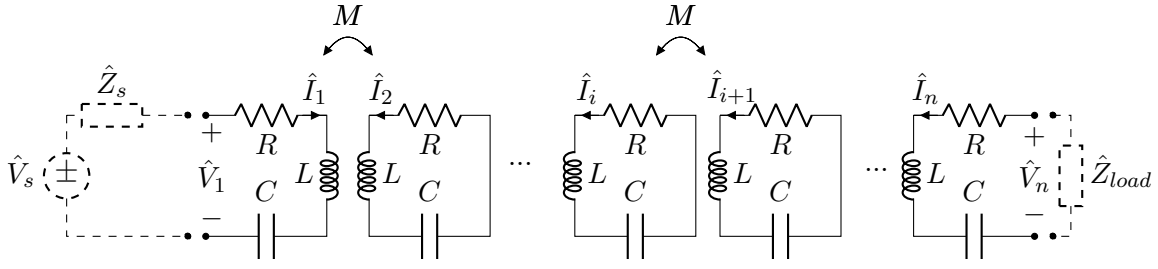


Figure 4.3: Equivalent frequency-domain circuits of a resonator array.

where  $R_{battery}$  is the resistance of the battery pack. However, also in this case, different receiver terminations can be adopted and the load equivalent resistance changes accordingly.

A mathematical model for generically arranged resonator arrays can be derived writing the Kirchhoff voltage law equations for each array cell. Assuming operation at the generic frequency  $f$ , the system of  $n$  KVL equations written in phasor form results:

$$\begin{aligned}
 \hat{V}_1 &= \hat{Z}\hat{I}_1 + j\omega M\hat{I}_2 \\
 0 &= \hat{Z}\hat{I}_2 + j\omega M\hat{I}_1 + j\omega M\hat{I}_3 \\
 &\vdots \\
 0 &= \hat{Z}\hat{I}_{i-1} + j\omega M\hat{I}_{i-2} + j\omega M\hat{I}_i \\
 0 &= \hat{Z}\hat{I}_i + j\omega M\hat{I}_{i-1} + j\omega M\hat{I}_{i+1} \\
 &\vdots \\
 0 &= \hat{Z}\hat{I}_{n-1} + j\omega M\hat{I}_{n-2} + j\omega M\hat{I}_n \\
 \hat{V}_n &= \hat{Z}\hat{I}_n + j\omega M\hat{I}_{n-1}
 \end{aligned} \tag{4.5}$$

where  $\hat{Z} = R + j\omega L + 1/(j\omega)$  is the impedance of a resonator. This system of equations can be written more compactly in matrix form as:

$$\hat{\mathbf{V}} = \hat{\mathbf{Z}}\hat{\mathbf{I}} \tag{4.6}$$

where  $\hat{\mathbf{I}}$  is the phasor current vector and  $\hat{\mathbf{V}} = [\hat{V}_1 \ 0 \ \dots \ 0 \ \hat{V}_n]^T$  the phasor voltage vector.  $\hat{\mathbf{Z}}_{i,\hat{Z}_T}$  is the  $n \times n$  impedance matrix of the resonator array and has the form:

$$\hat{\mathbf{Z}} = \begin{bmatrix} \hat{Z} & j\omega M & 0 & 0 & \dots & 0 \\ j\omega M & \hat{Z} & j\omega M & 0 & \dots & 0 \\ 0 & \vdots & \ddots & \vdots & \dots & \vdots \\ \vdots & \vdots & \vdots & \ddots & \vdots & 0 \\ \vdots & \dots & 0 & j\omega M & \hat{Z} & j\omega M \\ 0 & \dots & \dots & 0 & j\omega M & \hat{Z} \end{bmatrix} \tag{4.7}$$

which is a symmetric Toeplitz matrix, namely the terms of each descending diagonal are constant and the matrix is symmetric. The ‘‘Toeplitz form’’ of this matrix is due to the choice of identical and equally spaced resonators, while its symmetry

is due to the reciprocity of the network. Moreover, only the terms on the three central diagonals are different from zero, having neglected the coupling between non-adjacent cells. In general, a Toeplitz matrix is easier to be inverted, since it presents only  $2n - 1$  degrees of freedom, instead of  $n^2$ , thereby simplifying the solution of (4.6). These properties have been exploited to derive mathematical closed expressions of the network parameters [113].

### 4.1.2 Two-port Representation

To evaluate the performance of the system in terms of efficiency and transmitted power, it is possible to model the resonator array as a two-port network [114]. This representation also allows the voltage gain and transadmittance parameters to be derived, which are useful for defining the control strategy of the system when used in practical applications. The array of resonators is represented with the associated impedance matrix, but depending on the needs of the designer, also other configurations can be exploited [115]. As discussed in Sec. 2.2.3, general expressions of power and efficiency can be derived from the two-port representation. Being  $\hat{\mathbf{Z}}_{i, \hat{Z}_T}$  symmetric, the system (4.6) is reciprocal and can be reduced to the form:

$$\begin{bmatrix} \hat{V}_1 \\ \hat{V}_n \end{bmatrix} = \begin{bmatrix} \hat{Z}_{11} & \hat{Z}_m \\ \hat{Z}_m & \hat{Z}_{22} \end{bmatrix} \begin{bmatrix} \hat{I}_1 \\ \hat{I}_n \end{bmatrix} \quad (4.8)$$

where the impedance matrix terms are found as:

$$\begin{aligned} \hat{Z}_{11} &= \left. \frac{\hat{V}_1}{\hat{I}_1} \right|_{\hat{I}_n=0} & \hat{Z}_{22} &= \left. \frac{\hat{V}_n}{\hat{I}_n} \right|_{\hat{I}_1=0} \\ \hat{Z}_m &= \left. \frac{\hat{V}_1}{\hat{I}_n} \right|_{\hat{I}_1=0} = \left. \frac{\hat{V}_n}{\hat{I}_1} \right|_{\hat{I}_n=0}. \end{aligned} \quad (4.9)$$

Then, rearranging (4.5) enforcing (4.9), the analytical expressions of the impedance matrix parameters for an array of  $n$  resonators are obtained. They can be deduced by removing the equations of all the resonators but the first and the last ones, resulting in:

$$\hat{Z}_{11} = \hat{Z} + \hat{Z}_{n-1,0}^{eq} \quad (4.10)$$

$$\hat{Z}_{22} = \hat{Z} + \hat{Z}_{n-1,0}^{eq} \quad (4.11)$$

$$\hat{Z}_m = j^{3-n} (\omega M)^{n-1} \prod_{k=1}^{i-1} \frac{1}{\hat{Z} + \hat{Z}_{k,0}^{eq}}. \quad (4.12)$$

where  $\hat{Z}_{n-1,0}^{eq}$  is the equivalent impedance of an array with  $n-1$  and short-circuit load, while  $\hat{Z}_{k,0}^{eq}$  is the equivalent impedance of an array of  $k$  resonators terminated

in short-circuit. The equivalent impedance of an array of  $l$  resonators terminated with a generic load  $\hat{Z}_{end}$  is defined according to [113] as:

$$\hat{Z}_{l,\hat{Z}_{end}}^{eq} = \frac{(\omega M)^2}{\hat{Z} + \frac{(\omega M)^2}{\dots + \frac{(\omega M)^2}{\hat{Z} + \frac{(\omega M)^2}{\hat{Z} + \hat{Z}_{end}}}}}. \quad (4.13)$$

These expressions are valid for any array of the type depicted in Fig. 4.3, with any number of resonators  $n$ , power source and load. Moreover, they can be extended to the case of a generic array with different cell parameters and mutual inductance, still assuming the nearest-neighbour approximation holds. Indeed, the equivalent impedance can still be calculated according to (4.13), considering the proper value of mutual inductance and resonator impedance. In case of identical and equally spaced cells, a closed expression for the recursive formula (4.13) is derived in [113] and is:

$$\hat{Z}_{l,\hat{Z}_{end}}^{eq} = \frac{f^l(2(\omega M)^2 - g\hat{Z}_{end}) + h^l(f\hat{Z}_{end} - 2(\omega M)^2)}{f^l(f + 2\hat{Z}_{end}) - g^l(g + 2\hat{Z}_{end})} \quad (4.14)$$

where  $f = \hat{Z} - \sqrt{\hat{Z}^2 + 4(\omega M)^2}$  and  $g = \hat{Z} + \sqrt{\hat{Z}^2 + 4(\omega M)^2}$ .

### 4.1.3 Model Validation

The analytical formulation of the two-port impedance matrix parameters has been verified through numerical simulations. In particular, circuit simulations have been carried out, that basically consist in solving the KVL equations enforcing (4.9). The open-circuit condition of a port of the system (required for the calculation of the parameters) is obtained connecting that port to an auxiliary impedance  $\hat{Z}_{aux}$  and enforcing it has a value large enough to make the port current nearly null. Then, the required voltage and current are obtained solving the system (4.6) that incorporates  $\hat{Z}_{aux}$ . As an example, for the parameter  $\hat{Z}_{11}$ , an auxiliary impedance  $\hat{Z}_{aux} = 10^9 \Omega$  has been series connected to the  $n$ th resonator. Then, a fictitious voltage  $\hat{V}_1 = 1V$  has been set and the current  $\hat{I}_1$  has been obtained from (4.6). The dual procedure holds for the calculation of  $\hat{Z}_{22}$ .

The mutual impedance  $\hat{Z}_m$  can be determined both terminating the first or the last resonator with  $\hat{Z}_{aux}$ . Terminating the output port  $n$ , the voltage  $\hat{V}_n$  and the current  $\hat{I}_1$  are needed. The port voltage is calculated as:

$$\hat{V}_n \Big|_{\hat{I}_n=0} = j\omega M \hat{I}_{n-1} \quad (4.15)$$

while the currents  $\hat{I}_1$  and  $\hat{I}_{n-1}$  are determined solving (4.6) (that involves  $\hat{Z}_{aux}$ ).

### 4.1.4 Results

The numerical simulations have been carried out considering the parameters of the resonator array prototype used in the experimental setup. In particular, each resonator of the array is realised with a 6-turn square winding of 153 mm side length. The stranded wire conductors have a section of 2.5 mm<sup>2</sup>, that results in an intrinsic resistance  $R = 0.05 \Omega$  and a self-inductance  $L = 11.9 \mu\text{H}$ . The mutual inductance between the adjacent resonators is  $M = -1.67 \mu\text{H}$ . The lumped capacitors connected to the coils present a capacitance of 1  $\mu\text{F}$ , making the system resonate at  $f_0 = 45.1$  kHz.

Simulations of arrays with a different number of resonators have been performed, which resulted in very good agreement with the values calculated through the analytical expressions. The real and imaginary parts of the two-port impedance parameters obtained with the two different approaches are shown in Fig. 4.4 for different numbers of resonators. In particular, a difference between the simulated and analytically calculated values is found only at the tenth significant digit and therefore it cannot be appreciated in the graphs. The  $\hat{Z}_{11}$  and  $\hat{Z}_{22}$  parameters are equal and present only real values, and this can be addressed to the assumption of perfect resonance operations. Indeed, the continued fraction (4.13) does not present complex terms when  $\hat{Z}$  is real. However, the magnitude initially oscillates between very large and small values, mirroring the case of ideal resonator array [113]. In particular, large values occur for an odd number of array resonators, while low values for an even one. This clearly suggests that important power reflections can occur when the array is formed by an odd number of resonators. The mutual inductance  $\hat{Z}_m$  can have a non-null real or imaginary part depending on the number of resonators  $n$ , but not both. This has an impact on the output voltage phase angle, while it is irrelevant to the power transmission. Moreover, both the real and imaginary components oscillate around zero and their amplitude decrease as  $n$  increases. However, for arrays with an even number of resonators, the  $\hat{Z}_m$  is imaginary and its amplitude much larger than the one found when  $n$  is odd, suggesting a better transmitter-receiver coupling in arrays composed of an even number of resonators.

### 4.1.5 Power and Efficiency

To evaluate the performance of the system it is possible to derive the efficiency and power transfer of a two-port network as described in Sec. 2.2.3. The efficiency of the resonator array has been calculated as in (3.4), while the optimal load values  $R_l^{\eta_{max}}$  that maximise the efficiency are found with (2.33). In particular, the values of  $R_l^{\eta_{max}}$  evaluated for arrays with a different number of resonators have been plotted in Fig. 4.5a. The values oscillate depending on the number of resonators, especially for low  $n$ . As the number of cells increase, the trend converges to the value  $R_l^{\eta_{max}} = 0.48 \Omega$ , which can be considered the resistive load that maximise the efficiency for the considered array parameters. The convergence of the curve shows that, even for quite large numbers of cells, there is a unique optimal load value. This peculiarity

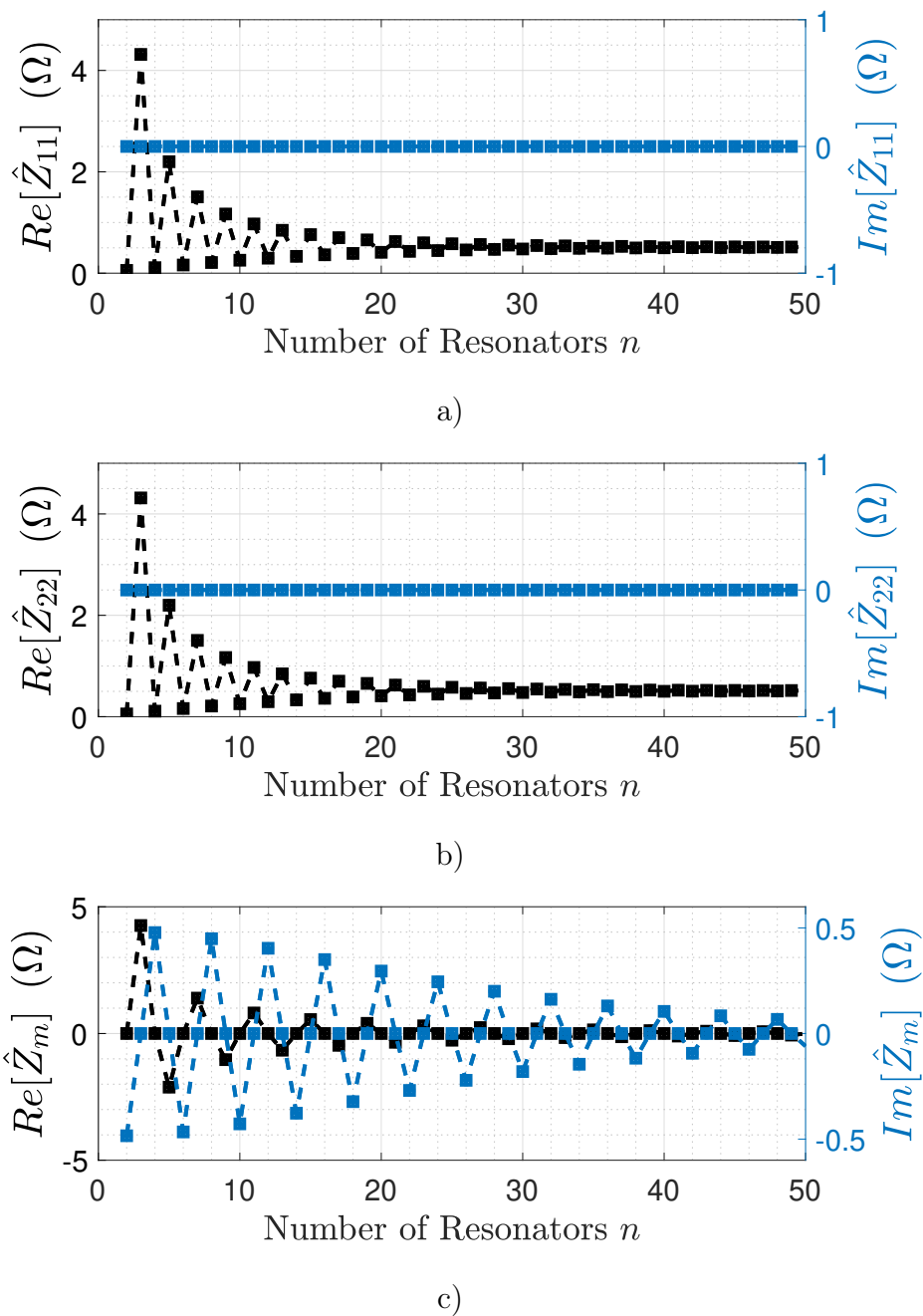
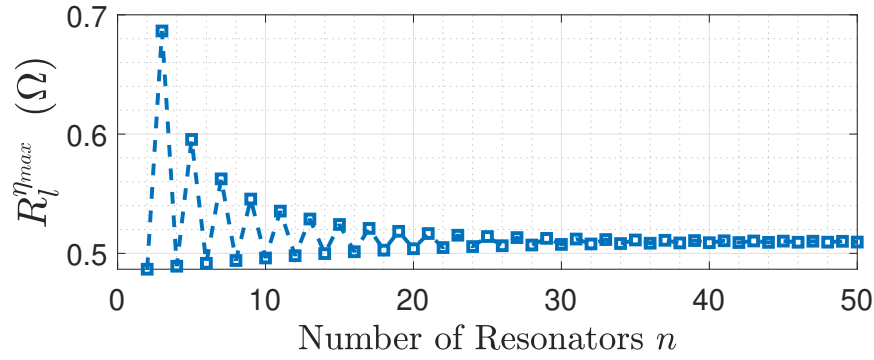
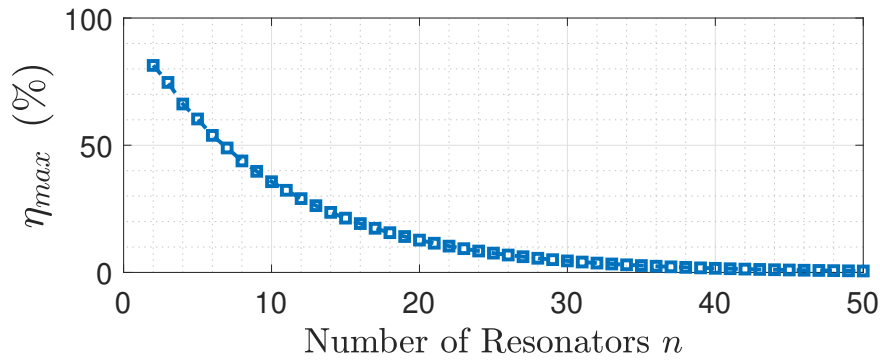


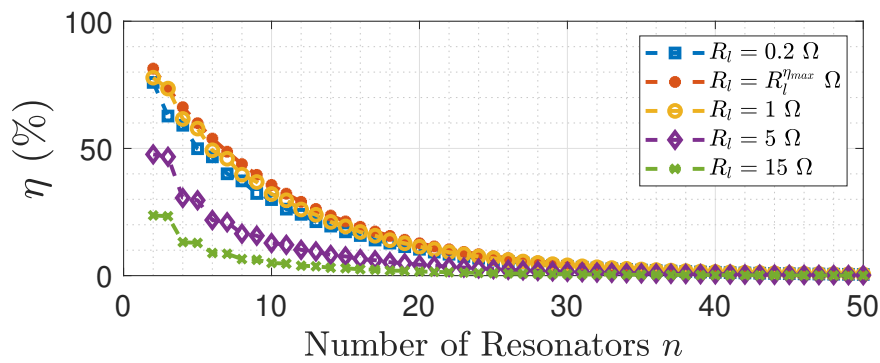
Figure 4.4: Impedance matrix parameters for arrays with different numbers of resonators at the resonant frequency  $f_0$ . The square markers refer to the formulas (4.10)-(4.12) and the circle markers to the numerical solution of (4.6).



a)



b)



c)

Figure 4.5: Considering a different number of array resonators, (a) shows the optimal resistance values for maximum efficiency, (b) the maximum efficiency achievable with the considered resonator parameters and (c) the efficiency for different loads.

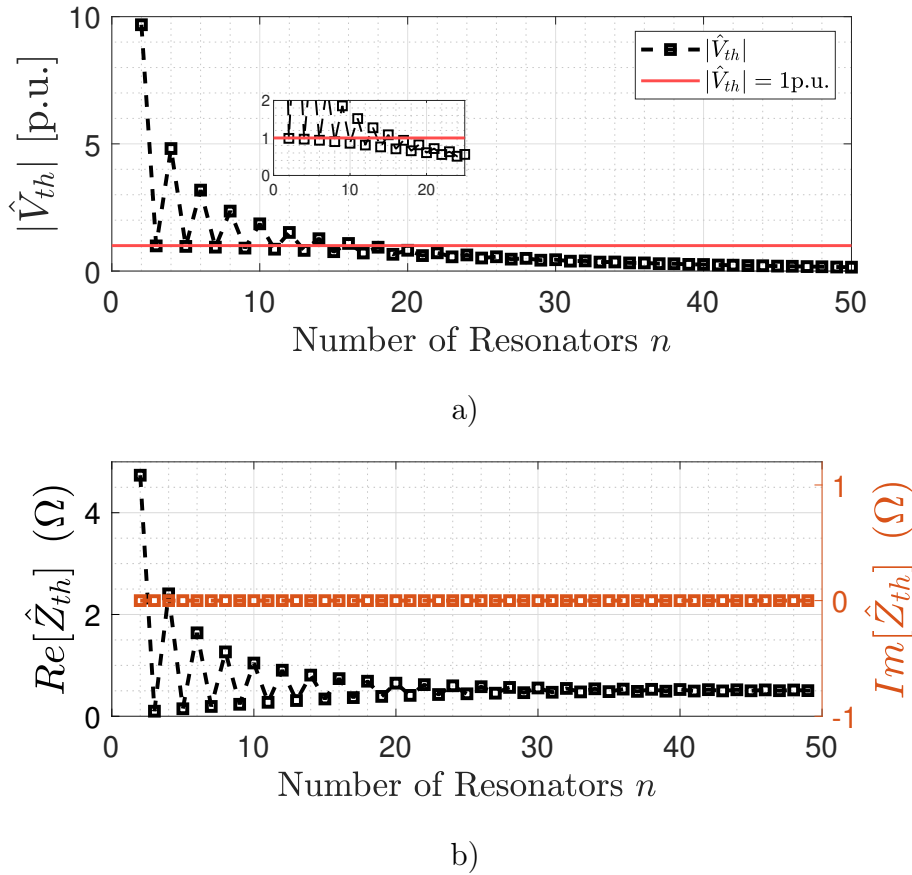


Figure 4.6: Equivalent Thévenin (a) voltage source and (b) impedance for arrays as a function of the number of cells.

can be attributed to the symmetry of the structure. In fact, if the resonators had different parameters or were even only positioned non-symmetrically, this would not be possible. For the considered arrays, the maximum efficiency (namely the efficiency for optimum load) is shown in Fig. 4.5b. As expected, it shows a decreasing trend as the number of resonators increases. The efficiency of arrays with different number of cells is then plotted in Fig. 4.5c for different generic loads, including the optimal one of  $0.48\Omega$ . Similar trends are observed for each considered load, which show how the efficiency decreases as the number of resonators increases. The higher efficiency is obtained for the optimal value of  $0.48\Omega$ , as expected. For what concerns the power transfer capability, this system has been characterised using the Thévenin equivalent circuit depicted in Fig. 2.6b. In particular, to consistently evaluate the effect of the relay coils, the voltage  $\hat{V}_{th}$  and impedance  $\hat{Z}_{th}$  of the equivalent real generator are plotted in Figs. 4.6a and 4.6b, respectively, for arrays with a different number of resonators. The Thévenin equivalent voltage corresponds to the no-load voltage of the array (the voltage at the receiver port when it is in open-circuit). In particular, it has been normalised with respect to the value of the ideal generator input voltage  $\hat{V}_g$ . For arrays with few cells, the value of  $\hat{V}_{th}$  fluctuates. The curve generally shows

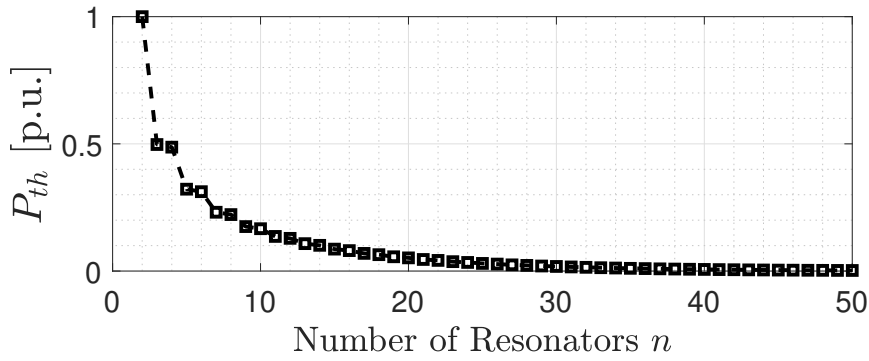


Figure 4.7: Available power at the receiver port of the resonator array as a function of the number of cells.

that the generator voltage is always attenuated when the array has an odd number of resonators. When these are instead even, the voltage is amplified until  $n = 16$ , to be then attenuated. This peculiarity suggests the existence of a limit number of resonators for which the no-load input voltage is amplified that depends on the cell parameters. The angle of  $\hat{V}_{th}$  is 0 for  $n$  odd and  $\pi/2$  for  $n$  even, according to the behaviour of  $\hat{Z}_m$  (see Fig. 4.4c). The impedance  $\hat{Z}_{th}$  has a similar trend, but is mirrored, and is always real. In fact, in perfect resonance, the impedances  $\hat{Z}_{11}$  and  $\hat{Z}_{22}$  are always real. According to the theorem of the maximum power transfer, the maximum power on the load can be extracted when this is equal to the complex conjugate of the impedance generator. Thus, the values of  $\hat{Z}_{th}$  also correspond to the required loads for the maximum power transfer, being them real. The maximum available power on the load is still varying depending on the number of resonators and array parameters. It is depicted in Fig. 4.7 and presents a decreasing trend with an increase in the relay coils. This can be addressed to the presence of the coils resistance, which inevitably leads to power losses.

## 4.2 Resonator Arrays with a Receiver

IPT devices that use relay coils to improve performance find few practical applications, both real and industrial. This is because they are formed but many elements that occupy a not negligible space. If in a real system there is the possibility of inserting intermediate coils, why not directly feed the one closest to the receiving coil? In the author's knowledge, there is no evidence of systems of practical interest with this structure, especially for power applications. However, resonator arrays can be exploited as transmitters, offering the possibility to the receiver to collect power efficiently in different points of space, resulting in a structure of the type depicted in Fig. 4.8. Furthermore, the power transfer can also take place with the receiver in motion and therefore operate as a dynamic IPT system. In general, both for static and dynamic applications, this type of system is enjoying growing interest in

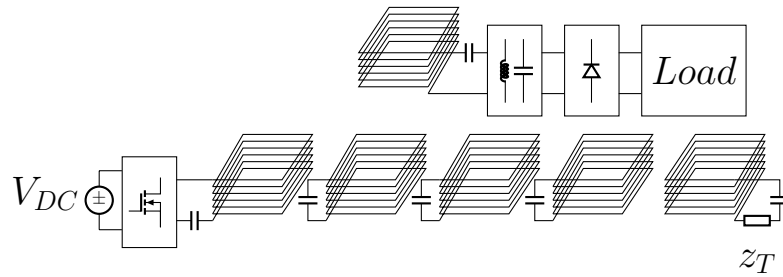


Figure 4.8: Schematic representation of an IPT system with a resonator array and a receiver over it.

the industrial and consumer electronics fields, as it requires a very limited number of components. In fact, apart from the supply coil and the receiving coil, all the circuits are passive and composed only of windings and capacitors. However, the low number of controllable variables can lead to a very high sensitivity of the system parameters to the load and coupling conditions, requiring specific and suitable control strategies. In this work, as it is in high-power IPT systems, the power source is composed of an inverter, whereas the load is commonly a battery. The resulting system is very similar to traditional LLC battery chargers, in which the DC/AC stage feeds the DC/DC one through a transformer with the difference that, in this case, the transformer stage is realised with an array of resonators and the receiver coil [116, 117]. In modern LLC converters, the high-power rate required by the load makes the soft-switching operations of the input inverter necessary [116, 118], as discussed in Sec. 2.4, and the design of power electronic components and the control strategy require an adequate model of the system. For this reason, an equivalent circuit model of the array of resonators with a receiver is derived, with the idea of evaluating its performance. Different equivalent models can be defined and have been proposed [119, 115, 56], even though they usually apply to simple network topologies. The case of an array of resonators becomes complicated to be treated analytically, especially when the receiver can be freely positioned over any resonator of the array. However, similarly to the approach proposed in Sec. 4.1.2, a two-port network representation is established starting from the definition of the impedance matrix of the system, and the analytical expressions of the impedance matrix terms also presented. The model has been validated both numerically and experimentally.

### 4.2.1 Circuit Model

The same resonator array presented in Sec. 4.1 is here considered. It is composed of  $n$  cells and a further resonator is introduced that acts as a receiver. This receiver coil is free to be placed over any cell of the array and then the mutual inductance

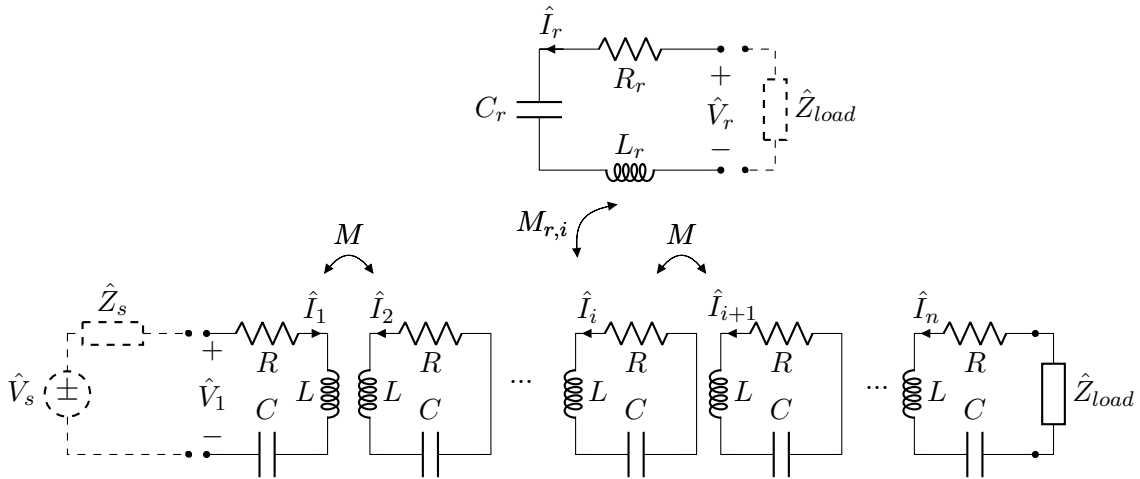


Figure 4.9: Equivalent circuit of an IPT system with a resonator array and a receiver over it.

$M_{r,i}$  between the receiver and the  $i$ th facing cell is the same for each position, being all the cells identical. The receiver coil is characterised by a resistance  $R_r$  and self-inductance  $L_r$ . It resonates with a series lumped capacitor of capacitance  $C$  at the resonant frequency  $f_0 = 1/(2\pi\sqrt{L_r C_r})$ . All the circuits (including the receiver one) resonate at the same frequency  $f_0$ . A general equivalent load  $\hat{Z}_{load}$  is still considered, which is assumed connected to the receiver circuit, as described in Sec. 2.5. As a power source, the inverter considered in Sec. 2.4 and modelled in Sec. 4.1.1 is adopted. A further degree of freedom can be obtained introducing a termination impedance  $\hat{Z}_T$  in the last cell of the array which can be adjusted to maximise the transfer efficiency, as described in [49]. Indeed, the results presented in Sec. 4.1.4, clearly highlight the strong dependency of the array efficiency and power transfer on the number of resonators. In particular, depending on whether  $n$  is even or odd, the parameters can considerably vary, especially for small  $n$ . The termination impedance can then be used to deactivate the last resonator if required. Moreover, to avoid further power consumption,  $\hat{Z}_T$  is used as short-circuit (SC) or open-circuit (OC), and it can be realised with a switching device with the proper safety circuit (i.e. freewheeling circuit). Different modulation strategies have been proposed for the termination impedance [48], that allows similar operating conditions of the array at any position of the receiver. Assuming the system operates at the cell resonant frequency, the analysis is carried out considering the fundamental components of currents and voltages, considered as phasors at the resonant angular frequency  $\omega_0 = 2\pi f_0$ . The resulting circuit model is depicted in Fig. 4.9. The system of  $n+1$  KVL equations that describes the behaviour of the resonator voltages and

currents can be written as:

$$\begin{aligned}
\hat{V}_1 &= \hat{Z}\hat{I}_1 + j\omega M\hat{I}_2 \\
0 &= \hat{Z}\hat{I}_2 + j\omega M\hat{I}_1 + j\omega M\hat{I}_3 \\
&\vdots \\
0 &= \hat{Z}\hat{I}_{i-1} + j\omega M\hat{I}_{i-2} + j\omega M\hat{I}_i \\
0 &= \hat{Z}\hat{I}_i + j\omega M\hat{I}_{i-1} + j\omega M\hat{I}_{i+1} + j\omega M_{r,i}\hat{I}_r \\
&\vdots \\
0 &= \hat{Z}\hat{I}_{n-1} + j\omega M\hat{I}_{n-2} + j\omega M\hat{I}_n \\
0 &= (\hat{Z} + \hat{Z}_T)\hat{I}_n + j\omega M\hat{I}_{n-1} \\
\hat{V}_r &= \hat{Z}_r\hat{I}_r + j\omega M_{i,r}\hat{I}_i
\end{aligned} \tag{4.16}$$

where the last equation refers to the receiver. Similarly to the 1D array case, this system can be arranged in matrix form. It must be noticed that, depending on the receiver position, the system of KVL equations changes, since the array cell coupled with the receiver changes. Consequently, also the impedance matrix changes accordingly. In general, it is possible to rewrite (4.6) as:

$$\hat{\mathbf{V}} = \hat{\mathbf{Z}}_{i,\hat{Z}_T} \hat{\mathbf{I}} \tag{4.17}$$

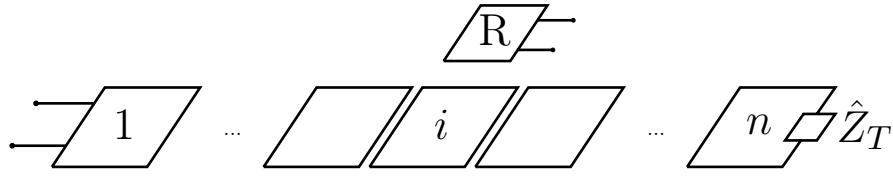
where  $\hat{\mathbf{I}}$  is the phasor current vector and  $\hat{\mathbf{V}} = [\hat{V}_1 0 \dots 0 \hat{V}_n]^T$  the phasor voltage vector.  $\hat{\mathbf{Z}}_{i,\hat{Z}_T}$  is a  $(n+1) \times (n+1)$  impedance matrix of the system when the receiver is coupled with the generic  $i$ th resonator and is written as:

$$\hat{\mathbf{Z}}_{i,\hat{Z}_T} = \begin{bmatrix} \hat{Z} & j\omega M & 0 & 0 & \cdots & 0 \\ j\omega M & \hat{Z} & j\omega M & 0 & \cdots & 0 \\ 0 & \vdots & \ddots & \vdots & \cdots & j\omega M_{i,r} \\ \vdots & \vdots & \vdots & \ddots & \vdots & \vdots \\ \vdots & 0 & \cdots & j\omega M & \hat{Z} + \hat{Z}_T & 0 \\ 0 & 0 & j\omega M_{r,i} & 0 & \cdots & \hat{Z}_r \end{bmatrix} \tag{4.18}$$

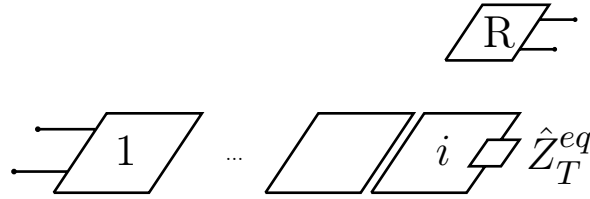
The last row and column appear due to the added receiver KVL equation, and their non-zero terms change position as the receiver moves and couples to different array resonators. In general, for each receiver position, a different system of equations must be solved to determine the circuit variables. Moreover,  $\hat{\mathbf{Z}}_{i,\hat{Z}_T}$  incorporates also the termination impedance, which can be zero (or SC) or very large (OC) and also affects the system solution. It must be noticed that an OC terminated array basically corresponds to a similar array with one less resonator. The current and voltage are in turn functions of both the receiver position and array termination, thereby complicating the design of the control system with respect to traditional isolated power converters. No closed or even recursive analytical expressions have been found to generally describe them.

## 4.2.2 Two-port Representation

A 2x2 impedance matrix can be again adopted to obtain a compact representation of the array of resonators. Differently from the case of the single array, the output



a)



b)

Figure 4.10: Schematic representation of (a) an array of  $n$  resonators with a receiver  $R$  over the  $i$ th cell, terminated with  $\hat{Z}_T$  and (b) the correspondent compacted array terminated with the equivalent impedance (4.21).

port is the receiver port, while the input port is the one of the first array coil, as depicted in Fig. 4.8. The  $(n+1) \times (n+1)$  impedance matrix is symmetric, meaning that the system is reciprocal and a unique mutual term  $\hat{Z}_m$  is considered. The two-port network is defined as:

$$\begin{bmatrix} \hat{V}_1 \\ \hat{V}_r \end{bmatrix} = \begin{bmatrix} \hat{Z}_{11} & \hat{Z}_m \\ \hat{Z}_m & \hat{Z}_{22} \end{bmatrix} \begin{bmatrix} \hat{I}_1 \\ \hat{I}_r \end{bmatrix} \quad (4.19)$$

where

$$\begin{aligned} \hat{Z}_{11} &= \left. \frac{\hat{V}_1}{\hat{I}_1} \right|_{\hat{I}_r=0} & \hat{Z}_{22} &= \left. \frac{\hat{V}_r}{\hat{I}_r} \right|_{\hat{I}_1=0} \\ \hat{Z}_m &= \left. \frac{\hat{V}_1}{\hat{I}_r} \right|_{\hat{I}_1=0} = \left. \frac{\hat{V}_r}{\hat{I}_1} \right|_{\hat{I}_r=0}. \end{aligned} \quad (4.20)$$

These terms are defined for a specific termination impedance and receiver position and can be derived rearranging the system of KVL equations. To simplify the calculation, the resonators that follow the one covered by the receiver - namely from the  $(i+1)$ th to the  $n$ th one - can be substituted with their equivalent impedance seen from the  $i$ th cell. The expression of the equivalent impedance is reported in (4.13), where in this case  $m = n-i$  and  $\hat{Z}_{end} = \hat{Z}_T$ . This choice allows passing

from the original array (schematically represented in Fig. 4.10a) to a reduced one (schematically represented in Fig. 4.10b) composed of the remaining  $i$  resonators, terminated with the impedance

$$\hat{Z}_T^{eq} = \hat{Z}_{n-i, \hat{Z}_T}^{eq}, \quad (4.21)$$

and the receiver coupled with the last cell. Being the receiver coupled with the last cell only, the reduced array can be considered as a 1D array where the mutual impedance between the last and second-last cells is  $M_{r,i}$ . Thus, the considerations made in Sec. 4.1.1 still hold. The system can be then described by  $i+1$  KVL equations (instead of the original  $n+1$ ), resulting in:

$$\begin{aligned} \hat{V}_1 &= \hat{Z}\hat{I}_1 + j\omega M\hat{I}_2 \\ 0 &= \hat{Z}\hat{I}_2 + j\omega M\hat{I}_1 + j\omega M\hat{I}_3 \\ &\vdots \\ 0 &= \hat{Z}\hat{I}_{i-1} + j\omega M\hat{I}_{i-2} + j\omega M\hat{I}_i \\ 0 &= (\hat{Z} + \hat{Z}_T^{eq})\hat{I}_i + j\omega M\hat{I}_{i-1} + j\omega M_{r,i}\hat{I}_r \\ \hat{V}_r &= \hat{Z}_r\hat{I}_r + j\omega M_{i,r}\hat{I}_i \end{aligned} \quad (4.22)$$

which can be further reduced by removing the equations of all the resonators but the first one and the receiver to the two-port network equations system:

$$\begin{aligned} \hat{V}_1 &= \hat{Z}_{11}\hat{I}_1 + \hat{Z}_{1r}\hat{I}_r \\ \hat{V}_r &= \hat{Z}_{22}\hat{I}_r + \hat{Z}_{r1}\hat{I}_1. \end{aligned} \quad (4.23)$$

After some mathematical manipulations, the analytical expressions of the impedance matrix terms are found as:

$$\hat{Z}_{11} = \hat{Z} + \hat{Z}_{n-1, \hat{Z}_T}^{eq} \quad (4.24)$$

$$\hat{Z}_{22} = \hat{Z}_r + \frac{(\omega M_{r,i})^2}{\hat{Z} + \hat{Z}_T^{eq} + \hat{Z}_{i-2,0}^{eq}} \quad (4.25)$$

$$\hat{Z}_m = \frac{M_{r,i}}{M} \left( \frac{1}{(j\omega M)^{i-2}} \prod_{k=1}^{i-1} \hat{Z}_{k, \hat{Z}_T}^{eq} \right). \quad (4.26)$$

These formulas are valid for arrays of the type described in Sec. 4.1, that can have any number of resonators, termination impedance values and the receiver aligned with any array resonator. Moreover, an analytical and closed formulation of the  $\hat{Z}_{11}$  and  $\hat{Z}_{22}$  parameters can be found introducing the closed expressions of the array input impedance presented in [113] in (4.24) and (4.25).

### 4.2.3 Model Validation

The analytical expressions (4.24)-(4.26) are validated with numerical simulations based on the system circuit model, where the required currents and voltages are

calculated with (4.17). As discussed in Sec. 4.1.3, an additional termination with a very large value ( $10^8 \Omega$ ) is added in the port that must present a null current to emulate the open-circuit condition. Then, the parameter  $\hat{Z}_{11}$  can be calculated as in (4.20) introducing the auxiliary impedance  $\hat{Z}_s$  in the receiver port so that  $\hat{I}_1 \approx 0$ . Similarly,  $\hat{Z}_{22}$  is calculated as in (4.20) enforcing  $\hat{I}_r \approx 0$  through  $\hat{Z}_s$  connected to the input port. The mutual impedance  $\hat{Z}_m$  is calculated at the receiver port, thereby introducing  $\hat{Z}_s$  in the receiver. In particular, the receiver voltage  $\hat{V}_r$  is calculated as:

$$\hat{V}_r \Big|_{\hat{I}_r=0} = j\omega M_{r,i} \hat{I}_i. \quad (4.27)$$

#### 4.2.4 Results

The simulations have been carried out considering the array of resonator described in Sec. 4.1.4, in which the last resonator port ( $n$ th) has been short-circuited or kept open. A further condition has been considered, that is the termination of the array with the resistance  $R_l^{\eta_{max}}$ . This resistance value maximises the efficiency of the array and it has been introduced in Sec. (2.2.3). Hereinafter, this condition is referred as array optimal termination and the optimal  $\hat{Z}_T$  is named  $\hat{Z}_{T_{opt}}$ . For this array is results in  $0.48\Omega$ . The receiver coil is realised with 5-turns copper winding, wound around a circular plastic core with a diameter of 9 cm. It presents resistance  $R_r = 0.055 \Omega$  and a self-inductance  $L_r = 3.8 \mu\text{H}$ , whereas the mutual inductance between the receiver and the facing resonator of the array is  $1.13 \mu\text{H}$ . It is connected to a lumped capacitance  $C_r$  of  $3.3 \mu\text{F}$  that makes the receiver resonate at the array cells resonant frequency. It must be noticed that there are several parameters that can vary and affect the system performance, that are the receiver load, receiver position and array termination. For a meaningful discussion, the number of array cells has been fixed to  $n = 25$  and the cases of SC, OC and optimal array termination have been considered. The simulations consider operations at the cell resonant frequency  $f_0$ . The two-port network parameters have been calculated and reported in Figs. 4.11 for the SC termination, Fig. 4.12 for the OC termination, and 4.13 for the case of optimal termination, as a function of the receiver position and still considered perfectly alignment of the receiver with the facing cell. The plots report both the values obtained with the formulas (4.24)-(4.26) and the numerical solution of (4.17). The points completely overlap, testifying a perfect agreement between analytical and simulation results.

Unlike the case of a single array, the parameters  $\hat{Z}_{11}$  and  $\hat{Z}_{22}$  have different behaviour. The trend of  $\hat{Z}_m$  is instead similar to the one of the previous case. Moreover, it can be noticed that both the real and imaginary parts of  $\hat{Z}_{22}$  and  $\hat{Z}_m$  are dramatically affected by the receiver position, while for  $\hat{Z}_{11}$  they are constant.

**Impedance  $\hat{Z}_{11}$**  For both terminations, the parameter  $\hat{Z}_{11}$  assumes a real value, which is the same for any receiver position. This indicates that the receiver does not interact with the array, as it can be seen from Figs. 4.11a, 4.12a and 4.13a. It

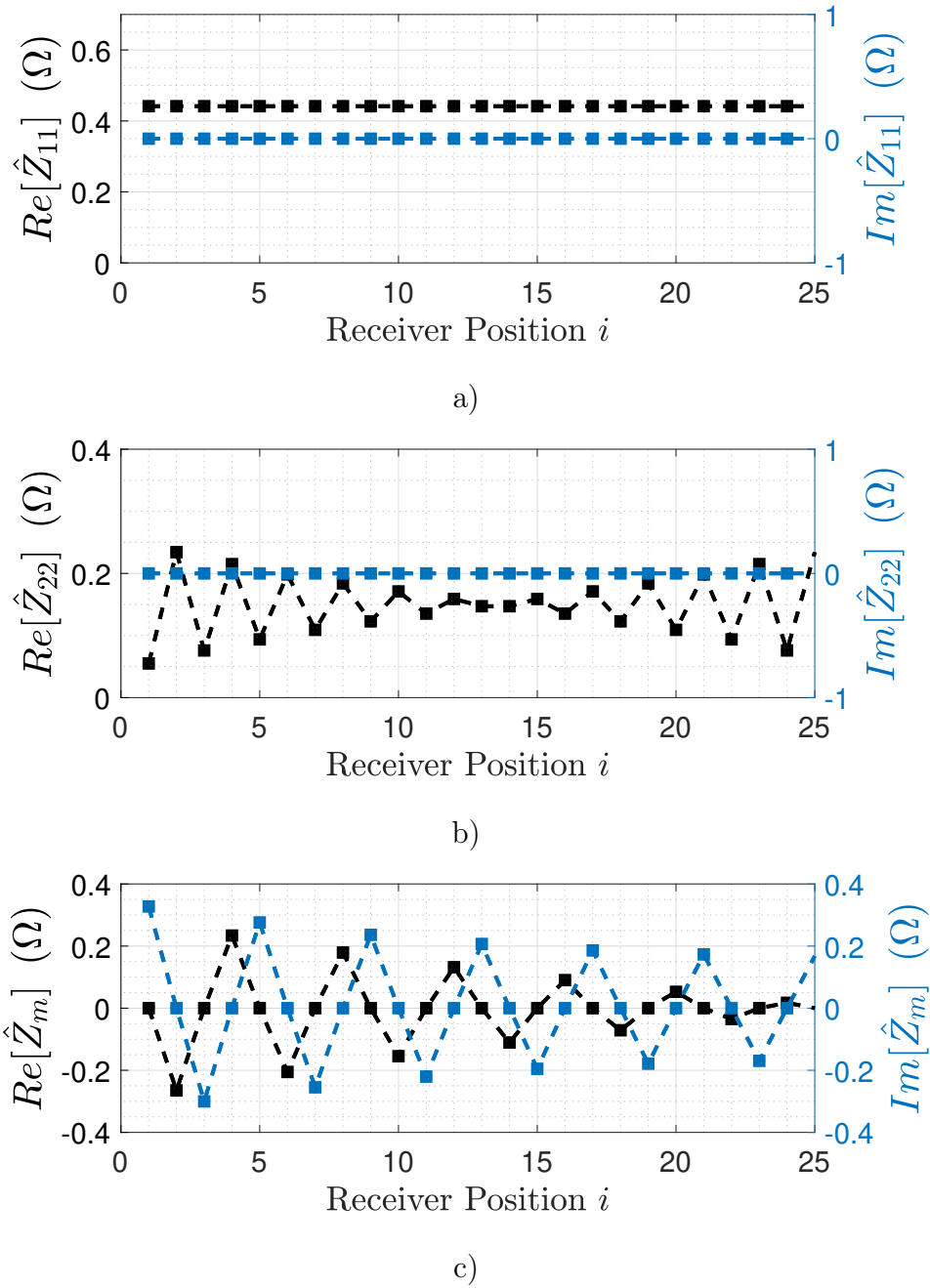


Figure 4.11: Impedance matrix parameters as a function of the receiver position for an array of 25 cells terminated in short-circuit. The square markers refer to the formulas (4.10)-(4.12) and the cross markers to the numerical solution of (4.6).

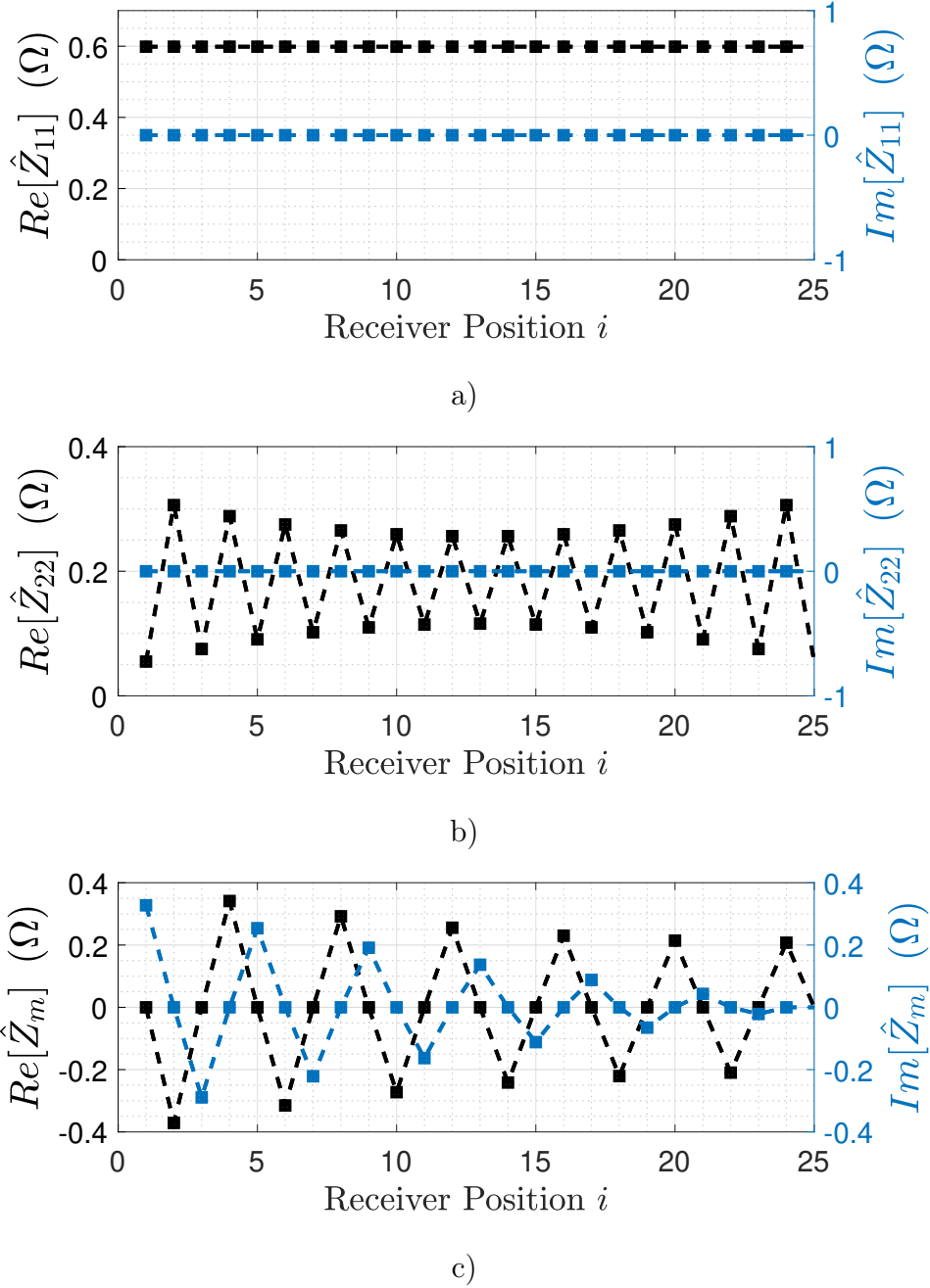


Figure 4.12: Impedance matrix parameters as a function of the receiver position for an array of 25 cells terminated in open-circuit. The square markers refer to the formulas (4.10)-(4.12) and the cross markers to the numerical solution of (4.6).

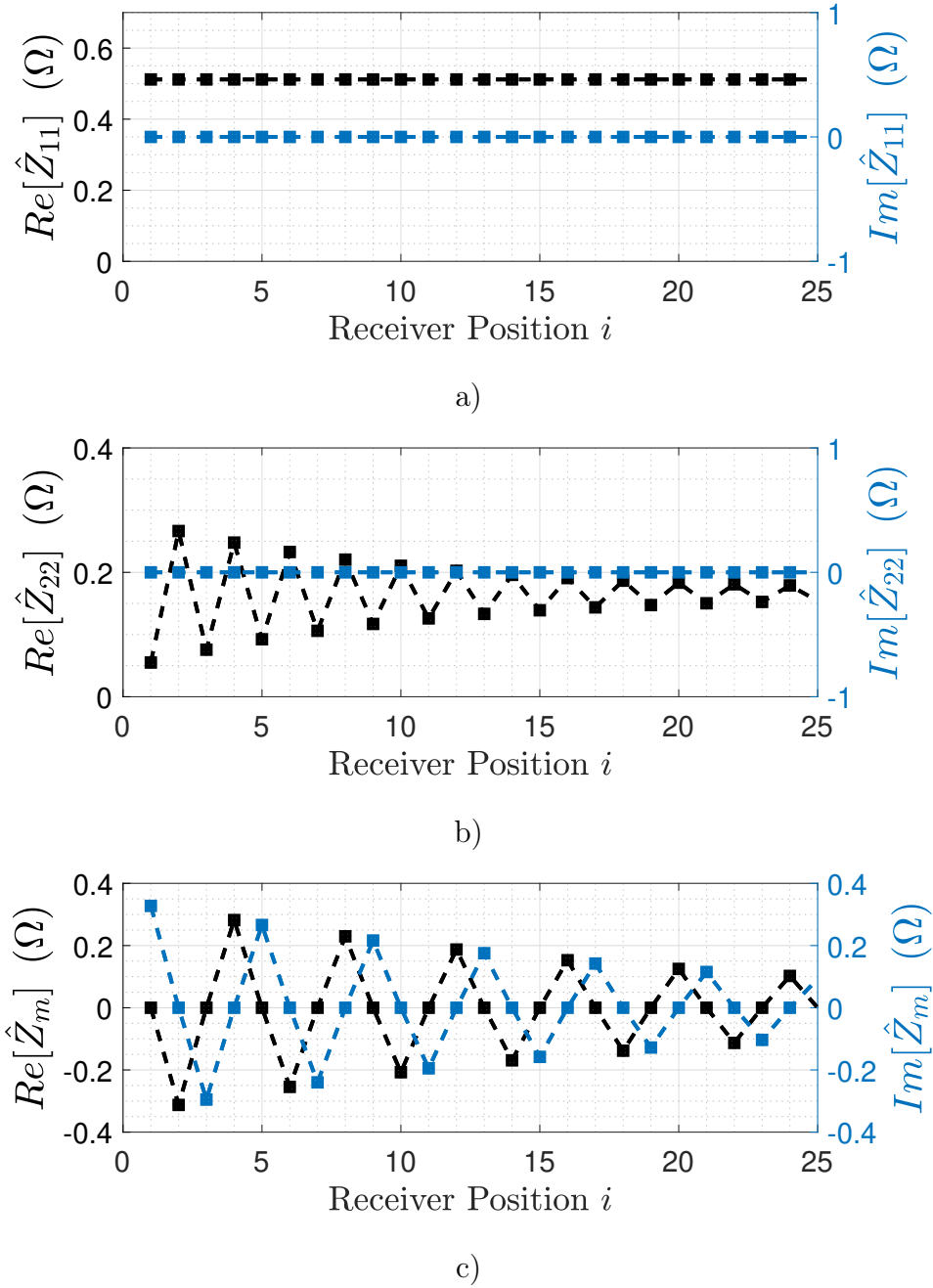


Figure 4.13: Impedance matrix parameters as a function of the receiver position for an array of 25 cells terminated in the optimal load. The square markers refer to the formulas (4.10)-(4.12) and the cross markers to the numerical solution of (4.6).

can be explained considering its definition. Indeed, it basically corresponds to the array input impedance in absence of the receiver, which presents a real value being the system in resonance condition. That value is however affected by the number of cells and array termination, and thus it differs in the two cases (with different  $\hat{Z}_T$ ). A detailed analysis of the input impedance is provided in [113].

**Impedance  $\hat{Z}_{22}$**  The impedance  $\hat{Z}_{22}$  is still real and oscillates according to the receiver position. In particular, in case of SC and OC terminations it presents an average value of  $0.16 \Omega$ , while it is  $0.14 \Omega$  in case of matched termination, shown in Figs. 4.11b, 4.12b and 4.13b, respectively.

It can be noticed that, in case of SC and OC terminations,  $\hat{Z}_{22}$  oscillates with decreasing amplitude until the receiver covers the cells in the first half of the array ( $i < n/2$ ), whereas the trend is inverted for  $i > n/2$ . This can be explained considering that, for an SC array, both  $\hat{Z}_T^{eq}$  and  $\hat{Z}_{i-2,0}^{eq}$  oscillate according to [113]. This results in the trends depicted in Figs. 4.11b and 4.12b. As the receiver approaches the central array resonator, the  $\hat{Z}_T^{eq}$  and  $\hat{Z}_{i-2,0}^{eq}$  tend to the same value with opposite periodicity. The limit case occurs for  $i = (n \pm 1)/2$ , where the two contributions compensate each other. Differently, in case of a matched array (see Fig. 4.13b),  $\hat{Z}_T^{eq}$  is always equal to the matching impedance and, assuming  $M_{r,i}$  constant, the only varying term of (4.25) is  $\hat{Z}_{i-2,0}^{eq}$ , which behaves as the input impedance of a short-circuited array (described in [113] and in Sec. 4.1.4).

**Impedance  $\hat{Z}_m$**  The term  $\hat{Z}_m$  presents a real and an imaginary part that both oscillate around zero and whose amplitudes decrease as the receiver approaches the last array resonators. It must be noticed that  $\hat{Z}_m$  presents real values when the receiver is aligned with even-numbered resonators (regardless of  $n$  being even or odd), which can be also negative. This parameter expresses the link between the input and output ports of the network and, for magnetically coupled resonators, it is usually associated to the overall impedance between the ports. The higher mutual impedance values are found in case of OC termination, that basically corresponds to the same array in SC but with one less resonator.

## 4.2.5 Transformer Equivalent Circuit

The array of resonators with a receiver can be described with the model of the real transformer (depicted in Fig. 4.14), which is the most common model for the analysis and design of isolated power converters. By exploiting the parameters of the two-port network that represents the array, it is possible to describe the system with the typical parameters of classic transformers. In this way, the design of the power inverter and energy conversion devices downstream of the receiver can be designed according to the usually adopted techniques. Furthermore, the representation of the array as a transformer allows for deducing further information about its operation and performance. The model consists of three complex parameters, namely a trans-

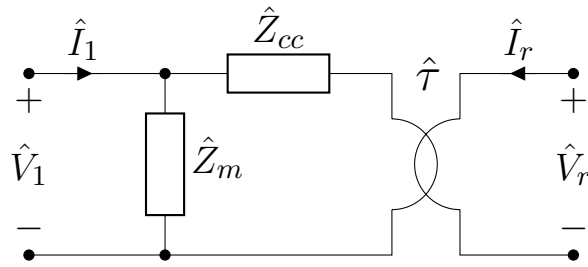


Figure 4.14: Equivalent frequency-domain circuits of a resonator array.

verse impedance  $\hat{Z}_M$ , a longitudinal impedance  $\hat{Z}_{sc}$ , and an ideal transformer with transformer ratio  $\hat{\tau}$ . In particular,  $\hat{Z}_M$  is also called “magnetising impedance” and indicates the reactive power necessary for the transfer of active power, while  $\hat{Z}_{sc}$  is called “short-circuit impedance”, since it can be determined through the short-circuit test of the transformer (which consists in estimating the parameter when the output port is short-circuited and feeding the device at the rated current). Thus, the associated impedance matrix can be written as:

$$\begin{bmatrix} \hat{V}_1 \\ \hat{V}_r \end{bmatrix} = \begin{bmatrix} \hat{Z}_M & \frac{\hat{Z}_M}{\hat{\tau}} \\ \frac{\hat{Z}_M}{\hat{\tau}} & \frac{\hat{Z}_{sc} + \hat{Z}_M}{\hat{\tau}^2} \end{bmatrix} \begin{bmatrix} \hat{I}_1 \\ \hat{I}_r \end{bmatrix}. \quad (4.28)$$

Equating the terms of the impedance matrices of the two models (4.8) and (4.28), the parameters of the real transformer two-port network result:

$$\begin{aligned} \hat{\tau} &= \frac{\hat{Z}_{11}}{\hat{Z}_m} \\ \hat{Z}_M &= \hat{Z}_{11} \\ \hat{Z}_{sc} &= \hat{\tau}^2 \hat{Z}_{22} - \hat{Z}_{11}. \end{aligned} \quad (4.29)$$

They are plotted as a function of the receiver position when the array is terminated in SC, OC and  $\hat{Z}_{T_{opt}}$  in Figs. 4.15 and 4.16 and 4.17. The parameters show a strong dependence on the position of the receiver, with different characteristics according to the termination. This behaviour can be easily explained by observing the definition of the parameter itself, which directly derives from the terms of the impedance matrix that represents the two-port. Specifically, the transformer ratio  $\hat{\tau}$  is complex, and its amplitude oscillates as the position of the receiver varies, with the average value that increases as the receiver moves away from the source. Terminating the array with  $\hat{Z}_{T_{opt}}$ , these oscillations are dramatically smoothed, and  $|\hat{\tau}|$  still increase with the receiver position  $i$ . For all the three considered terminations, the angle of the transformer ratio presents a periodic behaviour. It basically indicates the variation of the receiver voltage angle in relation to the number of resonators of the array placed in between the receiver and the power source. The magnetising

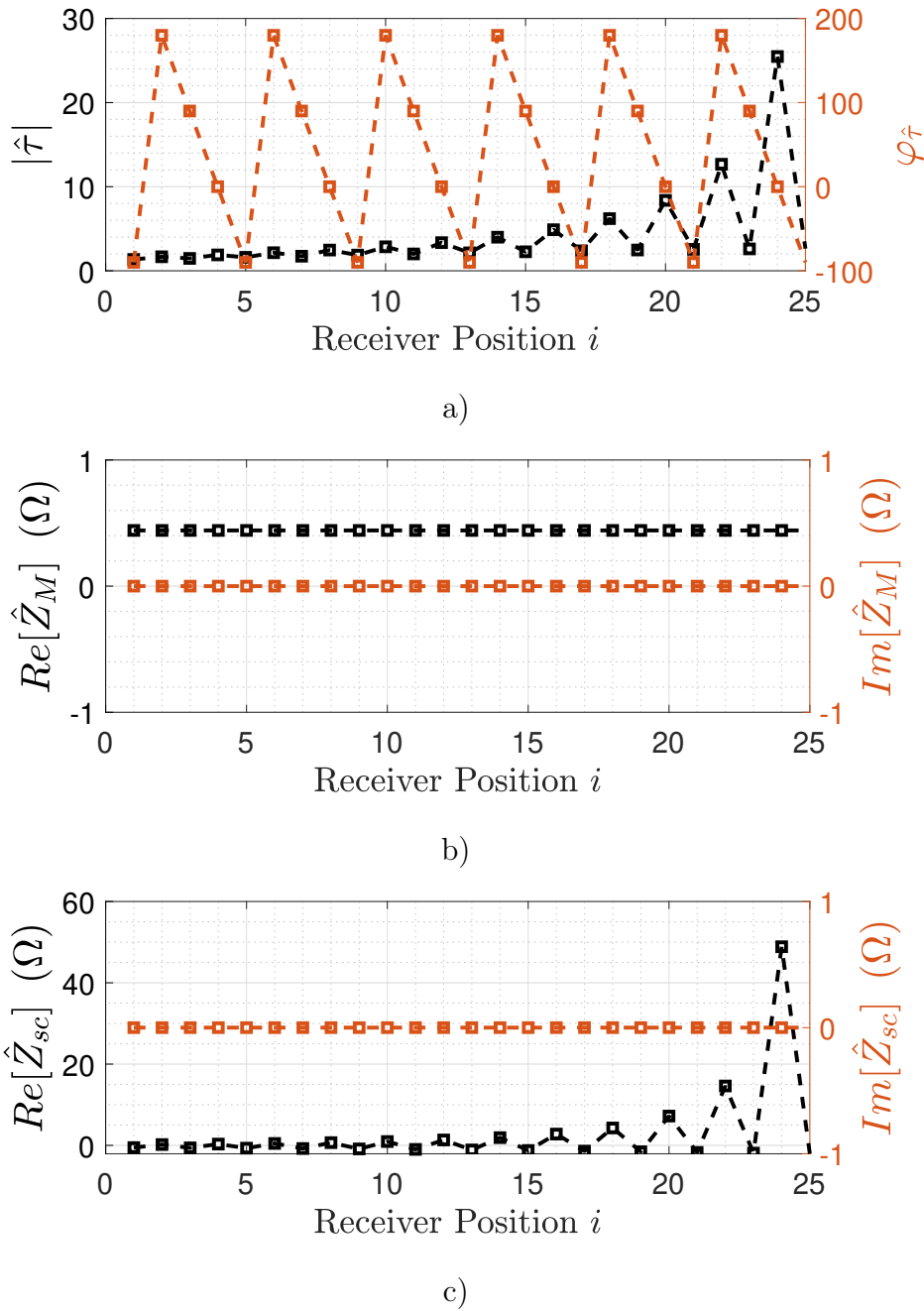


Figure 4.15: Real transformer parameters as a function of the receiver for an SC terminated array.

reactance  $\hat{Z}_m$  exactly corresponds to  $\hat{Z}_{11}$ , which is purely real and constant for any receiver position. This parameter is directly related to the coupling between the input and output coils, which assumes high values in traditional transformers and very low values in IPT systems (which are in fact weakly coupled). Thus, in traditional transformers,  $\hat{Z}_M$  is negligible during load operation, as the current it drains is much smaller than that which circulates on  $\hat{Z}_{sc}$ . Unfortunately, however, in resonator arrays and in general in all weakly coupled systems, it cannot be neglected,

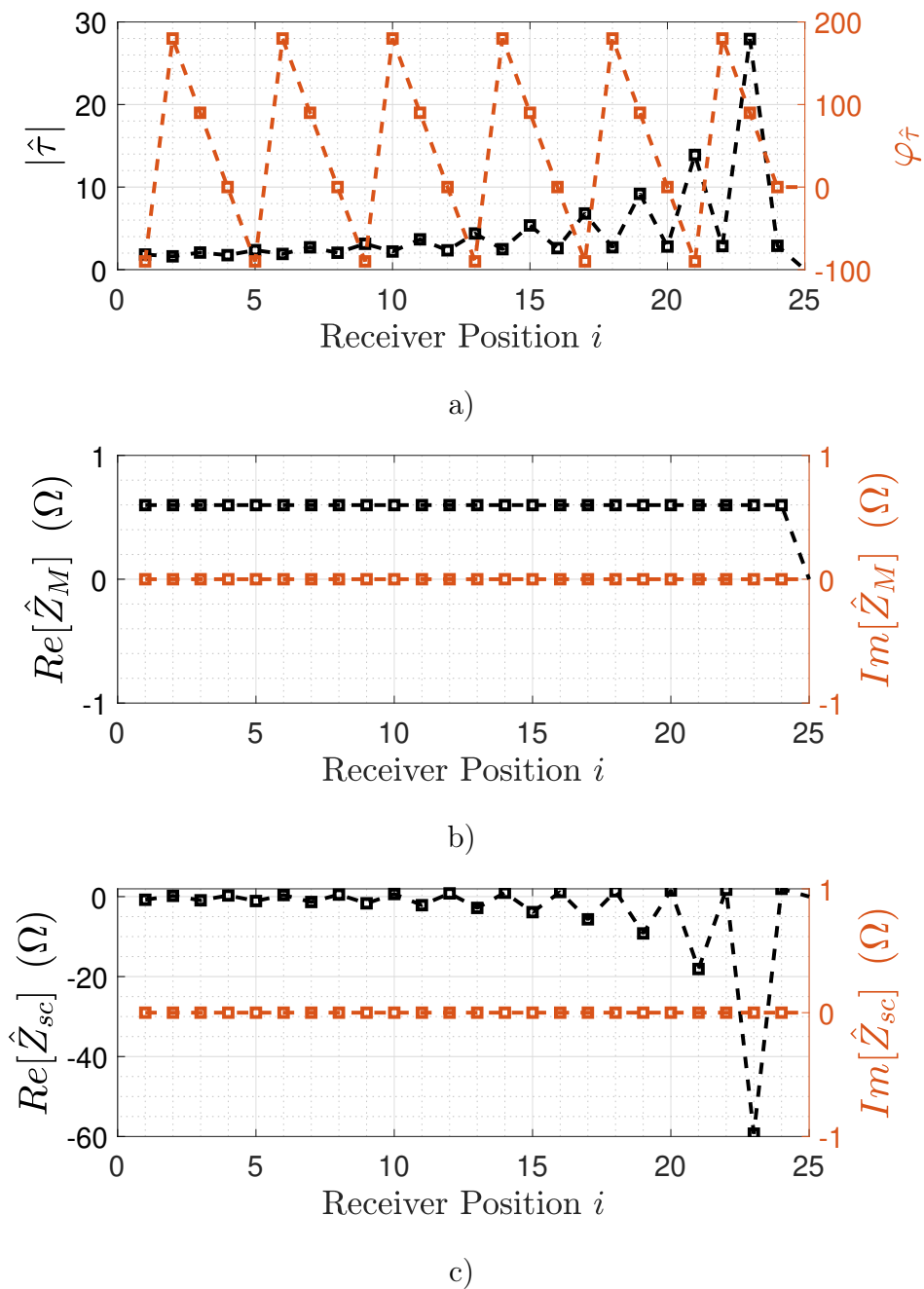


Figure 4.16: Real transformer parameters as a function of the receiver for a OC terminated array.

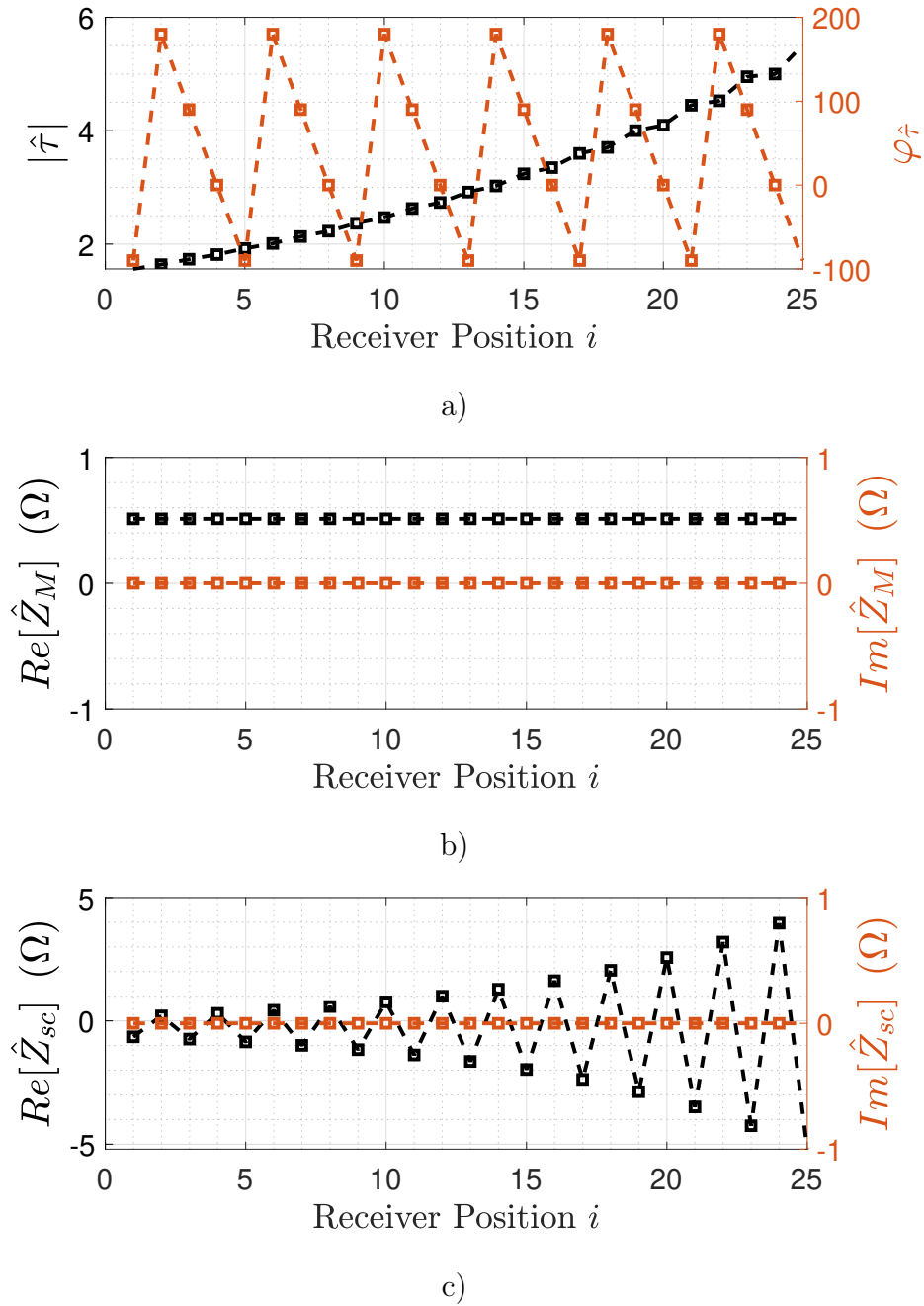


Figure 4.17: Real transformer parameters as a function of the receiver for an optimally terminated array.

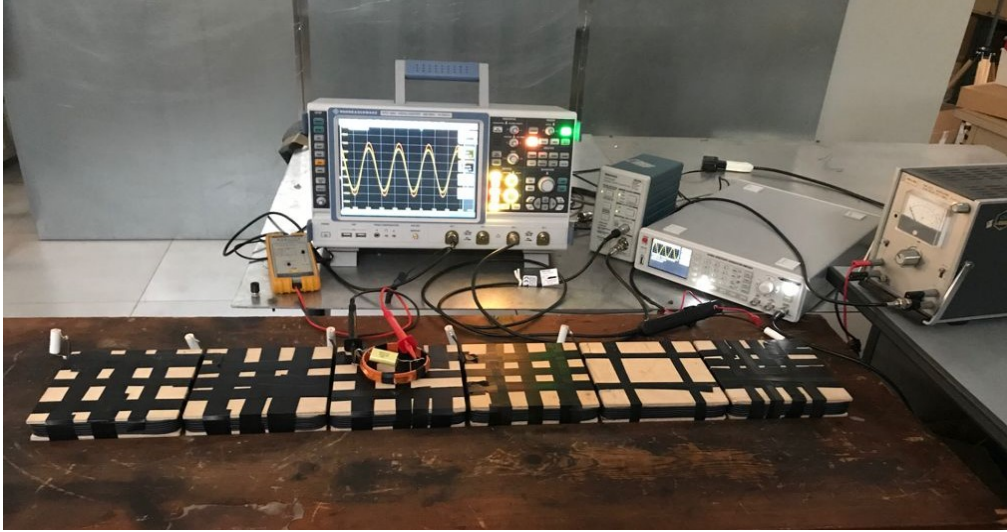
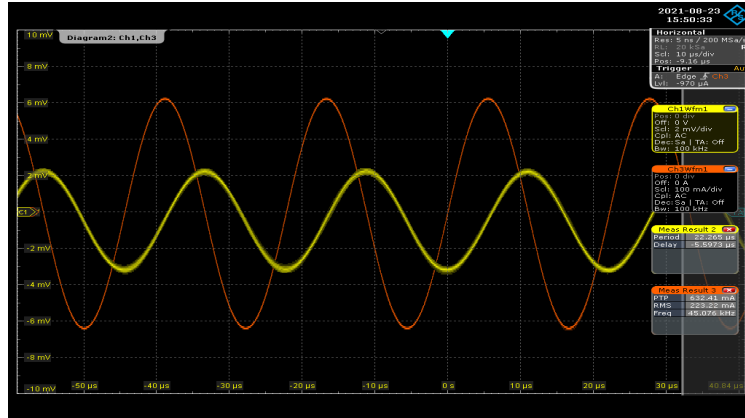


Figure 4.18: Experimental Setup.

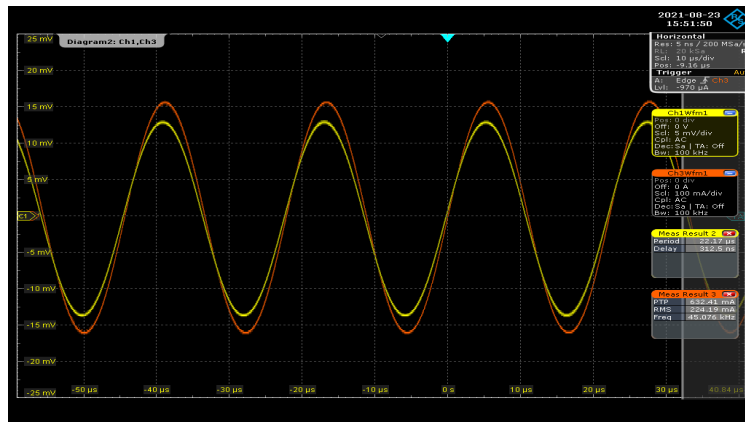
since it presents very low values that lead to very high magnetising currents, as can be deduced from Figs. 4.15, 4.16 and 4.17. The SC impedance  $\hat{Z}_{cc}$  is real for any receiver position and array termination, and oscillates between negative and positive values for all the terminations considered. In particular, for SC and  $\hat{Z}_{T_{opt}}$  terminations, the minimum values are found when the receiver is aligned with the odd cells of the array, while in the OC case when it is aligned with even cells. It is important to note that the behaviour of  $\hat{Z}_{sc}$  in the SC and OC case is exactly mirrored.

### 4.3 Experimental Validation

The analytical and numerical procedures for the extraction of the two-port impedance matrix parameters have been experimentally validated. The experimental setup, that comprises a resonator array with a receiver, an oscilloscope with the proper probes and the power source is depicted in Fig. 4.18. The impedance parameters have been estimated according to (4.20) measuring the currents and voltages at the system input and output ports. The measurements have been performed by feeding the array with a sinusoidal voltage at the resonant frequency of the cells, supplied by a Hameg signal generator and amplified by an analog amplifier. For the current measurements, a Tektronix TCP305A probe amplified by a Tektronix "TCPA 300" has been used, while an isolated Pico probe "TA057" with a bandwidth of 25 MHz has been chosen for the voltage measurements. Both the probes have been connected to a Rohde&Schwarz RTO 1004 oscilloscope with a sampling capability of 10 GSa/s and bandwidth of 600 MHz. Figs. 4.19a and 4.19b show the current (orange) and voltage (yellow) waveforms recorded for the estimation of  $\hat{Z}_m$  when the receiver is aligned with the 3rd and 4th array cell, respectively. In particular, from Fig. 4.19a it can be seen that the input current lags the output voltage by  $\frac{\pi}{2}$ , whereas in Fig.



a)



b)

Figure 4.19: Voltage (in yellow) and current (in orange) waveforms at the receiver port when the receiver is coupled to (a) the 3rd and (b) the 4th array cell.

4.19a the two waveforms are in phase, as predicted in Sec. 4.2.4.

The results of the measurements are compared with the analytical and numerical predictions for the SC and  $\hat{Z}_{T_{opt}}$  termination in Figs. 4.20 and 4.21, respectively, as a function of the receiver position. The graphs show a perfect agreement between the analytical and experimentally estimated values. The most significant deviation is found for  $\hat{Z}_{22}$ , with both terminations considered. This difference can be attributed to the unwanted coupling between the receiver and the nearby resonators of the array. In general, the dominant coupling is the one between the receiver and the cell below, and these results prove that the error introduced by neglecting the other receiver couplings is acceptable. The model faithfully describes the operation of the system. It can be observed that the parameters  $\hat{Z}_{11}$  and  $\hat{Z}_m$  have been estimated feeding the first resonator of the array with the receiver port in OC, enforcing a null receiver current. Thus, for both measurements, the receiver does not interact with the array. Instead, the current and voltage considered for the estimation of  $\hat{Z}_{rr}$  have been directly measured at the receiver port, which slightly couples even with

array cells adjacent to the one below. This effect is more evident when the receiver is above even numbered resonators, since the equivalent impedance of the system seen by the receiver port presents higher values and the circulating current lower magnitudes.

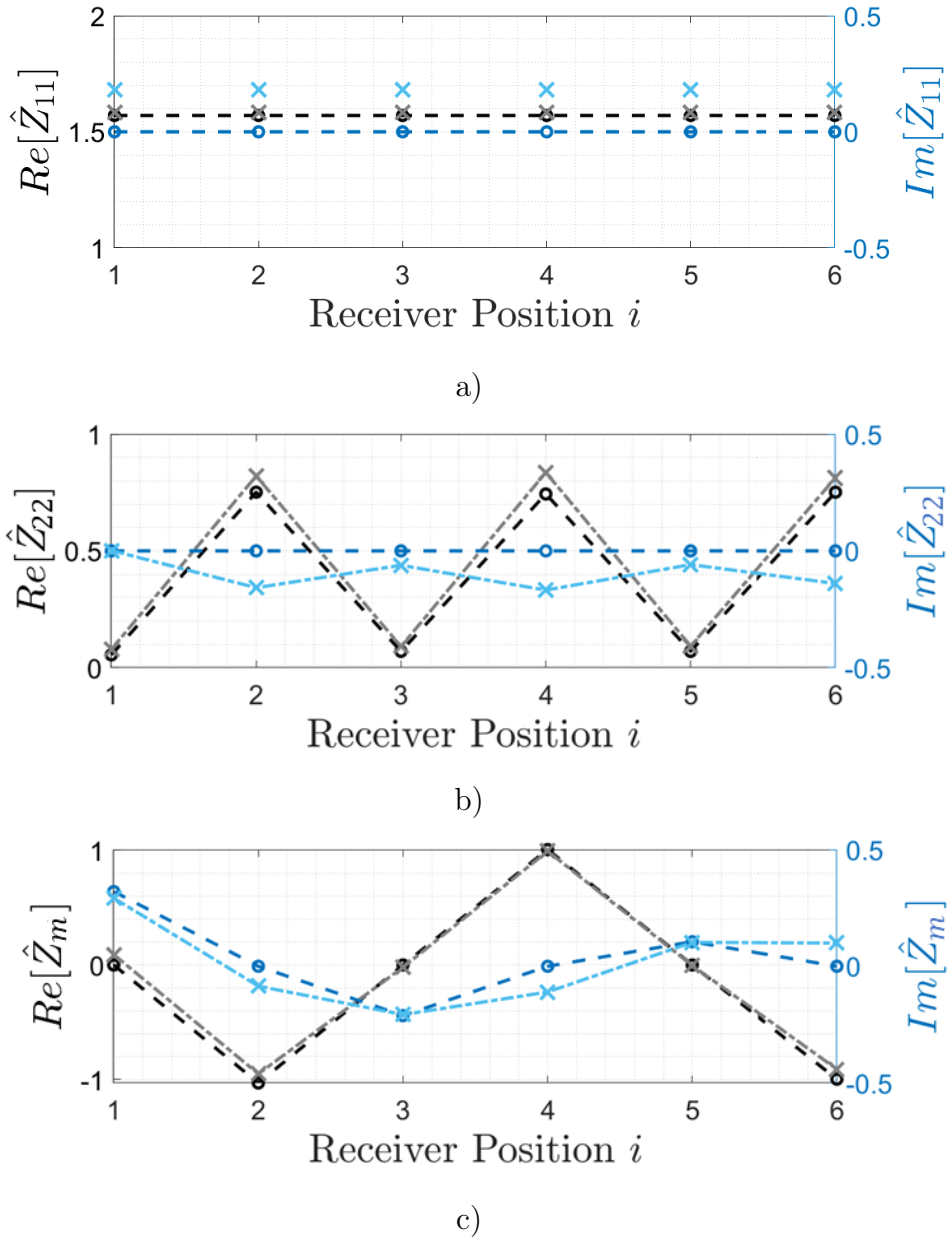


Figure 4.20: Two-port impedance parameters as a function of the receiver position for an array of 6 resonators at the resonant frequency of 45.1kHz in case of SC termination. The circle and cross markers refer to the formulas (4.24)-(4.26) and experimental results, respectively.

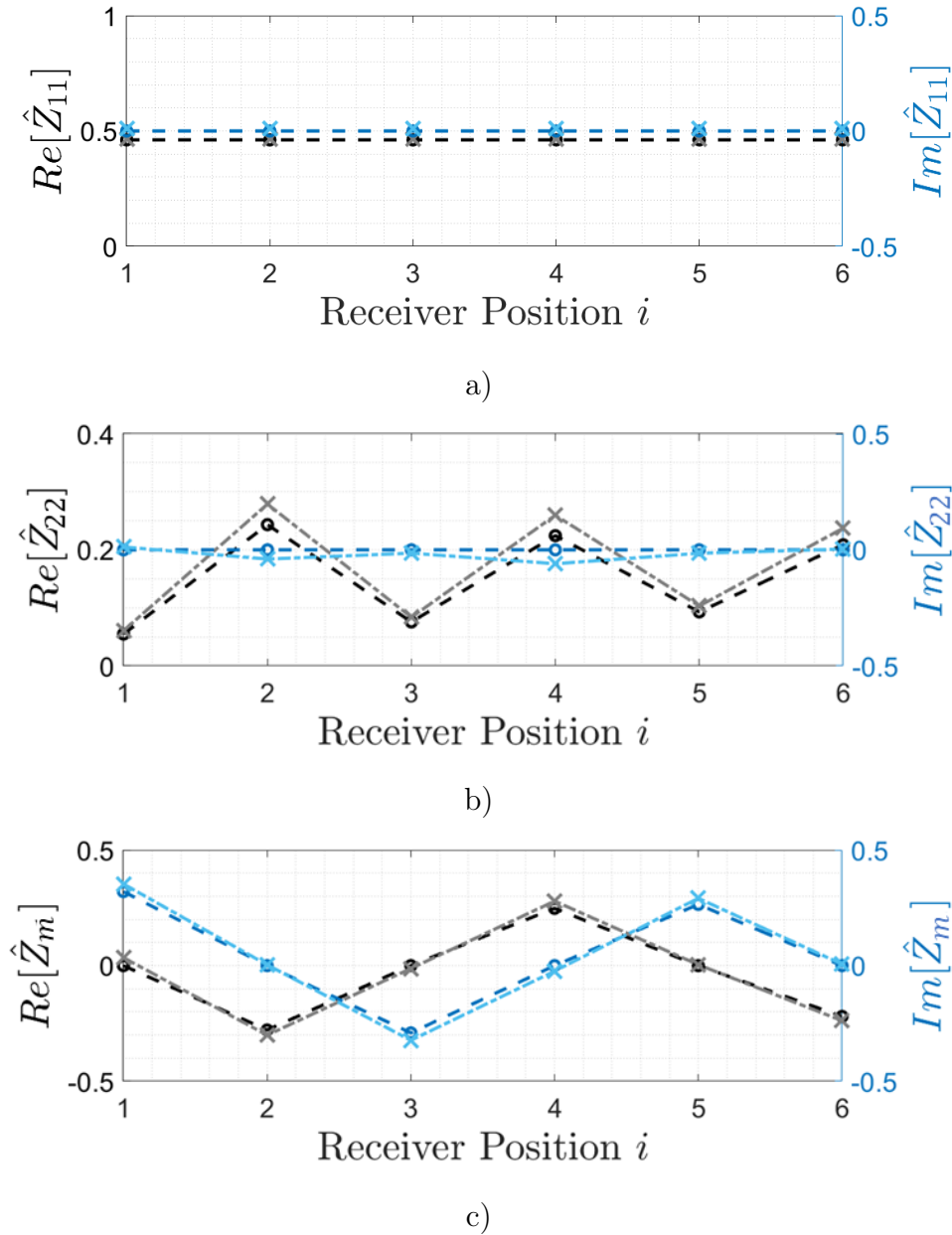
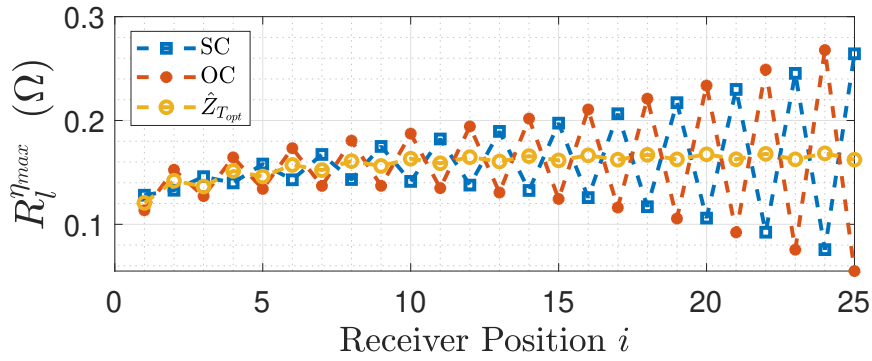
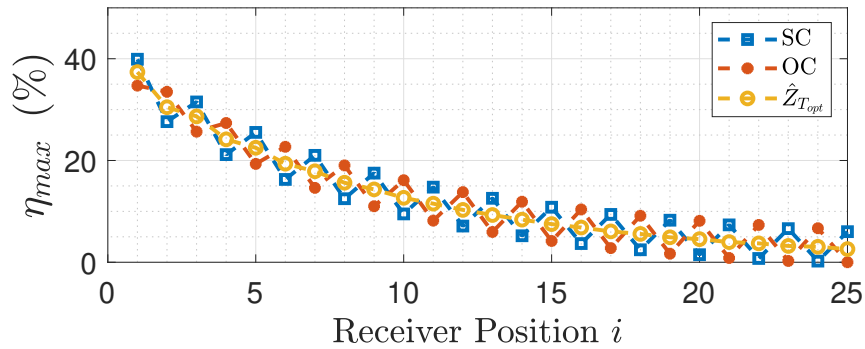


Figure 4.21: Two-port impedance parameters as a function of the receiver position for an array of 6 resonators at the resonant frequency of 45.1kHz with the array terminated in  $\hat{Z}_{T_{opt}}$ . The circle and cross markers refer to the formulas (4.24)-(4.26) and experimental results, respectively.



a)



b)

Figure 4.22: (a) Resistive load values that allow maximum efficiency and (b) maximum achievable efficiency as a function of the receiver position, for an array of 25 cells in different termination conditions.

### 4.3.1 Power and Efficiency

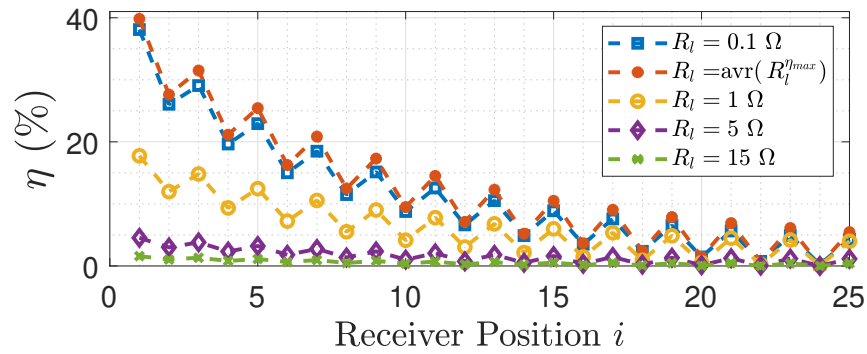
To complete the characterisation of the system, the performance in terms of efficiency and transmitted power were evaluated. Initially, the load resistance that allows the maximum efficiency was calculated according to (2.33) and reported in Fig. 4.22a as a function of the position of the receiver and for the different termination conditions, i.e. SC, OC and  $\hat{Z}_{T_{opt}}$ . The trends differ according to the termination of the array. In the case of SC or OC terminations, the values oscillate with mirrored trends, while their mean values correspond to the ones obtained with  $\hat{Z}_{T_{opt}}$  termination. For this latter case, the optimum load is approximately the same for each position. SC termination presents the maximum value of  $R_l^{\eta_{max}}$  when the receiver is aligned with odd-numbered resonators, while the minima occur when  $i$  is even. OC termination leads to a reversed characteristic. It is also interesting to observe that the maximum efficiency decreases when the resonator moves away from the source and that, in the case of SC and OC terminations, it does so by oscillating around the trend obtained with  $\hat{Z}_{T_{opt}}$  termination. When considering generic loads, the efficiency gradually decreases as the receiver moves away from the source, as it can be expected. The

efficiency trends are plotted as a function of the receiver position and for different loads in Figs. 4.23a, 4.23b and 4.23c when the array is terminated in SC, OC and  $\hat{Z}_{T_{opt}}$ . A load value  $R_{l_{AVR}}$  has been introduced. It basically corresponds to the average value of  $R_l^{max}$  and is  $0.15\Omega$ . It was introduced as there is no single optimum load, and an average of the load values that maximise efficiency was chosen as a reference. The choice is justified by the fact that, being the standard deviation of the optimal load values quite small, loading the receiver with  $R_{l_{AVR}}$  we can consider the maximised efficiency. Indeed, the curves show how the average optimum load actually leads to the highest efficiency and that this decreases dramatically when the load differs from that value. Furthermore, the terminations in SC and OC also lead in this case to fluctuating trends in a mirrored manner. In general, even for generic loads, the system presents maximum efficiency if it is terminated in:

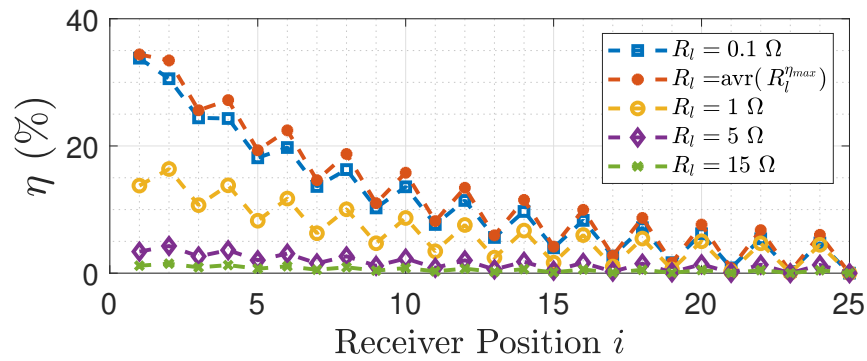
- SC if  $i$  is odd
- OC if  $i$  is even

while terminating in  $\hat{Z}_{T_{opt}}$  clearly introduces further losses. Thus, despite the more smoothed behaviour, it is not convenient to insert further resistance in the circuit, to limit energy losses. Obviously, if the array is formed by an odd number of resonators, the oscillation of the efficiency curve is reversed, and the termination modulation strategy must be suitably modified. This last consideration leads to the definition of a control strategy that allows maximum efficiency alternating SC termination with OC with an appropriate switching circuit. This technique has been discussed in [49, 48].

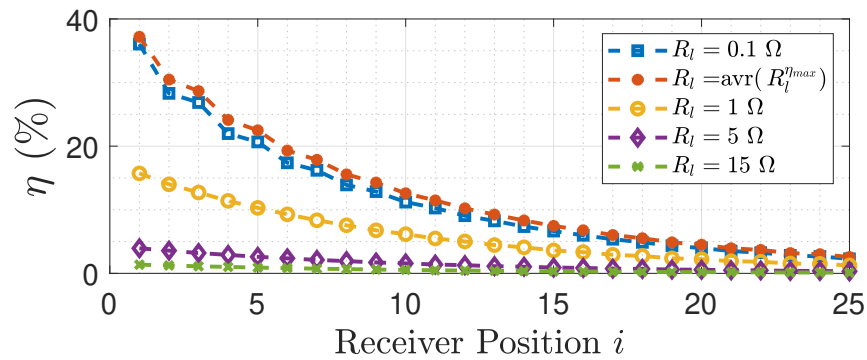
It is then possible to calculate the parameters of the Thévenin equivalent circuit of the system at the receiver port, whose impedance indicates the optimum load value to obtain the maximum power transfer. It is represented as a function of the position of the receiver in Fig. 4.24 considering the 3 different terminations. The peculiarity of the trend lies in the inversion of the oscillating trend when the receiver is over the second half of the array. In fact, in the case of SC and  $\hat{Z}_{T_{opt}}$  termination, the equivalent impedance has higher values when the receiver is aligned with odd cells and vice versa, as it can be seen in Fig. 4.24a. In the case of OC termination, the impedance has the same trend as the other two up to  $i < n/2$ , and then reverses. This exactly reflects the behaviour of the  $\hat{Z}_{22}$ , which dominates in the calculation of  $\hat{Z}_{th}$ . It is now important to observe how the maximum and minimum values of the power as a function of the position of the receiver also depend on the output load (see Fig. 4.24b), unlike the efficiency, for which the above considerations are valid for any load. Let  $\hat{Z}_{th_{AVR}}$  be the average load value among those that maximise power. Plotting the power as a function of the receiver position for the three different termination conditions, it is possible to see how the behaviour changes as the load changes. It is shown in Figs. 4.25a, 4.25b and 4.25c as a function of the receiver position and for different terminations in case  $R_l < R_l$ ,  $R_l = \hat{Z}_{th_{AVR}}$  and  $R_l > \hat{Z}_{th_{AVR}}$ , respectively. The traced curves clearly show that, depending on whether the load is greater or smaller than the average one, the termination



a)



b)



c)

Figure 4.23: System efficiency as a function of the receiver position and for different loads when the array is terminated in (a) SC, (b) OC and (c)  $\hat{Z}_{T_{opt}}$ .

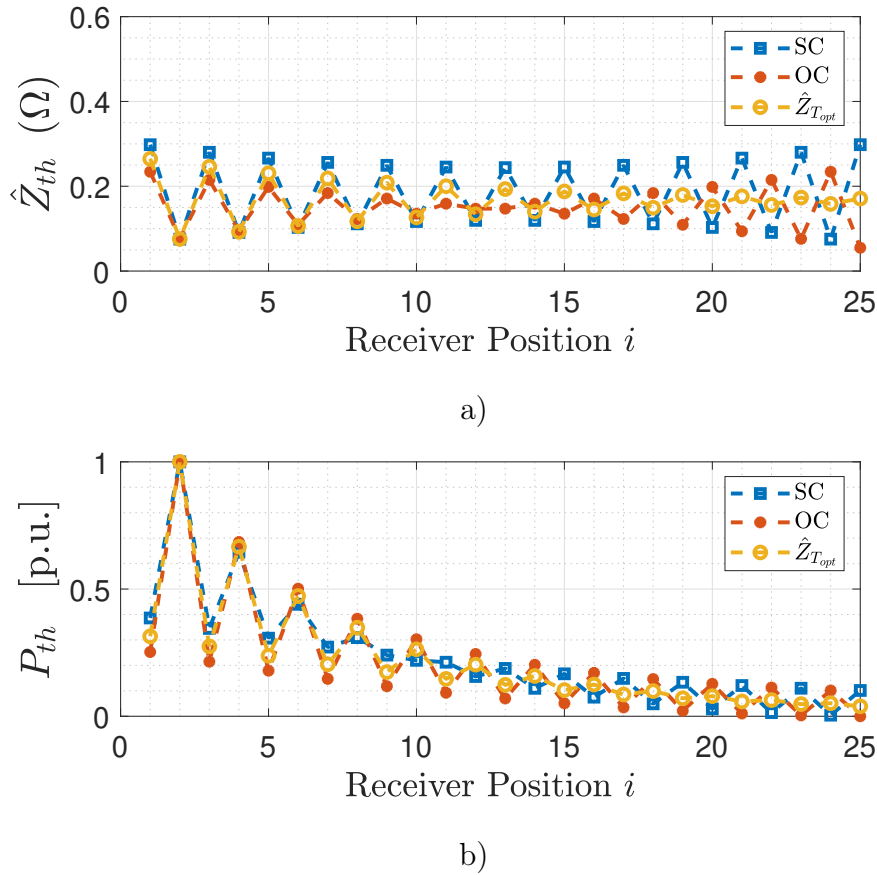
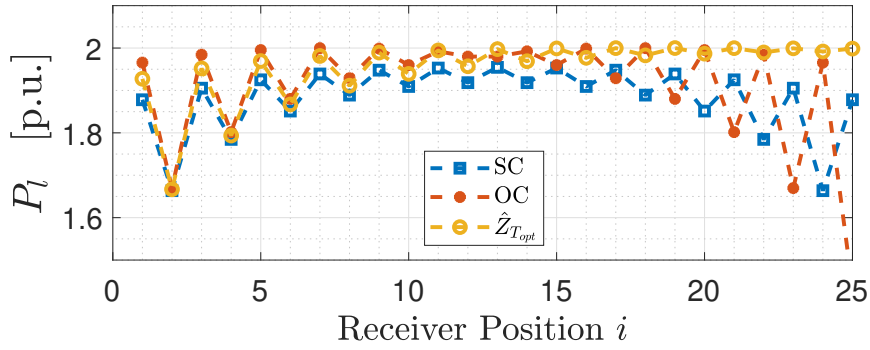
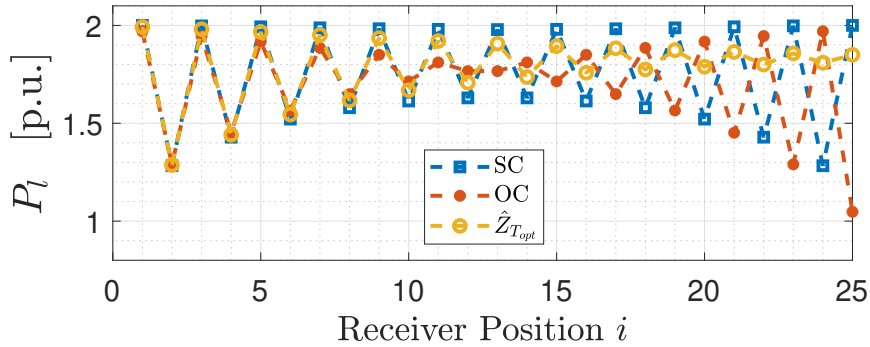


Figure 4.24: (a) Thévenin equivalent impedance and (b) maximum available power at the receiver port.

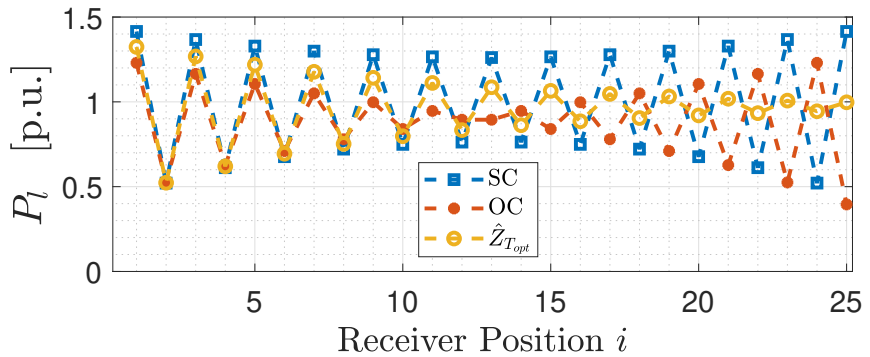
condition that allows the maximum power transfer for the considered load changes. This behaviour has a huge impact on the control strategy, which should somehow consider possible load variations during operations. The considerations made so far, which derive from an in-depth circuit analysis of the system, outline the guidelines for the design of both the system and control strategy. Similarly to the technique proposed in [49] for maximising the efficiency, it is possible to switch between SC or OC terminations of the array to maximise the transmitted power based on the load and position of the receiver. Furthermore, it must be considered that, in the case of loads lower than the average optimal one, the link between the position and the appropriate modulation vary according to whether the receiver is on the first or second half of the array, as can be deduced from the graphic relation of power. Overall, it can be concluded that, for an array with an odd number of resonators, the control strategy for maximum efficiency depends on the load. In particular, the case of  $R_l = \hat{Z}_{th_{AVR}}$  can be associated to the case of a load larger than the average one, but similar results are obtained with the opposite choice. However, it can be noted that, for  $i < n/2$ , the power transmitted in the case of OC or SC is very similar. This behaviour reflects the one of the available power (see. Fig. 4.24b), as well as



a)



b)



c)

Figure 4.25: Power transferred to a load (a)  $R_l < \hat{Z}_{th_{AVR}}$  (b)  $R_l = \hat{Z}_{th_{AVR}}$  and (c)  $R_l > \hat{Z}_{th_{AVR}}$ , as a function of the receiver position and for different terminations.

the equivalent impedance  $\hat{Z}_{th}$  and it is strongly related to the  $\hat{Z}_{22}$  parameter. This latter is in turn affected by the receiver geometry and parameters, as well as by the coupling with the array resonators. It is therefore possible to obtain different (albeit similar) behaviour of the parameters by properly designing the system. However, the transmitted power generally decreases with an increasing number of resonators, even if it is possible to maximise it obtaining considerable results. Overall, the optimal control is summarised in the following paragraphs.

**Load**  $R_l < \hat{Z}_{th_{AVR}}$  The system transferred power is maximum if the array is terminated in:

- $i \leq n/2$ 
  - OC if  $i$  is odd
  - SC if  $i$  is even
- $i \geq n/2$ 
  - SC if  $i$  is odd
  - OC if  $i$  is even

**Load**  $R_l > \hat{Z}_{th_{AVR}}$  The system transferred power is maximum if the array is terminated in:

- $\forall i$ 
  - SC if  $i$  is odd
  - OC if  $i$  is even

At last, it must be noticed that if the array is formed by an odd number of resonators, the SC and OC termination conditions are reversed. Overall, it can be seen that the power can actually be maximised, but the power available to the load still has some oscillations based on the termination adopted. This is due to the oscillations of the available power  $P_{th}$ , whose trend is once again a consequence of the peculiar behaviour of the two-port network parameters. Thus, even with the optimal load for maximum power, the transferred power would oscillate. Thus, even with a load  $R_l = \hat{Z}_{th}$  the transferred power would oscillate depending on the receiver position.

## 4.4 Doubly-Fed Resonator Array for Maximum Efficiency and Power Transfer

From the analysis of the system performance conducted so far, it is possible to see that the efficiency and the output power can be maximised. However, from the graphs of Fig. 4.25 it can be clearly seen that, regardless of the type of termination, when the receiver is coupled to even-numbered cells the transmitted power is much lower than in the case where it is coupled with the odd-numbered ones. Thus, while the real-time change of the termination from SC and OC can allow the efficiency to be maximised, the power transfer presents maximum and minimum values that considerably vary. In high-power applications, this can be the major limitation, as it is crucial to extract the maximum power possible from the source, which is then efficiently transferred to the load. Furthermore, it is not taken for granted that loads can operate discontinuously.

Still ensuring maximum efficiency, the power transmitted to the load can be increased ensuring that the receiver is always aligned with even-numbered cells. This is possible by introducing an additional power driver in the second cell of the array as illustrated in Fig. 4.26, which powers the system when the receiver is coupled to odd cells. Deactivating the first cell  $i$  would become even. To keep the efficiency high, it is advisable to carry out the modulation between SC and OC again. This has a key effect on the reflected impedance of the array segment following the  $i$ th cell made of  $n-i$  resonators. Considering this segment terminated in SC, its equivalent impedance seen by cell  $i$ th assumes low values (ideally zero) if  $n-i$  is even and high values (ideally infinite) if  $n-i$  is odd. To improve power transmission, its reflected impedance to the resonator  $i$ th should be as low as possible and, therefore, it is desired that the line be terminated in SC if  $n-i$  is even or OC if  $n-i$  is odd (this modulation allows the maximisation of the power). It follows that to maximise the power it is necessary to have  $i$  odd and  $n-i$  even and terminated in SC. Therefore, the modulation of the source and termination must be synchronised. The proposed control strategy is:

- if  $i$  is odd
  - Power  $\hat{V}_{s1}$ 
    - \* SC termination if  $n$  is odd
    - \* OC termination if  $n$  is even
- if  $i$  is even
  - Power  $\hat{V}_{s2}$ 
    - \* OC termination if  $n$  is odd
    - \* SC termination if  $n$  is even

This control strategy was applied to the array of 25 resonators described in Sec. 5.3.4. The transmitted power as a function of the position of the receiver is plotted in Fig. 4.27 for three different load conditions. The graph shows that the power on the load is now approximately constant as the position of the receiver varies, and above all close to the maximum obtainable values set by the system parameters. As a final note, it is important to discuss the feasibility of such a power driver. In fact, the power source has been schematised as real independent voltage sources, which can however correspond to a single inverter with a suitable topology. The driver requires to be able to power the first cell by short-circuiting the second and to power the second by leaving the first in an open circuit (therefore deactivated).

#### 4.4.1 Design Considerations

To preserve the simplicity of these devices, it is reasonable to think of using a single converter with two additional switches to open and close the first and second

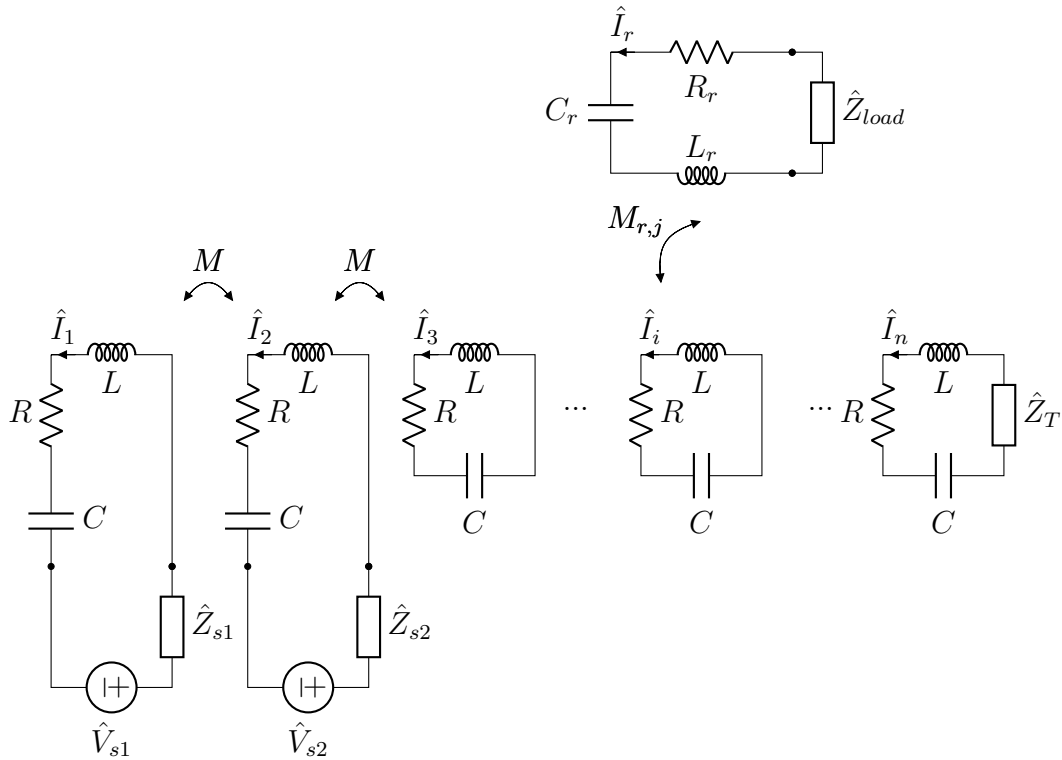


Figure 4.26: Doubly-fed array with fixed termination.

cells, respectively. However, direct connections of switches in series to inductors (in some applications even power) lead to overvoltages that can damage components. Therefore, if only one power source is used, it is necessary to consider free-wheeling paths for the current of the coils by introducing suitable diodes. In this thesis, the control circuit is not discussed as the goal is to show the feasibility of a resonator array that allows for the maximisation of the transmitted power and efficiency. It is important to notice that, for consistency, the whole discussion was done considering the measured parameters of the resonator array built in the laboratory. However, the system is not optimised for power transfer. For the system to transfer consistent power (at least some kW), the coils should be redesigned and ferromagnetic cores incorporated. This would allow the self- and mutual inductance coefficients to be dramatically increased, with a consequent increase in the efficiency and power transfer. Furthermore, as shown in Chapter 3, the dimensioning of the system must be carried out based on the load to be powered. In fact, the results of Sec. 4.3.1 show how it is possible to define an optimal load value that allows the transmitted power to be maximised after setting the system parameters. For arrays with a receiver, a design procedure based on analytical formulas is almost impossible given the complexity of the model. In any case, by calculating the system parameters through the analytical expressions proposed, it is possible to implement an iterative calculation

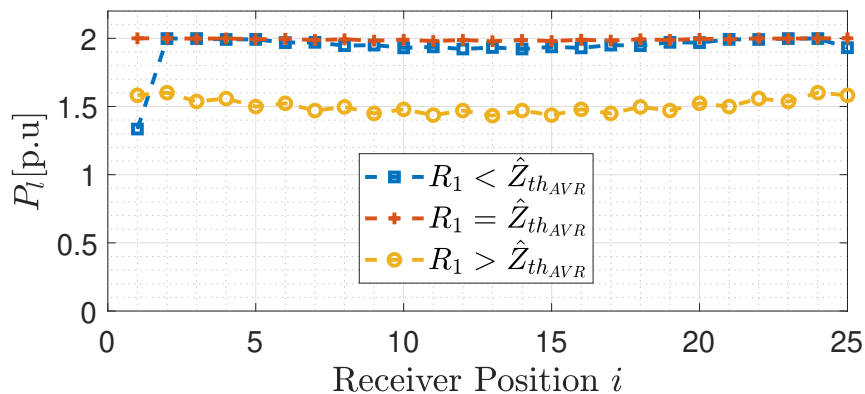


Figure 4.27: Power transferred to a load (a)  $R_l < \hat{Z}_{th_{AVR}}$  (b)  $R_l = \hat{Z}_{th_{AVR}}$  and (c)  $R_l > \hat{Z}_{th_{AVR}}$ , as a function of the receiver position and for different terminations for a doubly-fed array controlled to maximise efficiency and power transfer.

procedure that allows the optimisation of the system parameters on the basis of the load requirements.

## 4.5 Conclusions

In this chapter, a study of the performance of arrays of resonators employed for IPT has been carried out. In particular, the two-port model described through the impedance matrix has been adopted to represent the system, simplifying the analysis and allowing the comparison of this kind of apparatuses with traditional transformers or IPT devices. In particular, original analytical expressions of the two-port network parameters have been proposed and numerically validated, both for simple arrays and for resonator arrays with a receiver. For this second case, experimental validations have been performed on a working prototype. The experimental results are in perfect agreement with the predictions obtained through the analytical formulas and highlighted a strong dependence of the system parameters on the position of the receiver. The efficiency and transmitted power have been studied for both array configurations, also considering various load conditions. Furthermore, the load values that allow the maximisation of efficiency or transmitted power have been presented and discussed. Overall, this study highlighted that resonator arrays are a very cheap and structurally simple alternative to traditional IPT systems, allowing them to extend the power transfer distance. Unfortunately, however, for a fixed array structure, system parameters vary drastically based on the load and location of the receiver, making system control very complicated. The attention was focused on arrays with a receiver, as they are solutions of real practical interest, especially for industrial applications. An optimal control strategy that allows both the transmitted power and the efficiency to be maximised has been proposed. It should be noted that, in the literature, control strategies for this kind of devices have been

---

presented only for maximising the efficiency, which however cannot guarantee the maximisation of the transmitted power. With this technique, combined with an optimised design of the system (maximisation of self- and mutual inductances of the coils) it is possible to obtain IPT apparatuses with performances comparable to the traditional two-coils systems, with the crucial advantage of transmitting the power even with the receiver placed far from the source coil.

## Chapter 5

# Distribution of Currents in Resonator Arrays: Magneto-inductive waves and Standing Wave Pattern

Resonator arrays are devices composed of coupled resonant circuits and are mostly used as devices for IPT. Their behaviour in terms of efficiency and transmitted power has been thoroughly discussed in the previous chapter, with also the definition of a control strategy aimed at maximising the efficiency and the transmitted power. In particular, a representation of these systems as two-port networks has been proposed, also providing analytical expressions for the terms of the impedance matrix. This type of representation has allowed a consistent comparison between traditional IPT devices and those using resonator arrays with a receiver, useful for evaluating their behaviour when connected to other system components. However, this model includes only four system variables, namely the current and voltage of the input and output ports. The currents and voltages of the intermediate resonators are not explicit and therefore the two-port model does not allow their analysis. In literature, the presence of power reflections has been mentioned to explain the failure to transfer the whole power to the load [64, 66, 47, 69]. In fact, as shown in Chapter 4 and known from the basics of circuit theory, the power transferred to a load strongly depends on the value of the load itself. In resonator arrays, especially when they are employed to feed a receiver, the optimisation of the load is almost impossible, due to the great dependence of the parameters on the position of the receiver [47]. This leads to an important amount of reflected power (i.e. that is supplied by the source but not absorbed by the load), which is dissipated by the resonators. The result can be severe overloads of the cell windings, with consequent thermal stress. Furthermore, the dissipated power dramatically decreases the efficiency. This implies that the resonators must be dimensioned to withstand even

very intense thermal and electrical stresses with a low power transferred to the load. An optimised project requires a thorough and complete knowledge of the behaviour of the system, also able to foresee possible critical aspects that can lead to a malfunction or breakdown of the system. In this framework, an in-depth study of the resonator currents is performed considering different operating conditions. It is important to notice that, since the array operates in resonance, the resonator currents are limited by the resistance of the wires only, which should be kept very small to limit losses. The analysis is performed with both the circuit analysis and the theory of magneto-inductive waves [64], which is based on the classical transmission line (TL) theory. The results have also been experimentally validated with a prototype of resonator array.

## 5.1 Magneto-Inductive (MI) Waves

Magneto-inductive waves resulted as a by-product of the research on metamaterials [64]. A possible definition metamaterial is provided in [54], that defines these objects as assemblies of resonant magnetic and electric circuits that behave as a continuous medium with positive and/or negative dielectric and magnetic properties. In particular, magnetic metamaterials are considered, that basically consist of periodic structures of magnetically coupled resonant circuits, mostly made of coils (wound or printed on PCBs) that all resonate at the same frequency thanks to their self-capacitance or a properly connected lumped capacitor. Each resonator can be also referred to “unit cell” or “meta-atom”, while the resulting structure is commonly named “lattice”, recalling the concept of molecular structure of traditional natural materials. Metamaterials can consist of one-dimensional, two-dimensional or even three-dimensional structures, whose applications range from optical lenses (also with the definition of an invisibility cloak) [51, 53] up to power and data transmission [120, 121, 122]. When considering one-dimensional lattices, it is straightforward to understand the analogy between resonator arrays and metamaterials, which are in fact two different ways of considering the same devices.

In this frame, a new kind of wave has been defined, called magneto-inductive wave by Shamonina *et al.* [64]. The nature and mechanism of this phenomenon can be understood considering the structure of these metamaterials. In general, the currents and voltages of the resonators spread in the lattice thanks to the magnetic coupling they experience. In fact, by energising a coil with a power source, a 90 degrees-displaced voltage (and a corresponding current) is induced in the coupled resonators, which in turn induces a voltage (and thus a current) in the other coupled cells. This behaviour mirrors the one of a wave that propagates in the lattice thanks to the cells mutual coupling and, in the case of magnetic metamaterials, it corresponds to a current wave. This wave has been introduced in [67]. More rigorously, the waves can be described for 1D metamaterials resorting to the circuit model also used in Chapter 4 and reported in Fig. 5.1. Indeed, two coupled resonant circuits can be seen as a two-port, where the relation between the phasors of input and output current

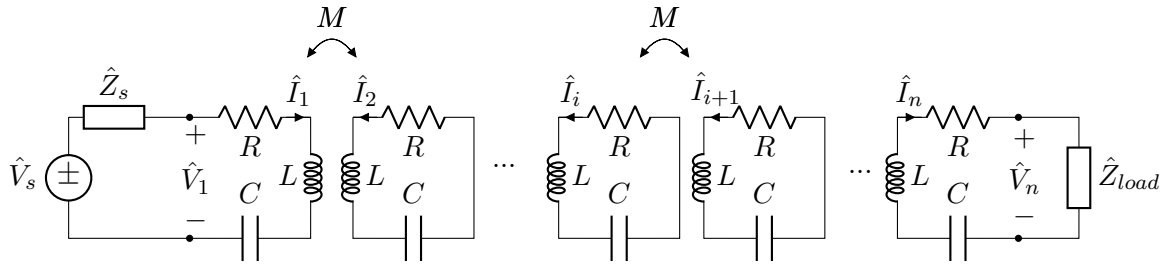


Figure 5.1: Equivalent frequency domain circuits of a resonator array.

and voltage is defined by the electromagnetic properties of the physical system. In particular, the two-port networks that support waves are defined in terms of chain matrices  $\hat{\mathbf{T}}$ , also named ABCD matrices [123]. Exploiting this representation of magnetically coupled coils and assuming the nearest-neighbour approximation, the  $n$ -cells array can be modelled as a cascade of  $n-1$  two-ports (shown in Fig. 5.2), that phase-shift and attenuate their input current and voltage. For two adjacent resonators  $i$  and  $i+1$  the voltages and currents at the input and output ports of the two-port network are related as:

$$\begin{bmatrix} \hat{V}_i \\ \hat{I}_i \end{bmatrix} = \hat{\mathbf{T}}_{i,i+1} \begin{bmatrix} \hat{V}_{i+1} \\ \hat{I}_{i+1} \end{bmatrix} \quad (5.1)$$

where

$$\hat{\mathbf{T}}_{i,i+1} = \begin{bmatrix} \hat{A}_{i,i+1} & \hat{B}_{i,i+1} \\ \hat{C}_{i,i+1} & \hat{D}_{i,i+1} \end{bmatrix} \quad (5.2)$$

The chain matrix terms can be found from the impedance matrix representation of series resonant coupled coils discussed in Sec. 2.3.1 as described in [123, 124], resulting in:

$$\begin{aligned} \hat{A}_{i,i+1} &= -\frac{\hat{Z}_i}{\hat{Z}_{M_{i,i+1}}} \\ \hat{B}_{i,i+1} &= \hat{Z}_{M_{i,i+1}} - \frac{\hat{Z}_i \hat{Z}_{i+1}}{\hat{Z}_{M_{i,i+1}}} \\ \hat{C}_{i,i+1} &= -\frac{1}{\hat{Z}_{M_{i,i+1}}} \\ \hat{D}_{i,i+1} &= -\frac{\hat{Z}_{i+1}}{\hat{Z}_{M_{i,i+1}}}. \end{aligned} \quad (5.3)$$

where  $\hat{Z}_i$  and  $\hat{Z}_{i+1}$  are impedances of the coils and  $\hat{Z}_{M_{i,i+1}}$  the mutual impedance associated to their magnetic coupling. In arrays with identical resonators of impedance  $\hat{Z}$ , these terms reduces to  $\hat{Z}_i = \hat{Z}_{i+1} = \hat{Z}/2$  and  $\hat{Z}_1 = \hat{Z}_n = \hat{Z}$ , while the mutual impedance  $\hat{Z}_{M_{i,i+1}} = j\omega M$ . Thus, the array can be described by three different  $\hat{\mathbf{T}}_{i,i+1}$  matrices only. Hereinafter, the transmission matrices associated with the two-port networks that involve the first and last array resonators are referred to  $\hat{\mathbf{T}}_{1,2}$  and  $\hat{\mathbf{T}}_{n-1,n}$ , respectively, the one that represents the coupling between two adjacent array resonators (i.e. the generic  $i$ th and  $(i+1)$ th) is simply named as  $\hat{\mathbf{T}}_{MI}$

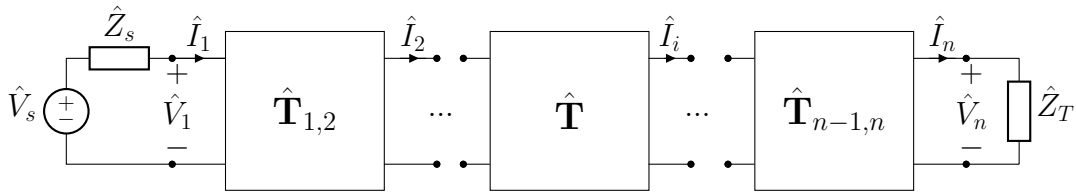


Figure 5.2: Equivalent representation of a resonator array by a cascade connection of two-port networks.

and results:

$$\hat{\mathbf{T}}_{MI} = \begin{bmatrix} -\frac{\hat{Z}}{2j\omega M} & j\omega M \left(1 + \frac{\hat{Z}^2}{4(\omega M)^2}\right) \\ \frac{1}{-j\omega M} & -\frac{\hat{Z}}{2j\omega M} \end{bmatrix} \quad (5.4)$$

This representation suggests an analogy between TL and resonator arrays. Indeed, the chain matrix is typically used to model transmission lines as it allows the representation of the entire line with a single chain matrix obtained as the product of the chain matrices of the individual cascaded TL sections. For a generic transmission line segment of length  $d$ , the chain matrix can be also expressed as [125]:

$$\hat{\mathbf{T}}_{MI-TL} = \begin{bmatrix} \cosh(\hat{\gamma}d) & \hat{Z}_0 \sinh(\hat{\gamma}d) \\ \frac{1}{\hat{Z}_0} \sinh(\hat{\gamma}d) & \cosh(\hat{\gamma}d) \end{bmatrix}. \quad (5.5)$$

where  $\hat{Z}_0$  is the characteristic impedance of the TL segment,  $d$  its length and  $\hat{\gamma} = \alpha + j\beta$  is the propagation constant, with  $\alpha$  the attenuation constant and  $\beta$  the phase constant. The analogy between TL and resonator arrays is formally established enforcing  $\hat{\mathbf{T}}_{MI} = \hat{\mathbf{T}}_{MI-TL}$  and thus, equating (5.4) and (5.5) the characteristic impedance and propagation constant of the considered line segment can be found as:

$$\hat{Z}_0 = \sqrt{(\omega M)^2 + \frac{\hat{Z}^2}{4}} \quad (5.6)$$

which becomes  $\hat{Z}_0 \approx \omega_0 M$  for a low-loss array operating in resonance, being  $Z_i = Z_{i+1} = R^2/4 \approx 0$ , and

$$\hat{\gamma} = \frac{1}{d} \cosh^{-1} \left( -\frac{\hat{Z}}{2j\omega M} \right). \quad (5.7)$$

The term  $d$  is the physical length of the unit, which was introduced to consider the spatial dimension of the system and, in this case, corresponds to the side-length of each resonator forming the array. It is important to note that, while the voltages  $\hat{V}_1$  and  $\hat{V}_n$  correspond to the input and output voltages of the array, the other generic port voltages cannot be identified in the real circuit (and therefore in its representation in Fig. 5.2). Instead, the currents correspond exactly to those circulating in the coils with  $\hat{I}_i$  and  $\hat{I}_1$  the  $i$ th and first resonator phasor currents, respectively.

For this reason, the study focuses on current waves only. For an infinitely long or matched 1D metamaterial, the current wave is called magneto-inductive wave and is then defined as:

$$\hat{I}_i = \hat{I}_1 e^{-\hat{\gamma}(i-1)d} \quad (5.8)$$

where  $\hat{I}_i$  is the  $i$ th resonator phasor current and  $\hat{I}_1$  the first resonator phasor current, assumed as the source one. These relations state that, for the same spatial interval  $d$ , the voltages and currents change by the same amount, which is in this case  $e^{-\hat{\gamma}d}$ . This behaviour corresponds to that of a wave that propagates and attenuates in the direction of the space defined by the TL line, which is in this case also referred to as MI waveguide. The attenuation constant per cell of the MI wave defined in (5.7) can be expressed as [47]:

$$\alpha d = \sinh^{-1} \left( \frac{1}{kQ} \right) \quad (5.9)$$

where  $k = 2M/L$  is the coupling coefficient between adjacent cells and  $Q = \omega_0 L/R$  the quality factor of the single cell, being  $\omega_0 = 2\pi f_0$  the resonant angular frequency. The current wave attenuation is due to the resistance  $R$  of each cell and becomes stronger as the coupling between adjacent cells weakens. The propagation of MI waves is governed by the dispersion equation which in case of low losses gives the following simple relationship [47, 64]:

$$\cos(\beta d) = \left( \frac{\omega_0^2 - \omega^2}{k\omega^2} \right) \quad (5.10)$$

from which the limits in frequency of the propagation band can be found enforcing  $|\cos(\beta d)| = 1$ . For operations at  $\omega_0$ , the attenuation is minimum and the phase shift per cell is  $\beta d \approx \pi/2$ . The wavelength of MI waves is  $\lambda_{MIW} = 4d$ , since the wave experiences a phase shift of  $\beta$  each space interval  $d$ . The analogy with TLs also suggests the possibility of matching the MI waveguide to avoid MI-standing waves. This condition is achieved if the array is terminated in a lumped impedance equal to the characteristic one of the MI waveguide, defined as [64]:

$$\hat{Z}_0 = j\omega M e^{-\hat{\gamma}d}. \quad (5.11)$$

For a low-loss MI waveguide,  $\hat{Z}_0$  simplifies to  $\hat{Z}_0 \approx \omega_0 M$  for  $f = f_0$ , as already introduced in (5.6) and Sec. 4.1.5. In resonance and matching conditions, the currents in a low-loss MI waveguide (i.e.  $R \ll \omega_0 M$ ) have the same magnitude and the power transferred to the terminal resonator is maximum [69, 46]. Similar considerations can be extended to the case of 2D and 3D lattices, which however are not discussed in this work.

## 5.2 Standing Waves and Current Peaks

The analogy between resonator arrays and TLs, although not essential to describe their operation, is able to provide useful information regarding the operation of these

devices. The description of the current in the resonators as a propagating wave allowed a simple definition of the termination that allows the maximisation of both the efficiency and power transmitted as a matching condition. This consideration also leads to conclude that, if the load is different from that of matching  $\hat{Z}_0$ , reflections of the power at the output port of the MI waveguide occur, which in turn lead to reflections of the MI wave. In mismatching conditions, therefore, standing current waves arise, with very high current peaks, increasing losses and resonator thermal stress. This phenomenon can be studied through the theory of MI waves, that requires a comprehensive and precise modelling of the circuit and connected devices since the reflections of the waves strongly depend on the boundary conditions of the line, as is known from the TL theory. Resonator arrays are usually fed by switching power converters, while the load is typically a battery charging system, whose modelling has been already discussed in Sec. 2.4 and 2.5, respectively. Thus, at the resonance frequency of the resonators, the power source can be modelled as a voltage source with a series impedance and the load as a resistance. For the sake of generality, the termination impedance  $\hat{Z}_T$  has been considered as an array load. The standing wave pattern in a TL can be determined by studying the propagation and reflections experienced at the two terminals. The first reflection that the current wave undergoes is due to the mismatching of the termination impedance  $\hat{Z}_T$ , which usually differs from the characteristic impedance  $\hat{Z}_0$  which can be quantified through the termination reflection coefficient  $\hat{\rho}_T$  defined as:

$$\hat{\rho}_T = \frac{\hat{Z}_T - \hat{Z}_0}{\hat{Z}_T + \hat{Z}_0}. \quad (5.12)$$

Similarly, also the backward wave can experience reflections at the source terminals and thus the source reflection coefficient  $\hat{\rho}_s$  is introduced as:

$$\hat{\rho}_s = \frac{\hat{Z}_s - \hat{Z}_0}{\hat{Z}_s + \hat{Z}_0}. \quad (5.13)$$

where  $\hat{Z}_s$  is the source internal impedance.

When the ends of the line are connected to power converters, it is difficult to control the terminations, as they strongly depend on the operating conditions as well as on the circuitry. Usually, as discussed in Sec. 2.4, voltage source inverters present a nearly null internal impedance while the load is modelled as a resistance that depends on the output voltage and transferred power, as introduced in Sec. 2.5. Moreover, there are some control strategies of the converters downstream of the receiver which allow the desired input impedance to be obtained. They are solutions developed to achieve maximum power transfer and allow a significant improvement of the system performance. However, as they are not very common in high-power applications, especially in the industrial field, they are not considered. However, the analysis is independent of the type of converter connected to the receiver.

The standing wave pattern is the result of the multiple reflections occurring at the input and termination sides of the line, whose superposition leads to the actual

distribution of currents. The final mathematical expression is given in [124, 123] for waves in traditional TLs and it can be extended to the case of MI waveguides. After some mathematical manipulation, the current in the generic  $i$ th resonator of the array can be defined as:

$$\hat{I}_i = \frac{\hat{V}_s}{\hat{Z}_s + \hat{Z}_0} \frac{e^{-\hat{\gamma}(i-1)d} - \hat{\rho}_T e^{-2\hat{\gamma}(n-1)d} e^{\hat{\gamma}(i-1)d}}{1 - \hat{\rho}_S \hat{\rho}_T e^{-2\hat{\gamma}(n-1)d}}. \quad (5.14)$$

This current distribution is the result of the mismatching of both sides of the line and corresponds to a standing wave pattern for MI wave, which exhibits maxima and minima with a periodicity that depends on the wavelength of the individual wave. Depending on the nature of the type of termination, the resulting reflected wave interferes differently with the incident one, thus leading to different configurations of standing wave patterns. Standing wave patterns also lead to power reflections, with a consequent dramatic decrease of the power transfer capability and efficiency [47], together with important stress of the circuit components.

According to [124], the shape of a standing wave pattern can be identified by specifying:

- the ratio of the current magnitude maximum to the minimum in the standing wave pattern (standing wave ratio);
- the distance between two consecutive maxima or minima;
- the location of any current minimum, with reference to a specified coordinate.

The standing wave ratio (SWR) is introduced to quantify the magnitude of the wave peaks and it is defined as:

$$SWR = \frac{|\hat{I}_i|_{\max}}{|\hat{I}_i|_{\min}} \quad (5.15)$$

where  $|\hat{I}_i|_{\max}$  and  $|\hat{I}_i|_{\min}$  are the maximum and minimum current magnitudes in the waveguide, respectively. The distance between consecutive current maxima or minima corresponds to half wavelength, which is  $2d$  for a MI wave, being its wavelength  $\lambda_{MIW} = 4d$ . It must be noticed that, considering the attenuation due to the losses, the magnitude of the current peaks is expected to be lower as the waveguide gets longer, as the current wave experiences a stronger attenuation. The location of the current minima can be deduced from the length of the waveguide in the terms of wavelength and the type of termination, together with their distance.

### 5.2.1 Numerical Simulations

Applying the current calculation procedure just introduced to the array prototype presented in Chapter 4, it is possible to verify the presence of MI standing waves in the structure. It must be noticed that, to enhance the performance of the array, a

higher operating frequency of  $f_0 = 147$  kHz has been chosen. The resonator coils are the same and thus the capacitors have been modified accordingly to make them resonate at  $f_0$ . The resulting array parameters are reported in Tab. 5.1.

The simulations are performed for different values of the reflection coefficients  $\hat{\rho}_T$  and  $\hat{\rho}_s$ , that leads to different current distributions. Assuming the internal inverter impedance  $\hat{Z}_S = 0\Omega$  ( the inverter is realised with GaN transistors), the source reflection coefficient results  $\hat{\rho}_S \approx -1$ , that lead to perfect reflections. The termination reflection coefficient  $\hat{\rho}_T$  is instead affected by the termination, whose effect in terms of efficiency and power transfer has been investigated in [69].

The standing wave pattern of the current can be appreciated in Fig. 5.3, where the magnitude of the current wave as a function of the position in the array for the case of short-circuit SC termination, open-circuit OC termination and perfect load matching (which corresponds to the optimal load  $R_l^{\eta_{max}}$  discussed in Sec. 4.1.5) is shown. It must be noticed that, being the considered TL an array of resonators, the OC termination corresponds to an array with one less resonator. This feature is crucial in the following analysis. As expected, the plot shows that in the case of a matching termination no standing wave patterns occur, unlike in the cases of SC and OC. In particular, the amplitude of the currents is approximately the same in each resonator and shows a slight decrease as the distance of the considered resonator from the source increases. This testifies to the presence of attenuation due to the resistance of the windings. Furthermore, the amplitude of the current peaks is much greater in the OC case, which corresponds to an array with an odd number of resonators. On the contrary, in case of SC termination, the resonator current magnitudes are very low, with the peaks having amplitude comparable to that obtained in the case of matching. The analysis was deepened by evaluating the SWR of the current for arrays with a different number of resonators terminated in SC and perfect matching, and it is depicted in Fig. 5.4. As already mentioned, the OC termination of an array corresponds to the same array with one less resonator. In particular, the blue curve refers to arrays with SC termination, whereas the red one

Table 5.1: Resonator array parameters

<i>Quantity</i>	<i>Symbol</i>	<i>Value</i>	<i>Unit of Measure</i>
Resonator Resistance	$R$	0.11	$\Omega$
Resonator Self-inductance	$L$	12.5	$\mu\text{H}$
Resonators Mutual Inductance	$M$	-1.55	$\mu\text{H}$
Capacitance	$C$	93.1	nF
Resonance Frequency	$f_0$	147	kHz
Characteristic Impedance	$\hat{Z}_0$	1.43	$\Omega$
Input Impedance	$\hat{Z}_s$	0.01	$\Omega$
Input Voltage	$V_{in}$	3.6	$V_{rms}$

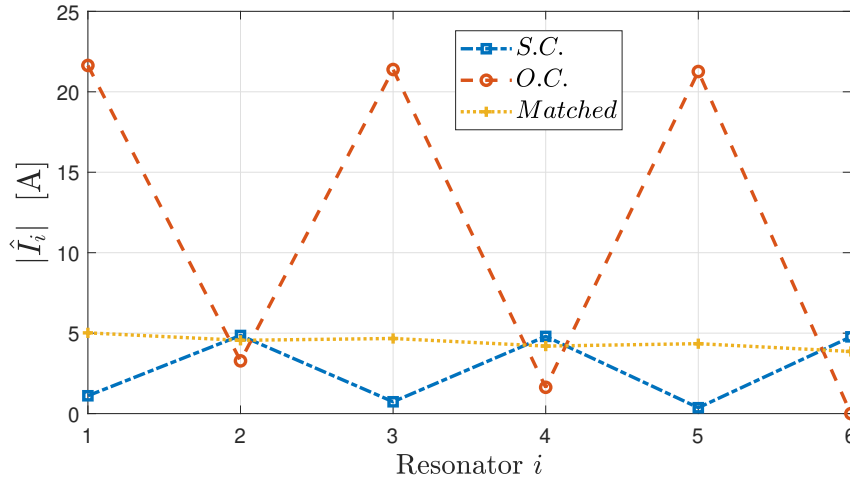


Figure 5.3: MI wave standing wave patterns for different termination loads.

is obtained with a perfect matching. This plot again confirms the effectiveness of the matching terminations in ensuring a uniform current distribution, with a  $\text{SWR} \approx 1$  for any  $n$ . The blue curve, which refers to SWR in SC terminated arrays, presents very large values when  $n$  is odd and lower values if  $n$  is even, as already noted for the array of 6 resonators in Fig. 5.3. For each of the three terminations considered, the SWR decreases as the number of line resonators increases. This testifies that the current wave attenuates much more as it passes through more resonators.

### 5.2.2 Lossless and low-loss array

According to the TL theory and with reference to an array composed of  $n$  resonators, the current maxima can occur in the resonators whose index  $i$  is

$$i = n - 2m, \quad (5.16)$$

where  $m = 0, 1, 2, \dots, m < n/2$ , is an integer number. This indicates that a current maximum always occurs in the last resonator of the array, regardless of the number of resonators. From (5.16) it follows that the current maxima are found in the even resonators for an array with an even number of cells, and in the odd resonators for an array with an odd number of cells.

The value of the MI SWR and thus the values of the maximum current magnitude can be obtained using (5.14). When the array has an even number of cells, the even resonators experience current maxima with amplitude defined as:  $|\hat{V}_s / (\hat{Z}_s + \hat{Z}_0)|$ , while the odd-resonators currents are null.

Instead, when the array is composed of an odd number of cells, the denominator of (5.14) becomes zero, compromising the convergence of the formula. However, its value can be evaluated as the limit when the number of resonators  $\xi$  approaches  $n$  as:

$$\hat{I}_i = \lim_{\xi \rightarrow n} \frac{\hat{V}_s}{\hat{Z}_s + \hat{Z}_0} \frac{e^{-\hat{\gamma}(i-1)d} - \hat{\rho}_T e^{-2\hat{\gamma}(\xi-1)d} e^{\hat{\gamma}(i-1)d}}{1 - \hat{\rho}_S \hat{\rho}_T e^{-2\hat{\gamma}(\xi-1)d}}. \quad (5.17)$$

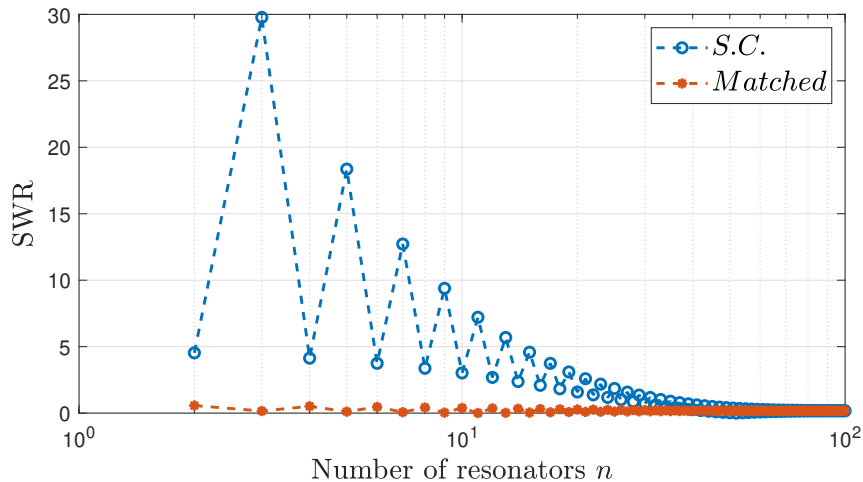


Figure 5.4: Standing wave ratio for arrays of different lengths and different termination conditions.

Performing the calculation for different values of  $i$ , it is found that the current magnitude in the odd resonators tends to the infinite, whereas  $|\hat{V}_s/(\hat{Z}_s + \hat{Z}_0)|$  in the even resonators.

These results are exact in lossless arrays with (ideal) resonators, even if they can be considered acceptable even in the case of resonators with low R and limited attenuation. Thus, for low-loss arrays, the amplitude and location of the current maxima do not vary much with respect to the case of a lossless array and the considerations here presented are still valid.

Concerning the lossless case, the presence of attenuation in the resonators leads to a slight reduction of the current maxima and a slight increase in the value of the currents in the odd resonators (which are no longer zero) in arrays with an even number of resonators, as testified by Fig. 5.3. In arrays with an odd number of resonators, the attenuation produces a significant reduction of the current maxima and the current magnitude in the even resonators decreases. Overall, the SWR is more pronounced as the MI waveguide becomes shorter, being the input energy spread among fewer resonators. Moreover, the values of the SWRs in Fig. 5.4 for a very large number of resonators equal the ones obtained with the matching terminations, net of the numerical error and the uncertainty on the parameters. This confirms the classic theory of the TLs, which states that the behaviour of the waves in matched or infinitely long TL is equivalent and no reflections occur at the termination.

### 5.3 Resonator array with a receiver

In this section, the modelling approach presented in Sec. 5.1 is extended for the configuration of a resonator array with a receiver presented in Sec. 4.2.4 and its equivalent circuit is reported in Fig. 5.5. The receiver resonator is here assumed

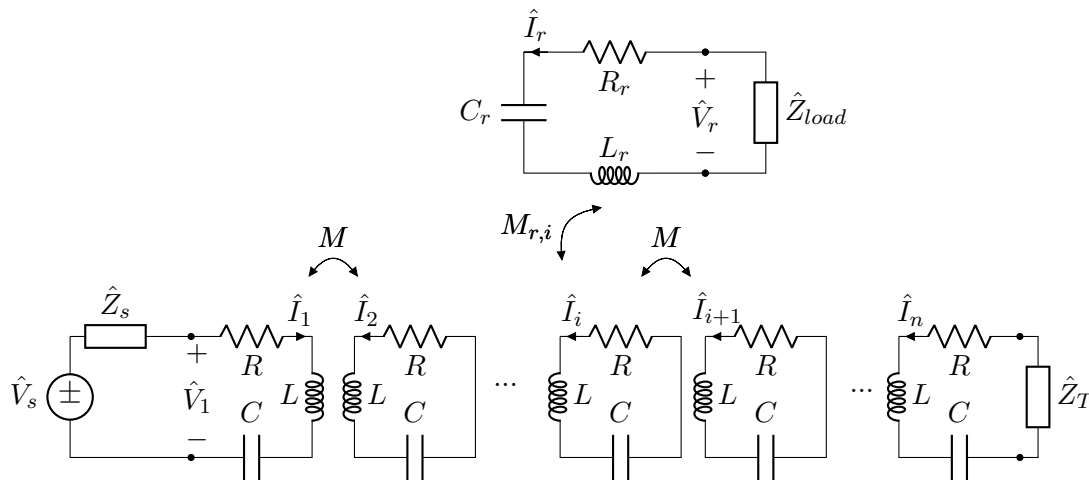


Figure 5.5: IPT system with a resonator array and a receiver over it.

identical to the array resonators, allowing the analysis to be simplified. However, this choice does not affect the generality of the analysis. The receiver is placed 10mm above the array and connected to a load  $\hat{Z}_{load}$ , as represented in Fig. 5.5. The last cell of the array is terminated in an additional impedance  $\hat{Z}_T$  that can assume arbitrary values. Unlike the previous section, in this case the analysis was conducted considering the receiver also in non-perfect alignment positions. This means that the receiving coil can be coupled to more resonators of the array and, in particular, at most with two, since it is identical to them. The mutual inductance  $M_{r,i}$  between the receiver circuit and the  $i$ th resonator of the array is now a continuous function of the receiver position. The receiver position is defined by the coordinate  $x$ , that points to the direction of the space in which the array lies and has its zero in correspondence of the first resonator. For  $x = 0$ , the receiver is perfectly aligned with the first cell. Being all the resonators identical, the mutual inductance as a function of the position  $x$  behaves as reported in Fig. 5.6 considering the receiver coupled to three different consecutive resonators. As can be seen, the mutual inductance between the receiver and a cell of the array is different from zero only for two consecutive resonators at a time.

The mutual inductance coefficients between the receiver and the array cells affect the circuit parameters and thus its dependence on the coordinate  $x$  makes all the circuit variables functions of  $x$ . For a complete analysis, different positions of the receiver have been considered.

### 5.3.1 Equivalent transmission line

The TL approach to the modelling of resonator arrays with a receiver is here discussed, whose definition allows interesting insights to be attained. Using chain

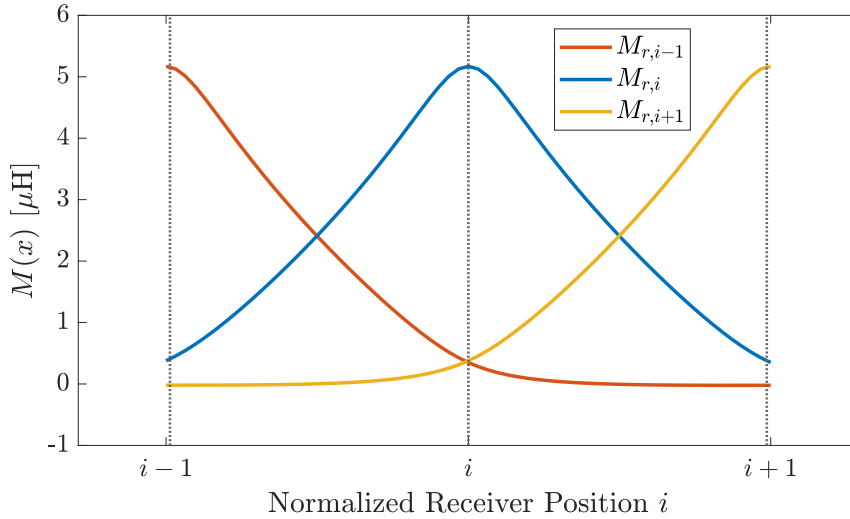


Figure 5.6: Mutual inductance between the receiver and three consecutive resonators of the array, as a function of the receiver position at a receiver height of  $10\text{mm}$ .

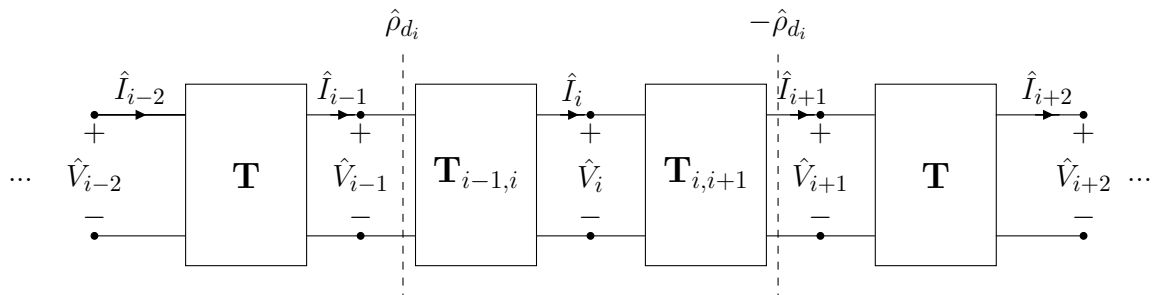


Figure 5.7: Section of the equivalent TL of a resonator array with a receiver coupled with the  $i$ th resonator.

matrices to represent inductive couplings between resonators, there are several possibilities for including the receiver. In general, it can be seen as a short line segment deriving from the main line, which is the array. In particular, it is equivalent to considering the receiver as a  $\lambda/4$  long TL segment. Similar considerations are reported in [65, 66]. Having as objective the study of the current distribution in the array, it is convenient to include the receiver in the chain matrices which represent the array resonators coupled to the receiver. In this way the information on the receiver current is lost but it is possible to trace the analysis back to that of a simple 1D waveguide, drawing useful information in an intuitive way.

### 5.3.2 Perfectly aligned receiver

In case the receiver couples to one resonator only, the receiver can be embedded into the equivalent circuit of the facing array resonator as the reflected impedance  $\hat{Z}_d$ .

In fact, according to [46, 126, 47], for a receiver coupled to the  $i$ th array cell, it is possible to write the KVL equation:

$$j\omega M\hat{I}_{i-1} + (\hat{Z} + \hat{Z}_{d_i})\hat{I}_i + j\omega M\hat{I}_{i+1} = 0 \quad (5.18)$$

where

$$\hat{Z}_{d_i} = \frac{(\omega M_{r,i}(x)|_{\max})^2}{\hat{Z}_r}. \quad (5.19)$$

The equivalent TL representing this system configuration can be obtained from that of the resonator array without a receiver considering the increased impedance  $\hat{Z} + \hat{Z}_{d_i}$  of the  $i$ th resonator. The transmission matrices  $\hat{\mathbf{T}}_{i-1,i}$  and  $\hat{\mathbf{T}}_{i,i+1}$  that involve the  $i$ th resonator modify consequently. In particular,  $\hat{Z}_i$  in (5.3) becomes  $\hat{Z}_i = (\hat{Z} + \hat{Z}_{d_i})/2$ , while the mutual impedance  $\hat{Z}_{M_{i,i+1}}$  is not altered. According to (5.6), also the characteristic impedance of that TL segments changes. Indeed, the modified transmission matrices  $\hat{\mathbf{T}}_{i-1,i}$  and  $\hat{\mathbf{T}}_{i,i+1}$  present a characteristic impedance  $\hat{Z}_{0_{i-1,i}} = \hat{Z}_{0_{i,i+1}} = \hat{Z}_{0_d} \neq \hat{Z}_0$ . This clearly corresponds to a discontinuity in the MI waveguide, leading to reflections of MI waves that come from the power source and the termination at the interfaces between the TL with different  $\hat{Z}_0$ . They are indicated with dashed vertical lines in Fig. 5.7. The reflection phenomenon can be quantified through the reflection coefficient at these interfaces. For forward MI waves travelling from the power source towards the termination (positive  $x$  direction), the reflection coefficient at the interface between the  $i-1$  and  $i$  cells is:

$$\hat{\rho}_{d_i} = \frac{\hat{Z}_{0_d} - \hat{Z}_0}{\hat{Z}_{0_d} + \hat{Z}_0}, \quad (5.20)$$

while it is  $-\hat{\rho}_{d_i}$  at the interface between the  $i$  and  $i+1$  cells. The reflection coefficients for backward MI waves (that travel in the negative  $x$  direction) at these interfaces are the opposite of the ones for forward MI waves. Reflections can be avoided by eliminating the discontinuities, that is by making sure that the characteristic impedance of the TL segments that include cells coupled to the receiver is equal to  $\hat{Z}_0$ . This possibility has been explored in [47]. Besides the trivial solution, the exact receiver matching for resonance operation is found enforcing:  $\hat{Z}_{load} = \hat{Z}_{load}^m$  where

$$\hat{Z}_{load}^m = \frac{\omega_0 M_{r,i}^2(x)|_{\max}}{M e^{-\alpha d}} - R. \quad (5.21)$$

This condition is very difficult to be met, since the receiver load is defined by the circuitry connected to it. Power electronics circuits that allow the control of the input impedance can be used to match the receiver to the MI waveguide.

### 5.3.3 Receiver coupled to two array resonators

When the receiver couples to two resonators, it can still be embedded in the array introducing a reflected impedance and a controlled voltage source in the facing

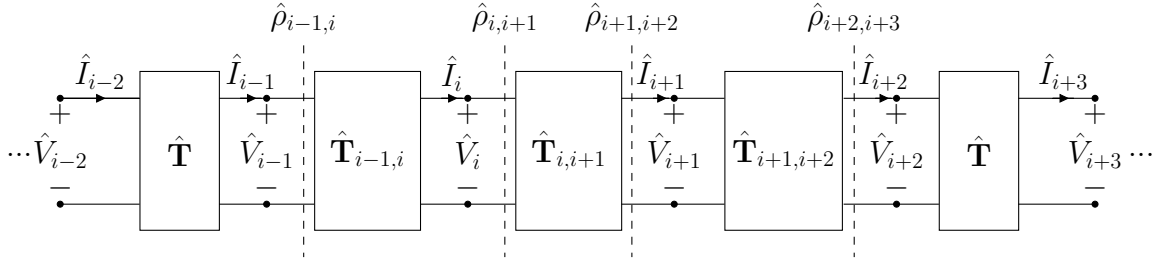


Figure 5.8: Section of the equivalent TL of a resonator array with a receiver coupled to the  $i$ th and  $(i+1)$ th resonators.

cells. This can be seen from the KVLs of these resonators, that must include a further coupling introduced by the receiver. In the case of perfect alignment, the contribution of the controlled voltage sources is negligible and the model is reduced to the one described in the previous section. Assuming the receiver couples to the  $i$ th and  $(i+1)$ th resonators, the impedances of the  $i$ th and  $(i+1)$ th resonators and the mutual impedances between the  $i$ th and  $(i+1)$ th resonators and the adjacent ones modify accordingly. In turn, also the associated transmission matrices  $\hat{\mathbf{T}}_{i-1,i}$ ,  $\hat{\mathbf{T}}_{i,i+1}$  and  $\hat{\mathbf{T}}_{i+1,i+2}$  change, resulting in the equivalent TL depicted in Fig. 5.8. The parameters of the chain matrices are derived from the KVL equations written for the receiver and the  $i$ th and  $(i+1)$ th array resonators:

$$j\omega M_{r,i}\hat{I}_i + j\omega M_{r,i+1}\hat{I}_{i+1} + \hat{Z}_r\hat{I}_r = 0 \quad (5.22)$$

$$j\omega M\hat{I}_{i-1} + \hat{Z}\hat{I}_i + j\omega M\hat{I}_{i+1} + j\omega M_{r,i}\hat{I}_r = 0 \quad (5.23)$$

$$j\omega M\hat{I}_i + \hat{Z}\hat{I}_{i+1} + j\omega M\hat{I}_{i+2} + j\omega M_{r,i+1}\hat{I}_r = 0 \quad (5.24)$$

Substituting  $\hat{I}_r$  from (5.22) in (5.23) and (5.24) it is possible to obtain:

$$j\omega M\hat{I}_{i-1} + \left(\hat{Z} + \hat{Z}_{d_i}(x)\right)\hat{I}_i + \left(j\omega M + \hat{Z}_{d_{i,i+1}}(x)\right)\hat{I}_{i+1} = 0 \quad (5.25)$$

and

$$\left(j\omega M + \hat{Z}_{d_{i,i+1}}(x)\right)\hat{I}_i + \left(\hat{Z} + \hat{Z}_{d_{i+1}}(x)\right)\hat{I}_{i+1} + j\omega M\hat{I}_{i+2} = 0 \quad (5.26)$$

with

$$\hat{Z}_{d_i}(x) = \omega^2 \frac{M_{r,i}(x)^2}{\hat{Z}_r} \quad (5.27)$$

$$\hat{Z}_{d_{i+1}}(x) = \omega^2 \frac{M_{r,i+1}(x)^2}{\hat{Z}_r} \quad (5.28)$$

$$\hat{Z}_{d_{i,i+1}}(x) = \omega^2 \frac{M_{r,i}(x)M_{r,i+1}(x)}{\hat{Z}_r} \quad (5.29)$$

The new terms of  $\hat{\mathbf{T}}_{i-1,i}$ ,  $\hat{\mathbf{T}}_{i,i+1}$  and  $\hat{\mathbf{T}}_{i+1,i+2}$  are found as in (5.3) considering:

$$\hat{Z}_i(x) = \frac{\hat{Z} + \hat{Z}_{d_i}(x)}{2} \quad (5.30)$$

$$\hat{Z}_{i+1}(x) = \frac{\hat{Z} + \hat{Z}_{d_{i+1}}(x)}{2} \quad (5.31)$$

and

$$\hat{Z}_{M_{i,i+1}}(x) = \hat{Z}_{M_{i+1,1}}(x) = j\omega M + \hat{Z}_{d_{i,i+1}}(x). \quad (5.32)$$

The characteristic impedances of the TL segments are found from (5.3) and (5.6) and it is not real anymore, being the mutual impedance not purely imaginary. Moreover, they are different for each line segment that involves resonators coupled to the receiver and, being the mutual inductances  $M_{r,i}$  and  $M_{r,i+1}$  continuous function of the coordinate  $x$ , also dependent on the receiver position. In general,  $\hat{Z}_{0_{i-1,i}}(x) \neq \hat{Z}_{0_{i,i+1}}(x) \neq \hat{Z}_{0_{i+1,i+2}}(x) \neq \hat{Z}_0$ . In this condition, further reflections of MI waves travelling in the waveguide inevitably occur, that can be estimated through the reflection coefficients at the interfaces. These parameters are complex, and for forward MI waves can be generally defined as:

$$\hat{\rho}_{i,i+1}(x) = \frac{\hat{Z}_{0_{i,i+1}}(x) - \hat{Z}_{0_{i-1,i}}(x)}{\hat{Z}_{0_{i,i+1}}(x) + \hat{Z}_{0_{i-1,i}}(x)}. \quad (5.33)$$

They are shown in Fig. 5.8 in correspondence of the dashed lines to indicate the port at which they are calculated. The opposite value should be considered for backward MI waves. Overall, the equivalent TL can be considered as the cascade of three TL segments: the first comprising the resonators from the first to the  $(i-1)$ th, the second composed of the resonators coupled to the receiver (two-port networks represented by  $\hat{\mathbf{T}}_{i-1,i}$ ,  $\hat{\mathbf{T}}_{i,i+1}$  and  $\hat{\mathbf{T}}_{i+1,i+2}$ ) and the third comprising the resonators from the  $(i+2)$ th to the last one. In particular, the first and third segments of the TL result to be longer or shorter depending on the receiver position.

### 5.3.4 Numerical Simulations

The presented TL model has been applied considering the resonator array prototype presented in Chapter 4 tuned as described in Sec. 5.2.1. As already mentioned, the receiver coil is equal to the array cell ones. The mutual inductance coefficients between the receiver and the resonators of the array were calculated considering a space discretisation step of  $\Delta x = d/30$ .

The simulations have been performed considering SC, OC and matched terminations and different load resistance values. In particular, as described in Sec. 5.1 and, equivalently in Sec. 4.1.5, a matching load that allows the maximisation of the efficiency of the receiver TL segment can be found. For perfect alignment positions of the receiver the value can be found as in (5.6). In this condition, the mutual inductance  $M_{r,i}$  is 5.3  $\mu\text{H}$  and the optimal receiver load is  $\hat{Z}_{load,opt} = \omega M_{r,i} \approx 5\Omega$ . When

the receiver couples to more cells, the situation becomes more complex but the value can still be found from (5.3) and (5.6) considering the proper mutual inductance values. Assuming  $\hat{Z}_{load,opt}$  as reference receiver load, other two values  $\hat{Z}_{load,L} \ll \hat{Z}_{load,opt}$  and  $\hat{Z}_{load,H} \gg \hat{Z}_{load,opt}$  have been chosen to simulate low- and high-impedance conditions, respectively, and are  $\hat{Z}_{load,L} = 0.7\Omega$  and  $\hat{Z}_{load,H} = 15\Omega$ . Moreover, the load  $\hat{Z}_{load} = 15\Omega$  theoretically guarantees the matching of the receiver to the array and is calculated by (5.21). To understand the combined influence of terminations and load on resonator currents, the current distribution for a certain termination is analysed considering different loads. The termination impedance of the array  $\hat{Z}_T$ , which is the unique degree of freedom during the operation, can be adjusted to maximise the efficiency and the power transfer, as discussed in Chapter 4. In particular, to avoid the abrupt variations of the equivalent two-port parameters experienced with SC or OC terminations, it seems convenient to set  $\hat{Z}_T = \hat{Z}_0$ , i.e., matching only the array. In this way, the amount of power that is transferred in the TL segment after the discontinuity introduced by the receiver (terminal array segment) does not undergo reflections and is completely absorbed by the termination impedance. However, the presence of the receiver produces a discontinuity in the impedance of the line which inevitably leads to reflections, resulting in a standing wave pattern in the TL segment upward of the receiver. The current magnitudes of the resonators are reported in Fig. 5.9 as a function of the receiver position for the different values of load resistance, showing that severe current peaks occur in the odd-numbered resonators when the receiver is perfectly aligned with even-numbered resonators. The standing wave pattern in the array can be better visualised by plotting the resonator current magnitudes for positions of perfect alignment only, since they lead to the highest currents. These plots are reported in Fig. 5.10 considering the different loads  $\hat{Z}_{load,L}$ ,  $\hat{Z}_{load,opt}$  and  $\hat{Z}_{load,H}$ . As expected, no standing waves occur for the segment of the TL downstream of the resonator covered by the receiver, with the overt case when the receiver is coupled to the first resonator of the array. The reflections caused by the impedance discontinuity are more evident when the receiver is close to the power source, since this situation corresponds to the shortest equivalent TL, confirming the results of Sec. 5.2.1 and observed in Fig. 5.4.

When considering SC and OC terminations similar standing wave patterns are found. As anticipated in Chapter 4, the power and efficiency curves suggested the possibility of reflections of the currents in the array. When considering SC or OC terminations, the MI wave undergoes reflections both at the interface of the TL segments involving the receiver and at the end of the line, leading to standing wave patterns in the array segments upstream and downstream of the receiver. For a meaningful comparison of the array behaviour, the effect of all three terminations (i.e. SC, OC and matching) is considered for each one of the three load conditions considered. The magnitude of the resonator currents as a function of the receiver position is shown in Figs. 5.11, 5.13 and 5.15 for the receiver loads  $\hat{Z}_{load,L}$ ,  $\hat{Z}_{load,opt}$  and  $\hat{Z}_{load,H}$ , respectively. The standing wave patterns for positions of perfect alignment are plotted in Figs. 5.12, 5.14 and 5.16 considering the loads  $\hat{Z}_{load,L}$ ,  $\hat{Z}_{load,opt}$  and  $\hat{Z}_{load,H}$ , respectively. The plots

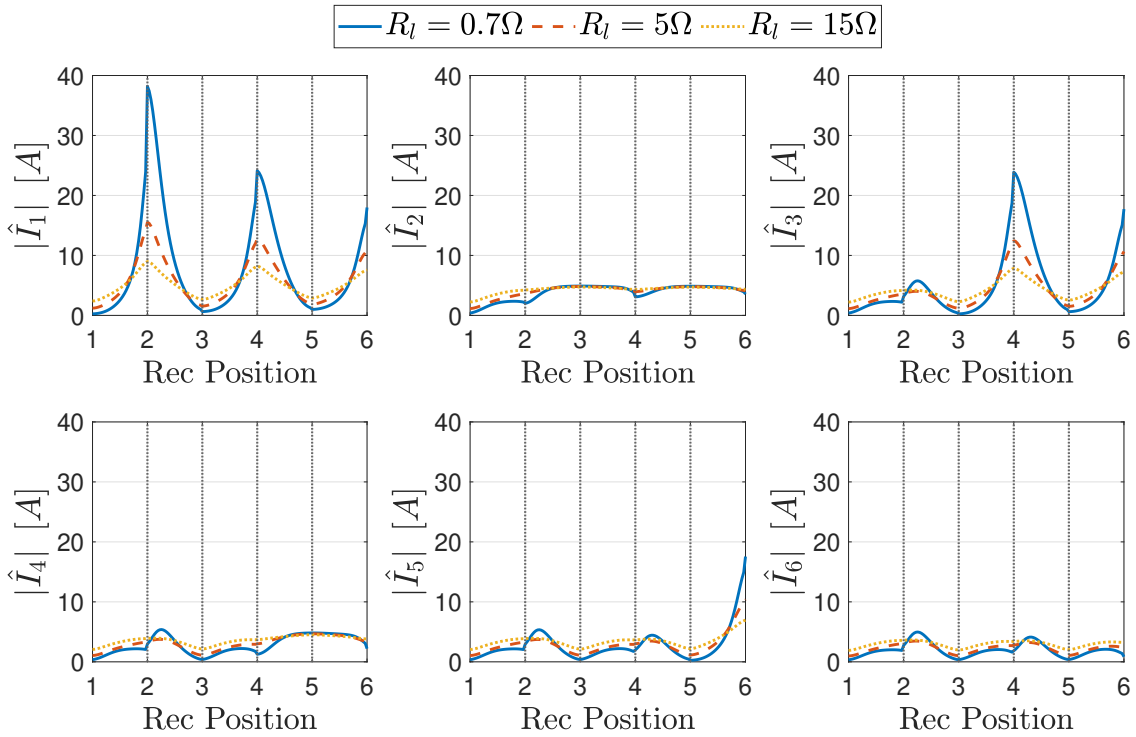


Figure 5.9: Current magnitude of each resonator as a function of the receiver position, for a matched array and different load resistances.

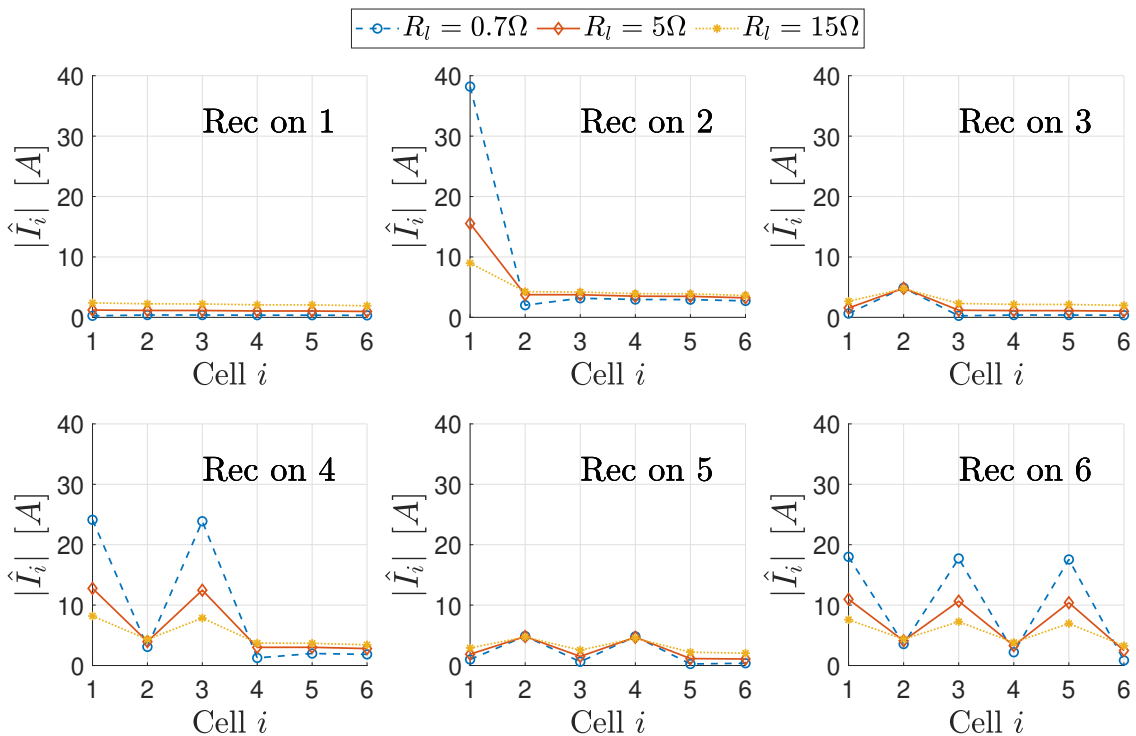


Figure 5.10: Standing wave patterns for different positions of the perfectly aligned receiver, a matched array and different load resistances.

highlight that the resonators covered by the receiver experience low current values, whereas the most severe peaks occur when the receiver covers the even resonators. Analysing the worst scenarios, it is possible to state that the receiver load  $\hat{Z}_{load}$  affects the amplitude of the current peaks, whereas their position is determined by the length and the boundary conditions of the equivalent TL (input and termination impedances). Considering resistive loads, the reflected impedance from the receiver  $\hat{Z}_{d_i}$  is real and then the phase shift experienced by the MI waves along the line is not altered, despite further reflections occur. The resulting standing wave pattern can be explained considering the defect impedance introduced by the receiver and the length of the TL segments upstream and downstream of the discontinuity.

**Case  $\hat{Z}_{load} = 0.7\Omega$**  For low values of  $\hat{Z}_{load}$  ( $|\hat{Z}_{load}| < |\hat{Z}_{load}^m|$ ), the receiver reflected impedance presents very high values and the array resonator covered by the receiver behaves as if it is open. For a receiver perfectly aligned with the  $i$ th resonator, the upstream TL segment is formed by  $i-1$  resonators and is terminated in SC, while the downstream one is composed of  $n-i$  cells and is terminated in  $\hat{Z}_T$ . Thus, according to Sec. 5.2.1 (see Fig. 5.4), the upstream SWR has higher values if  $i$  is even (since the  $i$ th cell is in OC), while the downstream segment experiences higher SWR values if:

- $n-i$  is odd with SC termination
- $n-i$  is even with OC termination.

This can be appreciated in Fig. 5.12. In the case the receiver couples to two resonators  $i$  and  $i+1$ , similar considerations hold, being the upstream TL segment composed of  $i-1$  cells and the downstream one of  $n-(i+1)$  cells. Overall, the current behaviour in the two line segments varies according to the receiver position, which determines their effective length and terminations, as it is shown in Fig. 5.11. It is interesting to notice that, when the receiver is aligned with an odd-numbered cell in the array, the SWRs of the TL segments are much lower than those for a receiver aligned with even-numbered resonators. In fact, being  $n$  even, the alignment with odd cells leads to upstream TL segments with an even number of resonators terminated in SC. Globally, for these cases, the power required at the source is limited. An exception is observed in the array current distribution of the downstream TL segment for SC and matched terminations. In these conditions, the even cells experience current peaks when the receiver is placed between an even and an odd cell. This may be explained considering that both upstream and downstream TL segments are composed of an odd number of cells and thus their SWRs have higher values, as discussed in Sec. 5.2.1.

**Case  $\hat{Z}_{load} = 5\Omega$**  If the receiver load increases, its reflected impedance decreases, thereby limiting the influence of the receiver on the coupled array resonators. As is it possible to see from Figs. 5.13 and 5.14, the trends of the currents and the SWRs are

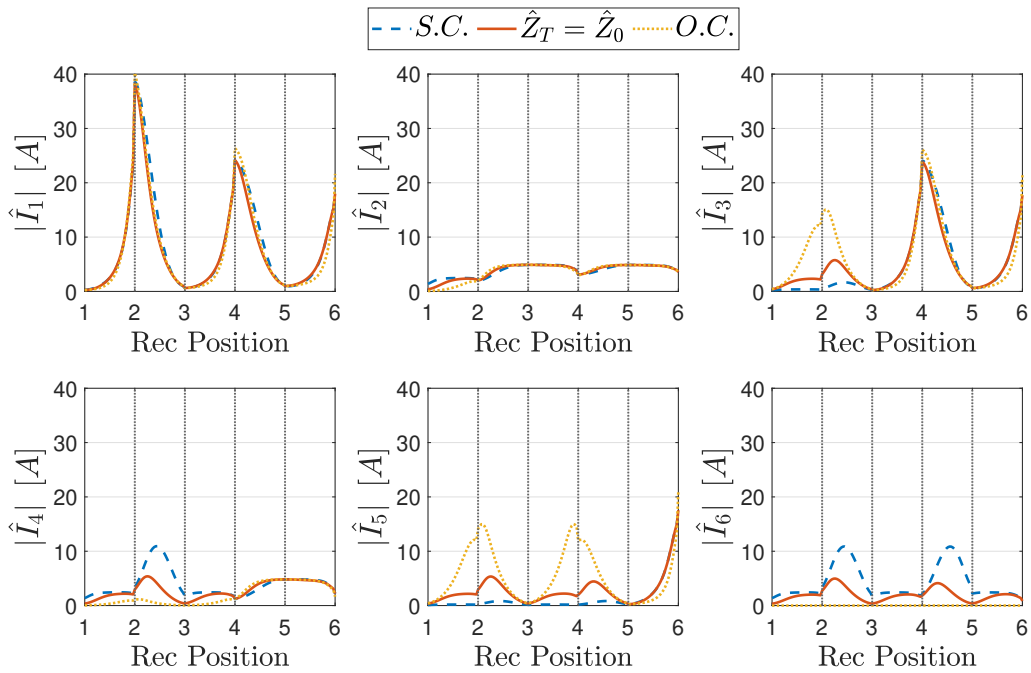


Figure 5.11: Magnitude of the currents of the array resonators as a function of the receiver position, for different terminations and a receiver load  $\hat{Z}_{load} = 0.7\Omega$ .

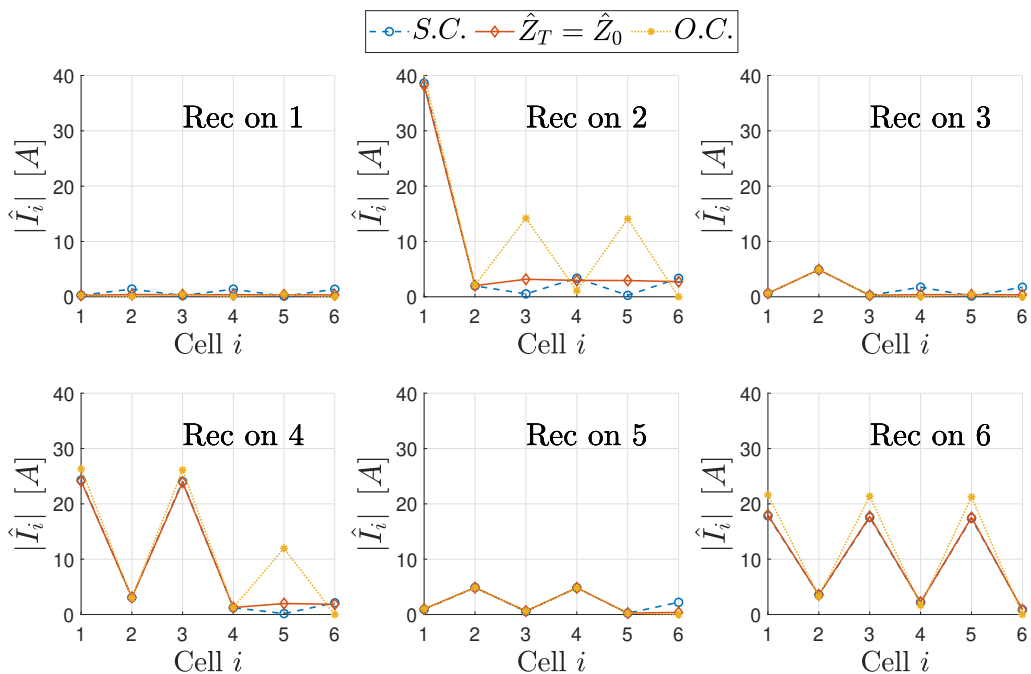


Figure 5.12: Standing wave patterns for different positions of the receiver, different terminations and a receiver load  $\hat{Z}_{load} = 0.7\Omega$ .

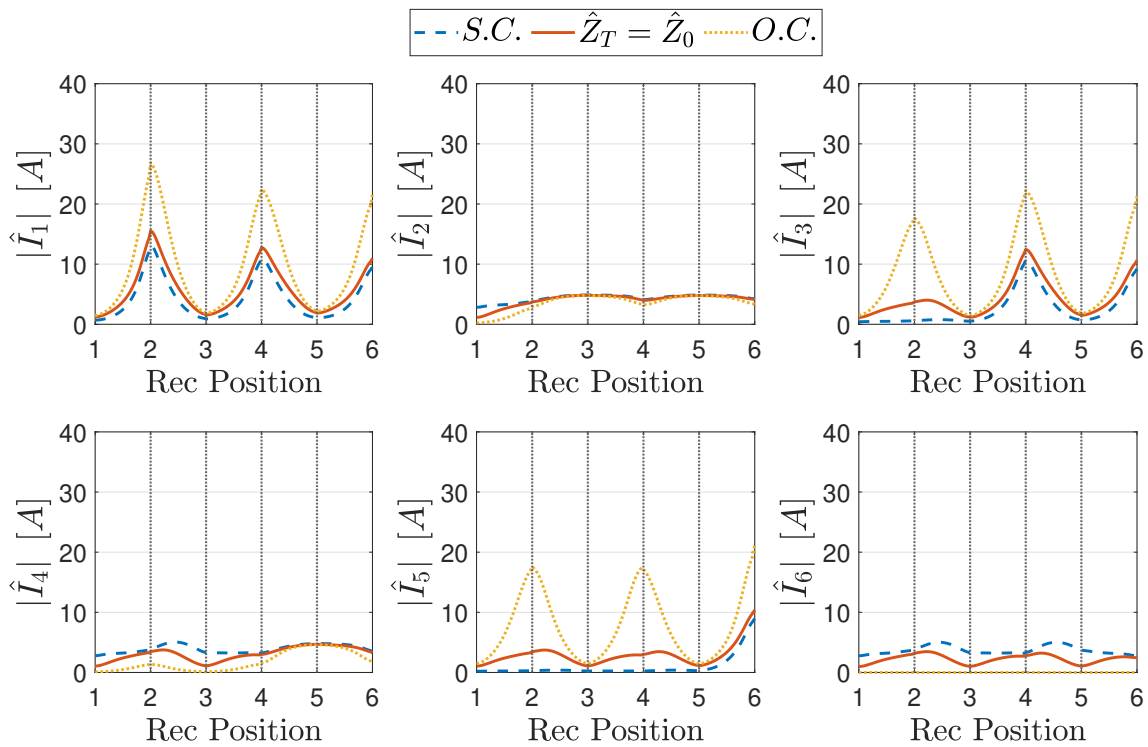


Figure 5.13: Magnitude of the currents of the array resonators as a function of the receiver position, for different terminations and a receiver load  $\hat{Z}_{load} = 5\Omega$ .

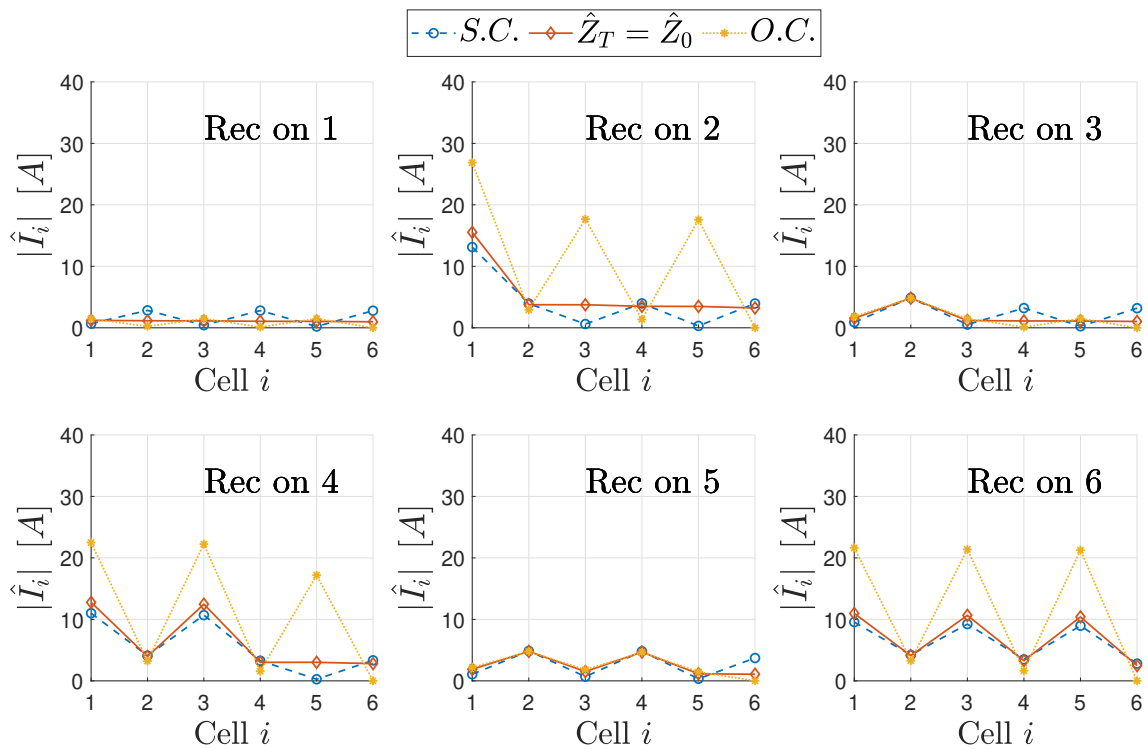


Figure 5.14: Standing wave patterns for different positions of the receiver, different terminations and a receiver load  $\hat{Z}_{load} = 5\Omega$ .

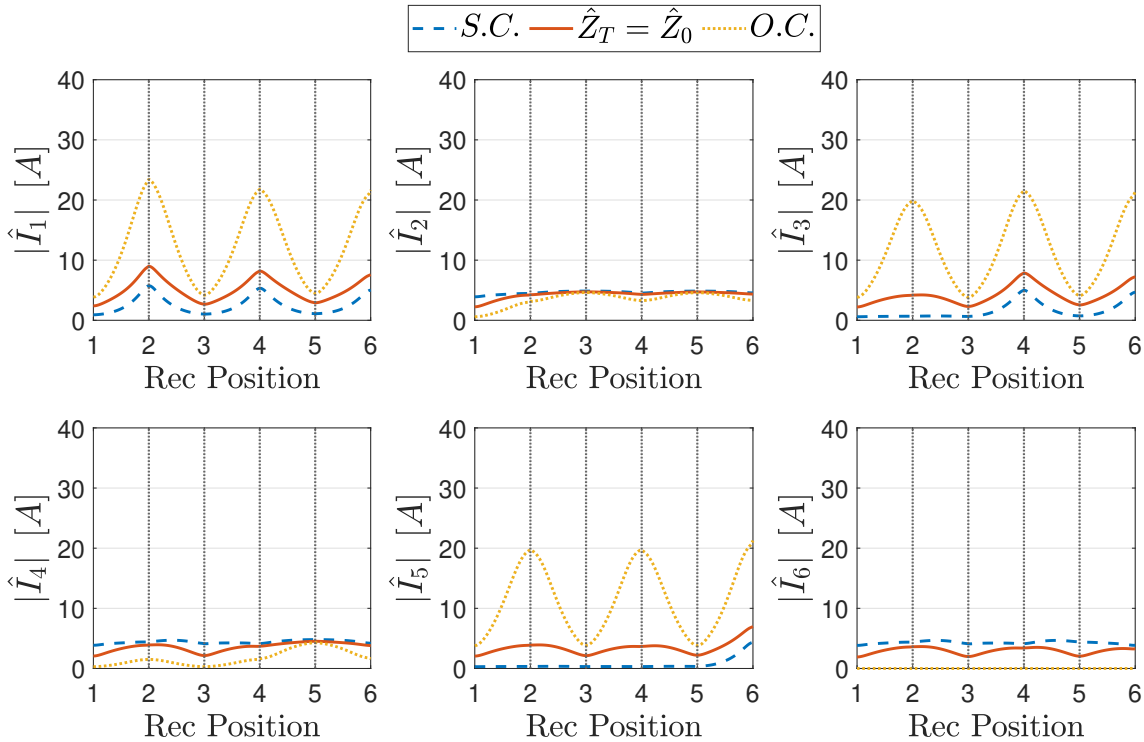


Figure 5.15: Magnitude of the currents of the array resonators as a function of the receiver position, for different terminations and a receiver load  $\hat{Z}_{load} = 15\Omega$ .

similar to those of the previous case but with currents of smaller magnitude. Indeed, the magnitude of the reflection coefficient is lower, being the reflected impedance introduced by the receiver smaller.

**Case  $\hat{Z}_{load} = 15\Omega$**  The last case considered concerns the load  $\hat{Z}_{load} = 15\Omega$ , which guarantees the matching of the receiver TL segment for perfect alignment positions obtained according to (5.21). The upstream equivalent TL segment is matched when the impedance  $\hat{Z}_i$  of the resonator facing the receiver is  $\hat{Z}_0$  ( $\hat{\rho}_{d_i} = 0$ ). In general,  $\hat{Z}_i = \hat{Z} + \hat{Z}_{d_i} + \hat{Z}_{TL,down}$ , where  $\hat{Z}_{TL,down}$  is the reflected impedance of the downstream TL segment to the  $i$ th resonator, whose value varies between zero and infinity depending on its length and termination, as shown in [126]. For a low-loss array  $\hat{Z}_i \approx \hat{Z}_{d_i} + \hat{Z}_{TL,down}$  and thus, considering the receiver matched,  $\hat{Z}_i \approx \hat{Z}_0$  only if  $\hat{Z}_{TL,down} \approx 0$ , namely only if:

- the downstream TL segment is composed of an even number of resonators and is terminated in SC;
- the downstream TL segment is composed of an odd number of resonators and is terminated in OC

This can be appreciated from Fig. 5.16, which illustrates the standing wave patterns in case of different array terminations. A matched upstream TL segment makes the

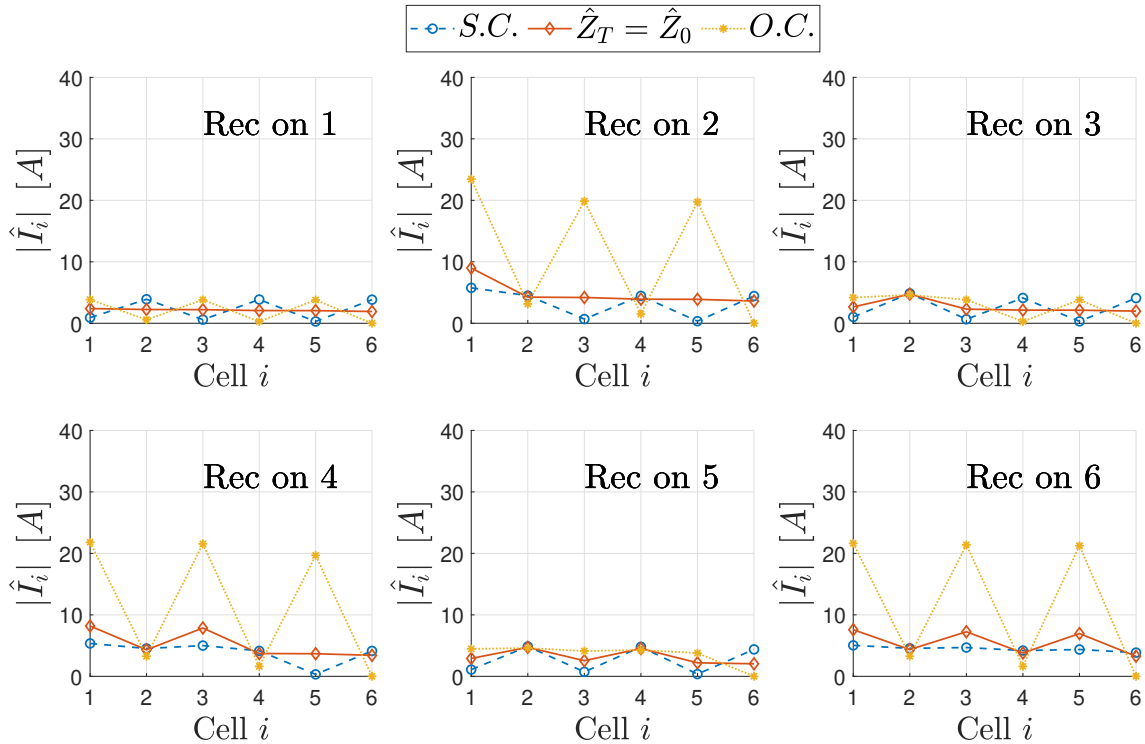


Figure 5.16: Standing wave patterns for different positions of the receiver, different terminations and a receiver load  $\hat{Z}_{load} = 15\Omega$ .

upstream resonator currents all equal. Instead, Fig. 5.15 indicates that for generic receiver positions current peaks (and in turn standing wave pattern) still occur for an array with an odd number of resonators. This increases the components thermal stress and may potentially lead to a breakdown of the whole apparatus.

## 5.4 Experimental verification

The numerical results were experimentally verified using the array prototype already described in Sec. 5.2.1 in the case of perfect termination match and a load of  $5\Omega$ . The input voltage is established with an H-bridge inverter and set to  $3.6V_{rms}$ . As already anticipated, the inverter employs GaN transistors, resulting in an internal impedance  $\hat{Z}_S = 0.01\Omega$ . In particular, it is an H-bridge inverter with four GaN MOSFET, driven by a Texas Instruments TMS320F28379D Launchpad DSP. The setup is shown in Fig. 5.18. The currents have been measured by means of a current probe Tektronix TCP302 amplified by a Tektronix "TCPA 300" and processed through an Agilent "Infiniium" 54855A oscilloscope with a sampling capability of 2 GSa/s and a bandwidth of 500 MHz. The results of the measurements are reported and are compared with the numerical predictions in Fig. 5.17. As expected, the measurement reveals the presence of standing wave patterns for the MI wave (current wave), with the highest values in correspondence to the positions of perfect alignment of the receiver with even resonators. The results of the measurements

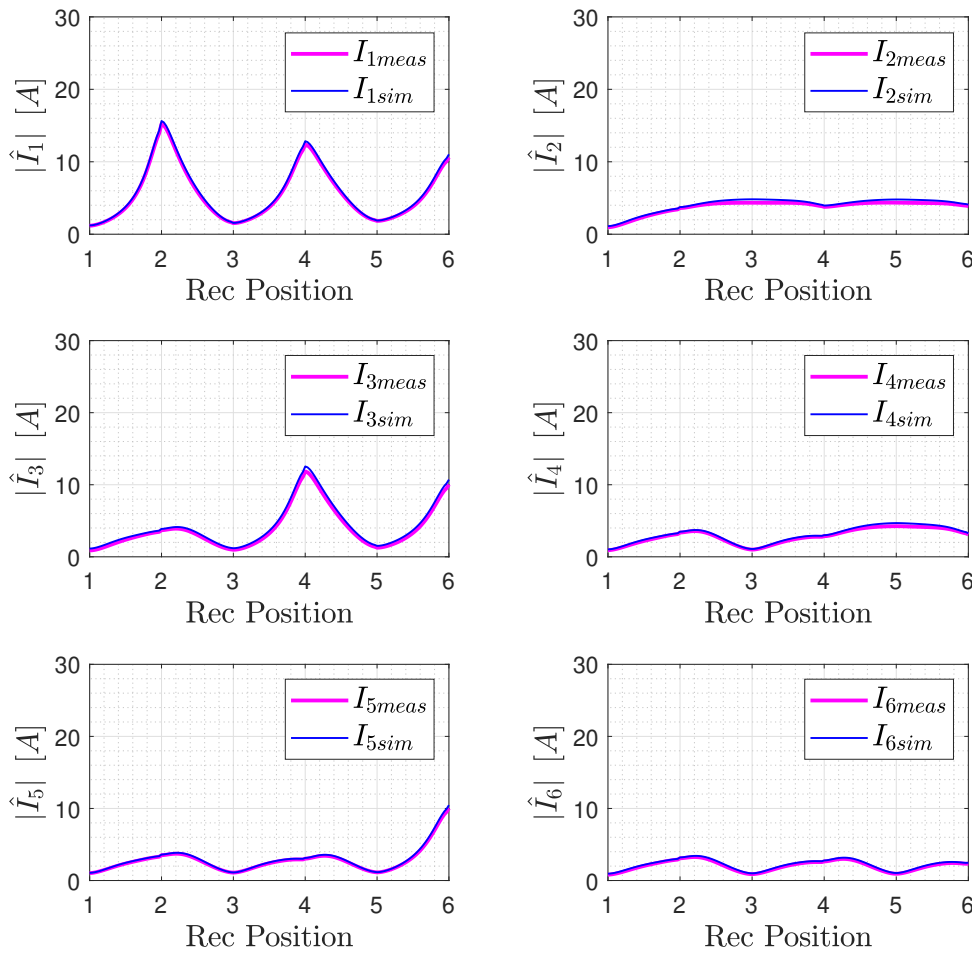


Figure 5.17: Comparison between the numerical and experimental values of the resonator current magnitude for different receiver positions in the case of  $\hat{Z}_T = 1.5\Omega$  and  $\hat{Z}_{load} = 5\Omega$ .

prove to be in perfect agreement with the numerical predictions, with a maximum error of 3.5 % in correspondence with the major current peaks.

## 5.5 Magnetic Near-Field of the Resonator Array with a Receiver

One of the main problems of IPT systems concerns the magnetic field they produce and its dangerous effect on objects and human beings present in the environment surrounding the device. In fact, since the magnetic field generated by these devices varies over time, it induces eddy currents in conducting objects, causing electromagnetic interference that can lead to the malfunction of the objects them-

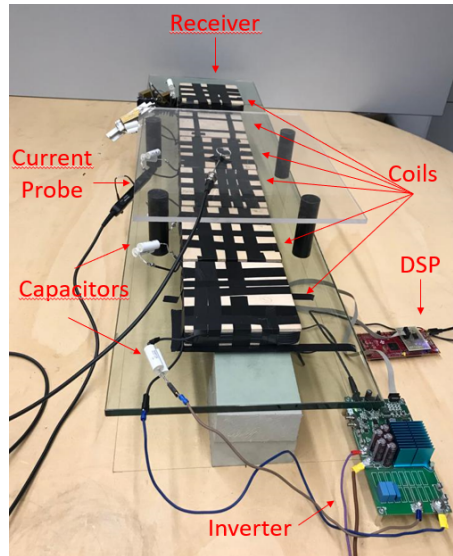


Figure 5.18: Experimental setup for the magnetic field measurements.

selves. Furthermore, even human tissues can experience induced currents, due to their non-zero electrical conductivity and this can lead to physiological problems [23, 24]. Most of the magnetic field analyses produced by IPT devices have been performed considering traditional two-coil systems, even for specific automotive applications [23, 127, 3]. The shielding of low-frequency magnetic fields has become an increasingly important issue, which concerns IPT devices of all kinds, from those for automotive applications to even those for consumer electronics. In this frame, resonator arrays appear as complex multicoil systems, which require efficient shielding to be used safely and to be in compliance with international standards. In the design phase of the shield, it is important to consider its effect on the system, which can lead to power losses and therefore to a decrease in efficiency. The screens are designed on the basis of the magnetic field they must attenuate, which, especially in the near-field, depends on the intensity and distribution of the system currents. As discussed in the previous sections, the resonators of the array can experience even very high currents due to the presence of the receiver. According to the operating conditions and the position of the receiver, the distribution of currents in the cells of the array changes considerably and, consequently, also the magnetic field it generates. Considering the resonator array used in the Chapters 4 and 5, an evaluation of the generated magnetic field was carried out considering a matched array with the matched receiver perfectly aligned with the last cell. The matching loads have been chosen to guarantee the reproducibility of the results also considering arrays with different coils and parameters. Note that this is also the condition chosen for the verification of the equivalent TL model proposed in Sec. 5.4 and the currents measured experimentally have been considered for the calculation of the magnetic field. In particular, the array is tuned to operate at 147kHz and powered by a voltage of 3.6 V, as in the case of Secs. 5.3.4 and 5.4. The overall magnetic field distribution

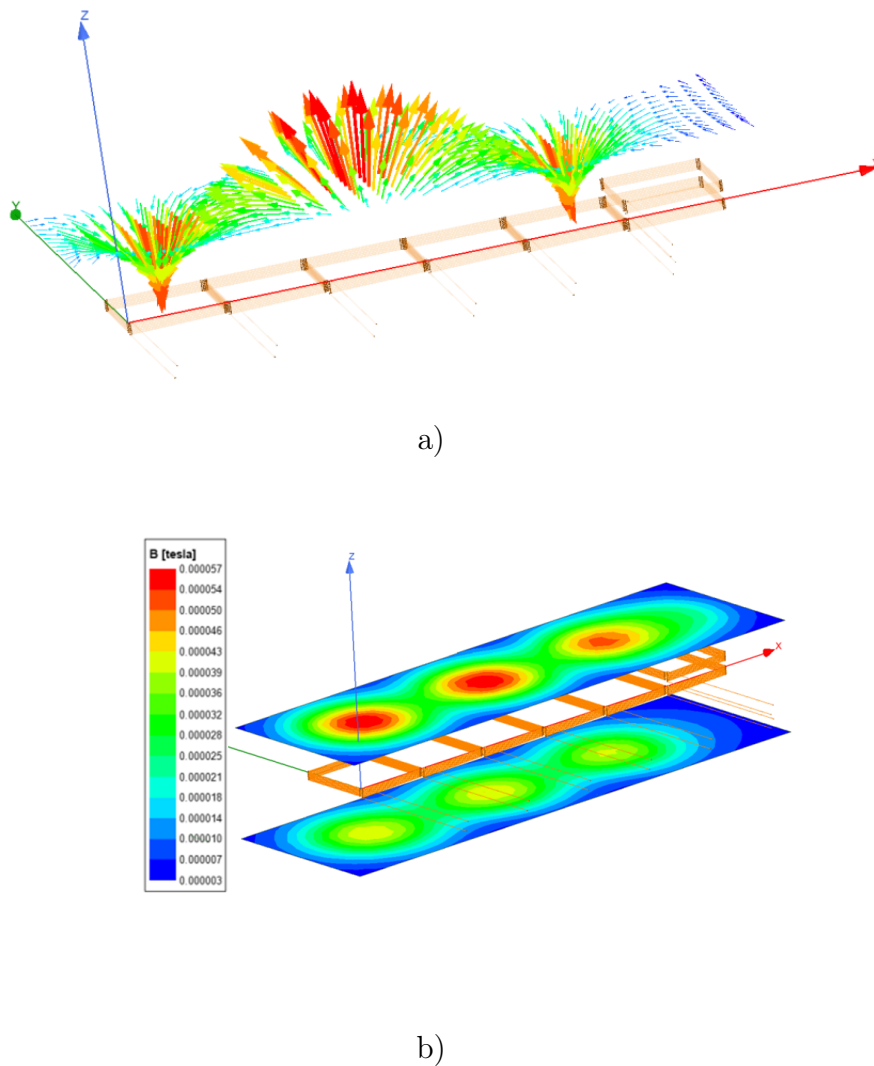


Figure 5.19: FEM calculated magnetic flux density on a plane 9.6cm above the array in (a) vector representation (b) magnitude.

is the result of the interaction of all the magnetic fields generated by each array cell and it has been evaluated by means of FEM simulations and by using closed-form expressions for the magnetic field generated by square coil [128]. Specifically, the magnetic field has been calculated on planes parallel to the array at a distance of 9.6 cm above and 12.5 cm below it. Indeed, being the considered system devoted to the supply of portable electronic devices, the more susceptible area to the magnetic field is the one in which people operate, i.e., right above the devices. The FEM results are affected by a 0.2% of final error and the mesh has been driven by an automatic adaptative procedure. The magnetic flux density vectors evaluated on the plane above the array are plotted in Fig. 5.19a for a fixed instant of time. As expected, the field is more intense in resonators with higher current, i.e. the odd-numbered ones (see. Fig. 5.19a). The direction of the vectors of the magnetic field generated

by the single coil depends on the phase of the current circulating in the coil itself and, considering that in the even cells the amplitude of the current is almost zero, the final distribution of the magnetic field will be determined by the currents in the odd resonators. For different instants of time the currents have different values and therefore the distribution of the field varies. As time varies, the resulting effect is that of a magnetic field standing wave in the direction of the space along which the array lies ( $x$  in this case), whose nodes are at a distance of  $2d$ , as predicted in Sec. 5.2. To evaluate the intensity of the field that stresses the shield, the intensity of the magnetic field is plotted for the upper plane in Fig. 5.19b. Being calculated for the same instant of time, this spatial field distribution corresponds to that of Fig. 5.19a. The maximum value is  $56\mu\text{T}$  on the plane above the array and  $42\mu\text{T}$  on the plane below it.

These results have been experimentally validated through measurements on the real prototype described in Sec. 5.4. In particular, the magnetic field has been estimated from the voltage induced on a circular probe of 2.8 cm in diameter, driven by a Hewlett-Packard 8591E spectrum analyser. Since the probe is much smaller than the current source loops (array coils), the magnetic flux density can be considered uniform across its surface. The average value of the normal component  $B_p$  of the magnetic field that links to the probe can be estimated as:

$$B_p = \frac{V_p}{\omega_0 A_p} \quad (5.34)$$

where  $V_p$  is the voltage induced in the probe,  $A_p$  its the probe area and  $\omega_0$  the frequency of the array currents. The measurements have been performed with the probe placed at the vertical distance of 9.6 cm above and 12.5 cm below the array in correspondence with the centre of the coils. In terms of the overall magnetic field, the resonator array with a receiver in the last cell results to be the worst condition since all the coils contribute, experiencing non-negligible current magnitudes (see Fig. 5.17). Indeed, even if the current peaks are stronger when the receiver is aligned with the first cell, the other array resonators do not experience considerable currents. In Figs. 5.20a and 5.20b the measured, FEM simulated and analytically calculated magnetic field at the centre of each array resonator is reported for the plane above and below the array, respectively.

The comparison clearly shows a very good agreement for the highest values of the magnetic flux density, whereas a mismatch between measurements and FEM simulations of about 10% occurs in the resonators with the lowest values of current. The difference between the measures and calculations can be attributed to the hypothesis of considering the magnetic flux density uniform over the entire probe area. In fact, it is reasonable to state that the higher the field, the greater its uniformity over the resonator. The results of the analytical calculations match the measured values for almost all the cells, and instead present an error of a few per cent in correspondence of the fourth cell. It should also be noted that, since the calculation methods are in any case approximate (even the analytical formulas are obtained with simplifications), an (even small) error is foreseeable.

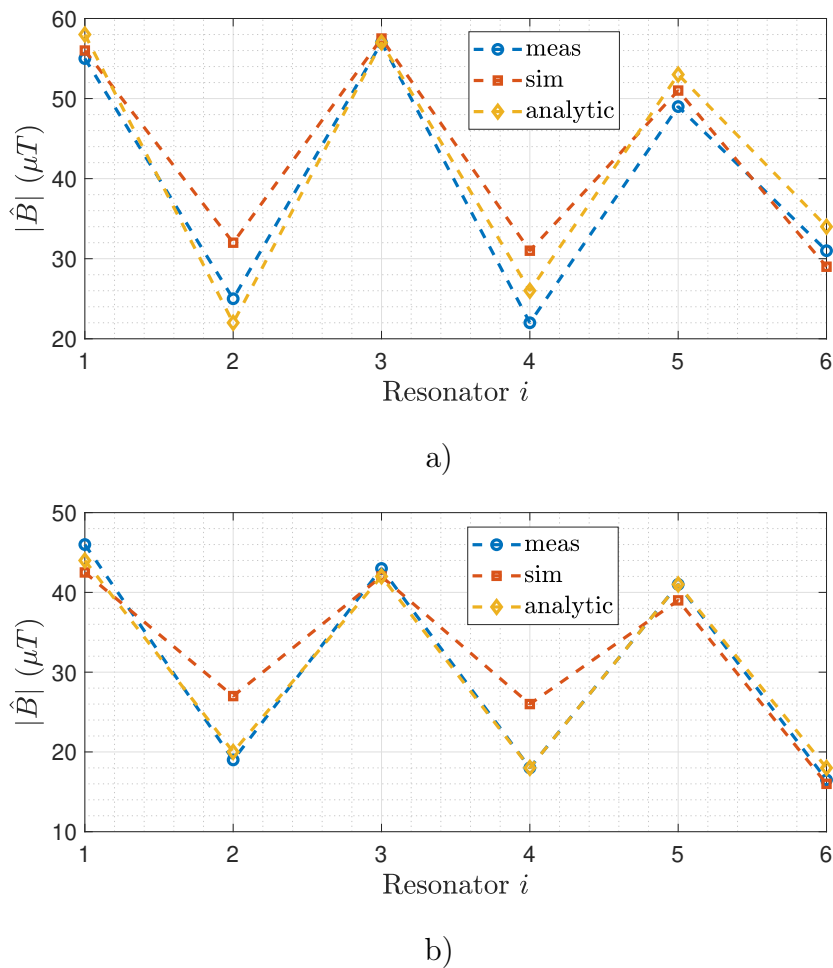


Figure 5.20: Comparison between magnetic flux density values obtained from measurements, FEM simulations and analytical calculation at the centre of the array resonators on a plane placed (a) 9.6 cm above and (b) 12.5 cm below the array.

### 5.5.1 Shielding the IPT System

Given the field that these IPT systems have been shown to produce, it is interesting to evaluate the possibility of shielding them, first of all considering traditional passive shields. A partial shielding of the magnetic field (at least for the legs of an individual sitting at the desk or table) can be obtained by introducing a planar shield below the array.

The shielding effectiveness of a planar shield can be calculated as described in [129] and [130]. Indeed, [130] specifically refers to the shielding effectiveness of multilayered magnetic shields generated by coaxial circular loops. However, the array is composed of square loops, and thus it is necessary to consider circular loops that, in terms of magnetic flux density, are equivalent to the square ones. According to [128], the radius of the circular loop equivalent to the square one is calculated enforcing that the magnetic flux density produced at a generic point of coordinate

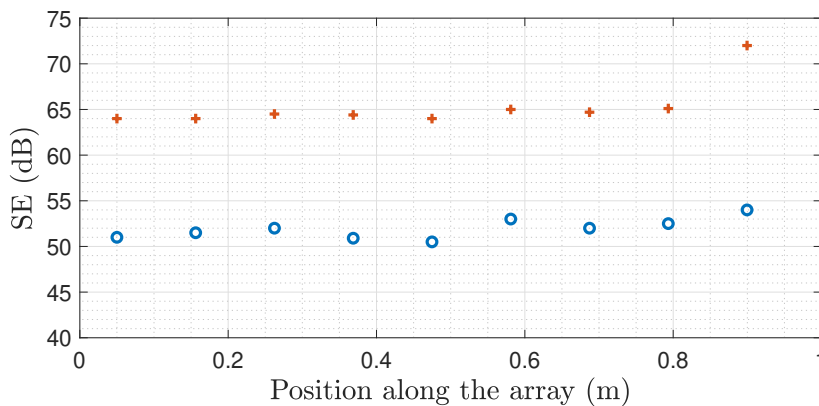


Figure 5.21: Shielding effectiveness of a single-layer aluminium planar shield and two-layer aluminum-Mumetal<sup>®</sup> registered planar shield

$z$  along the axis of the loop when both loops carry the same current is the same. The radius  $r_{eq}$  of the equivalent loop is found numerically solving:

$$\frac{r_{eq}^2}{(r_{eq}^2 + z^2)^{3/2}} - \frac{s^2}{\pi \left( z^2 + \left( \frac{s}{2} \right)^2 \right)^{3/2}} = 0 \quad (5.35)$$

where  $s$  is the square loop side-length. Applying the procedure proposed in [130], the shielding effectiveness (SE) of a single-layer aluminium shield and a two-layer shield with aluminium and Mumetal<sup>®</sup> are shown in Figs. 5.21, respectively. The SE is calculated considering the shield placed on the bottom of the array. Among the commercial thicknesses for shielding material, the aluminium layer is considered 0.28 mm thick, whereas the Mumetal<sup>®</sup> with a thickness of 0.05 mm. The resulting SE is plotted in Fig. 5.21. For the single-layer shield, it resulted in an average value of about 51 dB, whereas the average SE for the two-layer aluminum-Mumetal<sup>®</sup> shield is about 64 dB. As expected, the multilayer screen is more effective in shielding the array magnetic flux density, which, however, is more expensive. It is also important to underline that the presence of the shield always deteriorates the performances, since it introduces further losses due to its non-null conductivity.

## 5.6 Conclusions

The current distribution in the array of resonators has been analysed with the theory of MI waves. As in the previous chapter, it emerged that, for generic loads, reflections of the input power could occur. Resonator arrays have been studied as transmission lines, expressing them as a cascade of chain matrices. This approach allows the system behaviour to be analytically investigated, as well as it provides insights about the phenomena that occur. With this model, it was possible to calculate and define the matching load of the line and, in the case of a resonator array

with a receiver, also of the receiver TL segment. The distribution of the currents showed the presence of critical standing waves, with current peaks of considerable amplitude. In particular, the analysis of simple resonator arrays fed by an inverter has shown critical standing wave ratios in case the arrays are composed of an odd number of resonators. An analytical expression for the resonator currents of a generic array based on the TL analogy has been proposed and validated, in the hypothesis of nearest-neighbour interaction. The study of resonator arrays by means of the equivalent TL model was performed considering the different modulation strategies of the termination proposed in Chapter 4 and for different receiver positions. The study showed that also in this case the current distribution in the resonators is very uneven. A uniform efficiency and power transfer for all the receiver positions along the array can be reached at the expense of standing wave patterns of the resonator currents. The presence of a receiver introduces a discontinuity in resonator array TL causing reflections and then high current peaks, which in turn may lead to severe stress to the electric components. It is therefore important to appropriately dimension the system components, especially when used for powers in the order of kW, which are typical for industrial apparatuses. The intense currents circulating in the resonators generate a significant magnetic field, whose distribution mirrors current standing wave patterns. A proper shielding strategy is therefore necessary, and the study has shown how a planar single-layer aluminium shield or a two-layer aluminum-Mumetal<sup>®</sup> shield can still be adequate to shield the device.

With adequate control strategies, the efficiency of the system can be considerably increased, but the impact of the magnetic field generated on people and objects in the surrounding environment remains a problem that can limit the application of these devices.



## Chapter 6

# Receiver Coil Position Sensing in Resonator Arrays

In this chapter, an application of resonator arrays for position sensing is discussed. The possibility of using resonator arrays for detecting objects has been also discussed in [131, 132, 133], that exploit the interaction between metallic objects or tags and the resonator array. Resonator arrays are mainly devoted to very low-power systems, especially for consumer electronics applications. In this work, the detection of the exact location of an external resonator coupled with the array is performed exploiting the peculiar behaviour of the system input impedance. For a resonator array with a receiver, the input impedance behaviour has been thoroughly analysed in [126] considering perfectly aligned positions of the receiver with the cells of the array. A recursive analytic expression has been provided, in particular, as a continuous fraction, whose closed form is also proposed. However, all the discussion considers only positions of perfect alignment, limiting the use of the formula. For the detection of the position of the receiver, it is necessary to evaluate the input impedance as a continuous function of the position of the receiver. From a circuit analysis of these systems, an analytical expression of the input impedance of a resonator array coupled with an external resonator placed in a generic position is presented and its trend analysed for different parameter values. A simple and effective algorithm for the localisation of the external resonator is proposed, with a deep focus also on its digital implementation. This sensing technique can be exploited to build *ad hoc* sensors for industrial or consumer electronics applications, in which the external resonator does not act as a power receiver and the system is dimensioned to function only as a sensor. The possibility of exploiting this technique in power transfer devices has also been proposed, which can include both passive and active array resonators. The receiver position detection has been proven to be effective also in dynamic conditions, for which systems a simplified algorithm is proposed.

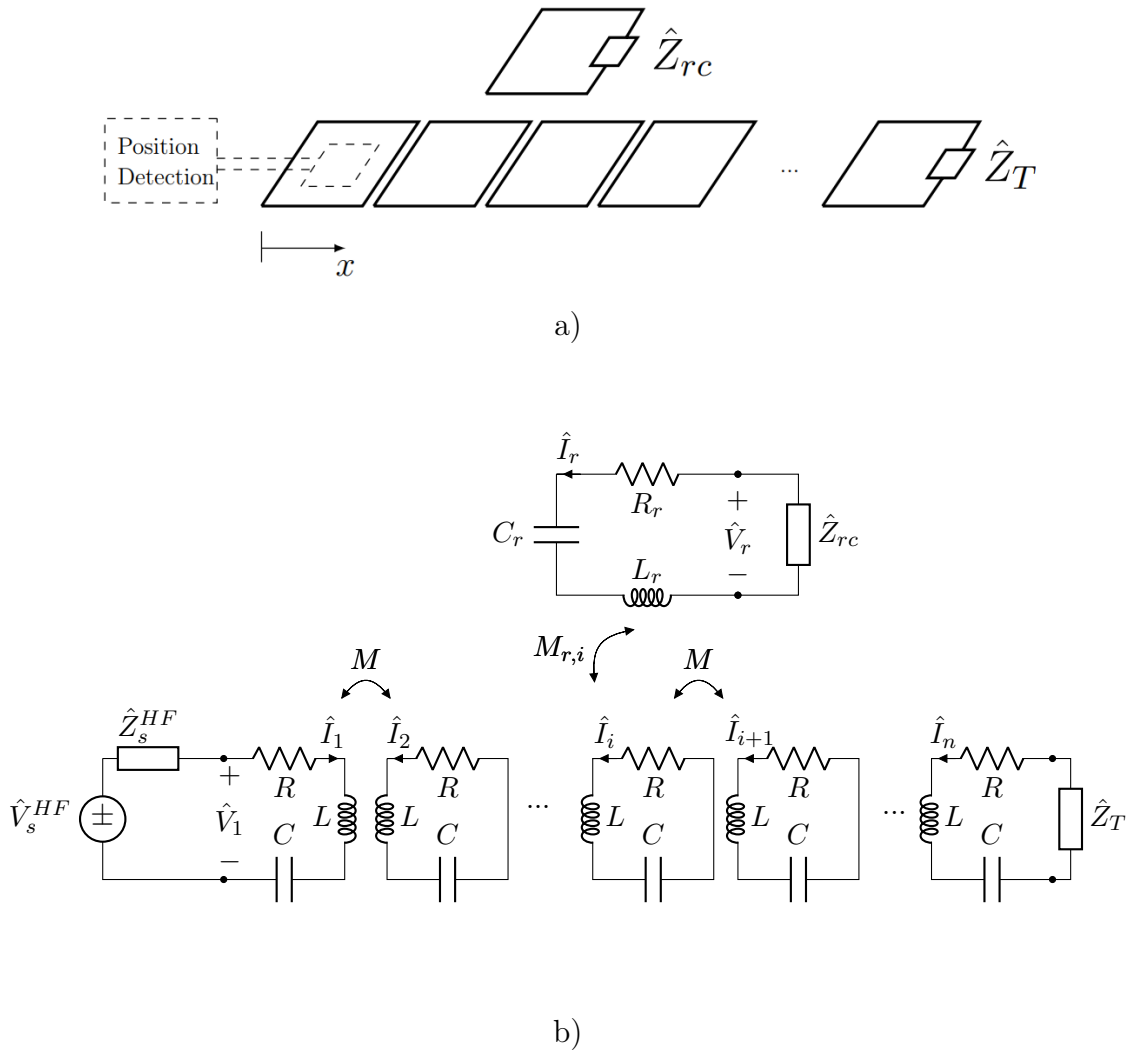


Figure 6.1: (a) Schematic representation of a resonator array with an external coil and (b) its equivalent circuit.

## 6.1 Input Impedance of a Resonator Array with a Receiver

A resonator array coupled with an external resonator (whose position has to be detected) is considered and schematically represented in Fig. 6.1a, where the position of the moving resonator along the array is denoted by the variable  $x$ . The array is composed of  $n$  identical and equally spaced coils, so that the mutual inductance  $M$  between each pair of adjacent resonators is the same and dimensioned such that the nearest-neighbour approximation can hold. Two additional impedances  $\hat{Z}_{rc}$  and  $\hat{Z}_T$  are added in the external and last array resonators, respectively. They provide two degrees of freedom which can modify the behaviour of the system and result crucial for the accuracy of the sensing, as discussed later. Due to the topology of the system, the better choice is a moving coil of the same size of the array resonators, or

slightly shorter. In fact, a bigger coil would couple with more array cells and then no perfect alignment positions would be found, making the input impedance expression unnecessarily complicated. Thus, a moving coil identical to the array resonators is considered for simplicity. The moving resonator can be placed at any position along  $x$  and thus the mutual inductance between the moving resonator and the generic  $i$ th resonator of the array varies according to the moving-resonator position  $x$ , as it is plotted in Fig. 5.6 for three consecutive array cells. The input impedance of the system can be studied by resorting to the circuit model already proposed in Chapter 4 and shown in Fig. 6.1b. Considering the system excited by a sinusoidal input voltage at the resonant frequency  $f_0$ , it is possible to consider all currents and voltages as phasors at the angular frequency  $\omega_0 = 2\pi f_0$  and the internal impedance of each array cell is  $R$  and the external coil impedance  $\hat{Z}_{rc}$ . Since the mutual inductance coefficients between the receiver and the facing cells depend on the receiver location, a relative coordinate  $\xi$  may be defined as:

$$\xi = x - (i-1)d \quad (6.1)$$

where  $x$  is the absolute coordinate along which the array lies,  $i$  indicates the first array cell facing the receiver and  $d$  the resonator size in the direction of  $x$ . Considering the moving resonator coupled with both the  $i$ th and  $(i+1)$ th cells of the array, a system of Kirchhoff voltage law (KVL) equations can be written as:

$$\begin{aligned} -\hat{V}_s + \hat{Z}_s \hat{I}_1 + \hat{Z} \hat{I}_1 + j\omega M \hat{I}_2 &= 0 \\ j\omega M \hat{I}_1 + \hat{Z} \hat{I}_2 + j\omega M \hat{I}_3 &= 0 \\ &\vdots \\ j\omega M \hat{I}_{i-2} + \hat{Z} \hat{I}_{i-1} + j\omega M \hat{I}_i &= 0 \\ j\omega M \hat{I}_{i-1} + \hat{Z} \hat{I}_i + j\omega M \hat{I}_{i+1} + j\omega M_{i,r}(\xi) \hat{I}_r &= 0 \\ j\omega M \hat{I}_i + \hat{Z} \hat{I}_{i+1} + j\omega M \hat{I}_{i+2} + j\omega M_{i+1,r}(\xi) \hat{I}_r &= 0 \\ j\omega M \hat{I}_{i+1} + \hat{Z} \hat{I}_{i+2} + j\omega M \hat{I}_{i+3} &= 0 \\ &\vdots \\ j\omega M \hat{I}_{n-1} + \hat{Z} \hat{I}_n + \hat{Z}_T \hat{I}_n &= 0 \end{aligned} \quad (6.2)$$

with one additional KVL equation for the receiver:

$$j\omega M_{r,i}(\xi) \hat{I}_i + j\omega M_{r,i+1}(\xi) \hat{I}_{i+1} + \hat{Z}_r \hat{I}_r = 0. \quad (6.3)$$

In order to write (6.2) in terms of the array currents only, the receiver coil current  $\hat{I}_r$  obtained from (6.3) can be substituted into (6.2), that becomes:

$$\begin{aligned}
-\hat{V}_s + \hat{Z}_s \hat{I}_1 + \hat{Z} \hat{I}_1 + j\omega M \hat{I}_2 &= 0 \\
j\omega M \hat{I}_1 + \hat{Z} \hat{I}_2 + j\omega M \hat{I}_3 &= 0 \\
&\vdots \\
j\omega M \hat{I}_{i-2} + \hat{Z} \hat{I}_{i-1} + j\omega M \hat{I}_i &= 0 \\
j\omega M \hat{I}_{i-1} + (\hat{Z} + \hat{Z}_{d_i}(\xi)) \hat{I}_i + (j\omega M + \hat{Z}_{d_{i,i+1}}(\xi)) \hat{I}_{i+1} &= 0 \\
(j\omega M + \hat{Z}_{d_{i+1,i}}(\xi)) \hat{I}_i + (\hat{Z} + \hat{Z}_{d_{i+1}}(\xi)) \hat{I}_{i+1} + j\omega M \hat{I}_{i+2} &= 0 \\
j\omega M \hat{I}_{i+1} + \hat{Z} \hat{I}_{i+2} + j\omega M \hat{I}_{i+3} &= 0 \\
&\vdots \\
j\omega M \hat{I}_{n-1} + \hat{Z} \hat{I}_n + \hat{Z}_T \hat{I}_n &= 0
\end{aligned} \tag{6.4}$$

where

$$\begin{aligned}
\hat{Z}_{d_i}(\xi) &= \omega^2 \frac{M_{i,r}^2(\xi)}{\hat{Z}_r} \\
\hat{Z}_{d_{i+1}}(\xi) &= \omega^2 \frac{M_{i+1,r}^2(\xi)}{\hat{Z}_r} \\
\hat{Z}_{d_{i,i+1}}(\xi) &= \hat{Z}_{d_{i+1,i}}(\xi) = \omega^2 \frac{M_{i,r}(\xi) M_{i+1,r}(\xi)}{\hat{Z}_r}.
\end{aligned} \tag{6.5}$$

The impedance terms (6.5) are usually called “defect impedances” and correspond to the reflection impedances of the receiver to the facing array resonators. Repeating the process by substituting in each equation the one relevant to the adjacent resonator, the remaining equation is the one of the first resonator, which becomes:

$$-\hat{V}_s + \left[ \hat{Z}_s + \hat{Z} + \hat{Z}_{i,i+1}^{eq}(\xi) \right] \hat{I}_1 = 0 \tag{6.6}$$

where  $\hat{Z}_{i,i+1}^{eq}(\xi)$  corresponds to the equivalent impedance seen from the first cell of the array with the external coil coupled with the  $i$ th and  $(i+1)$ th resonators. The array input impedance results in the recursive formula:

$$\begin{aligned}
\hat{Z}_{i,i+1}^{eq}(\xi) &= \frac{(\omega M)^2}{\hat{Z} + \frac{(\omega M)^2}{\dots + \frac{(\omega M)^2}{\hat{Z} + \hat{Z}_{d_i}(\xi) + \frac{(\omega M)^2 - \hat{\mathcal{D}}_{i,i+1}(\xi)}{\hat{Z} + \hat{Z}_{d_{i+1}}(\xi) + \frac{(\omega M)^2}{\hat{Z} + \frac{(\omega M)^2}{\dots + \frac{(\omega M)^2}{\hat{Z} + \hat{Z}_T}}}}}
\end{aligned} \tag{6.7}$$

where

$$\hat{\mathcal{D}}_{i,i+1}(\xi) = 2j\omega M \hat{Z}_{d_{i,i+1}}(\xi) + \hat{Z}_{d_{i,i+1}}^2(\xi). \tag{6.8}$$

In general, for each couple of facing resonators  $i$  and  $i+1$  the input impedance of the system can be defined as a continuous function of the space. This kind of function is named “continued fraction”, which is a recursive formula that can be calculated through an iterative process. Thus, it is difficult to express it as a function of the absolute coordinate  $x$ , since the continued fraction changes its form depending on the receiver position. To the best of the author’s knowledge, no closed analytical expressions are known for expressions of the type (6.7). However, these kinds of expressions can be handled by DSPs and computers and thus they can be easily computed numerically. For simplicity, the array input impedance for a generic receiver position  $x$  is considered and indicated as  $\hat{Z}_{eq}(x)$ .

While the input impedance of a resonator array without any moving-coupled resonator is purely real when the system is excited at its resonant frequency [126, 47], the presence of a moving resonator makes it complex. In this case, the imaginary part of  $\hat{Z}_{i,i+1}^{eq}(\xi)$  is not null even if the system operates at its resonant frequency. Considering all the cells operating in perfect resonance, the internal impedance  $\hat{Z}$  and the defect impedances  $\hat{Z}_{d_i}$ ,  $\hat{Z}_{d_{i+1}}$  and  $\hat{Z}_{d_{i,i+1}}$  of (6.5) result purely real, while  $\hat{D}_{i,i+1}$  is complex. Intuitively, it can be explained considering that the presence of the moving coil introduces a further coupling between the resonators it faces, with a consequent phase delay in the impedance seen from the array input port.

### 6.1.1 Simulations and Discussion

The behaviour of the input impedance  $\hat{Z}_{eq}(x)$  for the array prototype described in Sec. 5.4, where the receiver acts as an external coil and is loaded with  $\hat{Z}_{rc}$ . The input impedance is plotted in magnitude and phase in Figs. 6.2, 6.3 and 6.4 as a function of the receiver position for different values of load  $\hat{Z}_{rc}$  in case of short-circuit, matched and open-circuit terminations of the array, respectively. The magnitude of  $\hat{Z}_{eq}(x)$  is a continuous function of the spatial coordinate  $x$  and presents peaks for perfect alignment positions of the receiver, with a periodicity similar to what has been illustrated in [126]. Maximum values occur when the  $i$ th resonator faced by the external coil is odd and minimum values when even. This behaviour is the same for each array termination and moving coil load, as it is possible to see in Figs. 6.2, 6.3 and 6.4. This can be explained considering the behaviour of the resonator array with the external coil embedded in the facing array resonators through reflected impedances and controlled voltage sources, as discussed in Chapter 5. The system is reduced to an array of  $i$  resonators, terminated with the series of the defect impedance introduced by the moving coil and the equivalent impedance  $\hat{Z}_{n-i,\hat{Z}_T}^{eq}$  seen from the  $i$ th cell of the terminal segment of the original array, composed of  $n-i$  resonators and terminated with  $\hat{Z}_T$ , as illustrated in [126, 47]. When the defect impedance dominates over  $\hat{Z}_{n-i,\hat{Z}_T}^{eq}$ , the input impedance is affected by the number of resonators between the first array cell and the first resonator covered by the moving coil  $i$  only, while the values of  $\hat{Z}_{rc}$  have an effect on the magnitude of  $|\hat{Z}_{eq}(x)|$ . As  $\hat{Z}_{rc}$  increases, the presence of the moving coil affects less the array, with the limit case

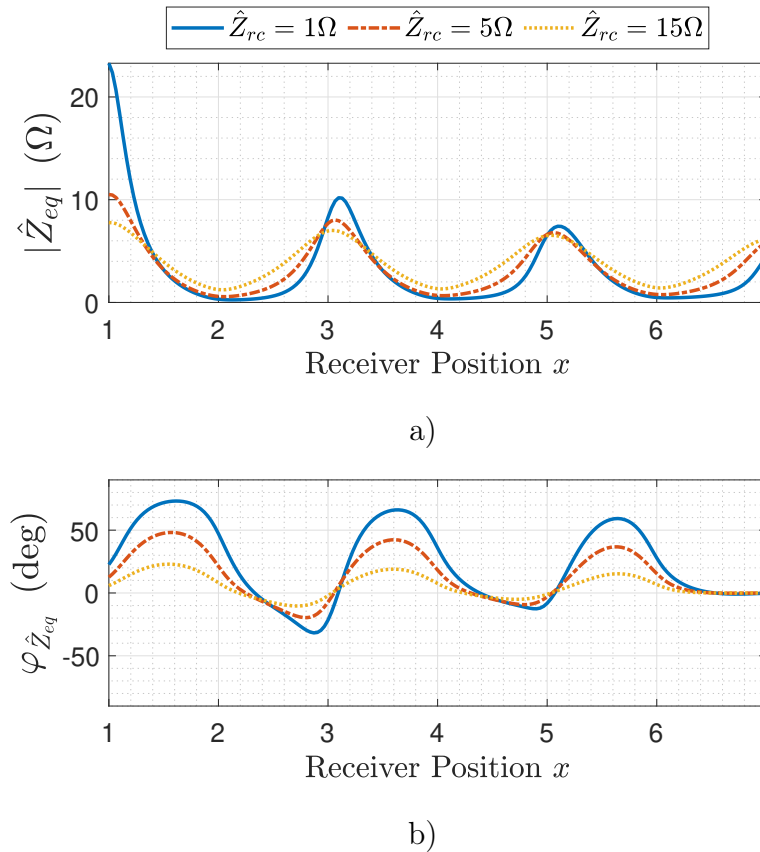


Figure 6.2: Array input impedance as a function of the receiver position with short-circuit termination for different values of load resistance  $\hat{Z}_{rc}$ , in magnitude (a) and phase (b).

of infinite  $\hat{Z}_{rc}$ , which makes the receiver-resonators coupling negligible. The phase of  $\hat{Z}_{eq}(x)$  presents maxima and minima depending on the coordinate  $x$ , with null values in case of perfect alignment positions. The asymmetry in the phase trends is due to the oscillatory behaviour of the equivalent impedance  $\hat{Z}_{n-(i+1),\hat{Z}_T}^{eq}$  of the terminating part of the array seen from the  $(i+1)$ th cell [46, 126], which smooths the phase shift introduced by the moving coil described by  $\hat{\mathcal{D}}_{i,i+1}$ . By means of  $\hat{Z}_{n-(i+1),\hat{Z}_T}^{eq}$ , it is possible to write  $\hat{Z}_{i,i+1}^{eq}(\xi)$  as:

$$\hat{Z}_{i,i+1}^{eq}(\xi) = \frac{(\omega M)^2}{\hat{Z}_+ + \frac{(\omega M)^2}{\dots + \frac{(\omega M)^2 - \hat{\mathcal{D}}_{i,i+1}(\xi)}{\hat{Z}_+ \hat{Z}_{d_i}(\xi) + \frac{(\omega M)^2 - \hat{\mathcal{D}}_{i,i+1}(\xi)}{\hat{Z}_+ \hat{Z}_{d_{i+1}}(\xi) + \hat{Z}_{n-(i+1),\hat{Z}_T}^{eq}}}}} \quad (6.9)$$

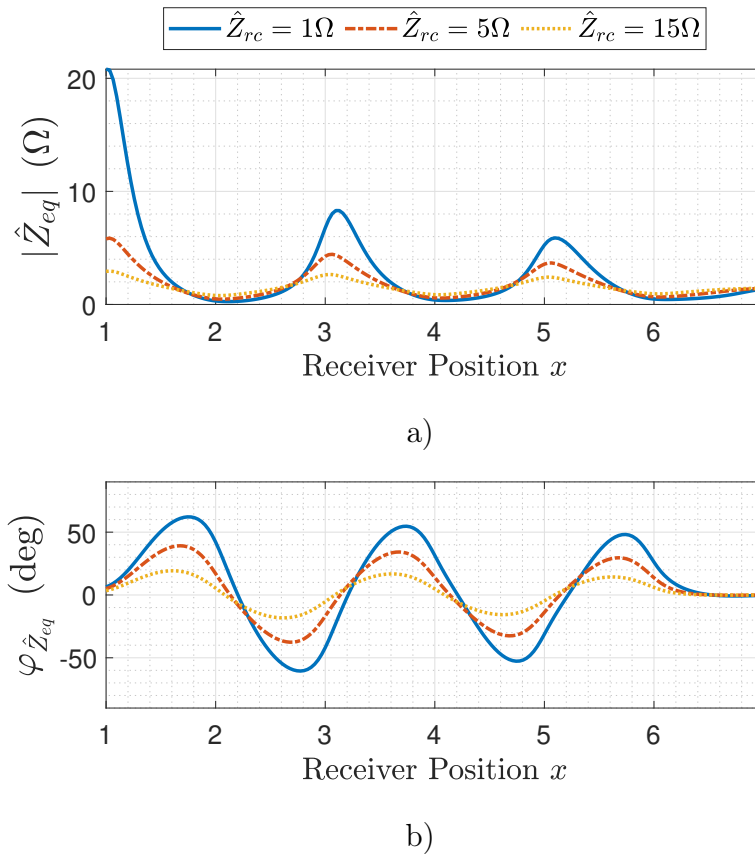


Figure 6.3: Array input impedance as a function of the receiver position with matched termination for different values of load resistance  $\hat{Z}_{rc}$ , in magnitude (a) and phase (b).

which clearly indicates that the phase shift is dominated by the ratio:

$$\frac{-\hat{\mathcal{D}}_{i,i+1}(\xi)}{\hat{Z} + \hat{Z}_{d_{i+1}}(\xi) + \hat{Z}_{n-(i+1),\hat{Z}_T}^{eq}} \quad (6.10)$$

where the terms  $\hat{\mathcal{D}}_{i,i+1}(\xi)$  and  $\hat{Z}_{d_{i+1}}(\xi)$  present the same values for each pair of resonators  $i$  and  $i+1$  that face the moving coil. The impedance  $\hat{Z}_{n-(i+1),\hat{Z}_T}^{eq}$  dramatically oscillates depending on the number of resonators  $n-(i+1)$  and the termination impedance  $\hat{Z}_T$  of the array. According to [126], the equivalent impedance of a short-circuited array presents maximum and minimum values for an even and odd number of resonators, respectively. The trend is opposite in case of open circuit termination. Moreover, the equivalent impedance is equal to the termination impedance when the array is perfectly matched. Considering the phase of the array equivalent impedance  $\varphi_{\hat{Z}_{eq}}(x)$  for the short-circuited array of six resonators plotted in Fig. 6.2(b), it can be seen that, when the first resonator faced by the moving coil  $i$  is odd, the terminating segment of the array is composed by an odd number of resonators  $n-i$  and the equivalent impedance  $\hat{Z}_{n-(i+1),\hat{Z}_T}^{eq}$  presents very low

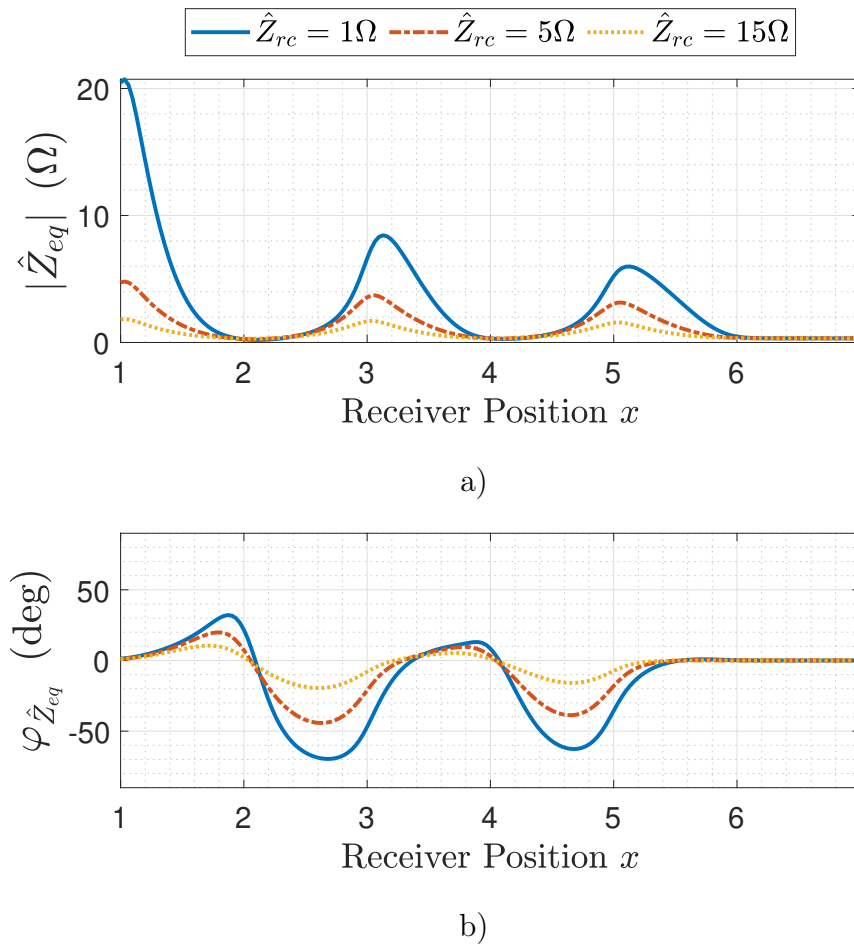


Figure 6.4: Array input impedance as a function of the receiver position with open-circuit termination for different values of load resistance  $\hat{Z}_{rc}$ , in magnitude (a) and phase (b).

magnitudes. Thus, the phase shift experienced by  $\hat{Z}_{eq}(x)$  presents its maximum values, according to (6.10). Oppositely, if  $i$  is even,  $\hat{Z}_{n-(i+1),\hat{Z}_T}^{eq}$  attenuates the phase shift. The opposite behaviour occurs when the array is terminated in OC. In case of matched termination,  $\hat{Z}_{n-(i+1),\hat{Z}_T}^{eq}$  behaves the same for any position and then the trend of  $\varphi_{\hat{Z}_{eq}}(x)$  is symmetric. Furthermore, for increasing values of  $\hat{Z}_{rc}$  the defect impedances (6.5) are smaller and the phase shift of  $\hat{Z}_{eq}(x)$  is less pronounced.

## 6.2 Resonator Array as a Linear Position Sensor: Design and Choice of the Array Parameters

The intrinsic resistance of the resonator windings is usually undesirable in resonant systems, since it leads to power losses and thermal heating. However, it guarantees the convergence of  $\hat{Z}_{eq}(x)$  to finite values and makes them different for any moving coil position. Indeed, both the magnitude and phase of the equivalent impedance are attenuated as the moving coil is positioned far from the array input resonator and the combination of their values is unique for any position  $x$  of the moving coil. Thus, once the array parameters are fixed, the measure of the array input impedance allows the estimation of  $x$ . The coils are designed to maximise the self- and mutual inductances and then the value of the intrinsic resistance is consequently found. The remaining degrees of freedom are the coil number, their size  $d$  in the  $x$  direction of the space, and the impedances  $\hat{Z}_T$  and  $\hat{Z}_{rc}$ , which are usually purely real to avoid altering the coil resonant frequency.

### 6.2.1 Termination conditions

Typical termination conditions for resonator arrays are SC, OC and matching [69, 47], which correspond to  $\hat{Z}_T = 0$ ,  $\hat{Z}_T \rightarrow \infty$  and  $\hat{Z}_T \approx \omega M$ , respectively. Values of  $\hat{Z}_{rc}$  have not been discussed in literature; theoretically, any real value of  $\hat{Z}_T$  and  $\hat{Z}_{rc}$  makes  $\hat{Z}_{eq}(x)$  convergent and univocally defined for any  $x$  and a meaningful choice is based on the sensitivity of the resulting  $\hat{Z}_{eq}(x)$  to the variation of the moving coil position, as can be understood from Figs. 6.2, 6.3 and 6.4. As a first consideration, it should be noticed that an open-circuit termination of the array is completely useless, since the last resonator does not interact with the others and thus the presence of the moving coil is not detected. Moreover, the behaviour of  $\hat{Z}_{eq}(x)$  is the same of considering the array one resonator shorter. A matching array termination results in a smoother trend of the input impedance function, but the sensitivity should be pronounced to help in identifying the argument  $x$  of  $|\hat{Z}_{eq}(x)|$ . Thus,  $\hat{Z}_T = 0$  is set. For what concerns  $\hat{Z}_{rc}$ , a similar argument is possible, which would lead to the choice of  $\hat{Z}_{rc} = 0$ . However, the high values the input impedance presents for  $i = 1$  can complicate the tuning of the sensor, since it strongly widens the range of values that should be measured. Overall, the convergence and univocity of the equivalent impedance function can be verified from its trajectory in the complex plane, that should be limited and should not present intersection points. An example is the curve plotted in Fig. 6.5, that shows the trajectory of the input impedance function in the complex plane according to the moving coil position  $x$  for given values of  $\hat{Z}_t$  and  $\hat{Z}_{rc}$ .

### 6.2.2 Sensitivity

The number of array coils is chosen according to the dimension of the object whose position has to be found and depending on the sensitivity of the input impedance function to the coordinate  $x$ , which is crucial since it determines the effective accuracy in the measure. The sensitivity of  $\hat{Z}_{eq}(x)$  can be defined for both its amplitude and phase as:

$$s_{mag}(x) = \frac{d|\hat{Z}_{eq}(x)|}{dx} \quad (6.11)$$

and

$$s_{ph}(x) = \frac{d\varphi_{\hat{Z}_{eq}}(x)}{dx}, \quad (6.12)$$

respectively. Theoretically, for an accurate measure they should present the largest magnitude possible, even though they risk diverging for some  $x$ , making their calculation very difficult. Practically, the sensitivity is mainly affected by the space variation of the mutual inductance  $M_{r,i}(x)$ , which contributes to  $\hat{Z}_{eq}(x)$  as shown in (6.5) and (6.7). Indeed, while the number of positive and negative peaks of both  $|\hat{Z}_{eq}(x)|$  and  $\varphi_{\hat{Z}_{eq}}(x)$  depends on the number of resonators, their variation of a moving coil coupled with the generic  $i$ th and  $(i+1)$ th cells depends on  $dM_{r,i}(x)/dx$ .

On the other hand, for a fixed array length  $L_x$  a higher number of array resonators leads to an input impedance function more sensitive to the position  $x$ , since it presents more periods and thus a more pronounced variation in space. Overall, a trade off between  $n$  and  $L_x$  has to be found depending on the geometry of the adopted coils and the trend of the mutual inductance  $M_{r,i}(x)$ .

The portion of space  $L_x$  in which the sensor has to operate can be covered by an arbitrary number of resonators, which determines the number of periods of  $|\hat{Z}_{eq}(x)|$  and  $\varphi_{\hat{Z}_{eq}}(x)$ . Theoretically, since the space variation of  $M_{r,i}(x)$  is continuous, at least an array of one resonator could be sufficient to make the sensor operate. However, the moving coil length has to be greater than half of the array resonator length, otherwise  $M_{r,i}(x)$  would result symmetric with respect to  $x$  and it would not be possible to distinguish whether the moving coil covers the first or second half of the resonator. Anyway, in practical applications, it is convenient to reduce the length of the moving coil and adapt it to the size of the object to which it is fixed. In this way, it is possible to cover the entire movement area of the object without altering the size of the moving coil. Then, the number of coils can be chosen according to the length  $L_x$  and the sensitivity parameters  $s_{mag}$  and  $s_{ph}$ .

### 6.2.3 Algorithm for the External-Coil Position Detection

Considering the system operating in resonance, the resonator impedance presents a positive real part only, which is due to the winding resistance of the coils and that makes the values of the array input impedance different for each moving coil position  $x$ . Indeed, while both the magnitude and phase of  $\hat{Z}_{eq}(x)$  can have the

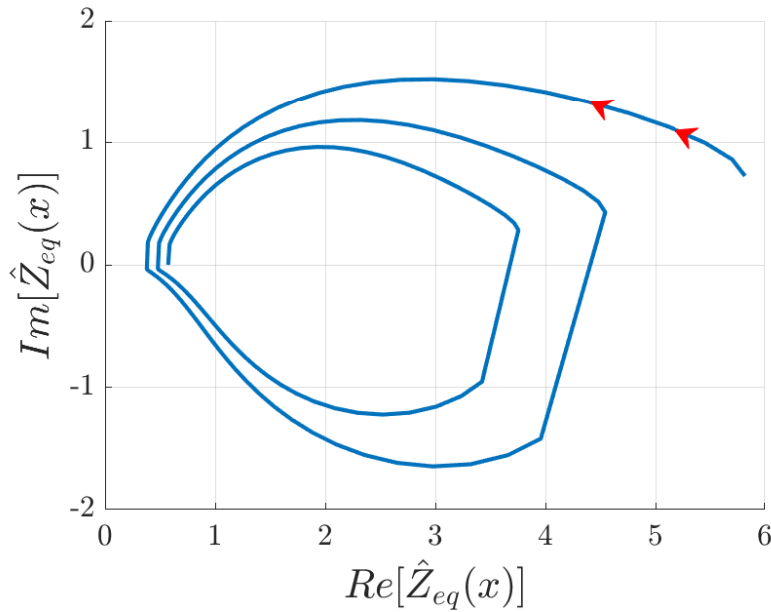


Figure 6.5: Input impedance trajectory as a function of the receiver position for the resonator array described in Sec. 6.1.1 with short-circuit termination and  $\hat{Z}_{rc} = 1\Omega$ . The function evolves for increasing  $x$  in the direction of the red arrows.

same value for different  $x$ , their combination is unique for a certain  $x$ . This can be appreciated from Fig. 6.5: there are no intersection points in the plot. This peculiarity can be exploited to detect the moving coil position simply starting from the measurement of the input impedance. The basic idea consists in feeding the first array resonator with a sinusoidal voltage  $v_1(t)$  at the resonant frequency  $f_0$  and measuring the current circulating in the same resonator  $i_1(t)$ , from which the input impedance can be estimated for any position of the moving coil as:

$$\hat{\tilde{Z}} = \frac{\hat{V}_1}{\hat{I}_1} \quad (6.13)$$

where  $\hat{I}_1$  and voltage  $\hat{V}_1$  are the phasors of the input current and voltage, respectively, at the resonant frequency. The superscript “ $\sim$ ” denotes estimated quantities. Then, comparing the estimated and (theoretically) calculated values it is possible to determine the moving coil position  $x$ . In particular, the calculated impedance should match the measured one within a tolerance margin, which is introduced in order to take into account the uncertainty due to measurement noise and the errors caused by the digital implementation of the algorithms and calculations. Mathematically, the conditions to be satisfied can be written as:

$$\| \tilde{Z} - |\hat{Z}^{eq}(x)| \| \leq \delta_Z \quad (6.14)$$

$$\| \tilde{\varphi} - \varphi_{\hat{Z}^{eq}(x)} \| \leq \delta_\varphi, \quad (6.15)$$

where  $\delta_Z$  and  $\delta_\varphi$  are the tolerance margins accepted for the magnitude and phase equalities, respectively.

### Discrete Implementation

Systems of practical interest require the algorithms to be implemented in digital environments by means of microprocessors and computers, which deal with discrete functions and signals only. Thus, the proposed algorithm for the detection of the moving coil location has to be formulated considering discrete quantities, leading to new issues and limitations such as sampling and truncation errors. As a first consideration, it should be noticed that the mutual inductance between the moving coil and the generic  $i$ th resonator  $M_{r,i}(x)$  is usually calculated numerically, being closed form expressions available for particular coil geometries only and, moreover, they do not apply in presence of non-homogeneous media, as it usually occurs when magnetic materials are used. For this reason,  $M_{r,i}(x)$  is assumed to be numerically calculated with a discretisation step  $\Delta x$  and thus, as a consequence, all the parameters defined according to  $M_{r,i}(x)$  are affected by the choice of  $\Delta x$ . In particular, the discrete formulation of the sensitivity reported in (6.11) and (6.12) can be written for a certain value of the (discretised) space coordinate  $x_k$  considering the difference quotients:

$$S_{mag}(x_k) = \frac{\Delta |\hat{Z}_{eq}|}{\Delta x}(x_k) \quad (6.16)$$

$$S_{ph}(x_k) = \frac{\Delta \varphi_{\hat{Z}_{eq}}}{\Delta x}(x_k). \quad (6.17)$$

These expressions clearly indicate that, assuming a fixed space interval  $\Delta x$ , the sensitivity of the input impedance is different for each  $\Delta x$ , suggesting the need of defining variable tolerance margins, that should be larger when the sensitivity is higher. Thus, for a certain moving coil location  $x_k$ , the inequalities reported in (6.14) and (6.15) become:

$$\| \tilde{Z} - |\hat{Z}^{eq}(x)| \| \leq \delta_Z(x_k) \quad (6.18)$$

$$\| \tilde{\varphi} - \varphi_{\hat{Z}^{eq}}(x) \| \leq \delta_\varphi(x_k), \quad (6.19)$$

where  $\delta_Z$  and  $\delta_\varphi$  are the tolerance intervals accepted for the  $k$ th reference position. Moreover,  $\delta_Z$  and  $\delta_\varphi$  can not be symmetric, since the difference between impedance values corresponding to two consecutive positions is in general not constant, as it is testified by the sensitivity functions. Thus, for both intervals, it becomes necessary to distinguish two different parameters that define the upper and lower limits. The simplest choice consists in defining backward and forward limits for  $\delta_Z$  and  $\delta_\varphi$ , that can be combined in order to determine the effective tolerance interval for  $|\hat{Z}_{eq}|$  and  $\varphi_{\hat{Z}_{eq}}$ . In the following, the procedure is illustrated considering only the module of the input impedance, but the same approach is adopted for the phase. It is omitted for simplicity. The backward limit for  $\delta_Z^B(x_k)$  can be defined for a generic position  $x_k$  as:

$$\delta_Z^B(x_k) = \frac{|\hat{Z}_{eq}(x_k)| - |\hat{Z}_{eq}(x_{k-1})|}{2}, \quad (6.20)$$

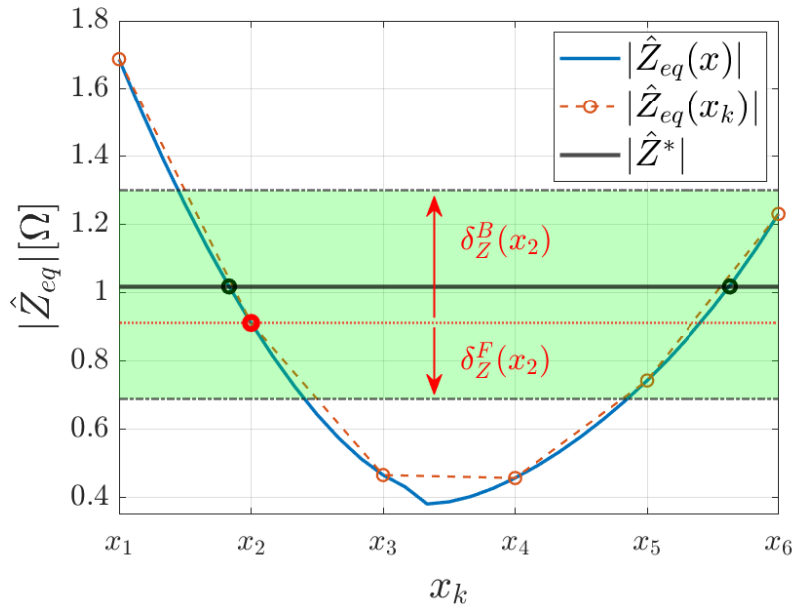


Figure 6.6: Feature of the input impedance magnitude of the resonator array described in Sec. 6.1.1, where the blue curve represents the calculated continuous function  $|\hat{Z}_{eq}(x)|$  and the dark-red dashed line its discrete version  $|\hat{Z}_{eq}(x_k)|$ . The black line indicates the value of the measured input impedance magnitude  $\hat{Z}^*$  (also indicated with  $\hat{\tilde{Z}}$ ) and the red dotted line the value of the function at the coordinate  $x_k$ . The green box represents the tolerance interval for  $x_2$ , bounded by the associated tolerance margins  $\delta_Z^B(x_2)$  and  $\delta_Z^F(x_2)$ .

while the forward limit  $\delta_Z^F(x_k)$  in  $x_k$  as:

$$\delta_Z^F(x_k) = \frac{|\hat{Z}_{eq}(x_{k+1})| - |\hat{Z}_{eq}(x_k)|}{2}. \quad (6.21)$$

where the superscripts  $B$  and  $F$  indicate the backward and forward limits, respectively. Then, the resulting intervals are set based on the trends of  $|\hat{Z}_{eq}|$  and  $\varphi_{\hat{Z}_{eq}}$ , that are described by the associated sensitivity parameters. For simplicity, let us consider the input impedance magnitude first. The following cases can be identified:

$S_{mag} \geq 0$  In case of positive  $S_{mag}$ ,  $|\hat{Z}_{eq}|$  is increasing and thus  $\delta_Z^B(x_k), \delta_Z^F(x_k) \geq 0$ . The tolerance interval can be defined as:

$$\left[ |\hat{Z}_{eq}(x_k)| - \delta_Z^B(x_k), |\hat{Z}_{eq}(x_k)| + \delta_Z^F(x_k) \right]. \quad (6.22)$$

$S_{mag} \leq 0$  Instead, for negative  $S_{mag}$ ,  $\delta_Z^B(x_k), \delta_Z^F(x_k) \leq 0$  and the interval is:

$$\left[ |\hat{Z}_{eq}(x_k)| + \delta_Z^F(x_k), |\hat{Z}_{eq}(x_k)| - \delta_Z^B(x_k) \right]. \quad (6.23)$$

A graphic representation of  $\delta_Z$  for  $S_{mag} \leq 0$  is shown in Fig. 6.6, in which a feature of the function  $|\hat{Z}_{eq}|$  is plotted. The black horizontal line represents the value of the measured impedance  $\tilde{Z}$ , that should be compared with the discrete values of  $|\hat{Z}_{eq}|$ . In the figure, the comparison is performed for  $x_k \equiv x_2$  and the red dot represents  $|\hat{Z}_{eq}(x_2)|$ . Then, the interval  $\delta_Z$  is coloured in green and contains the black line, meaning that the condition (6.18) is satisfied. It is important to notice that (6.18) or (6.19) can be met for different positions, but only one  $x_k$  allows both conditions to be fulfilled.

$S_{mag} = 0$  In case a maximum or minimum of  $|\hat{Z}_{eq}|$  is found at a considered coordinate  $x_k$ ,  $S_{mag}$  may be null and the limits of the interval should be defined differently. Indeed, if the function presents a minimum in  $x_k$ ,  $\delta_Z^B(x_k) < 0$  while  $\delta_Z^F(x_k) > 0$ , and thus they should both be considered as the upper limit. The larger in magnitude is chosen. Then, an arbitrary lower limit  $\delta_Z^{min}$  is introduced to complete the interval, leading to:

$$\left[ |\hat{Z}_{eq}(x_k)| - \delta_Z^{min}(x_k), |\hat{Z}_{eq}(x_k)| + |\delta_Z^{F,B}(x_k)| \right]. \quad (6.24)$$

The opposite situation occurs in case  $x_k$  corresponds to a maximum of the input impedance magnitude function, with the definition of an arbitrary upper limit  $\delta_Z^{max}$ , while as a lower limit the largest in magnitude between  $\delta_Z^B(x_k)$  and  $\delta_Z^F(x_k)$  is chosen. Thus, the intervals can be expressed as:

$$\left[ |\hat{Z}_{eq}(x_k)| - |\delta_Z^{F,B}(x_k)|, |\hat{Z}_{eq}(x_k)| + \delta_Z^{max}(x_k) \right]. \quad (6.25)$$

Similarly, this procedure also applies to the limits of the phase tolerance margin. A backward limit  $\delta_\varphi^B(x_k)$  and forward limit  $\delta_\varphi^F(x_k)$  are defined as in (6.20) and (6.21), respectively. Also, arbitrary minimum and maximum limits  $\delta_\varphi^{min}$  and  $\delta_\varphi^{max}$  are introduced, respectively, in case  $S_{ph} = 0$ .

Overall, the proposed definitions of tolerance margins guarantee that (6.18) and (6.19) are satisfied for at least one position  $x_k$ . However, the limits become larger as  $\Delta x$  increases, with the risk of finding more values  $x_k$  associated with a certain  $\tilde{Z}$  and  $\tilde{\varphi}$ . Thus, the discretisation step has to be the smallest possible, consistent with the machine precision. The proposed algorithm is schematically illustrated in Fig. 6.7.

## Hardware Implementation

The discrete implementation of the external coil position monitoring technique must be suitably accompanied by efficient and accurate measurements of the necessary

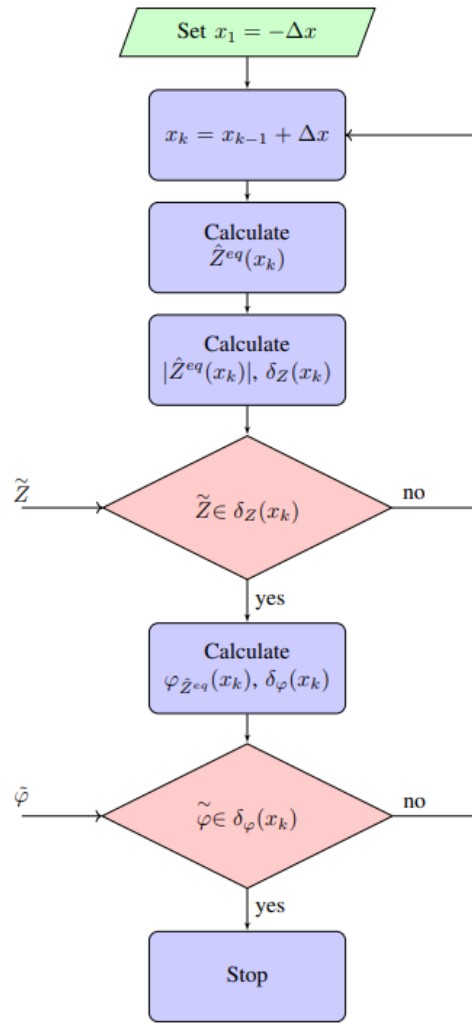


Figure 6.7: Flow chart illustrating the algorithm for the detection of the moving coil position.

quantities. To evaluate the feasibility of this type of sensor, it is advisable to evaluate the hardware implementation considering the performance of modern DSPs, which strongly affect the processing and the execution of the detection algorithm. The input impedance can be estimated from the input voltage and current phasors at the frequency  $f_0$ , which are extracted from the associated measured waveforms. The measurements of the voltage can be performed by using a compensated voltage divider, that can be galvanically isolated by a cascaded optically isolated voltage transducer. Similarly, the current can be recorded with an optically buffered resistive shunt by the same device. These optically isolated voltage transducers (such as AMC1202 [134], AMC3301 [135] and ACPL-790 [136]) have a bandwidth  $\Delta_f$  larger than 200 kHz, less than  $1 \mu\text{V}$  of input noise density, and a basic forward gain of 8.2. The uncertainty introduced by the input noise is negligible since an enough narrow band of at most some hundreds Hz centred round  $f_1$  is adopted for the voltage and current measure.

For what concerns the sampling, it can be carried out at 1 MSA/s. There is no necessity of performing a full FFT, except for initialisation and thus the spectral voltage and current components at  $f_1$  are estimated with a recursive FFT (a complete FFT is required only for initialisation) together with the adjacent components at  $f_1 - \Delta f$  and  $f_1 + \Delta f$ , to track the stability at  $f_1$ . This kind of algorithm requires few floating point operations, while modern DSPs have the computational power of more than several hundred of MFlops (floating point operations per second) [137, 138]. The FFT calculation can be performed in less than  $120\mu\text{s}$ .

The simplicity of the algorithm, combined with the high-performance digital controllers, allows this sensor to be used even in applications where the external coil moves at high speed.

### Position Detection of a Moving External Coil

It is straightforward to exploit this sensor even in contexts with moving mechanical parts, whether they are rotating or translating. As introduced in Sec. 2.2, the variation of the relative position between mutually coupled coils leads to the so-called motional induced electromotive force  $emf_M$  (see Chapter 2). It is associated with the variation of magnetic flux due to the displacement of the circuit (and therefore of the surface through which the magnetic flux is considered), and it is therefore an inevitable phenomenon in resonator systems with coupled coils in motion. However, the contribution of the  $emf_M$  to the voltage induced in the coils is often negligible compared to the  $emf_T$  in IPT systems of practical interest. This is due to the fact that the IPT devices are designed to work at relatively high frequencies (hundreds of kHz) and the spatial variation of the coils mutual inductance is minimised by design. It follows that the proposed algorithm can also be safely used to estimate the position of the external coil when it is in relative motion with respect to the array. With the appropriate structure, this type of sensor can also be applied to dynamic rotary systems, such as for example the estimation of the rotor position in an electric machine or the receiver position in a dynamic IPT system. Furthermore, the latter application also allows the same coils used for power transmission to be exploited, without therefore introducing further devices and modifying the structure of the system. However, it is evident that the power transfer and the sensing of the receiver position must not interfere during operation and thus the system must be designed *ad hoc*. This possibility, in an automotive context, has been analysed in the following, also presenting a simplified position estimation algorithm which requires less computing power.

## 6.3 Receiver-Coil Location Detection in a Dynamic Inductive Power Transfer System for Electric Vehicle Charging

In this section, a receiver position detection technique in a dynamic IPT system for automotive applications is proposed. The technique is based on the study of the input impedance of the resonator array previously proposed, and is applied to a dynamic IPT system for EV charging composed of a series of coils each fed by its own independent power source [109]. With the proper scale, the same apparatus can be exploited in automatic machines for industrial applications, where several moving parts may need to be powered. In dynamic IPT systems for automotive applications, the EV has to be charged in a very limited amount of time, which is proportional to the length of the coupling area and inversely proportional to its speed. To increase the length of the coupling area multiple charging coils may be used. Preserving the same structure and complexity of the charging lane, an array of cascaded resonating coils may be used, where the transmitter directly feeds the first coil and the magnetically coupled receiver on the vehicle can take the power flowing from the same unique transmitter through the intermediate relay coils [43, 139]. Although it has been shown in Chapter 4 that it is possible to maximise both the transmitted power and the efficiency by controlling only the input voltage, the study conducted in Chapter 5 on the currents and magnetic field generated by the system highlighted the risk of electromagnetic interference and physiological damage to the health of people or animals that are in the vicinity of the apparatus. For this reason, it is reasonable to think that an IPT system for automotive applications in civil environments requires greater control of the magnetic field emissions, especially considering the high power rates required by the charging processes of electric vehicles. On the basis of the current state of the art, a dynamic IPT system has been devised consisting of an array of magnetically coupled resonators powered, however, individually, with voltage sources typical of static IPT systems, analysed and discussed in Chapter 3. In these systems, the correct positioning and minimal misalignment are necessary to improve the efficiency [97, 140]. Different solutions can be adopted to detect the receiver position. In particular, external sensing systems can be used, based on optical signals [141], tag readers (RFID) [142] or GPS [143]. Other possibilities consist in introducing additional inductive sensors embedded with the IPT coils, such as ferrite antenna [144], interposed detection coils [145, 146], Hall sensor array [147] or TMR (tunnelling magnetoresistive) sensors foil [148] combined with specific coils systems whose parameters can be exploited for the receiver detection [149]. In this work, the basic idea consists in exploiting the existing IPT coils of the resonator array, and, specifically, its peculiar input impedance.

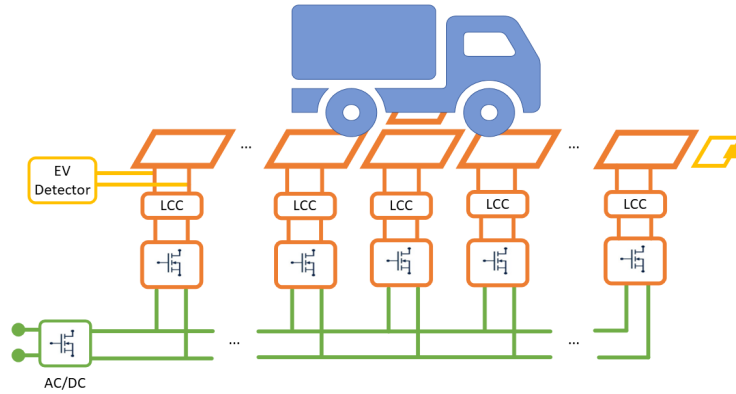


Figure 6.8: Schematic of the proposed dynamic IPT system. The EV detector block is devoted to the high-frequency measurement of the array input impedance.

### 6.3.1 System Architecture and Receiver Location Detection

Dynamic wireless power transfer systems for roadways [150, 151, 152] or industrial applications [36] are basically composed of an array of coils arranged in the direction along which the receiver moves. Each coil is fed by a proper supply system, that comprises the power source (typically a voltage source inverter) and a compensation network, as depicted in Figure 6.8. To increase the efficiency and reduce the magnetic field emission, only the coil facing the receiver is turned on, while the others are kept off. As a result, for each receiver position, the system operates as a simple two-coil IPT apparatus. It must be noticed that a suitable control system that synchronises the coil drivers is required to rapidly detect the receiver position and activate the proper coil. All the array coils operate at  $f_0 = 85$  kHz, as indicated in the automotive standard SAE J2954 regulating the static IPT systems [3]. The transmitting coils are fed by H-bridge inverters with an LCC compensation network, as illustrated in Figure 6.9. In particular, the primary LCC compensation network is tuned such that:

$$\omega_0 L_f = \frac{1}{\omega_0 C_f}, \quad \omega_0 L - \omega_0 L_f = \frac{1}{\omega_0 C} \quad (6.26)$$

where  $L_f$ ,  $C_f$  and  $C$  are the parameters of the lumped components involved in the LCC compensation network and  $L$  the self-inductance of the transmitting coils. In particular,  $L_f$  is chosen to ensure ZVS operations of the inverter. In order for the study to be consistent, the values of the system parameters have been chosen in line with those indicated in the SAE standard, which, on the basis of the nominal power and the distance between the transmitter and receiver, suggests limits for the self-inductances and coupling coefficient of the coils, as well as working frequency. The compensation network is tuned accordingly. The system parameter values are reported in Tab. 6.1.

The basic idea for the receiver coil location detection consists in feeding the first

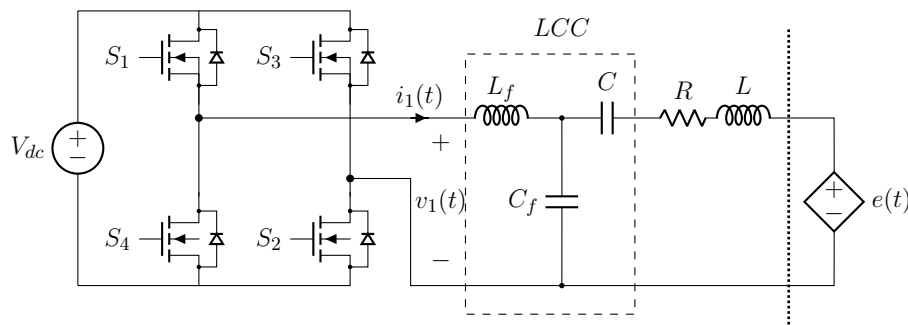


Figure 6.9: Equivalent circuit of the coil driver. It consists of the cascade of an H-bridge inverter and an LCC compensation network. The coil is modelled with a lumped impedance, resistance and the series-controlled voltage source to represent the coupling with the receiver and adjacent coils.

resonator of the array with a high-frequency voltage and estimating the impedance at that port. During charging operations, only the coil coupled with the receiver is fed by the power inverters (the others are deactivated), which operate at  $\omega_0$ . When a voltage at a generic frequency is induced in a coil (represented in the time domain by the controlled voltage source  $e(t)$  in Fig. 6.9), the resulting current depends on the circuitry connected to that coil, which in this case consists of an LCC network and an H-bridge inverter. In particular, the behaviour of the circuit can be understood by studying the behaviour of the equivalent impedance  $\hat{Z}$  seen by the controlled voltage source  $e(t)$ . According to [97] (also discussed in Sec. 2.4), the inverter can be assumed as an ideal voltage source, being its internal impedance much smaller than the resistance of the circuit connected to the inverter output port (more than one order of magnitude). Thus  $\hat{Z}$  is expressed as:

$$\hat{Z}(\omega) = R + j\omega L + \frac{1}{j\omega C} + \frac{j\omega L_f \frac{1}{j\omega C_f}}{j\omega L_f + \frac{1}{j\omega C_f}}, \quad (6.27)$$

and it is plotted in magnitude and phase as a function of frequency in Figs. 6.10a and 6.10b, respectively. These figures show two anti-resonance peaks: the first (at 52 kHz) below the IPT operating frequency  $f_0$  and the other (at 108.4 kHz) above  $f_0$ . For these two frequencies, the impedance seen from  $e(t)$  presents minimum values, meaning that the coil behaves as if it is in (series) resonance. Conversely, at  $f_0$  the  $\hat{Z}$  is maximum and the coil behaves as if it is open. It must be noticed that these considerations hold whether the inverter is working or not, being its internal impedance negligible with respect to  $j\omega L_f$ . Indeed, the MOS body diodes always allow the inverter output current to flow back to the DC-bus limited by their internal resistance only. The receiver circuit impedance is determined by the

Table 6.1: Resonator array parameters

<i>Quantity</i>	<i>Symbol</i>	<i>Value</i>	<i>Unit of Measure</i>
<b>Transmitting Coils</b>			
Primary Coils Mutual Inductance	$M$	-2.6	$\mu$ H
LCC Series Capacitance	$C$	82.3	nF
LCC Series Inductance	$L_f$	27.34	$\mu$ H
LCC Parallel Capacitance	$C_f$	0.128	$\mu$ F
WPT Resonance Frequency	$f_0$	85	kHz
Z measurement Frequency	$f_1$	108.365	kHz
Array Matching Impedance	$\hat{Z}_{match}$	1.75	$\Omega$
<b>Receiver</b>			
Receiver Coil Quality factor	$Q_r$	300	/
Receiver Coil Self-inductance	$L_r$	40	$\mu$ H
Receiver Series Capacitance	$C_r$	87.5	nF
WPT Resonance Frequency	$f_0$	85	kHz
On-board DC-bus Voltage	$V_{OBC_{dc}}$	520	V
Power Rate	$P$	520	kW

compensation network and load. It is easy to see that, whatever the compensation strategy adopted, only one resonant frequency at  $f_0$  is observed. This is due to the presence of the equivalent load of the on-board charging system, which is modelled as an equivalent resistance as in Sec. 2.5. Being it defined based on the on-board converter bus voltage and transferred power, it can present values of tens of Ohms. Overall, it is possible to conclude that, at the frequency  $f_1 = 108.4$  kHz (the upper anti-resonance is chosen without a loss of generality) the system behaves as an array of magnetically coupled resonators as described in these Chapters and shown in Fig. 6.11, coupled to a non-resonant receiver placed over it. The array can be modelled as in Sec. 4 and 5 and, in this case, the coils resonate due to the particular behaviour of the LCC network and voltage source inverter. To simplify the description, an equivalent (and fictitious) series capacitance  $C'_s$  that makes the coils resonate at  $f_1$  is introduced and defined as:

$$C'_s = \frac{1}{\omega_1 L}. \tag{6.28}$$

which describes the overall behaviour of the driver circuit upstream of the coil at the frequency  $f_1$ . As already discussed in both Chapters 4 and 5, an array termination impedance is usually introduced to modify the system behaviour and improve both the efficiency and the transmitted power. Furthermore, in Sec. 6.1 the effect of the termination condition on the input impedance has been discussed, which in this case is the parameter of interest. Thus, it is reasonable to introduce the termination  $\hat{Z}_T$ . However, the coils are designed for high power transfer rates and a further

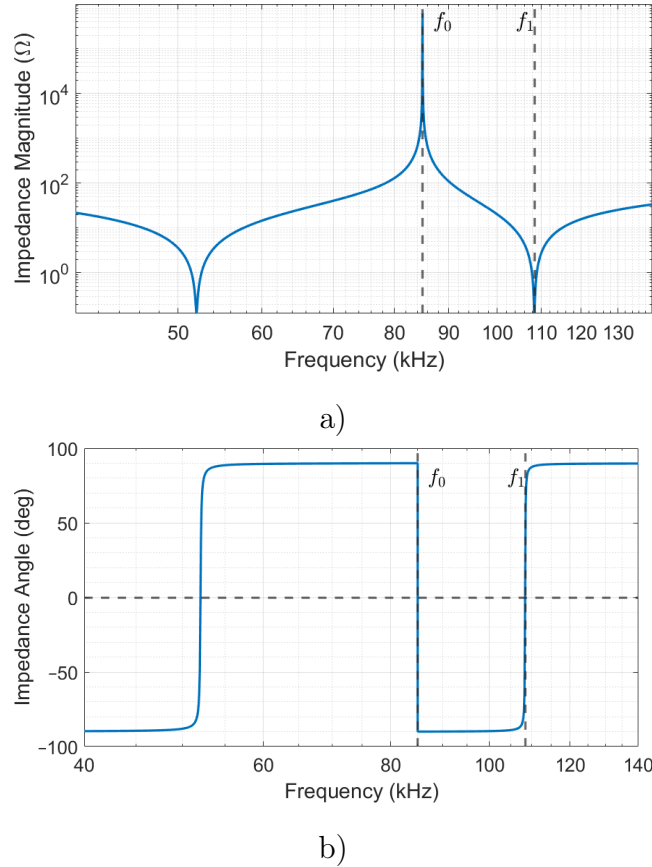


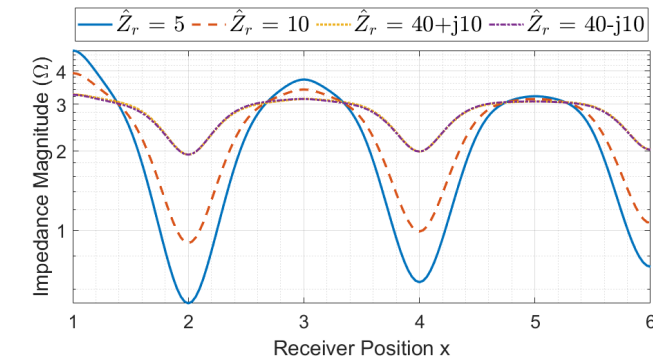
Figure 6.10: **(a)** Magnitude and **(b)** phase of the driver coil impedance  $\hat{Z}$  as a function of the frequency.

impedance may alter the operation of the IPT system at  $f_0$ . As a solution, a small resonator coupled to the last array coil can be introduced at the end of the array, dimensioned such that its reflected impedance acts as termination  $\hat{Z}_T$  at  $\omega_1$ . This additional coil allows the termination of the array to be found as:

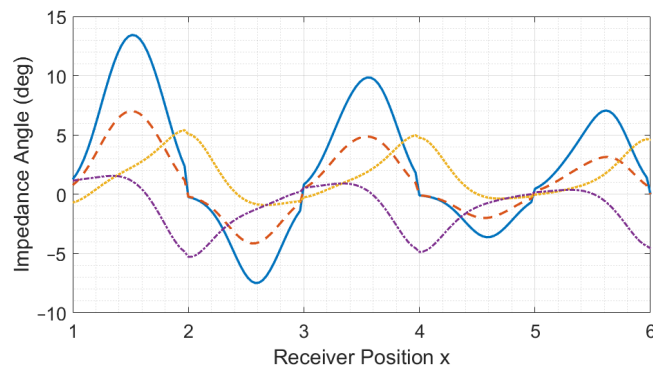
$$\hat{Z}_T = \frac{(\omega_1 M_{ac})^2}{\hat{Z}_{ac}} \quad (6.29)$$

where  $M_{ac}$  is the mutual inductance between the last array coil and the additional coil and  $\hat{Z}_{ac}$  the internal impedance of the additional resonator, which comprises an arbitrary lumped impedance  $\hat{Z}_{acT}$  that can be adjusted to achieve the desired  $\hat{Z}_T$  at  $f_1$ . The circuitry used to realise  $\hat{Z}_{acT}$  must be tailored such that it presents a very high impedance for  $f = f_0$ , so that it does not interfere during charging operations. Moreover, it is important to dimension the additional coil components in order to withstand the voltages induced by the last coil of the array during the IPT operations at  $f_0$ . Indeed, high currents may circulate in the last array coil and therefore induced voltages in the coupled circuits may not be negligible. The receiver impedance  $\hat{Z}_r$  is instead defined by the circuitry downstream it, namely the rectifier, battery charger and the battery itself. Depending on the matching





a)

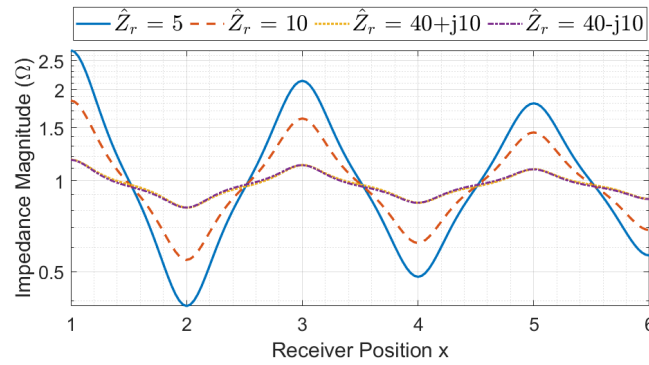


b)

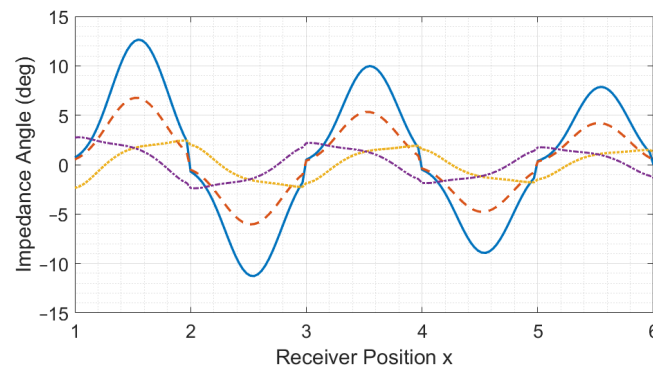
Figure 6.13: Array input impedance as a function of the receiver position with SC termination for different values of load resistance  $\hat{Z}_r$ , in magnitude (a) and phase (b).

line with the range proposed in the SAE standard [3]. The behaviour of the input impedance  $\hat{Z}_{eq}(x)$  is plotted in magnitude and phase in Figs. 6.13–6.15 as a function of the receiver position for different values of receiver impedance  $\hat{Z}_r$ , in case of SC, matched and OC terminations, respectively. In particular, both real and complex values of  $\hat{Z}_r$  have been considered as a comparison.

Similarly to the results of Sec. 6.1.1, the curves result slightly asymmetric. This can be addressed to the peculiar behaviour of  $\hat{Z}_{n-i, \hat{Z}_r}^{eq}$  (the reflected impedance of the coils that follows the one coupled with the receiver), which oscillates between very high and low values depending on the number of resonators of the array it is associated with (in this case  $n-i$ ) and its termination impedance [113]. Indeed, when switching from SC to OC termination, the array behaves as it has one less resonator and the trend of the input impedance is mirrored. This can be appreciated from Figs. 6.13 and 6.15, that show the mirrored trends of the input impedance magnitude, while the phase trends are both mirrored and shifted. Two different situations are thus identified: resonant receiver and non-resonant receiver.



a)

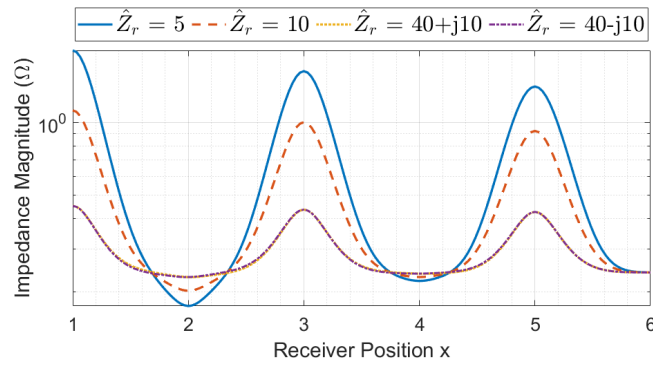


b)

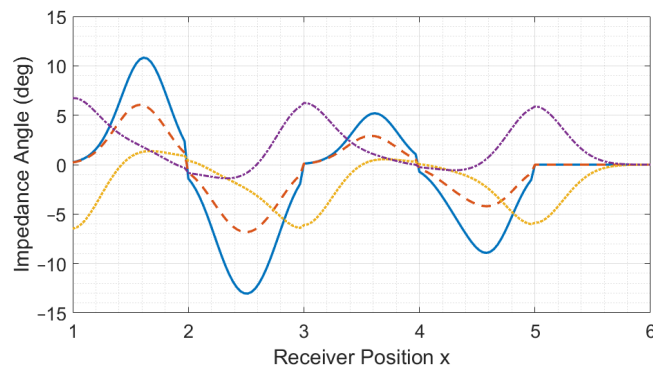
Figure 6.14: Array input impedance as a function of the receiver position with matched termination for different values of load resistance  $\hat{Z}_r$ , in magnitude (a) and phase (b).

**Perfectly Resonant Receiver** In the case of a perfect resonant receiver,  $\hat{Z}_r$  is real, while the array input impedance is still complex in general. In particular, it presents real values only in case of perfect alignment of the receiver, as already discussed in Sec. 6.1.1. Instead, the phase presents the maxima and minima values when the receiver is in between two array resonators and oscillates between positive and negative values. This is common for all the array terminations considered. Again, the lower the receiver load, the higher its influence on the input impedance, whose maxima and minima have larger values.

**Non-Resonant Receiver** For complex  $\hat{Z}_r$ , the maxima and minima of the input impedance magnitude are still found for perfect alignment positions and their values decrease as the receiver approaches the end of the array. The phase reaches the maximum and minimum values when the receiver is perfectly aligned with the facing array coils, resulting in a shifted trend with respect to the case of the resonant receiver. The phase behaviour in case of inductive or capacitive receiver load is mirrored. The change from SC to OC terminations also makes the curve “translate”.



a)



b)

Figure 6.15: Array input impedance as a function of the receiver position with OC termination for different values of load resistance  $\hat{Z}_r$ , in magnitude (a) and phase (b).

For inductive receiver loads, the input impedance presents an inductive behaviour when the receiver is aligned with even-numbered resonators for an SC terminated array and odd-numbered resonators terminating the array in OC. In the case of capacitive receiver load the behaviour is the opposite.

### Input Impedance Trajectory

In view of using it for detecting the receiver locations, the input impedance of the array should present a one-to-one behaviour with respect to the receiver position, meaning that at least the combination of the magnitude and phase of the input impedance is unique for any  $x$ . The trajectory of the input impedance in the complex plane is then studied for different terminations considering the receiver load  $\hat{Z}_r = 40 + j10[\Omega]$ . In Fig. 6.16 the input impedance for an SC terminated array is plotted.

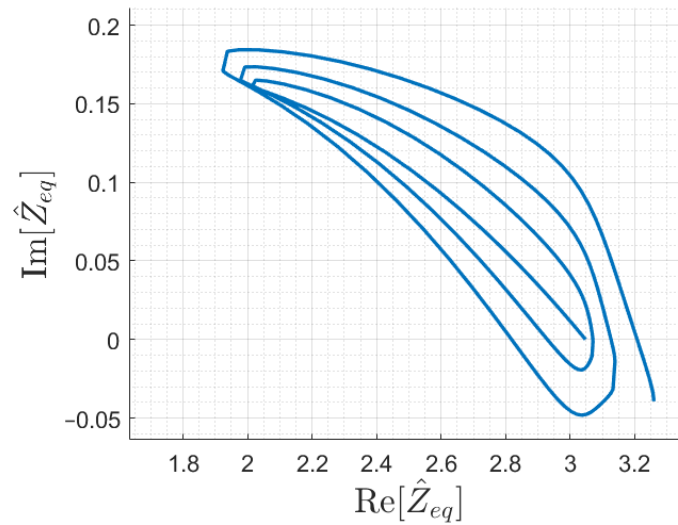


Figure 6.16: Input impedance trajectory as a function of the receiver position for the resonator array with a series-compensated receiver and SC termination.

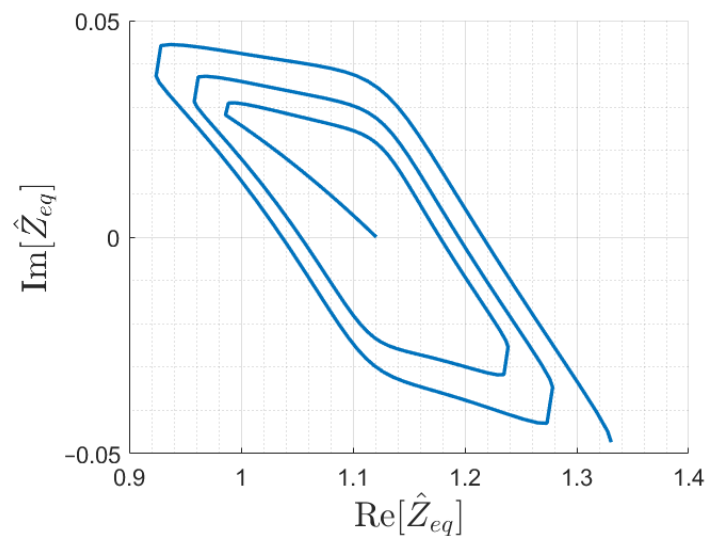


Figure 6.17: Input impedance trajectory as a function of the receiver position for the resonator array with 6 cells and series-compensated receiver, terminated with  $\hat{Z}_T = 0.8\Omega$ .

It is possible to notice that there is an intersection point. This means that the same complex input impedance value is possible for multiple receiver positions along the array. Intersections still occur even adopting the other usual terminations, namely OC and matching impedance. However, to ensure univocity, simulations proved that other terminations are required. In particular, for the considered system,  $\hat{Z}_{Tl} \approx 0.8\Omega$  can avoid intersections, and corresponds to  $\hat{Z}_{Tl} \approx \hat{Z}_{match}/2$ . The one-to-one behaviour is proved by the impedance trajectory of Fig. 6.17 for a

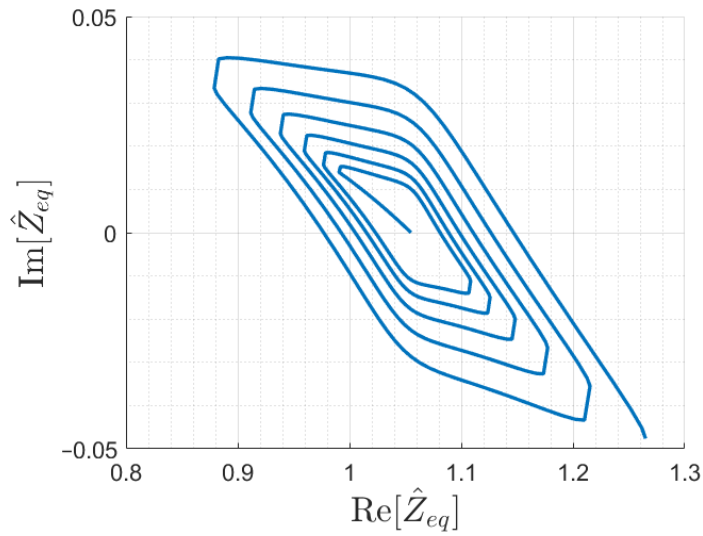


Figure 6.18: Input impedance trajectory as a function of the receiver position for the resonator array with 12 cells and series-compensated receiver, terminated with  $\hat{Z}_T = 0.8\Omega$

resonator with 6 cells, and has been verified also for a longer array of 12 cells as shown in Fig. 6.18.

### 6.3.2 Simplified Receiver Location Algorithm

The basic and most intuitive algorithm to detect the receiver position from the array input impedance has been described in Sec. 6.2.3. It can be done measuring its amplitude as the ratio between the first coil voltage and current at the frequency  $f_1$  and its phase with additional circuits, such as a PLL [153] or from the FFT (see Sec. 6.2.3).

However, being the resonator array devoted to dynamic IPT, it is possible to assume that:

- starting from the first one, the receiver couples consecutively with all the array coils;
- the function  $|\hat{Z}_{eq}(x)|$  is monotonic in the interval between two positions of perfect alignment.

First, it can be noticed that each time the receiver couples with a new array coil, the slope of the input impedance magnitude reverses. Thus, from the first assumption, it follows that the  $i$  and  $(i+1)$  resonators coupled with the receiver can be identified considering the number of changes in the sign of the derivative of the input impedance magnitude. The check of the function derivative can be easily done by evaluating the difference between function values at consecutive positions as:

$$\Delta\tilde{Z}_k = \tilde{Z}_{k+1} - \tilde{Z}_k \quad (6.30)$$

where  $\tilde{Z}_k$  and  $\tilde{Z}_{k+1}$  are the estimated impedance values associated with two successive positions  $x_k$  and  $x_{k+1}$ , respectively. Thus, when the vehicle enters the array, the receiver couples to the first array coil and so  $i = 1$ . Then, each time the sign of  $\Delta\tilde{Z}_k$  changes the position  $i$  and  $i+1$  can be updated.

From the second assumption, according to which the input impedance magnitude can be assumed monotonic for each pair of resonators coupled to the receiver, it follows that  $|\hat{Z}_{eq}(x)|$  is sufficient to estimate the receiver position  $x$ . In this manner, the detection of the receiver position, for which the calculated input impedance matches the estimated one, can be limited to the correct coil interval where  $|\hat{Z}_{eq}(x)|$  is monotonic. Once the coupled resonators  $i$  and  $i+1$  are found, the position  $x$  can be determined through (6.1) and enforcing (6.14).

---

**Algorithm 1** Receiver coil position detection

---

```

 $\tilde{Z}_0 = 0$ 
 $k = 1$ 
 $i = 1$ 
while  $x < nd$  do
    Acquire  $\tilde{Z}_k$ 
    if  $sgn[\Delta\tilde{Z}_k] \neq sgn[\Delta\tilde{Z}_{k-1}]$  then
         $i = i+1$  ▷ Change of coil
    end if
     $\xi = 0$ 
    while  $\| \tilde{Z}_k - |\hat{Z}_{i,i+1}^{eq}(\xi)| \| > \delta_Z$  do
         $\xi \leftarrow \xi + \Delta x$ 
    end while
     $x_k = x_{k-1} + \xi$ 
     $k = k+1$ 
end while ▷ End of array

```

---

In the event that the algorithm is used to determine which coil has to be activated for the power transfer, it is sufficient to know only which coils  $i$  and  $i+1$  it couples to. The basic algorithm is described with the pseudo-code shown in Algorithm 1.

The effective accuracy of the measurements is defined by the sensitivity parameters, as already discussed in Sec. 6.2.2. They are strongly affected by the geometry of the windings, which must be tailored based on the discretisation step and the number of array coils.

This algorithm for estimating the position of the receiver (or even just the coils coupled to it) can be performed in a limited number of operations. The measurement of the current and voltage can be done as described in Sec. 6.2.3. The computational power of modern DSPs guarantees very short calculation times and therefore the possibility of running these algorithms even in the presence of moving vehicles. At each algorithm run, the input impedance is calculated in one complex operation.

A vehicle travelling at 100 km/h travels at about 28 m per second. Considering, for example, a spatial discretisation  $\Delta_x$  of 5cm, the time available to the DSP for the calculation is about 18 ms, much higher than that required one for a single run of the algorithm.

## 6.4 Conclusions

The possibility of employing resonator arrays with a receiver (or a generic coupled external coil) as a passive sensor is proposed and discussed. It is applicable to any longitudinal array structure of magnetically coupled resonators and allows the external coil position to be estimated by measuring the array input impedance. This technique can be implemented in arrays specially developed as sensors, which can be introduced in systems with moving mechanical parts. Requiring little power, it is therefore possible to create arrays with inductors printed on flexible PCBs, which can be easily installed wherever desired. Attention should be paid when there are metal parts in the surrounding structure, which can modify the parameters of the resonators. It is however possible to consider these variations in the sensor calibration phase. Alternatively, the proposed technique can be implemented in systems devoted to IPT. In this framework, two possible systems can be considered: resonator arrays for IPT, in which only the first coil is powered, and resonator arrays with a driver circuit for each resonator. In the first case, the termination impedance can be read from the source coil with appropriate current and voltage sensors, knowing the voltage and therefore the equivalent load of the receiving system. Note that feedback from the receiver is always needed to check the input voltage properly. As a second case, the possibility of detecting the receiver location in dynamic IPT systems for automotive applications has been discussed, that can be implemented using the same structure of the system, therefore in a non-invasive way. This is possible only by introducing a suitable high-frequency impedance measurement system consisting in a current and voltage sensor with a DSP for the post-processing and impedance estimation. The effectiveness of this method has been proved considering a dynamic IPT system selecting the component parameter values in line with the SAEJ2954 standard, being the dynamic IPT not standardised yet. However, in order to make both the IPT and position sensing system work without interference, it was necessary to characterise the transmitting circuit of each coil and not only the compensation networks typically employed can be allowed. To implement this technique in automotive systems it is necessary to properly dimension the apparatus considering to satisfy both the requirements of the IPT system and that for the location of the receiver.



## Chapter 7

# 2D Resonator Arrays in IPT Systems: Considerations for Future Works

This chapter illustrates and discusses the results obtained from preliminary studies on 2D resonator arrays in IPT systems. The basic ideas for future developments are therefore illustrated and supported with the basic numerical simulations of 2D structures of magnetically coupled resonators used in IPT apparatuses. As already discussed in the Introduction, these types of structures are used for several purposes. Even focusing only on IPT systems, 2D resonator arrays find different applications based on how they are dimensioned and located in the apparatus. In particular, the most intuitive application (and the first to be analysed here) is to use these structures as transmitters to power one or more receivers which can be placed at any position on the plane. In this context, the 2D array can be seen as the extension of the one-dimensional array. 2D arrays can also be introduced into traditional two-coil systems, to increase efficiency in misalignment conditions and/or shield the magnetic field in certain regions of space. These two possible applications are also briefly explored. In these contexts, they are introduced in place of natural materials and, due to their exotic magnetic properties, are also named metamaterials. It can be seen that, in general, near-field 2D resonator arrays are modelled as coupled resonant circuits and, therefore, the theoretical approach is the same for all this kind of structures.

### 7.1 2D Resonator Arrays for IPT

In Chapter 4, resonator arrays have been discussed extensively, especially when used to power a receiver. It has been shown that, especially when appropriate control techniques are adopted, power can be efficiently transmitted to a load connected to the receiver. It is easy to think of introducing more coupled resonators also

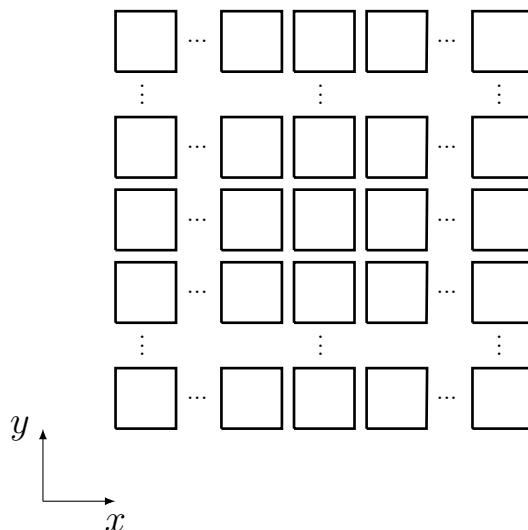


Figure 7.1: Schematic representation of a 2D array of resonators.

in other directions of space, to form a plane. In this way, by feeding even just one of the resonators of the 2D array, the whole structure is energised and each coil experiences a circulating current, that in turn generates a magnetic field. A receiving circuit connected to a load can therefore ideally receive power in any point of the plane. However, similarly to the case of 1D arrays, the currents in the resonators do not all have the same amplitude and are strongly influenced by the topology of the system, i.e. the circuit parameters, the power source connection point and the load value. Thus, the original structure requires to be modified to obtain the desired performance, by deactivating the appropriate resonators [61], changing their structures [63] or overlapping different arrays fed in several different points [62]. These solutions have been recently introduced and allow the distribution of the currents to be somehow controlled, with the ultimate aim of improving the performance in terms of transmitted power and efficiency in every point of the region covered by the plane. As first step, the suitable model to represent the system must be established.

## 7.2 Currents in 2D Resonator Arrays

Being the physical phenomena identical to those exploited in 1D resonator arrays, 2D resonator arrays can be modelled by means of the circuit theory and magneto-inductive waves. To discuss the models, a 2D array composed of  $N$  resonant RLC coils immersed in a linear medium and arranged to form a square lattice is considered, as represented in Fig. 7.1. The relation between the currents circulating in the loops can be found applying the KVL to each coil, considering operations in sinusoidal steady-state. The resulting system of equations can be expressed in

matrix form as:

$$\hat{\mathbf{V}} = \hat{\mathbf{Z}}_{\mathbf{M}}\hat{\mathbf{I}} \quad (7.1)$$

where  $\hat{\mathbf{Z}}_{\mathbf{M}}$  is the impedance matrix of the system,  $\hat{\mathbf{I}}$  is the vector of the phasor currents flowing in the resonators and  $\hat{\mathbf{V}} = [0\dots 0\hat{V}_s 0\dots 0]^T$  is the phasor voltage vector with  $\hat{V}_s$  the phasor supply voltage. Rigorously, the impedance matrix should include the coupling coefficients between all the coils composing the metamaterial [64] and is defined as:

$$\hat{\mathbf{Z}}_{\mathbf{M}} = \begin{bmatrix} \hat{Z}_{11} & j\omega M_{12} & j\omega M_{13} & \cdots & j\omega M_{1N} \\ j\omega M_{21} & \hat{Z}_{22} & j\omega M_{23} & \cdots & j\omega M_{2N} \\ \vdots & \vdots & \vdots & \vdots & \vdots \\ \vdots & \vdots & \vdots & \vdots & j\omega M_{(N-1)N} \\ j\omega M_{N1} & \cdots & \cdots & j\omega M_{N(N-1)} & \hat{Z}_{NN} \end{bmatrix}. \quad (7.2)$$

The impedance of the generic  $m$ th cell of the array results:

$$\hat{Z}_{mm} = R_{mm} + j\omega L_{mm} + \frac{1}{j\omega C_{mm}} \quad (7.3)$$

where  $R_{mm}$  is the resistance,  $L_{mm}$  the self-inductance and  $C_{mm}$  the capacitance of the  $m$ th coil. The desired value of this last parameter can be obtained by connecting lumped capacitors to the coil or exploiting the coil self-capacitance with a proper design. In particular, for low-frequency applications (up to a few GHz) the self-capacitances of the unit cells are too small and lumped capacitors are required to make the coils resonate at the desired frequency. In planar structures, the magnetic interaction of coplanar-coupled coils is characterised by a negative mutual inductance. In the majority of the applications, 2D resonator arrays are designed to form periodic lattices and thus all the coils are identical and positioned such that their mutual inductance coefficients are the same for pairs of resonators in symmetric positions with respect to the axis of the plane (that is the axis of the central resonator). The 2D array is considered excited in the central resonator with a sinusoidal voltage  $\hat{V}_s$ . The resonators are characterised by a resistance  $R = 0.015 \Omega$  and self-inductance  $L = 0.4 \mu\text{H}$ , whereas a lumped capacitance  $C = 60 \text{ nF}$  is chosen to make the system resonate at the frequency  $f_0 = 1 \text{ MHz}$ .

The distribution of the surface currents in 2D resonator arrays is dominated by the resonator mutual couplings and quality factor  $Q = \omega_0 L/R$ , whose impact is different depending on the lattice extension.

In general, the resonator resistance, self- and mutual inductances depend on the operating frequency due to skin and proximity effects, and these phenomena emphasise as the frequency increases. However, when considering resonators made of stranded-wire wound coils, those parameters can be considered frequency independent up to few MHz. In this condition, still considering the 2D array-unit cells perfectly resonant, it is possible to notice that the resistance, self- and mutual inductances depend on the system geometry only.

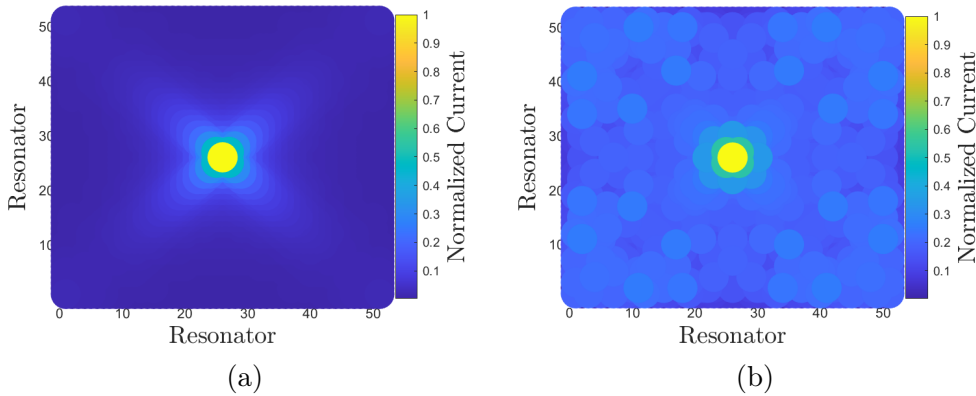


Figure 7.2: Current distribution of a  $51 \times 51$  2D array excited in the central resonator considering the interaction of each coil in case of (a)  $Q = 40$  and (b)  $Q = 260$  at the frequency  $f_0$ .

### 7.2.1 Effect of the resonator quality factor on current distribution

At a fixed frequency, different quality factors lead to different current distributions and this effect can be particularly appreciated as the extension of the 2D array increases. Considering a full impedance matrix  $\hat{\mathbf{Z}}_{\mathbf{m}}$  (all coils interact), for low-quality factors (i.e.,  $Q < 100$ ), obtained by increasing the resonator resistance or decreasing the operating frequency, the resonators laying on the diagonal of the lattice experience higher currents (see Fig. 7.2a). In particular, the current gradually decreases from the resonators closer to the power source towards the boundary ones, which experience a nearly null current amplitude. Reversely, as  $Q$  increases it is difficult to predict and control the current distribution, as shown in Fig. 7.2b. Indeed, while the central resonators still experience higher currents, the current distribution presents maxima and minima spread among all the lattice unit cells, whose locations are not known *a priori*. Intuitively, the above mentioned behaviour can be explained considering that the current distribution originates from the fed resonator (the central one in this case) and spreads to surrounding unit cells thanks to their mutual couplings, limited by the resonator resistance. A lower quality factor leads to stronger attenuation of the currents and, as a limit case, no current flows in the resonators furthest from the powered one. In this condition, these furthest cells do not affect the current distribution. In case of higher quality factors, all the lattice unit cells contribute to the resulting current distribution. According to [64, 67, 121, 61], this behaviour is analogous to the one of a current wave, which originates at the centre of the 2D array and diffuses in the lattice, which can be considered the medium. If the wave reaches the boundary of the medium, reflections occur, thereby leading to standing wave patterns. This phenomenon can be identified in Fig. 7.2b, where the resonators are characterised by a high  $Q$ . In case the medium presents a higher attenuation, the wave presents a very low amplitude at

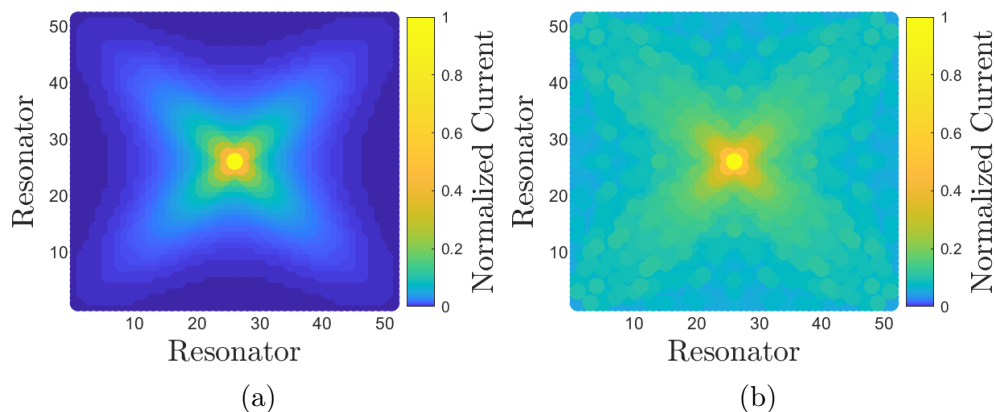


Figure 7.3: Current distribution of a  $51 \times 51$  2D array with (a)  $Q=25$  and (b)  $Q=170$ , excited in the central resonator considering all couplings between coils. The values have been normalised to the current of the central resonator.

the boundary and its reflections can be considered negligible. This occurred in a 2D array with low  $Q$ , whose current distribution is plotted in 7.2a. It must be noticed that in case of a sufficiently attenuated medium (so that the currents are null in the boundary resonators) it is possible to appreciate the propagation characteristic of this kind of wave, which tends to follow the diagonals of the lattice.

### 7.2.2 Effect of couplings on current distribution

Different models can be adopted to describe the 2D array behaviour. Although the most intuitive and most accurate evaluation of the current distribution can be obtained considering the full impedance matrix, simplified models allow a dramatic reduction of the computational effort and also allow the analytical description to be simplified. The models are compared considering  $51 \times 51$  2D array with high and low  $Q$  resonators to emulate an infinitely extended lattice (to appease the effect of the boundary unit-cells).

**All couplings between coils (full model)** When all the couplings between coils are considered the impedance matrix  $\hat{Z}_M$  is fully populated and the resulting current distribution is depicted in Figs. 7.3 for 2D resonator arrays with low quality factor ( $Q=25$ ) and large quality factor ( $Q=170$ ). The currents are normalised with respect to the one of the central resonator, which presents the highest value. Besides the centre, the resonators on the diagonals of the lattice tend to experience higher currents. This behaviour is more accentuated in the case of large  $Q$  2D array. In case of low  $Q$ , current maxima are spread among more cells.

**Adjacent Couplings only** The couplings between nonadjacent resonators can be neglected since the mutual inductance between two coils dramatically decreases

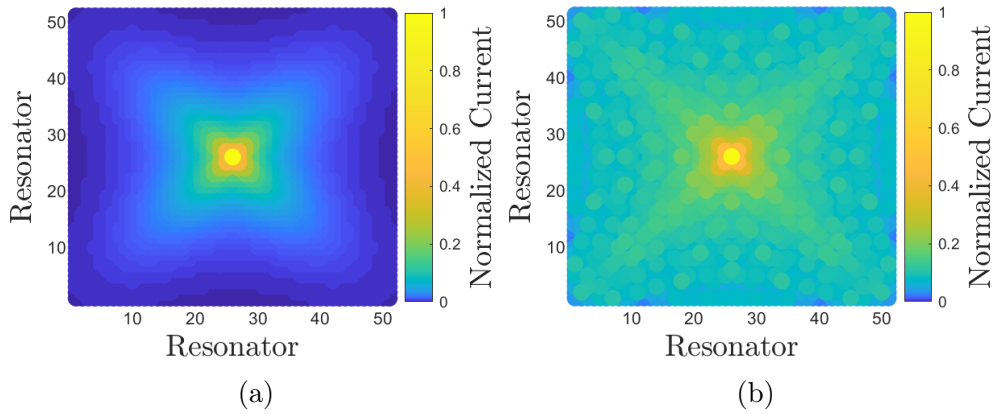


Figure 7.4: Current distribution of a  $51 \times 51$  2D array with (a)  $Q=25$  and (b)  $Q=170$ , excited in the central resonator considering the couplings between adjacent coils in the  $x$ ,  $y$  and diagonal directions of the lattice. The values have been normalised to the current of the central resonator.

as their distance increases, allowing  $\hat{\mathbf{Z}}_{\mathbf{m}}$  to be extremely simplified. Then, a first approximation consists in considering only the couplings between adjacent resonators in all ( $x, y$  and diagonal) directions. The current distribution is governed by the resonator mutual coupling  $M_{adj}$  along the  $x$  and  $y$  directions and  $M_{diag}$  along the diagonal directions. The current distribution obtained with this approximation is shown in Fig. 7.4 for 2D resonator arrays with small ( $Q = 25$ ) and large ( $Q = 170$ ) quality factors, respectively. The highest values of the current are found in the same positions as in the full model, although the values are slightly different. For the large and low  $Q$  arrays the current still concentrates along the diagonals, although this tendency is less pronounced than in the previous case. A higher  $Q$  leads to localised maxima and minima (see Fig. 7.4).

### Nearest-Neighbour Approximation and Magneto-Inductive Waves

Being  $M_{adj} \gg M_{diag}$ , a further approximation consists in neglecting the coupling between coils along the diagonals. With this assumption, referred to as "nearest-neighbour" approximation,  $\hat{\mathbf{Z}}_{\mathbf{m}}$  simplifies and the distribution of the currents is governed by the resonators-mutual couplings along the  $x$  and  $y$  directions of the space only. With this approximation the currents of resonators lying on the lattice diagonals markedly present the higher values for both the considered 2D resonator arrays, as it is shown in Fig. 7.5 for 2D resonator arrays with small (25) and large (170)  $Q$ , respectively. Under this approximation, the current distribution can be considered the result of the propagation of the MI wave [64, 67], for which the attenuation per cell can be written as [64]:

$$\alpha = \frac{1}{d} \sinh^{-1} \left( \frac{1}{2kQ} \right) \quad (7.4)$$

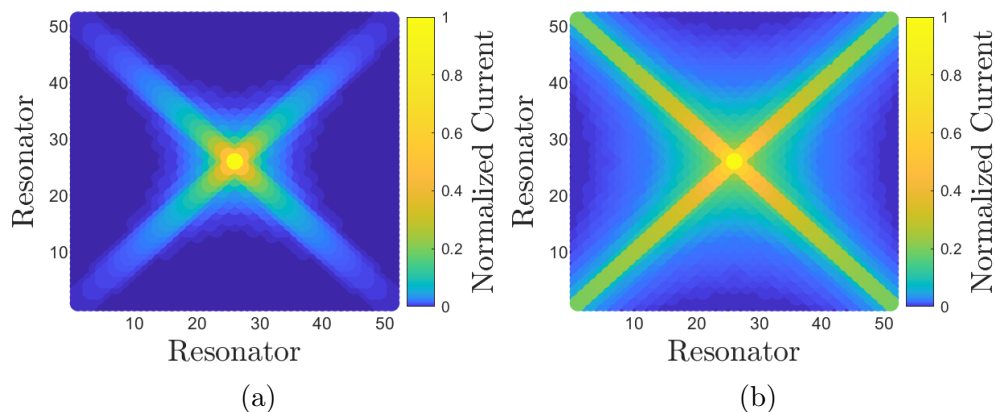


Figure 7.5: Current distribution of a  $51 \times 51$  2D array with (a)  $Q=25$  and (b)  $Q=170$ , excited in the central resonator considering the nearest-neighbour approximation. The values have been normalised to the current of the central resonator.

where  $k = 2M_{adj}/L$  is the coupling coefficient between adjacent cells in the directions  $x$  and  $y$ . With this definition, it is easy to see how low values of quality factors and coupling coefficients emphasise the attenuation of the current wave. The MI wave attenuation is proportional to the resistance  $R$  of each unit cell and becomes stronger as the coupling between the resonators weakens. A wave-based model allows a clear explanation of the obtained results when the 2D array emulates an infinite lattice, while it appears inaccurate in case of small and weakly attenuated 2D arrays. The current distribution can be considered the result of the superposition of forward and backward current waves, where the latter originate at the boundary of the 2D array. As it happens in finite traditional waveguides, standing wave patterns can arise, leading to local maxima and minima of the current [68, 61, 121]. It must be noticed that, in practical applications [63, 55], the extension of the 2D array is limited and the unit cells are designed to present high  $Q$  to avoid losses. The current distributions of a  $5 \times 5$  resonator array with  $Q=170$  are reported in Figs. 7.6a-7.6c considering all couplings between coils, the couplings between adjacent coils in the  $x$ ,  $y$  and diagonal directions, and the nearest-neighbour approximation, respectively. It can be seen that the results obtained with both the approximated models are unacceptable. In fact, even if the current distributions in the approximated cases recall the one obtained with the full-couplings model, for some resonators the difference can be even 40 %. In particular, the model that considers the couplings between adjacent coils in the  $x$ ,  $y$  and diagonal directions yields very high currents in the corner resonators and in those in the centre of the sides (in addition to the fed one), while in the nearest-neighbour approximation the highest current values occur in diagonal resonators. Taking as a reference the current distributions obtained with the full-coupling model, we can therefore conclude that the simplified model that considers the couplings between adjacent coils in the  $x$ ,  $y$  and diagonal directions leads to reliable results for extended 2D resonator arrays, while when these are

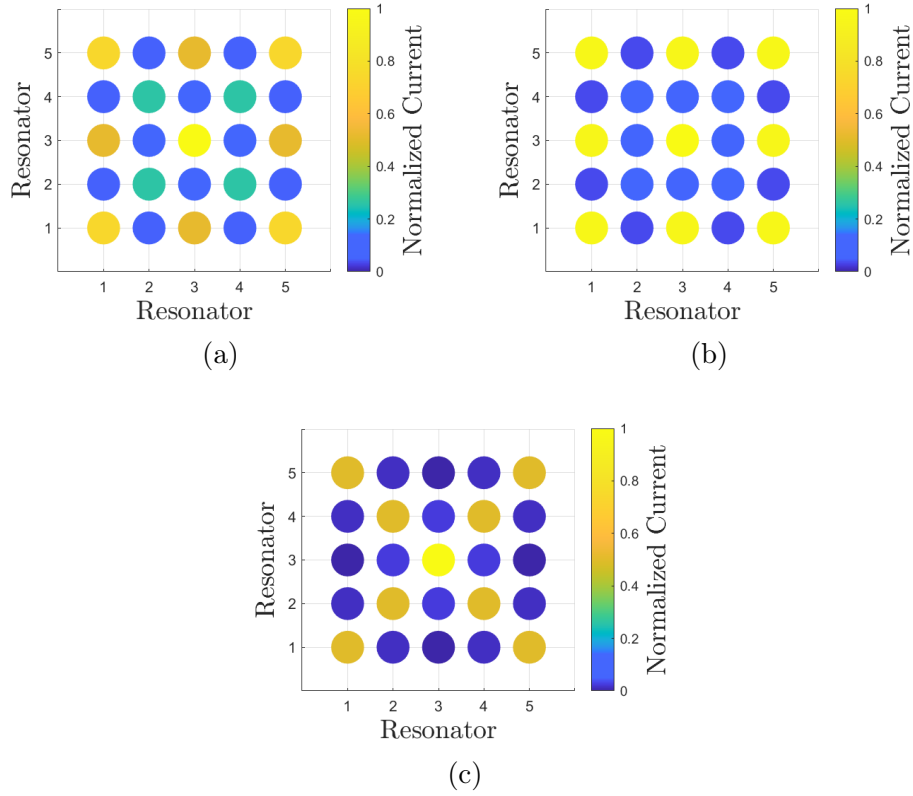


Figure 7.6: Current distribution of a  $5 \times 5$  2D array with  $Q=170$  excited in the central resonator considering: (a) all couplings between coils, (b) the couplings between adjacent coils in the  $x$ ,  $y$  and diagonal directions and (c) the nearest-neighbour approximation. The values have been normalised to the current of the central resonator.

limited (somehow related to the wavelength  $\lambda_{MIW} = 4d$  of the MI wave) the error increases (see Fig. 7.6). In the nearest-neighbour approximation is in any case difficult to consider the resulting current distribution acceptable, both for very large and nonlarge 2D resonator arrays. Thus, it is difficult to predict and control the current amplitude distribution.

### 7.2.3 Controlling the Resonator Currents: Terminated 2D Array

Similar to the one-dimensional case it is possible to think of terminating the lattice to control the current distribution. Two types of termination impedances are considered, that are  $\hat{Z}_{T_s}$  for the side resonators and  $\hat{Z}_{T_c}$  for the corner resonators, as depicted in Fig. 7.7. As an example, it is possible to try to obtain the same current magnitude in all the resonators, in view to powering different receivers that can be coupled with a cell. However, modelling the system based on the circuit theory clearly requires the KVLs are fulfilled. The KVL for the generic  $m$ th resonator can

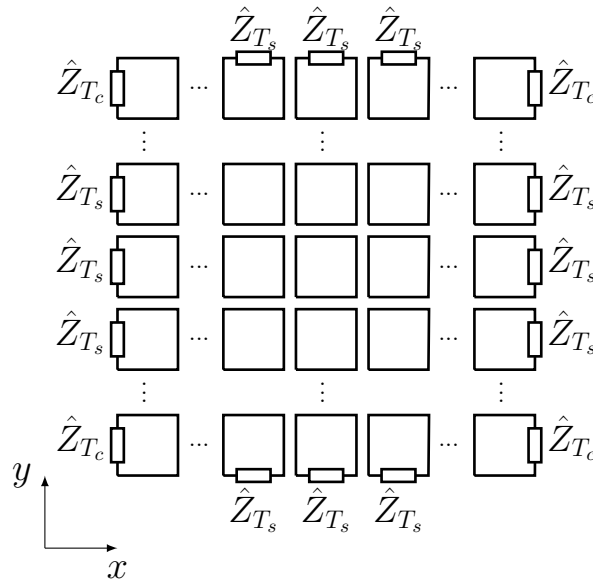


Figure 7.7: Schematic representation of the 2D array of resonators.

be written as:

$$0 = \hat{Z}_{mm}\hat{I}_{mm} + \sum_k^N j\omega_0 M_{mk}\hat{I}_k \quad (7.5)$$

where  $\hat{Z}_{mm}$  is the self-impedance of the coil and  $M_{mk}$  the mutual inductance between the  $m$ th and  $k$ th coil. Assuming the same phasor current  $\hat{I}$  for all the resonators, (7.5) becomes:

$$\hat{Z}_{mm} = -j\omega_0 \sum_k^N M_{mk}. \quad (7.6)$$

This condition can be met only with an accurate design of the lattice resonators, which may present different impedance values at the operating angular frequency  $\omega_0$  of the source coil or, in other words, they may result tuned at different resonant frequencies. However, assuming the unit-cells tuned at the same resonant frequency  $f_0$ , the imaginary part of their impedance is null, and (7.6) reduces to:

$$\text{Re}[\hat{Z}_{mm}] = -j\omega_0 \sum_k^N M_{mk} \quad (7.7)$$

which cannot be fulfilled being the left-hand-side term always real and the right-hand-side term always complex. This equation clearly indicates that a lossy lattice with equally resonant cell does not allow the same current in all the resonators.

**Lossless and Nearest-Neighbour Approximation** In nearest-neighbour approximation, it is assumed that resonators are coupled with their nearest ones only. In a square lattice, four couplings are then considered for a generic resonator out of the boundary and are characterised by the same mutual inductance  $M$ . In general, the condition (7.6) dramatically simplifies to:

$$\hat{Z}_{mm} = -j4\omega_0 M. \quad (7.8)$$

which indicates that the overall impedance has to compensate the induced voltage by near unit-cells. It must be noticed that this condition cannot be satisfied in case of perfect resonance operation, being (7.8) a special case of (7.6).

### 7.2.4 Optimisation Procedure

The KVLs show that it is not possible to obtain the same phasor current in each resonator, but they allow all the cells experience the same current magnitude, here named  $I$ . The phases of the cell currents are different and have values such that the KVL equations are satisfied. The numerical calculation of the termination impedances for achieving the same current in each cell is addressed as an optimisation problem, that consists in finding the values of  $\hat{Z}_{T_s}$  and  $\hat{Z}_{T_c}$  that minimise the normalised standard deviation  $\sigma_I$  of the resonator current magnitudes. It is a single-objective optimisation problem of two complex variables and it can be expressed as:

$$\min_{\hat{Z}_{T_s}, \hat{Z}_{T_c}} \sigma_I. \quad (7.9)$$

Thus, the objective function of the problem is the normalized standard deviation  $\sigma_I$ , which is defined as:

$$\sigma_I = \frac{1}{\mu_I} \sqrt{\frac{1}{N} \sum_k (|\hat{I}_k| - \mu_I)^2} \quad (7.10)$$

where

$$\mu_I = \frac{1}{N} \sum_k |\hat{I}_k| \quad (7.11)$$

is the mean value of the resonator current magnitudes. When  $\sigma_I \approx 0$ , the corresponding  $\mu_I$  can be considered the value of each resonator current magnitude  $I$ .

The problem has been solved implementing a Particle-Swarm Optimization (PSO) algorithm, which found the value of the four varying parameters, namely the real and imaginary parts of the edge and corner termination impedances. The calculation has been performed considering a sinusoidal input voltage of 1 V at  $f_0$ . After a first heuristic evaluation of possible limits for the parameter values, the variation range of each variable has been set to  $[-10,10]$  in order to leave the algorithm free to operate. Due to its stochastic nature, each run of the PSO algorithm provides different optimised parameter values, still ensuring convergence. Being the optimal

impedance values strictly correlated, to statistically reduce the uncertainty on the results several runs have been performed. Then, a clusterization procedure allowed the most recurrent solutions to be identified. In particular, the so called “k-means” algorithm has been implemented to group the results of the 200 PSO runs. This procedure partitions the 200 quaterns of values in  $k$  clusters minimising the difference between the quatern values and the cluster mean (named “centroid”), also ensuring the minimum within-cluster variance. For all the considered metasurfaces, it is found that the convergence is reached faster if the full model is used, at the cost of a higher residual  $\sigma_I$ .

Table 7.1: Simulation results.

$\hat{Z}_{T_s}$ [ $\Omega$ ]	$\hat{Z}_{T_c}$ [ $\Omega$ ]	$\sigma_I$	Observations
0.271-j0.154	-0.587-j0.195	0.0167	134
0.082+j0.128	-0.04+j10	0.24	1
-0.31-j0.12	0.474-j0.137	0.061	65

The results are summarised in Tab. 7.1, in which the optimum values for  $\hat{Z}_{T_s}$  and  $\hat{Z}_{T_c}$  with the corresponding normalised standard deviation  $\sigma_I$  are reported for a  $5 \times 5$  array. The map of the normalised currents obtained with the termination set that presented the highest number of observations in the clusters confirms the result, and it is shown in Fig. 7.8. However, the real part of the termination impedances, which is interpreted as a resistance, often results negative. In practical applications this condition can be met by means of active devices only, such as OP-AMP based circuits or thyristors. From our analysis, we noticed that within the realisations of the applied algorithm, sub-optimal results can be obtained in terms of current’s uniformity, resulting in termination impedances also having a positive real part, thereby indicating that passive components could be sufficient to terminate the lattice, at the cost of a higher  $\sigma_I$ . It is also important to note that the presence of a receiver can lead to an alteration of the current distribution in the array, based on the coupling and the power transferred. In any case, the procedure can be repeated by incorporating one or more receivers into the system model. Furthermore, it is planned to test other types of optimisation procedures, with the aim of maximising the current in certain arbitrarily chosen resonators. It is also worth mentioning that a terminated 2D array can be designed for achieving a uniform magnetic field over it [154]. A similar optimisation procedure has been implemented, whose objective function calculates the average magnetic field in the desired area.

### 7.3 2D Resonator Arrays as Metamaterials

In near-field systems, the most promising applications of 2D resonator arrays can be considered the magnetic field focusing and shielding. Several articles testify to the effectiveness of these arrays in improving the coupling of loosely coupled

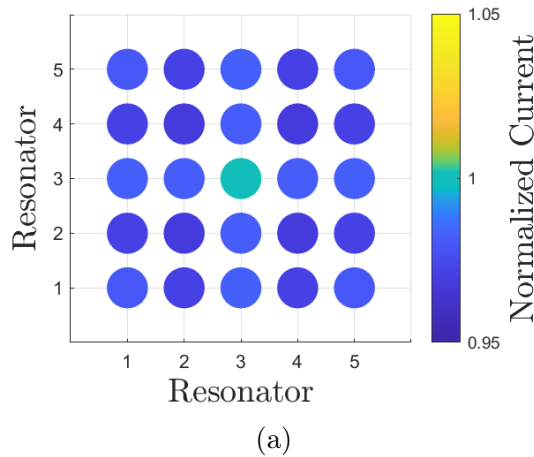


Figure 7.8: Current distribution of a  $5 \times 5$  metasurface excited in the central resonator considering all couplings between coils. The values have been normalised to the current of the central resonator.

resonators and hence the power transfer efficiency [57], as well as to attenuate the magnetic field in a certain region of the space. Their use mainly concerns high-frequency systems, where traditional materials (such as ferrites) are not used, due to the high losses they introduce and their weight [55, 57]. Acting as substitutes for traditional materials, 2D resonator arrays have been modelled as homogeneous slabs, based on their interaction with the electromagnetic field. The homogeneous slab is characterised by a Lorentzian-like complex magnetic permeability, that can present a magnitude lower or greater than that of the vacuum  $\mu_0$  depending on the frequency, as extensively discussed in [50]. This clearly means that, for a fixed system structure, the overall effect of the metamaterial on the magnetic field depends on the operating frequency at which the metamaterial cells are forced to work. This kind of behaviour is typical of both single coils and arrays of resonant coils. From a structure of coupled resonators is still possible to reduce the system to a unique circuit, as discussed in [56]. Thus, an equivalence is established between metamaterials, single resonant coils and natural materials characterised by a Lorentzian magnetic permeability.

The main characteristic is that the metasurface resonators are usually tuned to work at the same frequency, although each resonator can be tuned differently. The majority of the applications consider periodic metamaterials, i.e. all the resonators have the same self-inductance and capacitance (this latter can be lumped or distributed). Nonperiodic structures have been investigated in [155], which shows how the control of the resonator currents is possible with the appropriate tuning of the cells. The behaviour of the currents is reflected in the magnetic field and, consequently, in the efficiency of the IPT system. It must be noticed that, despite the resonators can resonate at a different frequency, the whole array can still be reduced to a unique equivalent R-L-C coil, as described in [56]. Thus, the associated magnetic permeability still presents the peculiar behaviour described by the Lorentz

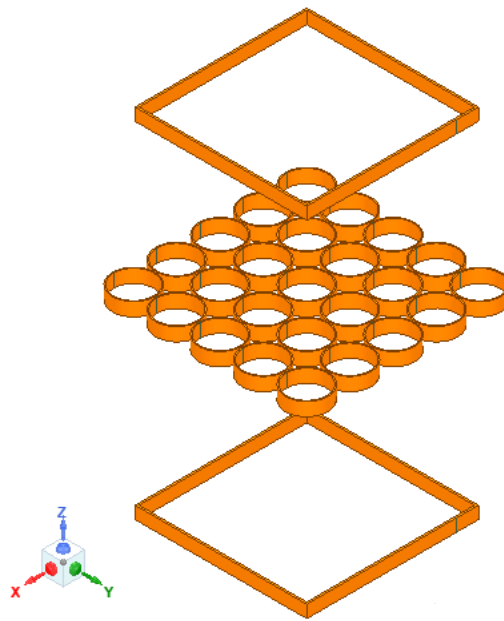


Figure 7.9: Isometric view of the system composed of a transmitter and a receiver square wound coils with the interposed  $5 \times 5$  array made of round wound coils.

dispersion model.

The possibility of different tuning of metamaterials cells has been here briefly explored for the magnetic field focusing and shielding. In particular, an optimisation procedure is defined to find the optimal tuning of each resonator.

### 7.3.1 Metamaterial for Magnetic Field Focusing

As a preliminary study, an array of  $5 \times 5$  magnetically coupled resonators has been considered. Each cell is formed by a winding of 12 turns made of a Litz wire conductor with 1mm in diameter, series connected to a lumped capacitor whose capacitance is found through an optimisation procedure. The transmitting and receiving coils are identical. They are realised with 6-turn square windings of 153 mm side length. The stranded wire conductors have a section of  $2.5 \text{ mm}^2$ . The lumped capacitors connected to the coils are chosen to make the coils resonate at  $f_0=85\text{kHz}$ . The metamaterial slab is interposed between the transmitter and receiver circuit, at different axial distances. The resulting system is depicted in Fig. 7.9. The calculation of the coil self- and mutual inductances is performed with a commercial software based on the finite element method (FEM). In particular, to reduce the complexity of the model and therefore reduce the calculation effort, the coils have been simulated considering their equivalent single-turn thick model. The equivalence is established enforcing that the current density in the multi- and single-turn coil models is the same, as described in Appendix A. From the FEM

simulations, the mutual inductance matrix  $\mathbf{M}_M$  is extracted, which is defined as:

$$\mathbf{M}_{M_{tot}} = \begin{bmatrix} L_{11} & M_{12} & M_{13} & \cdots & M_{1N} & M_{1R_x} & M_{1T_x} \\ M_{21} & L_{22} & M_{23} & \cdots & M_{1N} & M_{2R_x} & M_{2T_x} \\ \vdots & \vdots & \vdots & \vdots & \vdots & \vdots & \vdots \\ \vdots & \vdots & \vdots & \vdots & M_{(N-1)N} & \vdots & \vdots \\ M_{N1} & \cdots & \cdots & M_{N(N-1)} & L_{NN} & M_{NR_x} & M_{NT_x} \\ M_{R_x1} & \cdots & \cdots & M_{R_x(N-1)} & M_{R_xN} & L_{R_xR_x} & M_{R_xT_x} \\ M_{T_x1} & \cdots & \cdots & M_{T_x(N-1)} & M_{T_xN} & M_{T_xR_x} & L_{T_xT_x} \end{bmatrix} \quad (7.12)$$

where the subscript of each symbol denotes the winding to which the self- or mutual inductance coefficient refers. The metamaterial cells are numbered based on their position in the array as described for the metasurface of Fig. 7.1. However, the numbering of the cells is clearly arbitrary and does not affect the generality of the analysis. From  $\mathbf{M}_{M_{tot}}$ , the impedance matrix  $\hat{\mathbf{Z}}_{M_{tot}}$  at the angular frequency  $\omega$  can be derived, and results:

$$\hat{\mathbf{Z}}_{M_{tot}} = \begin{bmatrix} \hat{Z}_{11} & j\omega M_{12} & j\omega M_{13} & \cdots & j\omega M_{1N} & j\omega M_{1R_x} & j\omega M_{1T_x} \\ j\omega M_{21} & \hat{Z}_{22} & j\omega M_{23} & \cdots & j\omega M_{1N} & j\omega M_{2R_x} & j\omega M_{2T_x} \\ \vdots & \vdots & \vdots & \vdots & \vdots & \vdots & \vdots \\ \vdots & \vdots & \vdots & \vdots & j\omega M_{(N-1)N} & \vdots & \vdots \\ j\omega M_{N1} & \cdots & \cdots & j\omega M_{N(N-1)} & \hat{Z}_{NN} & j\omega M_{NR_x} & j\omega M_{NT_x} \\ j\omega M_{R_x1} & \cdots & \cdots & j\omega M_{R_x(N-1)} & j\omega M_{R_xN} & \hat{Z}_{R_xR_x} & j\omega M_{R_xT_x} \\ j\omega M_{T_x1} & \cdots & \cdots & j\omega M_{T_x(N-1)} & j\omega M_{T_xN} & j\omega M_{T_xR_x} & \hat{Z}_{T_xT_x} \end{bmatrix}. \quad (7.13)$$

It can be proved that the network is reciprocal and both  $\mathbf{M}_{M_{tot}}$  and  $\hat{\mathbf{Z}}_{M_{tot}}$  result symmetric. Moreover, being all the resonators identical, their resistance and self-inductance can be considered the same and are named as  $R_{res}$ ,  $L_{res}$ , respectively. Being the resonators made of Litz wires, it is assumed that the resistance and inductance parameters do not vary considerably with respect to the one calculated with FEM magnetostatic simulations. However, this assumption does not affect the generality of the analysis. The impedance of the cell in the generic position  $m$  reduces to:

$$\hat{Z}_{mm} = R_{res} + j\omega L_{res} + \frac{1}{j\omega C_{mm}} \quad (7.14)$$

while the capacitance can have a different value depending on the considered resonator. The resonant angular frequency of the generic  $m$ th resonator of the array is then expressed as:

$$\omega_{mm} = \frac{1}{\sqrt{L_{res}C_{mm}}} \quad (7.15)$$

It is convenient to introduce a coefficient  $K_{mm}$  for the generic  $m$ th resonator defined as:

$$K_{mm} = \frac{\omega_{mm}}{\omega_0} \quad (7.16)$$

which provides an indication of the deviation of the resonant angular frequency of the considered cell from the one at which the transmitting and receiving circuits work, that is  $\omega_0$ . The transmitter and receiver resistance and inductance parameters can be considered the same and are named as  $R$  and  $L$ , respectively. Moreover, the

transmitter and receiver circuits are tuned to operate at the reference frequency  $\omega_0$ , which is assumed fixed in this analysis and thus also their series capacitance is the same, referred to as  $C$ . Their impedances are then defined as, respectively:

$$\hat{Z}_{T_x} = R + j\omega_0 L + \frac{1}{j\omega_0 C} \quad (7.17)$$

and

$$\hat{Z}_{R_x} = R + R_{load} + j\omega_0 L + \frac{1}{j\omega_0 C} \quad (7.18)$$

where  $R_{load}$  is the receiver load defined as in Sec. 2.5. In this system, the efficiency of the power transfer is calculated as:

$$\eta_{tot} = \frac{\text{Re}[\hat{Z}_{M_{tot}}] |\hat{I}_{R_x}|^2}{\text{Re}[\hat{V}_s \hat{I}_{T_x}^*]} \quad (7.19)$$

where  $\hat{I}_{T_x}$  and  $\hat{I}_{R_x}$  are the transmitter and receiver resonator phasor currents, respectively. The currents are found solving the system:

$$\hat{\mathbf{V}} = \hat{\mathbf{Z}}_{M_{tot}} \hat{\mathbf{I}} \quad (7.20)$$

where  $\hat{\mathbf{I}}$  is the vector of the phasor currents flowing in the resonators and  $\hat{\mathbf{V}} = [0 \dots 0 \hat{V}_s]^T$  is the phasor voltage vector with  $\hat{V}_s$  the phasor supply voltage applied to the transmitter coil. The main goal of the metamaterial is to make the total efficiency  $\eta_{tot}$  of the system increase compared to the case in which only the transmitter and receiver circuits are present. For the two-coil system, the efficiency is defined as:

$$\eta_{ref} = \frac{\text{Re}[\hat{Z}_{M_{ref}}] |\hat{I}_{R_x,ref}|^2}{\text{Re}[\hat{V}_s \hat{I}_{T_x,ref}^*]} \quad (7.21)$$

where  $\hat{Z}_{M_{ref}}$  is the impedance matrix that considers the transmitter and receiver circuits only, and  $\hat{I}_{T_x,ref}$  and  $\hat{I}_{R_x,ref}$  the respective currents in absence of the meta-surface. These currents are obtained by solving:

$$\hat{\mathbf{V}} = \hat{\mathbf{Z}}_{M_{ref}} \hat{\mathbf{I}}_{ref} \quad (7.22)$$

where  $\hat{\mathbf{I}}_{ref}$  is the vector of the phasor currents flowing in the resonators and  $\hat{\mathbf{V}}_{ref} = [0 \ \hat{V}_s]^T$  is the phasor voltage vector with  $\hat{V}_s$  the phasor supply voltage applied to the transmitter coil.

### 7.3.2 Optimisation Procedure

The numerical calculation of the resonant frequency of the cells that allows the efficiency of the overall system  $\eta_{tot}$  to be maximised can be addressed as an optimisation problem. In particular, the problem consists in finding the values of the 25  $K_{mm}$  coefficients (see (7.16)) that maximise  $\eta_{tot}$ . This corresponds to finding

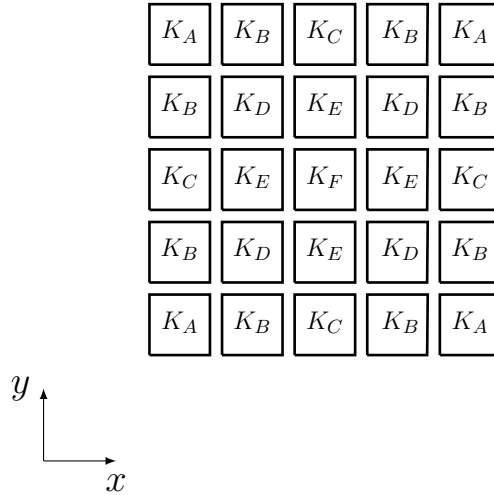


Figure 7.10: Schematic representation of the 2D array of  $5 \times 5$  resonators. The cells with the same tuning are indicated with the same parameter  $K$ . Six different tunings are possible.

the optimal values of the cell resonant angular frequencies  $\omega_{mm}$ . Formally, it is a single-objective optimisation problem of 25 variables and it can be expressed as:

$$\min_{K_{mm}} \left\{ \frac{1}{\eta_{tot}} \right\}. \quad (7.23)$$

To reduce the size of the problem, it is possible to exploit the symmetry of the system. Indeed, the resonators placed at the same distance from the axis of the system (that is the one of the transmitter and receiver coils) have the same coupling coefficients and therefore the same mutual inductances in the matrix  $\mathbf{M}_m$ . These resonators have the same impedance. In the  $5 \times 5$  array, the number of parameters reduces to six, named  $K_A$ ,  $K_B$ ,  $K_C$ ,  $K_D$ ,  $K_E$  and  $K_F$ , that corresponds to the variables of the optimisation process. The cells with the same tuning are indicated with the same parameter  $K$  in Fig. 7.10. The problem has been solved by implementing a PSO algorithm, which finds the value of the six varying coefficients  $K$ .

As a case study, the calculation has been performed considering a transmitter and receiver axial distance (in the  $z$  direction) of 300mm. In particular, the reference is set so that the receiver lies on the plane  $z = 0$  and, being the windings 11mm thick, the transmitter lies on the plane  $z = 311$ mm. The receiver is loaded with  $R_{load} = 2\Omega$  and the transmitter is fed by a sinusoidal voltage  $\hat{V}_s = 50V$  at the frequency  $f_0 = 85\text{kHz}$ . The system without the metamaterial has an efficiency of  $\eta_{ref} = 0.43$ . Then, the metamaterial is introduced and three different positions have been considered, in which the metasurface lies on the plane  $z_1 = 41$ mm (it is close to the transmitter),  $z_1 = 161$ mm (in the middle) and  $z_3 = 269$ mm (close to the receiver). After a first heuristic evaluation of possible limits for the parameter

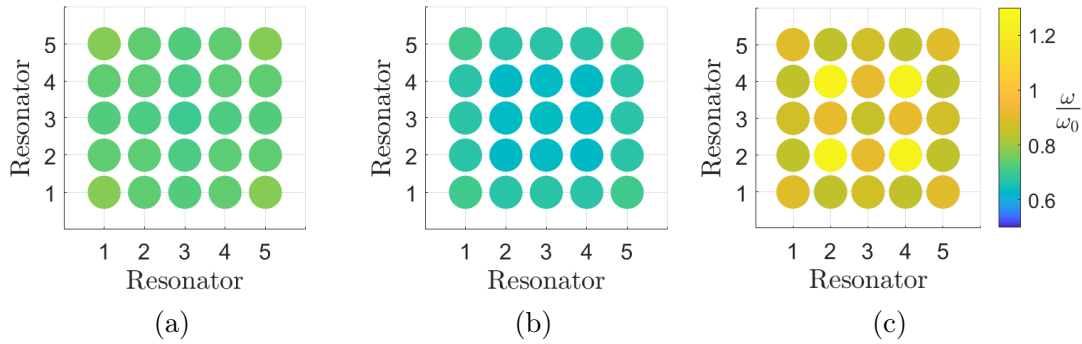


Figure 7.11: Resonant frequency of the metamaterial cells normalised with respect to the operating frequency  $\omega_0$  of the IPT system when the slab lies on the planes (a)  $z_1$ , (b)  $z_2$  and (c)  $z_3$ .

values, the variation range of each variable  $K$  has been set to  $[0.1, 5]$  in order to leave the algorithm free to operate. The tuning resulting from the optimisation is shown in Figs. 7.11a - 7.11c where the normalised resonant frequency of each resonator is plotted for the  $z_1$ ,  $z_2$ ,  $z_3$  slab positions, respectively. The resulting IPT system efficiency for the three cases are:

- $\eta_{tot} = 51\%$  for  $z_1$ ;
- $\eta_{tot} = 81\%$  for  $z_2$ ;
- $\eta_{tot} = 56\%$  for  $z_3$ ,

proving the effectiveness of the nonperiodic metamaterial in increasing the efficiency. The results show that in the case of a metamaterial close to the transmitter or receiver coils, the efficiency improvement is modest compared to the case in which it is placed in the middle. This can be easily explained considering that the couplings between the resonators of the metamaterial and the receiver are very weak when the slab is positioned on the  $z_1$  plane, and those between the resonators and the transmitter are very weak when the metamaterial lies on the plane  $z_3$ , due to their relative distance. This inevitably compromises the efficiency of the power transfer. In the case of metamaterial positioned on the plane  $z_2$ , the couplings of the cells to the transmitter and receiver coils are ideally equal and with a value large enough to make the system operate with 80 % of efficiency at  $f_0$ . The plots of Fig. 7.11 show that the optimal operations require the unit cells to be tuned differently. For the positions  $z_1$  and  $z_2$  the resonance frequency of the cells is lower than  $\omega_0$  and, therefore, the impedance of the cells is inductive at the working frequency. In the case of a slab close to the receiver, the cells exhibit a capacitive behaviour at  $\omega_0$ . Since the tuning is optimised to maximise the efficiency, results are strongly related to the mutual couplings between the circuits of the system, which strongly vary depending on the metamaterial position (neglecting skin and proximity effects).

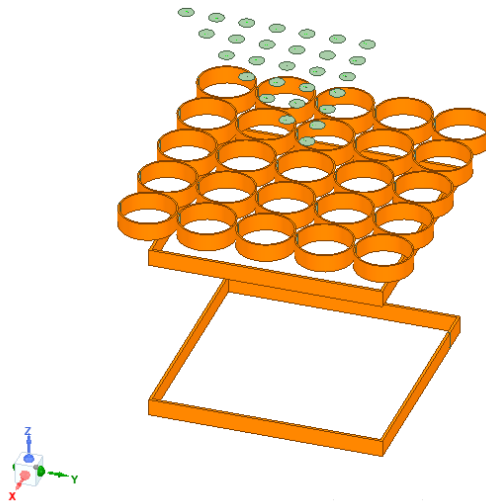


Figure 7.12: Isometric view of the system composed of the transmitting and a receiving square wound coils with the 5x5 array made of round wound coils. The green circles indicate the field probe coils.

However, it should be noted that in the positions  $z_1$  and  $z_2$  the tuning difference between the various cells is modest, and therefore, for the considered metasurface, it is reasonable to assume that an equal tuning leads to similar results, especially if we consider a practical implementation.

### 7.3.3 2D Resonator Array for Magnetic Field Shielding

As discussed in the Introduction, 2D arrays (or metamaterial slabs) can also be used to attenuate the magnetic field in a certain region of the space. In a IPT system, the shielding of the magnetic field in the vicinity of the structure is essential, whether the system operates at low power (i.e. for consumer electronics applications) or for high power (i.e. automotive applications). Metamaterials employed for magnetic field shielding present the same structure as the one used for magnetic field focusing. The different behaviour of the metamaterial slab depends on the resonator tuning. An optimised procedure for the tuning of the resonators is proposed and it is applied to the IPT system already described in 7.3.1.

However, now the aim is the shielding of the magnetic field in the region upstream of the receiver, but the same algorithm can be implemented for the tuning of metamaterials placed at any position. The arrangement of the coils is shown in Fig. 7.12. While the transmitter still lies on the plane  $z = 0$ , the receiver coils is now at the distance  $z = 111\text{mm}$ , so that an efficiency  $\eta_{ref}$  of 94% can be reached with the same load  $R_{load} = 2\Omega$ . This example aims at showing the effect of the different tuning of the resonators for the magnetic field shielding in a two-coils IPT system. The metamaterial is then placed on the plane  $z = 131\text{mm}$ , which is 20mm above the receiver. To evaluate the shielding effectiveness (SE) of the slab, it is essential to

identify the region in which the magnetic field is evaluated. In this example, a plane  $z_{SE} = 181\text{mm}$ , namely 40mm downstream of the metasurface, has been chosen. As already discussed in Sec. 7.3.1, the symmetry of the system allows only six variables to be considered. Similar considerations hold for the field points on the plane  $z_{SE}$ . Indeed, due to the system symmetry, the magnetic field at all the points in a symmetric position with respect to the  $z$  axis must have the same value in magnitude. Thus, the magnetic field for the optimisation procedure is evaluated in the 28 points depicted in Fig. 7.12. To evaluate the field with the numerical procedure, 28 additional small coils are introduced in the model as field probes, in correspondence of the field points. An arbitrary number  $N_p$  of probes can be however introduced, determining the resolution of the field map. These probe coils are enforced to be in open-circuit, and thus they do not affect the current distribution in the other circuits. In this way, assuming the probe coils are sufficiently small to consider the magnetic flux through their surface is uniform, the magnetic flux through the area of the  $i$ th field probe results:

$$B_i = \frac{V_i}{\omega_0 A_i} \quad (7.24)$$

where  $V_i$  is the amplitude of the phasor voltage  $\hat{V}_i$  induced in the  $i$ th probe by the system coils, which is expressed as:

$$\hat{V}_i = j\omega_0 \sum_k M_{ki} \hat{I}_k \quad (7.25)$$

with  $\hat{I}_k$  the current of the generic  $k$ th circuit of the IPT system and  $M_{ki}$  the mutual inductance between the  $k$ th circuit and the  $i$ th field probe. For the considered IPT system, the circuits are 27, namely 25 resonators forming the metasurface, the transmitter circuit and the receiver one. Then, an average magnetic field  $B_{\text{AVG}}$  is introduced for the calculation of the SE, which is defined as:

$$B_{\text{AVG}} = \frac{1}{N_p} \sum_i B_i. \quad (7.26)$$

The same procedure must be repeated considering the system without the metasurface to calculate the reference average magnetic field  $B_{\text{AVG},ref}$ , still at  $\omega_0$ , that corresponds to the average unshielded magnetic field on the plane  $z_{SE}$ . Then, the average shielding effectiveness is calculated as:

$$SE_{\text{AVG}} = 20 \log_{10} \frac{B_{\text{AVG}}}{B_{\text{AVG},ref}}. \quad (7.27)$$

### 7.3.4 Optimisation Procedure

The optimisation procedure consists in finding the optimal resonant angular frequencies of the metamaterial resonators such that the average shielding effectiveness is

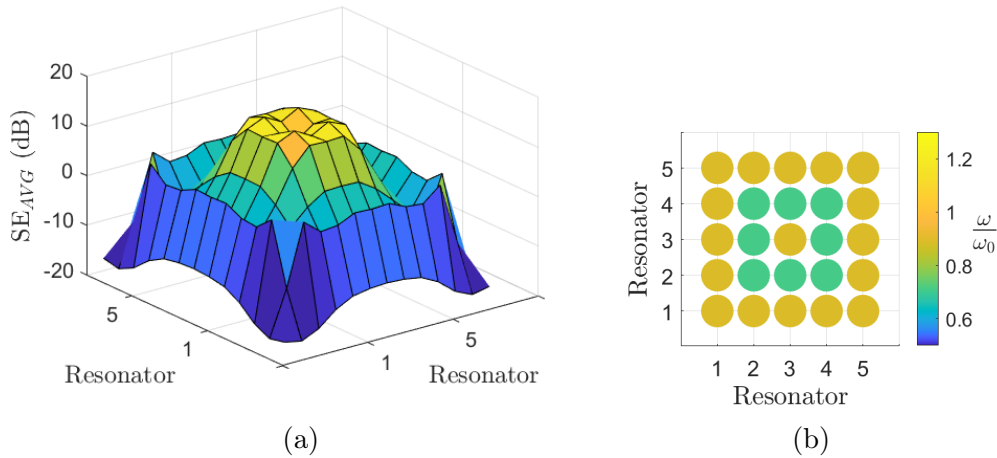


Figure 7.13: (a) Average SE in the plane  $z_{SE} = 40\text{mm}$  above the metamaterial and (b) resonant frequency of the cells normalised with respect to the operating frequency  $\omega_0$  of the IPT system when the slab is positioned at  $z = 131\text{mm}$ .

maximum. Mathematically, this procedure results in a multi-objective optimisation problem with 6 real variables expressed as:

$$\min_{K_{mn}} \left\{ \frac{1}{SE_{AVG}} \right\}. \quad (7.28)$$

The resulting SE for the plane at  $z = 40\text{mm}$  above the system is shown in Fig. 7.13a. The SE map is obtained with the cell tuning plotted in Fig. 7.13b, which shows that all the resonators present a resonant frequency lower than the  $\omega_0$ . At the centre of the plane the SE reaches 15dB, and then decreases when the points approach the boundaries of the plane. On the boundaries even negative values of SE are found, meaning that the field is amplified. It is reasonable to think that this is due to the fringing field, also referred to as edge-effect. To ensure a consistent SE in a wider area, it is required to extend the array, adding resonators or increasing their dimension.

Future developments of this algorithm foresee the addition of more objectives in the optimisation procedure, including that of maximising efficiency to prevent that the tuning for very high SE values deteriorates the efficiency of the system. In addition, the self-inductance of the individual cells can be also optimised. However, this requires working on the geometric model of the cell and not only on the circuit model.

## 7.4 Conclusions

Possible applications of 2D arrays of magnetically coupled resonators in IPT systems have been discussed. In general, it is shown that, depending on the extension of the

---

array and the cell parameters, the proper coupling model must be adopted. The idea of using the 2D array as a transmitter has revealed some critical issues in the control of the currents. Similarly to the case of 1D resonators, it is necessary to control more variables to properly manage the current distribution and ensure good performance. This can be achieved by inserting proper terminations on the boundaries, but they require a suitable control that has to be defined. When introduced into two-coil IPT devices, resonator arrays are treated as metamaterials. By properly tuning the resonators it is possible to improve efficiency in loosely coupled systems and an optimisation process has been proposed. These early results indicate that it is cost-effective in terms of efficiency to consider tuning the coils differently from each other. Moreover, the independent tuning of the metamaterial cells may also allow the magnetic field in a region of the space to be shielded. Future developments of this algorithm foresee extensions to consider the optimisation of the coil geometry and the number of cells. It can be concluded that, being the cells tuned differently, the metamaterial structure is no more periodic. This solution is suitable for the control of the magnetic near-field, for both focusing and shielding.



# Chapter 8

## Conclusions

The role of arrays of resonators in inductive power transfer systems has been discussed. As a first step, an analysis of the state of the art of passive compensation networks has revealed that the most efficient (and widespread) topologies are the series-series and series-parallel networks. In this frame, a simple circuit-based design procedure has been developed for both the compensation strategies, which aims at being simple to be implemented and therefore does not require complex iterative processes. Optimal values for the inductance of the transmitting and receiving coils can be easily found on the basis of the type of load, the power of the system and the coupling condition. What it can be noted is that a parallel compensation of the receiver requires a considerably smaller secondary inductance than that of the series compensation case, at the cost of a higher current circulating in the winding and, consequently, a more severe thermal stress and higher generated magnetic field. Starting from the typical two coils system, the 1D arrays have been introduced.

These systems have been modelled as two-port networks, in order to focus the analysis on transmitted power and efficiency. Furthermore, in order to consider resonator arrays for power applications, they must necessarily be interfaced with other electrical devices, i.e. voltage source inverters and rectifiers. By means of the two-port representation, the resulting system can be seen as a typical isolated power converter, in which the array takes the place of the transformer. Analytical formulas of the two-port network parameters have been provided, thus allowing a straightforward analysis of the system even in the design phase. The study of the transmitted power and efficiency then led to the definition of an optimal control technique for resonator arrays with a receiver fed at the first cell. A new doubly-fed array topology has been proposed, which allows more power to be extracted from the source and then efficiently transferred to the load. The result is a constant power transfer for each position of the receiver, always at maximum efficiency.

Unfortunately, the analysis of the distribution of currents in the array revealed that current peaks are present in some resonators depending on the position and load of the receiver. The theory of magneto-inductive waves was found to be crucial to

fully understand the physical mechanism governing the distribution of the currents in the resonators. It also allowed a closed form expression of the current of a generic cell of the array to be derived in the absence of a receiver. The modelling of the array as a transmission line in the presence of a receiver has been carried out. The analogy has been established considering the chain matrix representation of coupled circuits. The research has underlined that the presence of loads introduces discontinuities in the characteristic impedance of the transmission line associated to the array, inevitably leading to reflections of the current wave. The results show that, even at low loads and at power much lower than the nominal one, these reflections lead to current peaks with values close to the maximum ones tolerated by the coils, with consequent thermal and electrical stress. To limit this phenomenon, it is advisable to use control strategies that maximise the transmitted power and in particular the efficiency, with specific attention to the reactive power at the input, which leads to an increase in the circulating current without improving its performance. In fact, the efficiency is calculated on the basis of the active power only. The reactive power can be controlled by acting on the input impedance of the array, which is however difficult to be controlled. The magnetic field generated by the array has been shown to reflect the trend of the currents and, therefore, it presents very high values in the vicinity of the apparatus. Especially when employed in civil infrastructure or domestic environments, these systems require proper shielding.

A circuit-based study of 1D resonator arrays with a receiver has led to the definition of an analytical form of the input impedance of these devices. It is valid for a receiver at any position and with a dimension such that it is coupled with two cells at a maximum, but it can be extended to receivers of any size. The behaviour of the input impedance is first of all useful for evaluating the input reactive power of the array, based on which soft switching conditions for the power inverters can be evaluated. However, it can be also used to estimate the position of the receiver. The straightforward application consists in detecting the receiver location in resonator arrays with a receiver employed for IPT. It must be noted that the optimal control techniques above discussed require its knowledge. Moreover, another possible and promising way of exploiting the peculiar behaviour of the input impedance consists in realising sensors that have the structure of an array of resonators, which can be installed in machines or industrial equipment. The simplicity of the circuit guarantees its moderate cost and modern PCB printing techniques can lead to the creation of very compact and light arrays, of any size. A study of the electronic circuitry required for the impedance estimation also allowed their practical feasibility to be evaluated, revealing that with modern DSPs it is possible to implement the proposed algorithm in a few milliseconds. Furthermore, the possibility of implementing a simplified version of the algorithm was also illustrated in resonator arrays for dynamic IPT in which each coil is powered independently. Because of the high magnetic field generated by arrays with single excitation, it is worth considering powering the resonators independently when the power rate of the systems increases

(i.e. EV charging). If the coils are magnetically coupled, by introducing appropriate compensation networks (the LCC topology has been considered) in the resonator supply drivers, it is possible to identify frequencies at which the system acts as an array of resonators with a receiver (which may also be non-resonant). It is therefore possible to estimate the input impedance at the appropriate frequency to detect the receiver location. However, the function that represents the input impedance is strongly dependent on the system parameters, and thus the application of this sensing technique must be considered in the design phase. The robustness of the parameters that may occur during operations and installation conditions has to be considered. In addition to the design, a calibration of the measuring system is then necessary to take into consideration fundamental variations of these parameters, as generally happens when using measuring instruments.

The extension of one-dimensional to two-dimensional resonator arrays has been introduced. 2D arrays are suitable for various applications in IPT systems. The most intuitive is to use them as transmitters to power one or more receivers that can be placed at any position over the array. However, the control of the current distribution is very complicated and cannot be done by only acting on the power source. In analogy with 1D arrays, it has been thought of introducing suitable impedances in the boundary resonators, but it is however difficult to find a general control technique. Furthermore, variable impedances require additional circuits to be introduced into the system, complicating its structure.

Other applications consider the introduction of resonator arrays in traditional two-winding systems, to improve their performance or shield the magnetic field they generate. The possibility of finding the optimal tuning of each resonator has been explored, thereby leading to structures that are no longer periodic. Based on preliminary simulations, this tuning technique has been proven to be effective. It can therefore be stated that, in the near field, the periodicity of the array elements is not necessary and it is convenient to optimise the parameters of each array cell separately. This is due to the structure of the magnetic near-field, that presents different vector values of the field at any point of the space (except for symmetries of the source geometry). In fact, each cell will be excited according to its position with respect to the source of the field (i.e. the coils of the IPT system) and therefore its action on the overall magnetic field distribution must be evaluated *ad hoc*.

Resonator arrays have been proven to be systems of great practical interest for various applications in IPT apparatuses. Their simple structure guarantees low manufacturing costs and the possibility of adapting the device to different application contexts. With a proper design and control, both one-dimensional and two-dimensional resonator arrays can help in making inductive near-field wireless power transfer systems more efficient, safe and convenient.



# Appendix A

## Inductance Calculation

When performing numerical simulations of wound coils using finite elements method (FEM), the presence of different turns leads to a large amount of air-copper interfaces, which requires a very fine mesh. To decrease the problem size it is possible to consider an equivalent thick current loop in place of the  $n$ -turns wound coil, as shown in Fig. A.1. The transformation must fulfil the energy conservation principle, namely requires that the energy of the original and equivalent systems is the same. From this constraint, other assumptions which further simplify the model can be derived, such as:

- same current density  $\bar{J}$
- same coil area

where the latter requires to consider the thick conductor volume as the union of the conductor-turn volumes and a loop current of  $n$  times larger. The self-inductance  $L$  of the thick coil can be derived from the magnetic energy  $W_m$  as:

$$L = \frac{2W_m}{I^2} \tag{A.1}$$

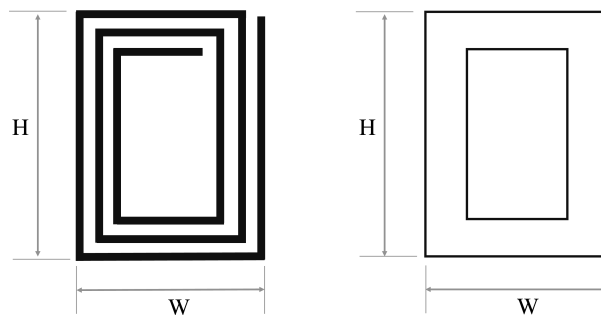


Figure A.1:  $n$  turn wound coil of size  $W \times H$  and its equivalent thick current loop.

The magnetic energy can be generally defined as:

$$W_m = \frac{1}{2} \iiint_{\tau} \bar{H} \cdot \bar{B} dV, \quad (\text{A.2})$$

or equivalently as:

$$W_m = \frac{1}{2} \iiint_{\tau} \bar{J} \cdot \bar{A} dV, \quad (\text{A.3})$$

where  $\tau$  is the volume of the (theoretically infinite) entire space and  $\bar{A}$  is the magnetic vector potential expressed as:

$$\bar{A} = \frac{\mu}{4\pi} \iiint_{\tau} \frac{\bar{J}}{r} dV \quad (\text{A.4})$$

with  $r$  the distance between the field point and the point source. Thus, if the equivalent winding inductance is defined preserving the distribution of  $J$ , it is possible to assume that the total stored energy  $W_m$  is the same. Hereinafter, the subscripts  $w$  and  $th$  denote that the related quantities are referred to the wound and thick representation of the coils. The self-inductance of a  $n$ -turns wound coil is defined as:

$$L_w = \frac{2W_m}{I_w^2} \quad (\text{A.5})$$

while for the thick loop it is:

$$L_{th} = \frac{2W_m}{I_{th}^2}. \quad (\text{A.6})$$

where  $I_w$  and  $I_{th}$  are the wound and thick coil currents, respectively. Being the  $W_m$  the same for the two systems, the self-inductance coefficients are related as:

$$L_w I_w^2 = L_{th} I_{th}^2. \quad (\text{A.7})$$

The currents of the two systems can be expressed as a function of the loop current density  $\bar{J}$ , which is assumed to be the same and perpendicular to the coil surface, resulting in:

$$\begin{aligned} JS_w &= I_w \\ JS_{th} &= I_{th} \end{aligned} \quad (\text{A.8})$$

and thus:

$$I_{th} = \frac{S_{th}}{S_w} I_w. \quad (\text{A.9})$$

The simplest and most intuitive way to size the equivalent thick coil is to set  $S_{th} = nS_w$ , and then excite it with  $I_{th} = nI_w$ . However, the goal is to obtain an equivalent system that is easier to analyse via FEM simulations. In particular, a planar winding for WPT requires 3D simulations as we have not seen particular symmetries in the system that allow us to reduce it to a 2D problem and therefore the model can be very extensive from a computational point of view. To facilitate the generation of the mesh in 3D problems, it is preferable to avoid curvilinear geometries and boundaries,

since they would require many elements (i.e. tetrahedrons in 3D problems) to obtain a satisfactory result. It is therefore convenient to consider a rectangular section for the dummy thick coil, which can be seen as the union of the circular sections of the single turns of the wound coil approximated with squares. To take into account this further approximation, the geometric factor  $\delta$  has been introduced and defined as:

$$\delta = \frac{S_{th}}{nS_w} \quad (\text{A.10})$$

leading to:

$$I_{th} = n\delta I_w. \quad (\text{A.11})$$

Introducing (A.11) in (A.7), it yields:

$$L_w = (n\delta)^2 L_{th}. \quad (\text{A.12})$$

These considerations can be extended to the calculation of the mutual inductance coefficient  $M_w$  between two current loops, defined as

$$M_w = \frac{W_m}{I_{w1} I_{w2}}, \quad (\text{A.13})$$

where  $I_{w1}$  and  $I_{w2}$  are the currents of the two coupled wound coils. Introducing equivalent thick coils, the mutual inductance is defined as:

$$M_{th} = \frac{W_m}{I_{th1} I_{th2}}. \quad (\text{A.14})$$

where  $I_{th1}$  and  $I_{th2}$  are the currents of the two coupled equivalent thick coils. Enforcing the conservation of energy, it holds:

$$M_w I_{w1} I_{w2} = M_{th} I_{th1} I_{th2} \quad (\text{A.15})$$

where the currents can be expressed, according to (A.8), as:

$$\begin{aligned} J_1 S_{w1} &= I_{w1} & J_1 S_{th1} &= I_{th1} \\ J_2 S_{w2} &= I_{w2} & J_2 S_{th2} &= I_{th2} \end{aligned} \quad (\text{A.16})$$

with  $J_1$  and  $J_2$  the magnitudes of the current density vectors (normal component) of the two coupled coils, assumed the same for the wound and thick coils representations. The thick and wound coil currents are related as:

$$I_{th1} = n_1 \delta_1 I_{w1} \quad I_{th2} = n_2 \delta_2 I_{w2} \quad (\text{A.17})$$

where geometric factors  $\delta_1$  and  $\delta_2$  are defined as, respectively:

$$\delta_1 = \frac{S_{th1}}{n_1 S_{w1}} \quad \delta_2 = \frac{S_{th2}}{n_2 S_{w2}}. \quad (\text{A.18})$$

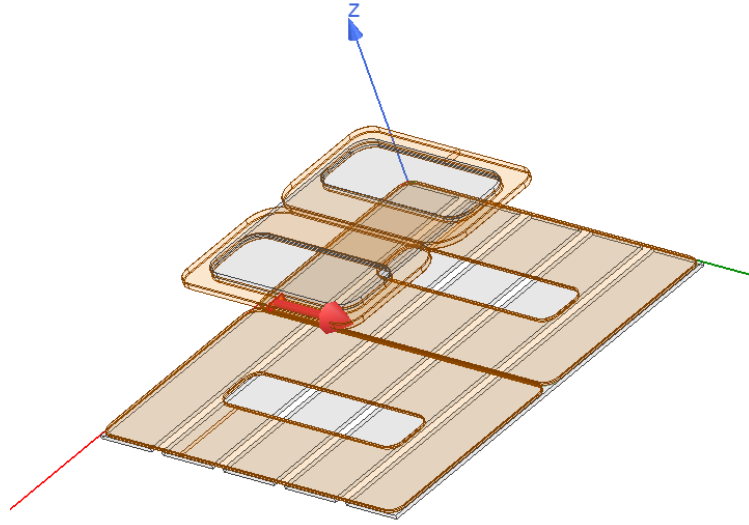


Figure A.2: Equivalent DD coils.

Introducing (A.17) in (A.15), it holds:

$$M_w = n_1 n_2 \delta_1 \delta_2 M_{th}. \quad (\text{A.19})$$

It can be also noticed that the coupling coefficient is invariant for the transformation. For wound and thick coils it is defined as, respectively:

$$k_w = \frac{M_w}{\sqrt{L_{w_1} L_{w_2}}} \quad k_{th} = \frac{M_{th}}{\sqrt{L_{th_1} L_{th_2}}} \quad (\text{A.20})$$

which can be easily proved to be equal, namely:

$$k_w = k_{th}. \quad (\text{A.21})$$

## Homogeneous DD Coils

The DD configuration (see Fig. A.2) is obtained considering two identical rectangular windings excited by currents with the same amplitude and opposite phases. Thus, both the transmitter and receiver circuits are represented by two thick coils, resulting in four total coils. The self- and mutual inductance coefficients of the real coils can be obtained by combining the ones of the four thick-coil model as:

$$\begin{aligned} L_T &= L_{T_1} + L_{T_2} + 2M_{T_1, T_2} \\ L_R &= L_{R_1} + L_{R_2} + 2M_{R_1, R_2} \\ M &= M_{T_1, R_1} + M_{T_1, R_2} + M_{T_2, R_1} + M_{T_2, R_2}, \end{aligned} \quad (\text{A.22})$$

where  $L_{T_1}$  and  $L_{T_2}$  are the self-inductances of the single thick coils that form the transmitting DD coil and  $L_{R_1}$  and  $L_{R_2}$  the self-inductances of the single thick coils that form the receiving DD coil. Then,  $M_{T_1, T_2}$ ,  $M_{R_1, R_2}$ ,  $M_{T_1, R_1}$ ,  $M_{T_1, R_2}$ ,  $M_{T_2, R_1}$  and  $M_{T_2, R_2}$  the corresponding mutual inductances.

# Bibliography

- [1] N. Tesla, "System of transmission of electrical energy," Mar. 1900.
- [2] M. Budhia, J. T. Boys, G. A. Covic, and C.-Y. Huang, "Development of a single-sided flux magnetic coupler for electric vehicle ipt charging systems," *IEEE Transactions on Industrial Electronics*, vol. 60, pp. 318–328, Dec. 2013.
- [3] SAE Recommended Practice J2954, "Wireless power transfer for light-duty plug-in/ electric vehicles and alignment methodology." SAE International: Troy, MI, USA, 2017.
- [4] L. Zhang, Y. Yang, Z. Jiang, Q. Chen, Q. Yan, Z. Wu, B. Zhang, J. Huangfu, and H. Chen, "Demonstration of topological wireless power transfer," *Science Bulletin*, vol. 66, pp. 974–980, May 2021.
- [5] Y. Cho, S. Lee, D.-H. Kim, H. Kim, C. Song, S. Kong, J. Park, C. Seo, and J. Kim, "Thin hybrid metamaterial slab with negative and zero permeability for high efficiency and low electromagnetic field in wireless power transfer systems," *IEEE Transactions on Electromagnetic Compatibility*, vol. 60, pp. 1001–1009, Sep. 2018.
- [6] J. C. Maxwell, *A Treatise on Electricity and Magnetism*. Oxford University, 1 ed., Oxford, UK, 1873.
- [7] N. Tesla, "Apparatus for transmitting electrical energy," Dec. 1914.
- [8] M. Qiu, "Research and classification of wireless power transfer with relative application," *Journal of Physics: Conference Series*, vol. 2108, p. 012036, Nov. 2021.
- [9] C. R. Valenta and G. D. Durgin, "Harvesting wireless power: Survey of energy-harvester conversion efficiency in far-field, wireless power transfer systems," *IEEE Microwave Magazine*, vol. 15, pp. 108–120, May 2014.
- [10] Q. Zhang, W. Fang, Q. Liu, J. Wu, P. Xia, and L. Yang, "Distributed laser charging: A wireless power transfer approach," *IEEE Internet of Things Journal*, vol. 5, pp. 3853–3864, June 2018.

- [11] A. Costanzo, M. Dionigi, D. Masotti, M. Mongiardo, G. Monti, L. Tarricone, and R. Sorrentino, "Electromagnetic energy harvesting and wireless power transmission: A unified approach," *Proceedings of the IEEE*, vol. 102, pp. 1692–1711, 2014.
- [12] M. P. Theodoridis, "Effective capacitive power transfer," *IEEE Transactions on Power Electronics*, vol. 27, pp. 4906–4913, Apr. 2012.
- [13] F. Lu, H. Zhang, and C. Mi, "A review on the recent development of capacitive wireless power transfer technology," *Energies*, vol. 10, Nov. 2017.
- [14] A. K. RamRakhyani, S. Mirabbasi, and M. Chiao, "Design and optimization of resonance-based efficient wireless power delivery systems for biomedical implants," *IEEE Transactions on Biomedical Circuits and Systems*, vol. 5, pp. 48–63, Feb. 2011.
- [15] Y. Yi, U. Buttner, Y. Fan, and I. G. Foulds, "Design and optimization of a 3-coil resonance-based wireless power transfer system for biomedical implants," *International Journal of Circuit Theory and Applications*, vol. 43, no. 10, pp. 1379–1390, 2015.
- [16] G. A. Covic and J. T. Boys, "Modern trends in inductive power transfer for transportation applications," *IEEE Journal of Emerging and Selected Topics in Power Electronics*, vol. 1, pp. 28–41, May 2013.
- [17] D. Patil, M. K. McDonough, J. M. Miller, B. Fahimi, and P. T. Balsara, "Wireless power transfer for vehicular applications: Overview and challenges," *IEEE Transactions on Transportation Electrification*, vol. 4, pp. 3–37, Dec 2017.
- [18] S. Li and C. C. Mi, "Wireless power transfer for electric vehicle applications," *IEEE Journal of Emerging and Selected Topics in Power Electronics*, vol. 3, pp. 4–17, Mar 2015.
- [19] V. Cirimele, M. Diana, F. Freschi, and M. Mitolo, "Inductive power transfer for automotive applications: State-of-the-art and future trends," *IEEE Transactions on Industry Applications*, vol. 54, pp. 4069–4079, May 2018.
- [20] R. Bosshard, U. Iruretagoyena, and J. W. Kolar, "Comprehensive evaluation of rectangular and double-d coil geometry for 50 kw/85 khz ipt system," *IEEE Journal of Emerging and Selected Topics in Power Electronics*, vol. 4, pp. 1406–1415, Aug. 2016.
- [21] L. Xue, V. Galigekere, G.-j. Su, R. Zeng, M. Mohammad, E. Gurpinar, S. Chowdhury, and O. Onar, "Design and analysis of a 200 kw dynamic wireless charging system for electric vehicles," in *2022 IEEE Applied Power Electronics Conference and Exposition (APEC)*, pp. 1096–1103, Houston, TX, USA, Mar. 20-24, 2022.

- [22] S. Sinha, S. Maji, and K. K. Afridi, "Comparison of large air-gap inductive and capacitive wireless power transfer systems," in *2021 IEEE Applied Power Electronics Conference and Exposition (APEC)*, pp. 1604–1609, Phoenix, AZ, USA, June 14–17, 2021.
- [23] T. Campi, S. Cruciani, F. Maradei, and M. Feliziani, "Magnetic field during wireless charging in an electric vehicle according to standard sae j2954," *Energies*, vol. 12, May 2019.
- [24] Z. M. Guilizzoni R., Harmon S., "Best practice guide for the assessment of emf exposure from vehicle wireless power transfer systems," *16ENG08 EMPIR MICEV consortium*, 2021.
- [25] H. Zhang, F. Lu, H. Hofmann, W. Liu, and C. C. Mi, "A four-plate compact capacitive coupler design and lcl-compensated topology for capacitive power transfer in electric vehicle charging application," *IEEE Transactions on Power Electronics*, vol. 31, pp. 8541–8551, Jan. 2016.
- [26] M. Z. Erel, K. C. Bayindir, M. T. Aydemir, S. K. Chaudhary, and J. M. Guerrero, "A comprehensive review on wireless capacitive power transfer technology: Fundamentals and applications," *IEEE Access*, vol. 10, pp. 3116–3143, Dec 2022.
- [27] W. Zhang and C. C. Mi, "Compensation topologies of high-power wireless power transfer systems," *IEEE Transactions on Vehicular Technology*, vol. 65, pp. 4768–4778, jun 2016.
- [28] C. Auvigne, P. Germano, D. Ladas, and Y. Perriard, "A dual-topology icpt applied to an electric vehicle battery charger," in *2012 XXth International Conference on Electrical Machines*, pp. 2287–2292, 2012.
- [29] M. Muratori, M. Alexander, D. Arent, M. Bazilian, P. Cazzola, E. M. Dede, J. Farrell, C. Gearhart, D. Greene, A. Jenn, M. Keyser, T. Lipman, S. Narumanchi, A. Pesaran, R. Sioshansi, E. Suomalainen, G. Tal, K. Walkowicz, and J. Ward, "The rise of electric vehicles—2020 status and future expectations," *Progress in Energy*, vol. 3, p. 022002, Mar. 2021.
- [30] R. Bosshard, J. W. Kolar, J. Mühlethaler, I. Stevanović, B. Wunsch, and F. Canales, "Modeling and  $\eta$  -  $\alpha$ -pareto optimization of inductive power transfer coils for electric vehicles," *IEEE Journal of Emerging and Selected Topics in Power Electronics*, vol. 3, pp. 50–64, mar 2015.
- [31] M. G. S. Pearce, H. Gao, A. Ramadugu, G. A. Covic, and J. T. Boys, "Robust double d topology for roadway ipt applications," in *2017 IEEE Energy Conversion Congress and Exposition (ECCE)*, pp. 2734–2741, Cincinnati, OH, USA, Oct. 1–5, 2017.

- [32] S. Li, W. Li, J. Deng, T. D. Nguyen, and C. C. Mi, "A double-sided lcc compensation network and its tuning method for wireless power transfer," *IEEE Transactions on Vehicular Technology*, vol. 64, pp. 2261–2273, Aug 2015.
- [33] J. L. Villa, J. Sallan, J. F. Sanz Osorio, and A. Llombart, "High-misalignment tolerant compensation topology for icpt systems," *IEEE Transactions on Industrial Electronics*, vol. 59, pp. 945–951, Aug. 2012.
- [34] J. Hou, Q. Chen, S.-C. Wong, C. K. Tse, and X. Ruan, "Analysis and control of series/series-parallel compensated resonant converter for contactless power transfer," *IEEE Journal of Emerging and Selected Topics in Power Electronics*, vol. 3, pp. 124–136, July 2015.
- [35] F. Grazian, W. Shi, J. Dong, P. van Duijsen, T. B. Soeiro, and P. Bauer, "Survey on standards and regulations for wireless charging of electric vehicles," in *2019 AEIT International Conference of Electrical and Electronic Technologies for Automotive (AEIT AUTOMOTIVE)*, pp. 1–5, Turin, Italy, July 2-4, 2019.
- [36] J. P. Smeets, T. T. Overboom, J. W. Jansen, and E. A. Lomonova, "Comparison of position-independent contactless energy transfer systems," *IEEE Transactions on Power Electronics*, vol. 28, pp. 2059–2067, Apr. 2013.
- [37] F. Zhang, S. A. Hackworth, W. Fu, C. Li, Z. Mao, and M. Sun, "Relay effect of wireless power transfer using strongly coupled magnetic resonances," *IEEE Transactions on Magnetics*, vol. 47, no. 5, pp. 1478–1481, 2011.
- [38] F. Zhang, S. A. Hackworth, W. Fu, C. Li, Z. Mao, and M. Sun, "Relay effect of wireless power transfer using strongly coupled magnetic resonances," *IEEE Transactions on Magnetics*, vol. 47, pp. 1478–1481, May 2011.
- [39] X. Zhang, S. L. Ho, and W. N. Fu, "Quantitative design and analysis of relay resonators in wireless power transfer system," *IEEE Transactions on Magnetics*, vol. 48, pp. 4026–4029, Nov. 2012.
- [40] J. Lee, K. Lee, and D.-H. Cho, "Stability improvement of transmission efficiency based on a relay resonator in a wireless power transfer system," *IEEE Transactions on Power Electronics*, vol. 32, pp. 3297–3300, Jan. 2017.
- [41] S. Moon, B. C. Kim, S. Y. Cho, C. H. Ahn, and G. W. Moon, "Analysis and design of a wireless power transfer system with an intermediate coil for high efficiency," *IEEE Transactions on Industrial Electronics*, vol. 61, pp. 5861–5870, June 2014.
- [42] A. Kurs, A. Karalis, R. Moffatt, J. D. Joannopoulos, P. Fisher, and M. Soljačić, "Wireless power transfer via strongly coupled magnetic resonances," *Science*, vol. 317, pp. 83–86, July 2007.

- [43] S. C. Moon and G. W. Moon, "Wireless Power Transfer System with an Asymmetric Four-Coil Resonator for Electric Vehicle Battery Chargers," *IEEE Transactions on Power Electronics*, vol. 31, pp. 6844–6854, oct 2016.
- [44] C. K. Lee, W. X. Zhong, and S. Y. R. Hui, "Effects of magnetic coupling of nonadjacent resonators on wireless power domino-resonator systems," *IEEE Transactions on Power Electronics*, vol. 27, pp. 1905–1916, Sep. 2012.
- [45] J. Lee and K. Lee, "Effects of number of relays on achievable efficiency of magnetic resonant wireless power transfer," *IEEE Transactions on Power Electronics*, vol. 35, pp. 6697–6700, Dec. 2020.
- [46] J. Alberto, U. Reggiani, L. Sandrolini, and H. Albuquerque, "Accurate calculation of the power transfer and efficiency in resonator arrays for inductive power transfer," *Progress In Electromagnetics Research B*, vol. 83, pp. 61–76, 2019.
- [47] C. J. Stevens, "Magnetoinductive waves and wireless power transfer," *IEEE Transactions on Power Electronics*, vol. 30, pp. 6182–6190, nov 2015.
- [48] F. S. Sandoval, A. Moazenzadeh, S. M. T. Delgado, and U. Wallrabe, "Double-spiral coils and live impedance modulation for efficient wireless power transfer via magnetoinductive waves," in *2016 IEEE Wireless Power Transfer Conference (WPTC)*, pp. 1–4, Aveiro, Portugal, 5-6 May, 2016.
- [49] F. S. Sandoval, A. Moazenzadeh, and U. Wallrabe, "Comprehensive modeling of magnetoinductive wave devices for wireless power transfer," *IEEE Transactions on Power Electronics*, vol. 33, pp. 8905–8915, Oct. 2018.
- [50] J. Pendry, A. Holden, D. Robbins, and W. Stewart, "Magnetism from conductors and enhanced nonlinear phenomena," *IEEE Transactions on Microwave Theory and Techniques*, vol. 47, pp. 2075–2084, Nov. 1999.
- [51] J. B. Pendry, "Negative refraction makes a perfect lens," *Phys. Rev. Lett.*, vol. 85, pp. 3966–3969, Oct 2000.
- [52] D. Schurig, J. J. Mock, B. J. Justice, S. A. Cummer, J. B. Pendry, A. F. Starr, and D. R. Smith, "Metamaterial electromagnetic cloak at microwave frequencies," *Science*, vol. 314, pp. 977–980, Nov. 2006.
- [53] J. B. Pendry, D. Schurig, and D. R. Smith, "Controlling electromagnetic fields," *Science*, vol. 312, pp. 1780–1782, June 2006.
- [54] G. V. Eleftheriades and K. G. Balmain, *Negative-Refraction Metamaterials: Fundamental Principles and Applications*. New York: Wiley, 2005.

- [55] D. Brizi, J. P. Stang, A. Monorchio, and G. Lazzi, "A compact magnetically dispersive surface for low-frequency wireless power transfer applications," *IEEE Transactions on Antennas and Propagation*, vol. 68, pp. 1887–1895, Jan. 2020.
- [56] D. Brizi, N. Fontana, S. Barmada, and A. Monorchio, "An accurate equivalent circuit model of metasurface-based wireless power transfer systems," *IEEE Open Journal of Antennas and Propagation*, vol. 1, pp. 549–559, Oct. 2020.
- [57] J. Zhou, P. Zhang, J. Han, L. Li, and Y. Huang, "Metamaterials and metasurfaces for wireless power transfer and energy harvesting," *Proceedings of the IEEE*, vol. 110, pp. 31–55, Nov. 2022.
- [58] M. J. Chabalko and D. S. Ricketts, "Low-frequency metamaterial permeability retrieval for near-field applications," in *2014 IEEE Antennas and Propagation Society International Symposium (APSURSI)*, pp. 233–234, Memphis, TN, USA, July 6-11, 2014.
- [59] S. A. Cummer, B.-I. Popa, and T. H. Hand, " $q$ -based design equations and loss limits for resonant metamaterials and experimental validation," *IEEE Transactions on Antennas and Propagation*, vol. 56, pp. 127–132, Jan. 2008.
- [60] B. Wei, S. Wang, C. Jiang, B. Jiang, H. He, and M. Liu, "Matrix metamaterial shielding design for wireless power transfer to control the magnetic field," *Materials*, vol. 15, Apr. 2022.
- [61] I. Khromova and C. J. Stevens, "Harnessing magneto-inductive waves for wireless power transfer," in *2018 IEEE Wireless Power Transfer Conference (WPTC)*, pp. 1–3, Montreal, QC, Canada, June 3-7, 2018.
- [62] F. Suárez Sandoval, S. M. Torres Delgado, A. Moazenzadeh, and U. Wallrabe, "A 2-d magnetoinductive wave device for freer wireless power transfer," *IEEE Transactions on Power Electronics*, vol. 34, pp. 10433–10445, Mar. 2019.
- [63] Y. Gao, M. Fu, H. Wang, and J. Liang, "A 2-d inductive power transfer network for powering massive neighboring iot devices," *IEEE Access*, pp. 1–1, Oct. 2022.
- [64] L. Solymar and E. Shamonina, *Waves in Metamaterials*. OUP Oxford, 2009.
- [65] R. R. Syms, E. Shamonina, and L. Solymar, "Magneto-inductive waveguide devices," *IEE Proceedings: Microwaves, Antennas and Propagation*, vol. 153, no. 2, pp. 111–121, 2006.
- [66] E. Shamonina and L. Solymar, "Magneto-inductive waves supported by metamaterial elements: Components for a one-dimensional waveguide," in *Journal*

- of Physics D: Applied Physics*, vol. 37, pp. 362–367, IOP Publishing, Feb. 2004.
- [67] E. Shamonina, V. A. Kalinin, K. H. Ringhofer, and L. Solymar, “Magnetoinductive waves in one, two, and three dimensions,” *Journal of Applied Physics*, vol. 92, no. 10, pp. 6252–6261, 2002.
- [68] M. Simonazzi, U. Reggiani, and L. Sandrolini, “Standing wave pattern and distribution of currents in resonator arrays for wireless power transfer,” *Energies*, vol. 15, Jan. 2022.
- [69] G. Puccetti, C. J. Stevens, U. Reggiani, and L. Sandrolini, “Experimental and numerical investigation of termination impedance effects in wireless power transfer via metamaterial,” *Energies*, vol. 8, pp. 1882–1895, Mar. 2015.
- [70] J. D. Jackson, *Classical Electrodynamics*. Wiley, 3 ed., 1999.
- [71] W. H. Hayt, *Engineering Electromagnetics*. New York : McGraw-Hill, 5 ed., 1989.
- [72] D. Bavastro, A. Canova, V. Cirimele, F. Freschi, L. Giaccone, P. Guglielmi, and M. Repetto, “Design of wireless power transmission for a charge while driving system,” *IEEE Transactions on Magnetics*, vol. 50, pp. 965–968, Feb. 2014.
- [73] M. Quirke, J. Barrett, and M. Hayes, “Planar magnetic component technology—a review,” *IEEE Transactions on Components, Hybrids, and Manufacturing Technology*, vol. 15, pp. 884–892, Oct. 1992.
- [74] Z. Ouyang and M. A. E. Andersen, “Overview of planar magnetic technology—fundamental properties,” *IEEE Transactions on Power Electronics*, vol. 29, pp. 4888–4900, Sep. 2014.
- [75] V. Väisänen, J. Hiltunen, J. Nerg, and P. Silventoinen, “Ac resistance calculation methods and practical design considerations when using litz wire,” in *IECON 2013 - 39th Annual Conference of the IEEE Industrial Electronics Society*, pp. 368–375, Vienna, Austria, Nov. 10-13, 2013.
- [76] M. Bartoli, N. Noferi, A. Reatti, and M. Kazimierczuk, “Modeling litz-wire winding losses in high-frequency power inductors,” in *PESC Record. 27th Annual IEEE Power Electronics Specialists Conference*, vol. 2, pp. 1690–1696 vol.2, Benevento, Italy, 23-27 June, 1996.
- [77] J. Ferreira, “Improved analytical modeling of conductive losses in magnetic components,” *IEEE Transactions on Power Electronics*, vol. 9, pp. 127–131, Jan. 1994.

- [78] M. Dionigi, M. Mongiardo, and R. Perfetti, "Rigorous network and full-wave electromagnetic modeling of wireless power transfer links," *IEEE Transactions on Microwave Theory and Techniques*, vol. 63, pp. 65–75, Dec. 2015.
- [79] C.-S. Wang, G. Covic, and O. Stielau, "Power transfer capability and bifurcation phenomena of loosely coupled inductive power transfer systems," *IEEE Transactions on Industrial Electronics*, vol. 51, no. 1, pp. 148–157, 2004.
- [80] H. Zhang, Y. Chen, S.-J. Park, and D.-H. Kim, "A hybrid compensation topology with single switch for battery charging of inductive power transfer systems," *IEEE Access*, vol. 7, pp. 171095–171104, Nov. 2019.
- [81] X. Qu, H. Han, S.-C. Wong, C. K. Tse, and W. Chen, "Hybrid ipt topologies with constant current or constant voltage output for battery charging applications," *IEEE Transactions on Power Electronics*, vol. 30, pp. 6329–6337, Jan. 2015.
- [82] Y. Chen, H. Zhang, S.-J. Park, and D.-H. Kim, "A switching hybrid lcc-s compensation topology for constant current/voltage ev wireless charging," *IEEE Access*, vol. 7, pp. 133924–133935, Sep. 2019.
- [83] W. Zhang, S.-C. Wong, C. K. Tse, and Q. Chen, "Analysis and comparison of secondary series- and parallel-compensated inductive power transfer systems operating for optimal efficiency and load-independent voltage-transfer ratio," *IEEE Transactions on Power Electronics*, vol. 29, no. 6, pp. 2979–2990, 2014.
- [84] Y. H. Sohn, B. H. Choi, E. S. Lee, G. C. Lim, G.-H. Cho, and C. T. Rim, "General unified analyses of two-capacitor inductive power transfer systems: Equivalence of current-source ss and sp compensations," *IEEE Transactions on Power Electronics*, vol. 30, pp. 6030–6045, Mar. 2015.
- [85] V. Cirimele, F. Freschi, and P. Guglielmi, "Wireless power transfer structure design for electric vehicle in charge while driving," in *2014 International Conference on Electrical Machines (ICEM)*, pp. 2461–2467, Berlin, Germany, Sep. 2-5, 2014.
- [86] J. Hou, Q. Chen, S.-C. Wong, X. Ren, and X. Ruan, "Output current characterization of parallel-series/series compensated resonant converter for contactless power transfer," in *2015 IEEE Applied Power Electronics Conference and Exposition (APEC)*, pp. 1625–1629, 2015.
- [87] V.-B. Vu, D.-H. Tran, and W. Choi, "Implementation of the constant current and constant voltage charge of inductive power transfer systems with the double-sided lcc compensation topology for electric vehicle battery charge applications," *IEEE Transactions on Power Electronics*, vol. 33, no. 9, pp. 7398–7410, 2018.

- [88] J. Yang, X. Zhang, K. Zhang, X. Cui, C. Jiao, and X. Yang, "Design of lcc-s compensation topology and optimization of misalignment tolerance for inductive power transfer," *IEEE Access*, vol. 8, pp. 191309–191318, Oct. 2020.
- [89] Z. Yan, Y. Zhang, B. Song, K. Zhang, T. Kan, and C. Mi, "An lcc-p compensated wireless power transfer system with a constant current output and reduced receiver size," *Energies*, vol. 12, no. 1, 2019.
- [90] Z. Huang, S.-C. Wong, and C. K. Tse, "Design methodology of a series-series inductive power transfer system for electric vehicle battery charger application," in *in Proc. IEEE Energy Conversion Congress and Exposition (ECCE)*, pp. 1778–1782, Pittsburgh, PA, USA, Sept. 14-18, 2014.
- [91] K. Aditya and S. S. Williamson, "Comparative study of series-series and series-parallel compensation topologies for electric vehicle charging," in *in Proc. IEEE 23rd International Symposium on Industrial Electronics (ISIE)*, pp. 426–430, Istanbul, Turkey, Jun. 1-4, 2014.
- [92] W. Zhang, S.-C. Wong, C. K. Tse, and Q. Chen, "Design for efficiency optimization and voltage controllability of series-series compensated inductive power transfer systems," *IEEE Transactions on Power Electronics*, vol. 29, no. 1, pp. 191–200, 2014.
- [93] K. V. Schuylenbergh and R. Puers, *Inductive Powering: Basic Theory and Application to Biomedical Systems*. Springer Science, 1 ed., 2009.
- [94] Y. Yao, Y. Wang, X. Liu, K. Lu, and D. Xu, "Analysis and design of an s/sp compensated ipt system to minimize output voltage fluctuation versus coupling coefficient and load variation," *IEEE Transactions on Vehicular Technology*, vol. 67, pp. 9262–9272, 2018 2018.
- [95] A. L. Ganga, V. Cirimele, R. Ruffo, and P. Guglielmi, "Fast hardware protection for a series-series compensated inductive power transfer system for electric vehicles," in *2017 IEEE Southern Power Electronics Conference (SPEC)*, pp. 1–6, Puerto Varas, Chile, Dec. 4-7, 2017.
- [96] G. Mattiussi and D. Varajao, *What are the advantages of SiC-based designs and how can you implement them? An overview of Infineon's SiC MOSFETs and dedicated gate driver ICs*. PSD Europe, Sep. 2020.
- [97] M. Simonazzi, L. Sandrolini, L. Zarri, U. Reggiani, and J. Alberto, "Model of misalignment tolerant inductive power transfer system for ev charging," in *in Proc. IEEE 29th International Symposium on Industrial Electronics (ISIE)*, pp. 1617–1622, Delft, The Netherlands, June 17-19, 2020.
- [98] N. Mohan, *Power Electronics: A First Course*. Wiley, 1 ed., 2011.

- [99] M. Kasper, R. M. Burkart, G. Deboy, and J. W. Kolar, "Zvs of power mosfets revisited," *IEEE Transactions on Power Electronics*, vol. 31, pp. 8063–8067, June 2016.
- [100] N. Femia, G. Di Capua, and R. A. P. Ohashi, "Harmonic analysis of diode-bridge rectifiers in wireless power transfer system," in *2017 14th International Conference on Synthesis, Modeling, Analysis and Simulation Methods and Applications to Circuit Design (SMACD)*, pp. 1–4, Giardini Naxos, Italy, June 12-15, 2017.
- [101] L. Geng, Z. Xue, S. Fan, D. Li, and B. Zhang, "Active rectifiers in wireless power transmission systems," in *2019 International Conference on IC Design and Technology (ICICDT)*, pp. 1–3, Suzhou, China, June 17-19, 2019.
- [102] P. Pham, S. Cochran, D. J. Costinett, and L. M. Tolbert, "Active rectifier design and synchronization control for 6.78 mhz wireless power transfer," in *2020 IEEE Energy Conversion Congress and Exposition (ECCE)*, pp. 5501–5508, Detroit, MI, USA, Oct. 11-15, 2020.
- [103] U. K. Madawala and D. J. Thrimawithana, "A bidirectional inductive power interface for electric vehicles in v2g systems," *IEEE Transactions on Industrial Electronics*, vol. 58, pp. 4789–4796, Feb. 2011.
- [104] L. Zhao, D. J. Thrimawithana, and U. K. Madawala, "Hybrid bidirectional wireless ev charging system tolerant to pad misalignment," *IEEE Transactions on Industrial Electronics*, vol. 64, pp. 7079–7086, Mar. 2017.
- [105] R. L. Steigerwald, "A Comparison Of Half-Bridge Resonant Converter Topologies," *IEEE Transactions on Power Electronics*, vol. 3, no. 2, pp. 174–182, 1988.
- [106] M. Chen and G. Rincon-Mora, "Accurate electrical battery model capable of predicting runtime and i-v performance," *IEEE Transactions on Energy Conversion*, vol. 21, pp. 504–511, June 2006.
- [107] O. Tremblay, L.-A. Dessaint, and A.-I. Dekkiche, "A generic battery model for the dynamic simulation of hybrid electric vehicles," in *2007 IEEE Vehicle Power and Propulsion Conference*, pp. 284–289, Arlington, TX, USA, Sep. 9-12, 2007.
- [108] A. Seaman, T.-S. Dao, and J. McPhee, "A survey of mathematics-based equivalent-circuit and electrochemical battery models for hybrid and electric vehicle simulation," *Journal of Power Sources*, vol. 256, pp. 410–423, June 2014.
- [109] M. Simonazzi, A. Campanini, L. Sandrolini, and C. Rossi, "Design procedure based on maximum efficiency for wireless power transfer battery chargers with lightweight vehicle assembly," *Energies*, vol. 15, Dec. 2021.

- [110] M. Simonazzi, A. Campanini, L. Sandrolini, and C. Rossi, "Single stage wireless power transfer battery charger for electric vehicles," in *in Proc. IEEE 15th International Conference on Compatibility, Power Electronics and Power Engineering (CPE-POWERENG)*, pp. 1–6, Florence, Italy, Jul. 14–16, 2021.
- [111] H. Yu, G. Zhang, L. Jing, Q. Liu, W. Yuan, Z. Liu, and X. Feng, "Wireless power transfer with HTS transmitting and relaying coils," *IEEE Transactions on Applied Superconductivity*, vol. 25, jun 2015.
- [112] W. Zhong, C. K. Lee, and S. Y. R. Hui, "General analysis on the use of tesla's resonators in domino forms for wireless power transfer," *IEEE Transactions on Industrial Electronics*, vol. 60, no. 1, pp. 261–270, 2013.
- [113] J. Alberto, U. Reggiani, L. Sandrolini, and H. Albuquerque, "Fast calculation and analysis of the equivalent impedance of a wireless power transfer system using an array of magnetically coupled resonators," *Progress In Electromagnetics Research B*, vol. 80, pp. 101–112, 2018.
- [114] L. Sandrolini, M. Simonazzi, S. Barmada, and N. Fontana, "Two-port network compact representation of resonator arrays for wireless power transfer with variable receiver position," *International Journal of Circuit Theory and Applications*, pp. 1–14, Dec. 2022.
- [115] A. Costanzo, M. Dionigi, F. Mastri, M. Mongiardo, J. A. Russer, and P. Russer, "Rigorous network modeling of magnetic-resonant wireless power transfer," *Wireless Power Transfer*, vol. 1, pp. 27–34, Mar. 2014.
- [116] P. Rehlaender, F. Schafmeister, J. Bocker, and T. Grote, "Analytical Topology Comparison for a Single Stage On-Board EV-Battery Converter," in *IEEE International Symposium on Industrial Electronics*, pp. 2477–2482, Vancouver, BC, Canada, Jun. 12–14, 2019.
- [117] A. Campanini, M. Simonazzi, M. Bosi, and C. Rossi, "Design and comparison between psfb and llc 400/48v dc/dc stage for on-board battery charger during total and partial cc-cv charging cycles," in *2022 IEEE 21st Mediterranean Electrotechnical Conference (MELECON)*, pp. 1102–1106, Palermo, Italy, June 14–16, 2022.
- [118] B. Esteban, M. Sid-Ahmed, and N. C. Kar, "A comparative study of power supply architectures in wireless ev charging systems," *IEEE Transactions on Power Electronics*, vol. 30, pp. 6408–6422, June 2015.
- [119] A. Costanzo, M. Dionigi, F. Mastri, M. Mongiardo, J. A. Russer, and P. Russer, "Rigorous design of magnetic-resonant wireless power transfer links realized with two coils," in *European Microwave Week 2014: Connecting*

- the Future, EuMW 2014 - Conference Proceedings; EuMC 2014: 44th European Microwave Conference*, pp. 414–417, Dec. 2014.
- [120] C. J. Stevens, C. W. T. Chan, K. Stamatis, and D. J. Edwards, “Magnetic metamaterials as 1-d data transfer channels: An application for magneto-inductive waves,” *IEEE Transactions on Microwave Theory and Techniques*, vol. 58, pp. 1248–1256, Apr. 2010.
- [121] C. W. T. Chan and C. J. Stevens, “Two-dimensional magneto-inductive wave data structures,” in *Proceedings of the 5th European Conference on Antennas and Propagation (EUCAP)*, pp. 1071–1075, Rome, Italy, 11-15 Apr., 2011.
- [122] C. J. Stevens, “Some consequences of the properties of metamaterials for wireless power transfer,” in *2015 9th International Congress on Advanced Electromagnetic Materials in Microwaves and Optics, METAMATERIALS 2015*, pp. 295–297, Institute of Electrical and Electronics Engineers Inc., Oxford, UK, Sep. 7-12, 2015.
- [123] D. Pozar, *Microwave Engineering*, vol. 2. 05 2004.
- [124] R. A. Chipman, *Schaum’s outline of theory and problems of transmission lines*,. McGraw-Hill, 1968.
- [125] W. T. Joines, W. D. Palmer, and J. T. Bernhard, *Microwave Transmission Line Circuits*. Artech House, 1 ed., 2013.
- [126] J. Alberto, U. Reggiani, and L. Sandrolini, “Circuit model of a resonator array for a WPT system by means of a continued fraction,” in *2016 IEEE 2nd International Forum on Research and Technologies for Society and Industry Leveraging a Better Tomorrow, RTSI 2016*, Bologna, Italy, Sept. 7-9, 2016.
- [127] T. Campi, S. Cruciani, V. De Santis, F. Maradei, and M. Feliziani, “Emc and emf safety issues in wireless charging system for an electric vehicle (ev),” in *2017 International Conference of Electrical and Electronic Technologies for Automotive*, pp. 1–4, Turin, Italy, June 15-16, 2017.
- [128] G. Giovannetti, “Comparison between circular and square loops for low-frequency magnetic resonance applications: theoretical performance estimation,” *Concepts in Magnetic Resonance Part B: Magnetic Resonance Engineering*, vol. 46B, no. 3, pp. 146–155, 2016.
- [129] L. Sandrolini, A. Massarini, and U. Reggiani, “Transform method for calculating low-frequency shielding effectiveness of planar linear multilayered shields,” *IEEE Transactions on Magnetics*, vol. 36, pp. 3910–3919, Nov. 2000.

- [130] L. Sandrolini, A. Massarini, and U. Reggiani, "Low-frequency multilayered magnetic shielding of circular loops," in *Proc. EMC Zurich '01, 14th International Zurich Symposium and Technical Exhibition*, pp. 17–22, Zurich, Switzerland, Feb. 20–22, 2001.
- [131] J. Yan, C. J. Stevens, and E. Shamonina, "A metamaterial position sensor based on magnetoinductive waves," *IEEE Open Journal of Antennas and Propagation*, vol. 2, pp. 259–268, Feb. 2021.
- [132] F. J. Herraiz-Martinez, F. Paredes, G. Zamora Gonzalez, F. Martin, and J. Bonache, "Printed magnetoinductive-wave (miw) delay lines for chipless rfid applications," *IEEE Transactions on Antennas and Propagation*, vol. 60, pp. 5075–5082, July 2012.
- [133] R. R. A. Syms, A. Voronov, and O. Sydoruk, "Hf rfid tag location using magneto-inductive waves," *IEEE Journal of Radio Frequency Identification*, vol. 6, pp. 347–354, June 2022.
- [134] Texas Instruments, "AMC1202 precision,  $\pm 50$ -mv input, basic isolated amplifier." <https://www.ti.com/product/AMC1202>, 2021.
- [135] Texas Instruments, "AMC3301 precision,  $\pm 250$ -mv input, reinforced isolated amplifier with integrated dc/dc converter." <https://www.ti.com/product/AMC3301>, 2021.
- [136] Broadcom, "ACPL-790B, ACPL-790A, ACPL-7900 precision isolation amplifiers." [https://www.mouser.it/datasheet/2/678/ub-005417\\_DS\\_ACPL-790x\\_2016-07-19-1143674.pdf](https://www.mouser.it/datasheet/2/678/ub-005417_DS_ACPL-790x_2016-07-19-1143674.pdf), 2016.
- [137] Texas Instruments, "Tms320c6652 and tms320c6654 fixed and floating-point digital signal processor." <https://www.ti.com/lit/gpn/tms320c6652.pdf>, 2019.
- [138] Texas Instruments, "Sm320c6712 floating point digital signal processors." <https://www.ti.com/lit/gpn/SM320C6712D-EP.pdf>, 2004.
- [139] M. Simonazzi, L. Sandrolini, and U. Reggiani, "Magnetic near field investigation and shielding effectiveness evaluation of an inductive power transfer system with a resonator array," in *2020 International Symposium on Electromagnetic Compatibility - EMC EUROPE*, pp. 1–5, Rome, Italy, Sep. 23–25, 2020.
- [140] J. Yang, X. Zhang, K. Zhang, X. Cui, C. Jiao, and X. Yang, "Design of LCC-s compensation topology and optimization of misalignment tolerance for inductive power transfer," *IEEE Access*, vol. 8, pp. 191309–191318, 2020.

- [141] L. Li, Y.-H. Liu, M. Fang, Z. Zheng, and H. Tang, "Vision-based intelligent forklift automatic guided vehicle (AGV)," in *2015 IEEE International Conference on Automation Science and Engineering (CASE)*, IEEE, aug 2015.
- [142] H.-Y. Yu, J.-J. Chen, and T.-R. Hsiang, "Design and implementation of a real-time object location system based on passive RFID tags," *IEEE Sensors Journal*, vol. 15, pp. 5015–5023, sep 2015.
- [143] J. Hernandez and C.-Y. Kuo, "Steering control of automated vehicles using absolute positioning gps and magnetic markers," *IEEE Transactions on Vehicular Technology*, vol. 52, pp. 150–161, jan 2003.
- [144] J. Y. Seong and S.-S. Lee, "Optimization of the alignment method for an electric vehicle magnetic field wireless power transfer system using a low-frequency ferrite rod antenna," *Energies*, vol. 12, p. 4689, dec 2019.
- [145] G. R. Nagendra, L. Chen, G. A. Covic, and J. T. Boys, "Detection of EVs on IPT highways," *IEEE Journal of Emerging and Selected Topics in Power Electronics*, vol. 2, pp. 584–597, sep 2014.
- [146] Y. Gao, A. A. Oliveira, K. B. Farley, and Z. T. H. Tse, "Magnetic alignment detection using existing charging facility in wireless EV chargers," *Journal of Sensors*, vol. 2016, pp. 1–9, 2016.
- [147] C. Liang, Y. Zhang, Z. Li, F. Yuan, G. Yang, and K. Song, "Coil positioning for wireless power transfer system of automatic guided vehicle based on magnetic sensing," *Sensors*, vol. 20, p. 5304, sep 2020.
- [148] X. Liu, C. Liu, W. Han, and P. W. T. Pong, "Design and implementation of a multi-purpose TMR sensor matrix for wireless electric vehicle charging," *IEEE Sensors Journal*, vol. 19, pp. 1683–1692, mar 2019.
- [149] S. Y. Jeong, H. G. Kwak, G. C. Jang, S. Y. Choi, and C. T. Rim, "Dual-purpose nonoverlapping coil sets as metal object and vehicle position detections for wireless stationary EV chargers," *IEEE Transactions on Power Electronics*, vol. 33, pp. 7387–7397, sep 2018.
- [150] S. G. Rosu, M. Khalilian, V. Cirimele, and P. Guglielmi, "A dynamic wireless charging system for electric vehicles based on DC/AC converters with SiC MOSFET-IGBT switches and resonant gate-drive," in *IECON 2016 - 42nd Annual Conference of the IEEE Industrial Electronics Society*, IEEE, Florence, Italy, Oct. 23-26, 2016.
- [151] S. Laporte, G. Coquery, V. Deniau, A. D. Bernardinis, and N. Hautière, "Dynamic wireless power transfer charging infrastructure for future EVs: From experimental track to real circulated roads demonstrations," *World Electric Vehicle Journal*, vol. 10, p. 84, Nov. 2019.

- 
- [152] K. Song, K. E. Koh, C. Zhu, J. Jiang, C. Wang, and X. Huang, “A review of dynamic wireless power transfer for in-motion electric vehicles,” in *Wireless Power Transfer - Fundamentals and Technologies*, InTech, jun 2016.
- [153] A. Grebene and H. Camenzind, “Phase locking as a new approach for tuned integrated circuits,” in *1969 IEEE International Solid-State Circuits Conference. Digest of Technical Papers*, vol. XII, pp. 100–101, Philadelphia, PA, USA, 19-21 Feb., 1969.
- [154] S. Barmada, N. Fontana, L. Sandrolini, and M. Simonazzi, “Optimal terminations of 2d meta-surfaces for uniform magnetic field applications,” *IEEE Transactions on Magnetics*, pp. 1–1, Dec. 2022.
- [155] D. Brizi and A. Monorchio, “An analytical approach for the arbitrary control of magnetic metasurfaces frequency response,” *IEEE Antennas and Wireless Propagation Letters*, vol. 20, pp. 1003–1007, Mar. 2021.